

**Imperial College
London**

**Layered double hydroxide-derived
oxygen carriers for chemical looping
processes**

Michael David High

2023

Supervised by: Professor Paul S. Fennell,

Dr Kyra L. Sedransk Campbell,

and Dr Qilei Song

This thesis is submitted for the degree of Doctor of Philosophy (PhD) to the Department of Chemical Engineering at the Imperial College London of Science, Technology and Medicine.

Abstract

In chemical looping combustion, the combustion reaction is split into two sub-reactions linked by metal oxide oxygen carriers to transfer oxygen from the air to the fuel. The oxygen carriers play a crucial role in chemical looping processes and must maintain high performance during extended redox cycling at high temperatures. The preparation of mixed metal oxides (MMOs) *via* the calcination of layered double hydroxide (LDH) precursors has been shown to achieve a high degree of dispersion of active metal oxide within the support due to the high degree of mixing of metals in the LDH structure. In this thesis, CuO-based oxygen carriers derived from LDHs for chemical looping processes were evaluated.

Novel CuO-based oxygen carriers supported on Al_2O_3 and MgAl_2O_4 were developed by tuning the synthetic chemistry of the LDHs prepared *via* co-precipitation at constant *pH*. The choice of co-precipitating agent was found to significantly affect the morphology of the LDHs and the dispersion of active CuO in the aluminate support phase in the MMOs. The oxygen carriers supported on MgAl_2O_4 showed much higher rates of oxygen release and re-oxidation and higher chemical stability than those supported on Al_2O_3 . The co-precipitation *pH* was determined to be an important parameter for tuning the mechanical properties of the MMOs. An increase in co-precipitation *pH* from 9.5 to 11 was found to decrease the porosity and increase the crushing strength of the MMOs. The higher-strength MMOs demonstrated near-constant conversion over extended redox cycling in a fluidised bed reactor.

For design, accurate knowledge of the intrinsic kinetics of the oxygen release reaction of the oxygen carriers is needed to scale up chemical looping reactors. The oxygen release kinetics were determined using an adapted effectiveness factor-based kinetic model. An activation energy of $51 \pm 3 \text{ kJ mol}^{-1}$ was calculated using an Arrhenius expression, which agreed well with values reported in the literature.

The formation mechanism of the Cu-Mg-Al LDHs was investigated by varying the co-precipitation *pH* value. The diameter and height of the LDH platelets and porosity of the bulk material were observed to generally decrease with increasing *pH*, except for LDHs synthesised at *pH* 10. The large LDH platelet diameters synthesised at *pH* 10 were attributed to an interplay of supersaturation, thermodynamic and electrostatic factors. The more porous MMOs synthesised at *pH* 9, 9.5 and 10 showed much higher rates of oxygen release than the less porous materials synthesised at *pH* 10.5, 11 and 11.5.

In this thesis, the LDH-MMO design strategy was shown to be effective for the development of CuO-based oxygen carriers with extremely high chemical stability and tuneable mechanical properties. The structural diversity of LDHs enables versatile combinations of metal ions to be highly dispersed in their structure, which could inspire the development of highly stable oxygen carriers for many emerging chemical looping processes.

Declaration of originality

I declare that the work presented in this thesis is primarily my own work and the work of others is appropriately referenced. I declare that I am the primary person responsible for the design, construction and preparation of this manuscript including the analysis of all the experimental data presented. Any work carried out as part of a collaborative work has been explicitly stated in the text.

Michael High, April 2023

Copyright declaration

The copyright of this thesis rests with the author. Unless otherwise indicated, its contents are licensed under a Creative Commons Attribution - Non Commercial 4.0 International Licence (CC BY-NC). Under this licence, you may copy and redistribute the material in any medium or format. You may also create and distribute modified versions of the work.

This is on the condition that: you credit the author and do not use it, or any derivative works, for a commercial purpose. When reusing or sharing this work, ensure you make the licence terms clear to others by naming the licence and linking to the licence text. Where a work has been adapted, you should indicate that the work has been changed and describe those changes.

Please seek permission from the copyright holder for uses of this work that are not included in this licence or permitted under UK Copyright Law.

Publications

This thesis led to the publication of the following papers:

High M, Patzschke CF, Zheng L, Zeng D, Gavalda-Diaz O, Ding N *et al.* Precursor engineering of hydrotalcite-derived redox sorbents for reversible and stable thermochemical oxygen storage. *Nat Commun* 2022; **13**: 5109.

High M, Patzschke CF, Zheng L, Zeng D, Xiao R, Fennell PS *et al.* Hydrotalcite-Derived Copper-Based Oxygen Carrier Materials for Efficient Chemical-Looping Combustion of Solid Fuels with CO₂ Capture. *Energy & Fuels* 2022; **36**: 11062–11076.

High M, Song Q, Campbell KLS, Fennell PS. Layered double hydroxide-derived copper-based oxygen carriers for chemical looping applications: Oxygen release kinetics and impact of loading on long-term performance. *Greenh Gases Sci Technol* 2023.

High M, Song Q, Campbell KLS, Fennell PS. Effect of co-precipitation pH on the growth of Cu-Mg-Al layered double hydroxides and the structure and performance of derived mixed metal oxides in chemical looping processes. (*in preparation*).

Papers and reports published during the PhD project but not used in this thesis:

Gonzalez-Garay A, Bui M, Freire Ordóñez D, **High M**, Oxley A, Moustafa N *et al.* Hydrogen Production and Its Applications to Mobility. *Annu Rev Chem Biomol Eng* 2022; **13**: 501–528.

High M. Carbon Capture Utilisation and Storage (CCUS) in Wales Senedd Research Briefing for the Welsh Parliament. 2022.

Fantuzzi A, Saenz Cavazos P, Moustafa N, **High M**, Bui M, Rutherford AW *et al.* Low-carbon fuels for aviation. 2023.

The Royal Society. Net zero aviation fuels: resource requirements and environmental impacts policy briefing. 2023.

Acknowledgements

Above all, I would like to thank my supervisors, Professor Paul Fennell, Dr Kyra Sedransk Campbell and Dr Qilei Song, for giving me the opportunity to study at Imperial College London. Paul, it has been a privilege to work with you and I will fondly remember my time in the Fennell group. Kyra, thank you for your scientific expertise, you pushed me to become a better researcher and it has been a pleasure to work with you. Qilei, thank you for your support and guidance during my studies and much of this work would not have been possible without you.

I would also like to thank all the present and past members of the Fennell, Campbell and Song groups. In particular, Dr Clemens Patzschke for his guidance and support throughout my PhD project and to Jose, with whom I started and ended this journey – it was great to experience this with you. I would also like to thank Jasper, David, Wahyu, Matt, Husain, Efty, Minos, Anqi, Rui, Zhiyu, Toby and Luke for their helpful discussions, assistance and company. I also thank Dr Patricia Carey and Kaho Cheung for their training and assistance in Analytical Services and the departmental staff who supported me.

I am fortunate to have many friends who have supported me over the past four years.

I would like to thank my friends at Imperial College London who have supported me along the way. Thanks to Frederik, Sean, Nadine, Paola, Lottie, Adam, Dale, Nikki, Anna-Maria and Anouk. Thank you all for the advice, friendships and memories. I'll never forget our time together. We made it through our studies and the pandemic and I look forward to celebrating your future successes.

I am very grateful to my friends, Georgie, Emily, Drasti, Claudia, Samara, Tiphaine, Sarah Atmore, Sarah Bailey, Zach, Miriam, Habiba, Deena, Niki, Courtney, Calyx, Diane, Zahra and Martin who have supported me throughout my PhD.

I am even more fortunate to have a wonderful family who continues to support me.

I thank my parents, Linda and Michael, for their endless support and confidence in me. I sincerely thank Jason, Stephanie, Callum, Karinna, James, Giorgio and Luca. None of you know what I do, but that's okay. To my triplets, Jamie and Adam, thank you for always being there for me. I feel blessed to have such a close relationship with you both.

Finally, to the most important person in my life, Sam. Thank you for your unending love, belief, patience and support.

Dedicated to my parents,

Linda and Michael

Start where you are. Use what you have. Do what you can.

Arthur Ashe

Table of contents

<i>Abstract.....</i>	<i>1</i>
<i>Declaration of originality.....</i>	<i>2</i>
<i>Copyright declaration</i>	<i>3</i>
<i>Publications</i>	<i>4</i>
<i>Acknowledgements.....</i>	<i>5</i>
<i>Chapter 1 - Introduction.....</i>	<i>19</i>
1.1 Problem statement	19
1.2 Project aims and objectives of the research project	23
1.3 Structure of the thesis	23
<i>Chapter 2 - Literature review.....</i>	<i>25</i>
2.1 Introduction	25
2.2 Chemical looping processes.....	26
2.3 Oxygen carrier requirements	31
2.5 Oxygen carrier materials.....	41
2.6 Natural ores and synthetic materials as oxygen carriers	44
2.7 Layered double hydroxides.....	52
2.8 Concluding remarks.....	59
<i>Chapter 3 - Experimental methods for material synthesis, characterisation and testing.....</i>	<i>61</i>
3.1 Introduction	61
3.2 Material synthesis	61
3.3 Material characterisation.....	64
3.4 Oxygen carrier testing.....	71
<i>Chapter 4 - Development of Cu-Mg-Al layered double hydroxides and derived oxygen carriers for chemical looping processes.....</i>	<i>80</i>
4.1 Introduction	80
4.2 Incorporation of Mg into the Cu-Al layered double hydroxide system	81
4.3 Thermodynamic analysis of the inhibition of Na-containing species in Cu-Mg-Al layered double hydroxide precursors.....	87
4.4 Effect of co-precipitating agent	90
4.5 Thermodynamic analysis of the inhibition of CuAl ₂ O ₄ by Mg.....	99
4.6 Concluding remarks.....	103
<i>Chapter 5 - Long term redox cycling of Cu-Mg-Al layered double hydroxide-derived oxygen carriers in thermogravimetric and fluidised bed systems.....</i>	<i>105</i>
5.1 Introduction	105
5.2 Redox cycling in a thermogravimetric analyser.....	106
5.3 Redox cycling in a fluidised bed reactor.....	114
5.4 Synthesis of Cu-Mg-Al layered double hydroxides and mixed metal oxides with higher Cu contents	128
5.5 Concluding remarks.....	132

Chapter 6 - Kinetics of oxygen release from CuO-based mixed metal oxides derived from layered double hydroxides	135
6.1 Introduction	135
6.2 Model to derive intrinsic oxygen release kinetics.....	140
6.3 Methodology.....	142
6.4 Results	151
6.5 Concluding remarks.....	159
Chapter 7 - Effect of co-precipitation pH on the growth of Cu-Mg-Al layered double hydroxides and the structure and performance of derived mixed metal oxides	160
7.1 Introduction	160
7.2 Methodology.....	161
7.3 Synthesis of layered double hydroxide precursors.....	163
7.4 Thermal and structural evolution of layered double hydroxide precursors during calcination to form mixed metal oxides	190
7.5 Characterisation of mixed metal oxides.....	197
7.6 Long-term performance of mixed metal oxides in chemical looping processes	200
7.7 Concluding remarks.....	209
Chapter 8 - Conclusions and future work.....	211
8.1 Conclusions	211
8.2 Future work.....	215
Appendix.....	219
Copyright permissions.....	225
Nomenclature	227
Bibliography.....	237

List of Figures

Figure 1-1: Global net anthropogenic GHG emissions ($\text{Gt}_{\text{CO}_2, \text{eq}} \text{ yr}^{-1}$) 1990–2019. (a) shows aggregate annual global net anthropogenic GHG emissions by GHG from 1990 to 2019. The fraction of global emissions for each GHG is shown for 1990, 2000, 2010 and 2019; as well as the aggregate average annual growth rate between these decades. At the right side of (a), GHG emissions in 2019 are broken down into individual components with the associated uncertainties (90% confidence interval) indicated by the error bars. (b) shows global anthropogenic emissions individually for the period 1990–2019, normalised relative to 100 in 1990. Shaded areas indicate the uncertainty range. Adapted from IPCC ⁶	20
Figure 1-2: Share of UK electricity generation by fuel source, 2000-2021. ⁷ Other renewables includes stations burning biomass (e.g. wood), landfill gas and sewage sludge.	21
Figure 2-1: The CLC process, where Me_xO_y and $\text{Me}_x\text{O}_{y-1}$ denote the oxidised and reduced oxygen carrier, respectively.	26
Figure 2-2: Annual publications containing the keyword “chemical looping” since 2000. Data from Clarivate Web of Science. © Clarivate 2023. All rights reserved. The decline in publications for 2022 could be related to the impact of the COVID-19 pandemic.	27
Figure 2-3: iG-CLC fuel reactor scheme. Coal is used as a representative solid fuel, adapted from Adanez et al. ⁵⁰	29
Figure 2-4: CLOU fuel reactor scheme. Coal is used as a representative solid fuel, adapted from Adanez et al. ⁵⁰	30
Figure 2-5: Modified Ellingham diagrams for (a) Mn oxides, (b) Cu oxides, (c) Fe oxides and (d) Ni oxides. Data from FactSage. ⁶³	32
Figure 2-6: Equilibrium oxygen concentrations of $\text{Cu}_2\text{O}/\text{CuO}$, $\text{Mn}_2\text{O}_3/\text{Mn}_3\text{O}_4$ and $\text{CoO}/\text{Co}_3\text{O}_4$ systems as a function of temperature. Determined using FactSage. ⁶³	34
Figure 2-7: Interactions of commonly used active phase and support combinations. Each tile indicates the possible solid-state reaction products and their effect on the reactivity and performance of the oxygen carriers. Green (or one diagonal line) and red outlines (or three diagonal lines) indicate good and bad performance, respectively. The performance of the tiles with orange outlines (or two diagonal lines) depends on the reactor conditions and amount of support incorporated in the oxygen carrier, adapted from De Vos et al. ⁸²	40
Figure 2-8: Idealised structure of Cu-Mg-Al LDHs produced using GSAS-II. ¹⁷⁴	52
Figure 3-1: Schematic of the automated co-precipitation rig. The pH of the reaction vessel was maintained by controlling the rate of alkaline solution addition, adapted from Patzschke. ¹¹⁵	62
Figure 3-2: Example pH profile during LDH synthesis using the automated co-precipitation rig. Target constant pH value of 9 during co-precipitation.	63
Figure 3-3: Simplified schematic of the in-situ XRD diffractometer used for high temperature XRD analysis. Adapted from Patzschke. ¹¹⁵	66
Figure 3-4: The results of the XRF calibration. Mass fractions measured by XRF against the actual mass fractions of the samples prepared via mechanical mixing for the determination of the (a) MgO and (b) Al_2O_3 calibration function.	67
Figure 3-5: Crushing force measurement of an MMO particle in the 300–425 μm size range. MMOs were calcined from LDHs co-precipitated at pH 11 for 300 min.	71

Figure 3-6: TGA and external gas supply set-up. Adapted from Patzschke. ¹¹⁵	72
Figure 3-7: Set-up of the 3kWe FBR, adapted from Patzschke. ¹¹⁵ Inset shows the behavior of a bubbling spouted bed reactor, adapted from Zhang. ²⁰⁵	76
Figure 3-8: Diagram of the measurement system modelled as dead time and (a) series of CSTRs and (b) a single CSTR, adapted from Patzschke. ¹¹⁵	78
Figure 3-9: Measured and deconvoluted signal from the gas analyser. Gas switching between 10 vol% O ₂ and N ₂ at 875°C in the FBR ($u/u_{mf} = 4$) compared to a step function.	79
Figure 4-1: XRD patterns of Cu-Mg-Al LDH precursors and calcined mixed metal oxides prepared using 1 M Na ₂ CO ₃ and 1 M NaOH. (a) XRD patterns of CuMgAl-LDHs and (b), CuMgAl-MMO. The crystalline pattern in (a) corresponds to CuAl hydrotalcite (JCPDS 46-0099, 37-0360; vertical lines), Cu ₆ Al ₂ (OH) ₁₆ CO ₃ ·4H ₂ O (JCPDS 37-0630) and Mg ₆ Al ₂ (OH) ₁₆ CO ₃ ·4H ₂ O (JCPDS 22-0700; vertical dashed lines). Crystalline patterns in (b) correspond to CuO (JCPDS 80-1268; vertical lines) and MgAl ₂ O ₄ (JCPDS 73-1959, vertical dashed lines), respectively. The molar ratio of Cu:Mg:Al in the LDHs varies from 3:0:2 to 3:1:2, as indicated.	82
Figure 4-2: Normalised weight percentage of Na ₂ O and MgO in the LDH precursors and calcined MMOs calculated from ICP and XRF measurements.	84
Figure 4-3: Characterisation of the Cu-Mg-Al LDH. (a) STEM and (b) HAADF-STEM images of the Cu-Mg-Al LDH precursor (c) element mapping of the Cu-Mg-Al-LDH precursor, Cu (red), Al (green), Mg (yellow), and O (blue); SEM images of the (d) Cu-Mg-Al LDH and (e) derived-MMO. The LDH precursor sample was prepared using a molar Cu:Mg:Al ratio of 3:1:2.	85
Figure 4-4: Characterisation of the Cu-Mg-Al MMO. (a-b) STEM image of the Cu-Mg-Al MMO; (c) HR-TEM images of the Cu-Mg-Al MMO; (d) STEM image of the calcined the Cu-Mg-Al MMO; (e) HR-TEM image of the Cu-Mg-Al MMO with insets showing the fast Fourier transform (FFT) patterns of different regions. The Cu-Mg-Al MMO sample was prepared by calcining up the CuMgAl-LDH (Cu:Mg:Al = 3:1:2) to 800°C and cooling down to room temperature.	86
Figure 4-5: Plots of equilibrium compositions (a) in the absence and (b) presence of Mg ions as a function of the pH value. The plots were generated with SPANA (formerly MEDUSA) using data from DATABASE (formerly HYDRA), ²¹² as well as literature values for the compounds listed in Table 4-3.	88
Figure 4-6: XRD patterns of Cu-Mg-Al LDH precursor and calcined MMOs prepared using 2 M NaOH. (a) XRD patterns of Cu-Mg-Al LDHs and (b) Cu-Mg-Al MMO. The crystalline patterns in (a) correspond to Cu-Al hydrotalcite (JCPDS 37-0360), and in (b) correspond to CuO (JCPDS 80-1268; vertical lines) and MgAl ₂ O ₄ (JCPDS 73-1959, vertical dashed lines), respectively. The molar ratio of Cu:Mg:Al in the MMOs varies from 3:0:2 to 3:1:2, as indicated, and calcined at 950°C for 3 h for analysis.	91
Figure 4-7: FTIR spectra of LDH precursors co-precipitated using (a) 2 M NaOH and (b) 1 M NaOH and 1 M Na ₂ CO ₃ , with varying molar compositions of Cu:Mg:Al = 3 : 0 : 2 to Cu:Mg:Al = 3 : 1 : 2. All samples were prepared at a constant pH of 9.5.	93
Figure 4-8: BET surface areas of the LDHs prepared using 2 M NaOH and 1 M NaOH and 1 M Na ₂ CO ₃ , and calcined MMOs for varying molar concentrations of Mg. All samples were prepared at a constant pH of 9.5.	94
Figure 4-9: SEM images of LDH and MMO materials. (a) LDH precursor produced using 2 M NaOH and (b) derived MMO, and (c) LDH precursor produced using 1 M NaOH and 1 M Na ₂ CO ₃ and (d) derived MMO. All samples were prepared at a constant pH of 9.5. All MMOs were calcined at 950°C for 3 h for analysis.	94

Figure 4-10: Characterisation of Cu-Al MMOs derived from Cu-Al LDH prepared by precipitation with 2 M NaOH without residual Na. (a) HAADF-STEM image of Cu-Al MMO calcined at 950°C. (b) EDX mapping showing the distribution of Cu (Red), Al (Green), and O (Blue), and overlay map of Cu and Al. 95

Figure 4-11: Characterisation of Cu-Mg-Al LDH precursor prepared by precipitation with 2 M NaOH and calcined MMOs. (a) STEM image of Cu-Mg-Al LDH precursor. (b) STEM image and (c) HRTEM image of Cu-Mg-Al MMOs calcined at 800°C for 3 h (Cu:Mg:Al = 3:1:2). (d) HAADF-STEM, (e) BF-STEM and (f) STEM images of Cu-Mg-Al MMO calcined at 950°C. (g) EDX mapping showing the distribution of Cu (Red), Al (Green), Mg (Yellow), and O (Blue), and (h) overlay of Cu and Al. 96

Figure 4-12: Characterisation of Na-stabilised Cu-Al MMOs derived from Cu-Al LDH prepared by precipitation with an aqueous solution containing 1 M NaOH and 1 M Na₂CO₃. (a) HAADF-STEM, (b) BF-STEM and (c) STEM images of Cu-Al MMO calcined at 950°C. (d) EDX mapping showing the distribution of Cu (Red), Al (Green), Na (Yellow), and O (Blue), and (e) overlay map of Cu and Al. 97

Figure 4-13: Characterisation of Cu-Mg-Al LDH precursor and calcined MMOs prepared by precipitation with 1 M NaOH and 1 M Na₂CO₃. (a) STEM image of Cu-Mg-Al LDH precursor. (b) STEM image and (c) HRTEM image of Cu-Mg-Al MMOs calcined at 800°C for 3 h (Cu:Mg:Al = 3:1:2). (d) HAADF-STEM, (e) BF-STEM and (f) STEM images of Cu-Mg-Al MMO calcined at 950°C. (g) EDX mapping showing the distribution of Cu (Red), Al (Green), Mg (Yellow), and O (Blue). 98

Figure 4-14: Comparison of the phase dispersion of the MMOs calcined from LDHs prepared using different synthesis conditions. Diagrams illustrating the composition and phase dispersion of the MMOs: (a) CuO/CuAl₂O₄ derived from Cu-Al LDH, (b) CuO/MgAl₂O₄ derived from low-crystallinity Cu-Mg-Al LDH, (c) CuO in Na-stabilised support, and (d) CuO in MgAl₂O₄ support derived from high-crystallinity Cu-Mg-Al LDH. (e) HAADF-STEM image and (f) element mapping of Cu-Al MMO synthesised from Cu-Al LDH, consisting of CuO/CuAl₂O₄. Cu:Al = 3:2, 2 M NaOH. (g) HAADF-STEM image and (h) element mapping of Cu-Mg-Al MMO derived from low-crystallinity Cu-Mg-Al LDH. Molar ratio of Cu:Mg:Al is 3:1:2, 2 M NaOH. (i) HAADF-STEM image and (j) element mapping of Cu-Al MMO derived from Cu-Al LDH with residual Na. The molar Cu:Al ratio is 3:2, 1 M NaOH + 1 M Na₂CO₃. (k) HAADF-STEM image and (l) element mapping of Cu-Mg-Al MMO calcined from high-crystallinity Cu-Mg-Al. Molar ratio of Cu:Mg:Al is 3:1:2, 1 M NaOH and 1 M Na₂CO₃. The combined element maps (f, i, l, o) only consist of Cu and Al. All the samples were calcined at 950°C for 3 h. 99

Figure 4-15: Plots of the thermodynamic equilibrium composition as a function of the oxygen concentration. (a, b) Cu-Al-O and (c, d) Cu-Al-Mg-O, and the temperatures (a, c) 600°C and (b, d) 1000°C. Data taken from FactSage and expanded with CuAl₂O₄ using Gibbs free energy data for the systems. 100

Figure 4-16: The phase composition as a function of the calcination temperature. (a) Cu-Al LDH with a Cu:Al molar ratio of 3:2, with co-precipitating agent of 2 M NaOH, (b) Cu-Mg-Al LDH with a Cu:Mg:Al molar ratio of 3:1:2, with co-precipitating agent of 2 M NaOH, (c) Cu-Al LDH with a Cu:Al molar ratio of 3:2, with co-precipitating agent of 1 M NaOH + 1 M Na₂CO₃; (d) Cu-Mg-Al LDH with a Cu:Mg:Al molar ratio of 3:1:2, with co-precipitating agent of 1 M NaOH + 1 M Na₂CO₃. The treatment temperatures were the following: (i) room temperature, (ii) 400°C, 3 h (iii) 600°C, 3 h (iv) 800°C, 3 h (v) 950°C, 3 h. The reference crystalline patterns are: CuO: JCPDS 80-1268, CuAl₂O₄: JCPDS 76-2295, MgAl₂O₄: JCPDS 73-1959, Cu₆Al₂(OH)₁₆CO₃·4H₂O: JCPDS 37-0630. 102

Figure 5-1: Redox cycling of Cu-Al MMO and Cu-Mg-Al MMO in a TGA at 900°C. (a) relative weight profiles for the first CLOU cycle, phase change between CuO and Cu₂O. The oxygen release was carried out under N₂ for 5 min, followed by re-oxidation in air for 3 min. (b) oxygen release capacities of the MMOs over 100 CLOU redox cycles. (c) relative weight profiles for the first CLC cycle, phase change between CuO and Cu. The reduction was carried out for 7 min in 5 vol% CO balanced with N₂, followed

by a 1 min N ₂ purge. The samples were then re-oxidised for 3 min in air, followed by a further 1 min in pure N ₂ . (d) oxygen storage capacities of the MMOs over 100 CLC redox cycles.	108
Figure 5-2: TGA profiles of long-term redox cycling of Cu-Mg-Al MMO. (a) relative weight profiles for the first and last CLOU cycle, phase change between CuO and Cu ₂ O. The oxygen release was carried out under N ₂ for 4 min, followed by re-oxidation in air for 2.5 min (b) oxygen release capacity over 500 cycles of oxygen release and re-oxidation. (c) entire relative weight profile.	109
Figure 5-3: XRD patterns of fresh, oxygen released/reduced and cycled Cu-Al MMOs and Cu-Mg-Al MMOs. XRD patterns of (a) Cu-Mg-Al MMOs and (b) Cu-Al MMOs during CLOU cycling in a TGA. XRD patterns of (c) Cu-Mg-Al MMOs and (d) Cu-Al MMOs during CLC cycling in a TGA.....	110
Figure 5-4: In situ high temperature XRD analyses. XRD profiles of Cu-Mg-Al MMO with (a) oxygen release in N ₂ and (b) oxidation in air. XRD profiles of Cu-Al MMO, with (c) oxygen release in N ₂ and (d) re-oxidation in air. All runs were performed at 900 °C.	111
Figure 5-5: Cu-Al-O system equilibrium phase diagram for a 1:1 molar mixture of CuO and Al ₂ O ₃ . The region for oxygen release and re-oxidation during CLOU are demarcated, calculated using thermodynamic data from Jacob & Alcock. ¹⁰⁹	112
Figure 5-6: Redox cycling of Cu-Al and Cu-Mg-Al in an FBR at 900°C. Oxygen profiles during full cycle periods for (a) oxygen release and (b) oxidation of the Cu-Al MMOs. Oxygen profiles during full cycle periods for (c) oxygen release and (d) oxidation of the Cu-Mg-Al MMOs. (e) conversion of the MMOs. Where PC is partial cycling (100 cycles of partial oxygen release and oxidation with full cycles every 20 cycles), and FC is full cycling (100 cycles of full oxygen release and oxidation).	116
Figure 5-7: XRD patterns of the Cu-Mg-Al LDH precursors co-precipitated at pH 9.5 and 11 and derived MMOs.	117
Figure 5-8: Characterisation of the pore structure of Cu-Mg-Al MMO-11. (a) The N ₂ adsorption-desorption isotherms and (b) N ₂ desorption and MIP pore size distributions for the Cu-Mg-Al LDH precursors and MMOs, respectively.	118
Figure 5-9: Shape and morphology evolution of Cu-Mg-Al LDHs and MMOs. (a) SEM image of the Cu-Mg-Al LDH-9.5. (b) SEM image of the freshly calcined the Cu-Mg-Al MMO-9.5. (c) STEM image of the Cu-Mg-Al LDH-9.5 precursor. (d) SEM image of the Cu-Mg-Al LDH-11. (e) SEM image of the freshly calcined the Cu-Mg-Al MMO-11. (f) STEM image of the Cu-Mg-Al LDH-11 precursor. ...	119
Figure 5-10: Redox cycling of Cu-Mg-Al MMO-11 in a TGA at 900°C. (a) oxygen release and storage profiles (CLOU), phase change between CuO and Cu ₂ O. The oxygen release was carried out under N ₂ for 5 min, followed by re-oxidation in air for 3 min. (b) cyclic reduction and oxidation (CLC), phase change between CuO and Cu. The reduction was carried out for 7 min in 5 vol% CO balanced with N ₂ , followed by a 1 min N ₂ purge. The samples were then re-oxidised for 3 min in air, followed by a further 1 min in pure N ₂ . (c) oxygen release capacities of the MMOs over 100 CLOU redox cycles. (d) oxygen storage capacities of the MMOs over 100 CLC redox cycles.....	120
Figure 5-11: Redox cycling of Cu-Mg-Al MMO-11 in an FBR at 900°C. Oxygen profiles during full cycle periods for (a) oxygen release and (b) oxidation during partial cycling of Cu-Mg-Al-11. Oxygen profiles during full cycle periods for (a) oxygen release and (b) oxidation during partial cycling of Cu-Mg-Al-11. (e) conversion of the MMOs. Where PC is partial cycling (100 cycles of partial oxygen release and oxidation with full cycles every 20 cycles), and FC is full cycling (100 cycles of full oxygen release and oxidation).	122
Figure 5-12: Post-cycling characterisation of the MMOs. (a) TGA profiles of freshly calcined particles, particles cycled for 100 cycles in an FBR with partial oxygen release (PC) and oxidation with full oxygen release every 20th cycle in an FBR; and particles cycled for 100 cycles with full oxygen release and oxidation in an FBR (FC) at 900 °C. (b) XRD patterns of fresh and cycled materials.	123

Figure 5-13: Morphological evolution of Cu-Mg-Al MMO-11 using imaging. Photos of Cu-Mg-Al LDH-11 precursors and derived MMOs in different states: (a) LDH precursor powders, (b) freshly calcined MMOs, (c) decomposed MMOs ($\text{Cu}_2\text{O}/\text{MgAl}_2\text{O}_4$), (d) reduced MMOs ($\text{Cu}/\text{MgAl}_2\text{O}_4$) reduction under 5 vol% CO balanced with N_2 , (e) MMOs after 100 cycles in the FBR. SEM image of the (f) freshly calcined MMOs and (g) their surface, and (h) STEM image. SEM image of the (i) cycled MMOs and (j) their surface, and (k) STEM image.	124
Figure 5-14: Pore size distributions of fresh and cycle MMOs from MIP analysis. (a) pore size distribution of fresh Cu-Mg-Al MMO-11 and cycled samples in FBR reactor derived from MIP, and (b) pore size distribution of fresh Cu-Mg-Al MMO-9.5 and cycled in FBR reactor derived from MIP	125
Figure 5-15: Gas concentration profiles of chemical looping combustive purification (CLCP) cycling of Cu-Mg-Al MMO-11 in FBR. (a) 2 vol% CO/N_2 used for the reduction and oxidation under 10 vol% O_2/N_2 at 400°C , (b) 2 vol% CO/N_2 used for the reduction and oxidation under 10 vol% O_2/N_2 at 800°C , (c) 1 vol% CH_4/N_2 used for the reduction and oxidation under 10 vol% O_2/N_2 at 800°C . (d) conversion profile for each testing mode over 20 CLCP cycles in an FBR.	126
Figure 5-16: Enhanced gas concentration profiles of chemical looping combustive purification (CLCP) cycling of Cu-Mg-Al MMO in FBR. (a) 2 vol% CO/N_2 used for the reduction and oxidation under 10 vol% O_2/N_2 at 400°C , (b) 2 vol% CO/N_2 used for the reduction and oxidation under 10 vol% O_2/N_2 at 800°C , (c) 1 vol% CH_4/N_2 used for the reduction and oxidation under 10 vol% O_2/N_2 at 800°C . The intrinsic accuracy of the measurement is 1.0% of reading, and the detection limits of the MGA3000C Multi-Gas Analyser (ADC Gas Analysis) are 500 ppm for CO, CO_2 and CH_4 and 1000 ppm for oxygen.	127
Figure 5-17: XRD patterns of fresh and cycled Cu-Mg-Al MMO-11 recovered after 20 redox-cycles in FBR. (a) fresh Cu-Mg-Al MMO-HS, (b) Cu-Mg-Al MMO-HS recovered after 20 CLC cycles in FBR at 400°C with 2 vol% CO/N_2 for the reduction and oxidation under 10 vol% O_2/N_2 , (c) Cu-Mg-Al MMO-HS recovered after 20 CLC cycles in FBR at 800°C with 2 vol% CO/N_2 for the reduction and oxidation under 10 vol% O_2/N_2 , (d) MMO recovered after 20 CLC cycles in FBR at 800°C with 1 vol% CH_4/N_2 for the reduction and oxidation under 10 vol% O_2/N_2	128
Figure 5-18: Characterisation of LDH-512s (a) XRD patterns of LDHs and MMOs, crystalline patterns correspond to \bullet $\text{Mg}_6\text{Al}_2(\text{OH})_{16}\text{CO}_3 \cdot 4\text{H}_2\text{O}$ (JCPDS 22-0700), \diamond CuO (JCPDS 80-1268) and $*$ MgAl_2O_4 (JCPDS 73-19.59); (b) N_2 adsorption and MIP pore size distributions of LDH-512s and MMO-512s.	129
Figure 5-19: SEM images of LDH-512s. SEM images of LDH-512-9.5 particles (a) at 80k magnification and (b) 150k magnification; SEM images of LDH-512-11 particles at (c) 80k magnification and (d) 150k magnification.	130
Figure 5-20: (a) oxygen release and storage profiles of the MMOs in a TGA at 900°C ; (b) oxygen release capacities over 100 redox cycles in a TGA at 900°C ; (c,d) oxygen release profiles for cycles 1, 60 and 100 in an FBR at 900°C for (c) MMO-512-9.5 and (d) MMO-512-11; (e) conversion of MMO-312-11, ²¹¹ MMO-512-9.5 and MMO-512-11 over 100 cycles of full oxygen release and oxygen storage in an FBR at 900°C	131
Figure 6-1: Equilibrium oxygen concentrations of $\text{Cu}_2\text{O}/\text{CuO}$, $\text{Mn}_2\text{O}_3/\text{Mn}_3\text{O}_4$ and $\text{CoO}/\text{Co}_3\text{O}_4$ systems as a function of temperature using FactSage. ⁶³	136
Figure 6-2: Gas flow in apparatus used to determine kinetics. (a) TGA (b) spouted-bed FBR.	139
Figure 6-3: Observed oxygen release rates in the TGA at 900°C for different sample masses.	143
Figure 6-4: Observed oxygen release rates in the FBR at 875°C for different sample masses ($u/u_{mf} = 4$).	146

Figure 6-5: Observed oxygen release rates in the FBR at 875°C for different u/u_{mf} (sample mass = 0.5 g).....	147
Figure 6-6: Rates of oxygen release for six particle size ranges using the averaged weight profile from cycles three to five in a TGA at 900°C.	151
Figure 6-7: Observed and fitted rate constants for each MMO-312-11 particle size fraction cycled in a TGA at 900°C.	153
Figure 6-8: Oxygen release rates in the FBR. (a) rates of oxygen release of MMO-312-11 between 850 and 962°C, and (b) rates of oxygen release with an enhanced y axis.	154
Figure 6-9: Arrhenius plot for the oxygen release from MMO-312-11s over the temperature range 850 to 962°C.	155
Figure 6-10: Arrhenius plot for the oxygen release from MMO-312-11s over the temperature range 850 to 937°C.	158
Figure 7-1: XRD patterns of the LDHs. The LDHs were co-precipitated for 300 min at constant pH values between 9 and 11.5 min using a constant flow rate of metal nitrate solution.	163
Figure 7-2: Unit cell of LDHs. (a) Relationship between the triple hexagonal cell to the primitive rhombohedral cell. The conventional cell of LDHs in (b) hexagonal representation with group R-3m (space group 166) and (c) rhombohedral representation of the same structure, adapted from Mohammadi et al. ²⁶⁷	164
Figure 7-3: Structure of LDH materials. (a) hexagonally packed atom positions in the brucite-like layer; and stacking of layers with (b) trigonal P-type (e.g. AC=CA), and (c,d) octahedral O-type interlayer sites (e.g. AC-BA and AC-AC) . Only the lower hydroxyl groups of the upper layer is shown. Large circles are hydroxyl groups, small circles are cations. Adapted from Bookin and Drits. ²⁶³	166
Figure 7-4: Scheme for derivation of two-layer polytypes. Adapted from Bookin and Drits. ²⁶³	167
Figure 7-5: Simulation of stacking faults using FAULTS. (a) XRD patterns showing non-uniform broadening of mid-range peaks for increasing amounts of 2H ₁ motif in 3R ₁ . (b) example of 2H ₁ stacking fault in 3R ₁ structure. Large circles are hydroxyl groups, small circles are cations.	168
Figure 7-6: Results of FAULTS simulations to determine stacking faults in LDH structure. For LDHs co-precipitated at (a) pH 9, (b) pH 9.5, (c) pH 10, (d) pH 10.5, (e) pH 11, and (f) pH 11.5 for 300 min.	170
Figure 7-7: Domain diagram of Al(OH) ₃ , Mg(OH) ₂ , and Mg–Al–NO ₃ LDHs. Solubility is denoted as S on the y axis. Reproduced with permission from Elsevier. ²⁸⁶	173
Figure 7-8: Plots of equilibrium compositions as a function of the pH value. The plot was generated with SPANA using data from DATABASE ²¹² as well as literature values for the compounds listed in Table 4-3.	174
Figure 7-9: SEM images of LDHs co-precipitated at pH values between 9 and 11.5 for 300 min (as indicated). Left to right: magnification of 30k, 50k and 150k.	176
Figure 7-10: Determination of platelet dimensions using SEM. Left to right: SEM images at 200k magnification, distribution of LDH platelet heights and diameters based on 90 platelets over three SEM images at 150k magnification, respectively for (a-c) LDH-9; (d-f) LDH-9.5; (g-i) LDH-10; (j-l) ; LDH-10.5; (m-o) LDH-11; (p-q) LDH-11.5.	177
Figure 7-11: Results of peak fitting to determine cell parameter c and FWHM ₀₀₃ . For LDHs co-precipitated at (a) pH 9, (b) pH 9.5, (c) pH 10, (d) pH 10.5, (e) pH 11, and (f) pH 11.5 for 300 min.	178

Figure 7-12: Results of peak fitting to determine cell parameter a and FWHM_{110} . For LDHs co-precipitated at (a) pH 9, (b) pH 9.5, (c) pH 10, (d) pH 10.5, (e) pH 11, and (f) pH 11.5 for 300 min.	179
Figure 7-13: Normalised trend in platelet diameter determined by XRD and SEM analysis. LDHs were co-precipitated at a constant pH value between 9 and 11.5 for 300 min.	180
Figure 7-14: Effect of Cu content on properties of Cu-Mg-Al LDHs. (a) XRD patterns of $\text{Cu}_x\text{-Mg}_{(1-x)}\text{Al}_2$ LDHs, where $x = 0$ to 4. SEM images of $\text{Cu}_x\text{-Mg}_{(1-x)}\text{Al}_2$ LDHs where (b) $x = 0$, and (c) $x = 2$. Reproduced with permission from Springer Nature. ²⁹²	181
Figure 7-15: Number of crystallites and type of bonds responsible for the morphology of LDH particles. Reprinted (adapted) with permission from ²⁹⁵ . Copyright 2023 American Chemical Society.....	182
Figure 7-16: FWHM and platelet dimensions determined by XRD analysis of LDHs co-precipitated at a constant pH value between 9 and 11.5 for 300 min. (a) $L(003)$, (b) FWHM_{003} , (c) $L(110)$ (d) FWHM_{110} of LDHs co-precipitated over 300 min. Platelet dimensions were calculated using the Scherrer equation.	183
Figure 7-17: SEM images of LDHs co-precipitated at a constant pH value between 9 and 11.5 (as indicated) at 100k magnification. Left to right: samples withdrawn after 5, 30, 90 and 300 min.	184
Figure 7-18: Distribution of LDH platelet diameters for LDHs co-precipitated at a constant pH value between 9 and 11.5. Left to right: samples withdrawn after 5, 30, 90 and 300 min. Platelet dimensions are based on 60 platelets over two SEM images (150k magnification) for LDHs synthesised for 5, 30, 90 min and 90 platelets over three SEM images (150k magnification) for LDHs synthesised for 300 min.	185
Figure 7-19: Platelet dimensions determined from SEM analysis of LDHs co-precipitated at a constant pH value between 9 and 11.5 for 300 min. (a) LDH diameter (b) LDH diameter including error bars equal to the standard deviation.....	186
Figure 7-20: Results of the zeta potential measurements for the LDHs synthesised at pH 9, 10 and 11. Zeta potentials were measured using a ZetaPALS (Brookhaven Instruments) at 25°C. The LDHs were dispersed in 10 mM NaCl using an ultrasonic probe and two solutions of 10 mM NaOH and 10 mM HCl were used to adjust the pH of the dispersion.	188
Figure 7-21: Thermogravimetric analysis profiles during calcination of LDH-10. (a) Relative weight and derivative weight profile and (b) selected MS signals during calcination of the LDH-10 from 50 to 900°C in a TGA using a heating rate of 10°C min ⁻¹	191
Figure 7-22: Derivative weight profiles for LDHs co-precipitated at a constant pH value between 9 and 11.5. Results of derivative weight profile fittings for LDHs co-precipitated at (a) pH 9, (b) pH 9.5, (c) pH 10, (d) pH 10.5, (e) pH 11, and (f) pH 11.5. The LDHs were calcined in a TGA over a temperature range of 50 to 900°C using a heating rate of 10°C min ⁻¹	192
Figure 7-23: FTIR spectra of the LDHs. FTIR spectra of (a) the LDHs co-precipitated at constant pH between 9 and 11.5 (b) LDH-10 calcined at varying temperatures (as indicated). Samples were calcined at each temperature under air and for 3 h.....	194
Figure 7-24: Phase composition of LDH-10 as a function of calcination temperature (as indicated). Samples were calcined at each temperature under air and for 3 h.	195
Figure 7-25: Pore size distribution of LDH-10 as a function of calcination temperature (as indicated). Pore size distributions were determined using MIP analysis and samples were calcined at the desired temperature under air and for 3 h.....	196
Figure 7-26: SEM images of MMOs derived from LDHs co-precipitated at a constant pH value between 9 and 11.5 for 300 min (as indicated). Left to right: at 300, 10k, 50k and 100k magnification.	197

Figure 7-27: Pore size distributions of MMOs. Derived from LDHs co-precipitated at a constant pH value between 9 and 11.5 (as indicated) determined using MIP.....	198
Figure 7-28: XRD patterns of MMOs derived from LDHs co-precipitated at a constant pH value between 9 and 11.5 for 300 min (as indicated). Reference patterns for CuO (JCPDS 80-1268; vertical lines) and MgAl ₂ O ₄ (JCPDS 73-1959, vertical dashed lines).....	200
Figure 7-29: CLOU cycling profiles in a TGA at 900°C. First and last CLOU cycles and long-term profiles, respectively, for MMOs derived from LDHs co-precipitated for 300 min at (a-b) pH 9, (c-d) pH 9.5, and (e-f) pH 10. The re-oxidation period for MMO-9 was 60 min rather than the 2.5 min used for the remaining MMOs due to the extremely slow rates of re-oxidation observed in the TGA.	202
Figure 7-30: CLOU cycling profiles in a TGA at 900°C. First and last CLOU cycles and long-term profiles, respectively, for MMOs derived from LDHs co-precipitated for 300 min at (a-b) pH 10.5, (c-d) pH 11, and (e-f) pH 11.5.....	203
Figure 7-31: CLC cycling profiles in a TGA at 900°C. First and last CLC cycles and long-term profiles, respectively, for MMOs derived from LDHs co-precipitated for 300 min at (a-b) pH 9, (c-d) pH 9.5, and (e-f) pH 10. The re-oxidation period for MMO-9 was 60 min rather than the 2.5 min used for the remaining MMOs due to the extremely slow rates of re-oxidation observed in the TGA.....	204
Figure 7-32: CLC cycling profiles in a TGA at 900°C. First and last CLOU cycles and long-term profiles, respectively, for MMOs derived from LDHs co-precipitated for 300 min at (a-b) pH 10.5, (c-d) pH 11, and (e-f) pH 11.5.....	205
Figure 7-33: Comparison of relative weight profiles of MMO-9 tested in a TGA at 900°C under CLOU conditions using re-oxidation atmospheres of 10 vol% O ₂ /N ₂ and air (as indicated).	206
Figure 7-34: Comparison of relative weight profiles of MMOs tested in a TGA at 900°C. (a) CLOU cycling mode, and (b) CLC cycling mode.	207
Figure 7-35: Oxygen release rates during oxygen release phase of the CLOU cycle.....	208
Figure 7-36: Results of the 500 CLC cycle experiments in a TGA at 900°C. Relative weight profiles for the first and last CLC cycles for extended cycling of the MMO-10 and MMO-11.....	209

List of Tables

Table 2-1: Oxygen capacities of commonly studied oxygen carrier systems.	36
Table 2-2: Melting point and Tammann temperature of commonly investigated oxygen carriers. ⁷⁸ ...	37
Table 2-3: Cu ores used as oxygen carriers in CLC systems, adapted from Matzen et al. ¹³⁷	45
Table 2-4: Common preparation methods used to synthesise oxygen carriers for chemical looping processes. ¹⁵¹	46
Table 2-5: Preparation and testing of CuO/Al ₂ O ₃ and CuO/MgAl ₂ O ₄ oxygen carriers for CLC and CLOU.....	47
Table 2-6: Chemical formulae of naturally occurring hydrotalcites. ¹⁷⁵	53
Table 2-7: Preparation conditions and material characteristics of Mg-Al LDHs synthesised via co-precipitation at constant pH.	55
Table 2-8: Main synthesis parameters for LDH prepared via co-precipitation.....	55
Table 2-9: Preparation conditions and material characteristics of Mg-Al LDHs synthesised via urea hydrolysis.	58
Table 3-1: Reagents used for synthesis of the co-precipitated LDH precursors.	62
Table 3-2: Insights from powder diffractogram peak features. ¹⁹⁵	65
Table 3-3: Parameters for the calculation of molecular diffusivity in the TGA.	74
Table 3-4: Minimum fluidisation velocity calculation. Based on the envelope density of inert sand bed material (2600 kg m ⁻³).	77
Table 4-1: Crystallite size of the LDHs produced using 1 M NaOH + 1 M Na ₂ CO ₃ , and crystallite size of the active and support phases of the calcined MMOs.	83
Table 4-2: Composition of LDH precursors and derived MMOs prepared using 1 M NaOH + 1 M Na ₂ CO ₃ , calculated from XRF and ICP measurements.	84
Table 4-3: Values for the equilibrium constants (k_r) and structures for the compounds added to the dataset used for the thermodynamic calculations with SPANA.	87
Table 4-4: The composition of LDH precursors and derived mixed metal oxides, prepared with 2 M NaOH calculated from XRF and ICP measurements.....	90
Table 4-5: Crystallite size of the MMOs derived from LDHs produced using 2 M NaOH and 1 M NaOH + 1 M Na ₂ CO ₃	92
Table 4-6: Summary of findings regarding Cu-Al and Cu-Mg-Al LDHs prepared via co-precipitation using NaOH and Na ₂ CO ₃ or NaOH.	104
Table 5-1: XRF results for the LDH-512s.	129
Table 6-1: Results of kinetic studies of CuO-based oxygen carriers for CLOU processes, adapted from Tian et al. ²⁴⁴	137
Table 6-2: Particle size ranges used for the TGA experiments to determine τ	142
Table 6-3: Results of the sample mass experiments performed in a TGA at 900°C.....	144

Table 6-4: Flow rates used for the kinetic experiments between 850 and 962°C in a TGA. Minimum fluidisation velocity calculations were based on the envelope density of inert sand bed material (300-425 μm , 2600 kg m^{-3}).....	148
Table 6-5: Input and calculated parameters for the calculation of the cross flow factor at 875°C with a 40 g of inert sand bed material (300-425 μm , 2600 kg m^{-3}).	150
Table 6-6: Effectiveness factors and maximum observed rates of oxygen release for each MMO-312-11 particle size fraction cycled in a TGA at 900°C.	152
Table 6-7: Comparison of the activation energy recovered in this work with published kinetic studies for CuO-based oxygen carriers for CLOU. Adapted from Tian et al. ²⁴⁴	156
Table 6-8: Maximum observed rate of oxygen release and ratio of mass transfer/observed rates of oxygen release of MMO-312-11 cycled in an FBR between 850 and 962°C.....	157
Table 7-1: Unit cell parameters and elemental compositions of the LDHs co-precipitated at pH values between 9 and 11.5 for 300 min.....	165
Table 7-2: Co-ordinates and occupancies of atomic positions in the AbCX layer	169
Table 7-3: LDH platelet dimensions. Determined using XRD and SEM for the LDHs co-precipitated at pH values between 9 and 11.5 for 300 min.....	175
Table 7-4: Physical constants for calculation of pH_{PZC} . (O–H distance is taken as 0.101 nm^{301}).....	187
Table 7-5: Results of derivative weight profile fittings and formulae of LDHs co-precipitated at a constant pH value between 9 and 11.5.....	193
Table 7-6: Porosity and crushing strengths of the MMOs. Derived from LDHs co-precipitated at a constant pH value between 9 and 11.5.....	199
Table 7-7: Theoretical and experimentally determined oxygen release and storage capacities, porosities and crushing strengths of the MMOs derived from LDHs co-precipitated at a constant pH value between 9 and 11.5 for 300 min.....	206

Chapter 1

Introduction

1.1 Problem statement

Scientists have established a clear correlation between climate change and the significant increase of greenhouse gases (GHGs) in the atmosphere since the start of the industrial revolution.¹ Climate change is a substantial global environmental problem that has far-reaching consequences for life on this planet. Despite international agreements to reduce GHG emissions, such as the Kyoto Protocol and the Paris Agreement, anthropogenic emissions of all major GHGs have continued to increase (**Figure 1-1b**). In its latest report in 2023, the Intergovernmental Panel on Climate Change (IPCC) warned that global GHG emissions must peak between 2020 to 2025, fall by 45% by 2030 and reach net zero by 2050 to limit global warming by 1.5°C above pre-industrial levels.² The timeline for these reductions positions the 2020s as the critical decade for implementing effective climate measures. The world is not currently on track to achieve the necessary reductions and meeting the 1.5°C limit will require immediate and decisive action to curb emissions.

Carbon dioxide, CO₂, from fossil sources is the largest source of GHGs, accounting for 64% of all GHG emissions in 2019 (**Figure 1-1a**).² The energy sector is an integral part of modern society. Historically, fossil fuels have been widely used because they are cheap, readily available, reliable and have a high energy density. Governments globally have also heavily subsidised fossil fuels to support energy security and affordability.^{3,4} The IPCC publishes regular assessment reports to identify pathways to reduce GHG emissions and limit the extent of climate change.^{1,5,6} Strategies to reduce CO₂ emissions include energy efficiency improvements and developing low-carbon energy technologies, such as renewable energy sources, nuclear power, as well as carbon capture and sequestration/storage (CCS).

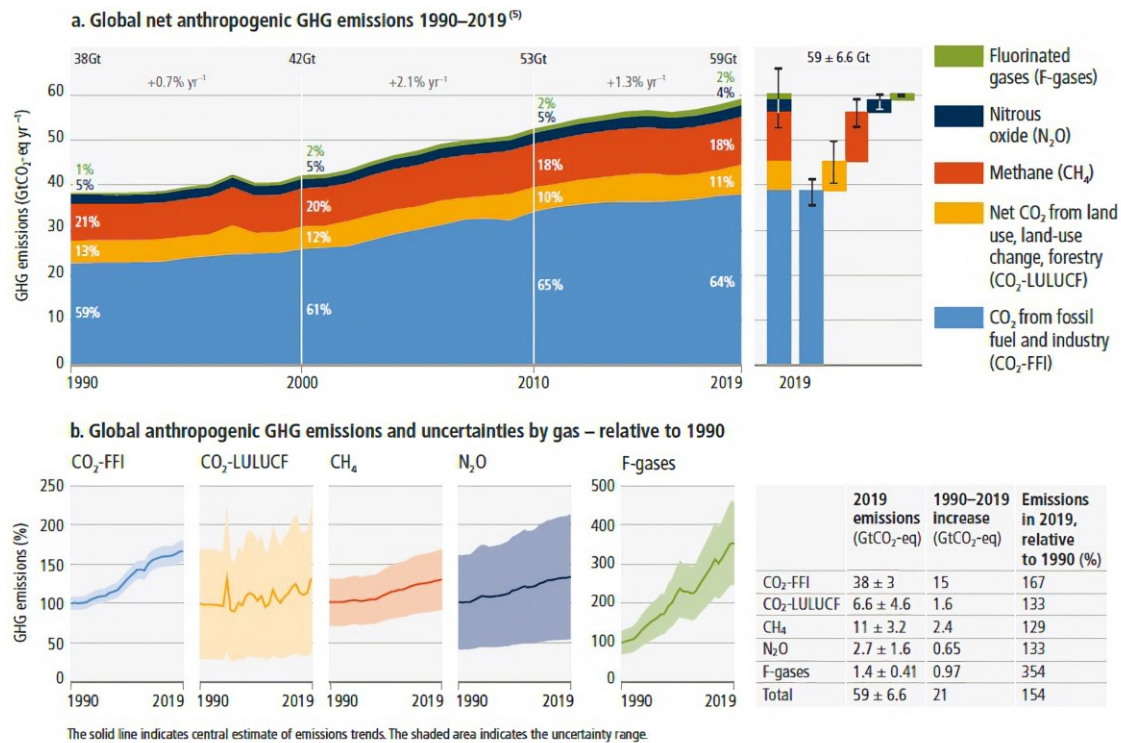


Figure 1-1: Global net anthropogenic GHG emissions (GtCO_{2,eq} yr⁻¹) 1990–2019. (a) shows aggregate annual global net anthropogenic GHG emissions by GHG from 1990 to 2019. The fraction of global emissions for each GHG is shown for 1990, 2000, 2010 and 2019; as well as the aggregate average annual growth rate between these decades. At the right side of (a), GHG emissions in 2019 are broken down into individual components with the associated uncertainties (90% confidence interval) indicated by the error bars. (b) shows global anthropogenic emissions individually for the period 1990–2019, normalised relative to 100 in 1990. Shaded areas indicate the uncertainty range. Adapted from IPCC⁶.

Figure 1-2 shows a breakdown of the United Kingdom (UK) electricity generation by fuel source. From 2011 to 2021, the share of UK electricity generated from renewable sources rose from 4 to 24%,⁷ in line with the global average of 28.4%.⁸ Despite the increase in renewable capacity, it is unlikely that renewable energy will completely replace fossil fuel-based energy in the medium term due to the flexibility that dispatchable fossil fuel-based power generation provides the electricity grid.⁹ However, the remaining fossil fuel-based power generation must be low-carbon. CCS is an option for decarbonising fossil fuel-based generation, where CO₂ is captured from the process flue gas and concentrated to be transported *via* pipeline or shipping to a storage site where it is stored in a subsurface geological formation. Bio-energy with CCS (BECCS) is an emerging technology where CCS-enabled power generation plants are fuelled by biomass.¹⁰ The biomass consumes atmospheric CO₂ and locks in carbon as it grows, which is released when it is combusted to generate power. In BECCS, the released CO₂ is captured and stored, resulting in potentially overall negative emissions depending on the emissions intensity of the biomass source.¹¹ The cost of CCS largely depends on the scale and CO₂ concentration of the process flue gas.¹² Expected costs for power generation are US\$ 50 – 70 per tonne

of CO₂ for CO₂ capture and US\$ 5 – 20 per tonne of CO₂ for transport and storage.¹² Capturing CO₂ is the costliest part of the process, and research is focused on reducing this cost to make CCS a more economically viable option for climate change mitigation. The UK government has recently committed to an industrial CCS cluster deployment programme for CCS.¹³ The strategy groups CO₂-intensive industries into geographical clusters to develop shared transportation and storage infrastructure to lower the overall risks and costs associated with CCS. In its latest spring budget in 2023, the UK government has also pledged to invest up to £20 billion over the next 20 years to deliver four carbon capture, usage and storage (CCUS) clusters to capture 20 to 30 MtCO₂ yr⁻¹ by 2050.¹⁴ The significant investment shows that CCS remains a relevant strategy for industrial decarbonisation and climate change mitigation.

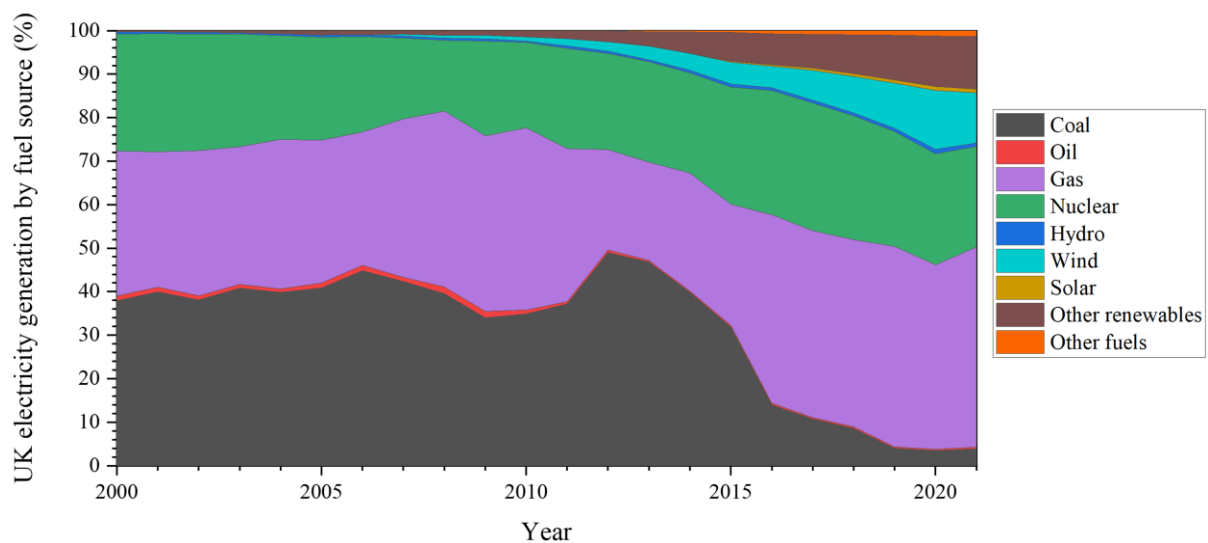


Figure 1-2: Share of UK electricity generation by fuel source, 2000-2021.⁷ Other renewables includes stations burning biomass (e.g. wood), landfill gas and sewage sludge.

The three main approaches for CO₂ capture are post-combustion capture, pre-combustion capture and oxy-fuel combustion:^{15,16}

- (i) Post-combustion capture involves capturing CO₂ from a flue gas after fuel combustion. Post-combustion capture technologies include chemical absorption, physical adsorption and membrane separation.
- (ii) Pre-combustion capture involves capturing CO₂ before fuel combustion. Typically, the fuel is converted to syngas *via* steam reforming or partial oxidation and CO₂ is removed from the syngas using chemical absorption, physical adsorption and membrane separation.
- (iii) Oxy-fuel combustion involves combusting the fuel in an atmosphere of pure oxygen or oxygen and recirculated flue gas rather than air. This produces a nitrogen-free flue gas with a high CO₂ concentration, which can be captured and stored. The oxygen used for oxy-fuel combustion is typically produced using a cryogenic air separation unit.

A major limitation of conventional CO₂ capture methods is the significant energy penalty associated with separating CO₂ from a diluted (*i.e.* containing nitrogen) process stream or producing oxygen from cryogenic distillation for oxy-fuel combustion and pre-combustion capture.¹⁷ An alternative approach for CO₂ capture is chemical looping combustion.¹⁸ Chemical looping combustion involves splitting the combustion reaction into two sub-reactions linked by an oxygen carrier, a solid metal oxide typically based on a transition metal, to transfer oxygen from the air to the fuel. The fuel is not combusted in the presence of nitrogen; therefore, the combustion products, steam and CO₂, are undiluted (*i.e.* nitrogen-free) and a pure stream of CO₂ can be obtained through simple condensation. Compared to other CO₂ capture technologies, chemical looping combustion has the significant advantage of lower process efficiency penalties because the total heat evolved over the two reactions is the same as conventional combustion, with inherent CO₂ capture.¹⁹ Chemical looping processes have also been applied to processes beyond combustion to produce low-carbon hydrogen and chemicals such as ammonia.²⁰

The oxygen carriers play a crucial role in chemical looping processes and must maintain high performance during extended redox cycling at high temperatures. One major challenge of chemical looping combustion is to achieve complete fuel conversion when solid fuels are used.¹⁹ A variant of chemical looping combustion is chemical looping with oxygen uncoupling,²¹ where the oxygen carriers release gaseous oxygen in the presence of fuel to improve the combustion and CO₂ capture efficiencies of the process.²² Oxygen carriers for chemical looping with oxygen uncoupling must have suitable thermodynamics for oxygen release at relevant temperatures. To date, over 11000 h of operation has been achieved in small-scale chemical looping combustion pilot facilities, with over 70% of the operational time using synthetic oxygen carriers as opposed to natural/waste materials.¹⁸ An evaluation of recent reviews assessing the progress in the development of oxygen carriers for chemical looping applications identified the following key research needs:^{23–26}

- (i) Design and synthesise synthetic oxygen carrier materials with desired properties for chemical looping processes, *e.g.* resistance to sintering and agglomeration,
- (ii) Obtain a better understanding of the structure-property relationships of oxygen carriers,
- (iii) Enhance the long-term reactivity, cyclability and mechanical properties of oxygen carrier materials over long-term redox cycling, and
- (iv) Exploration of preparation methods for the large-scale production of oxygen carriers with a high dispersion of active metal oxide within an inert support.

This PhD project has focused on these challenges by developing CuO-based oxygen carriers derived from layered double hydroxide precursors for chemical looping processes.

1.2 Project aims and objectives of the research project

The general aim of this research project is to evaluate the potential of CuO-based oxygen carriers derived from the calcination of layered double hydroxide precursors. The following experimental objectives were specified:

- Develop novel CuO-based oxygen carriers supported on Al_2O_3 and MgAl_2O_4 by tuning the synthetic chemistry of the layered double hydroxide precursors prepared *via* co-precipitation at constant *pH*.
- Assess the chemical, thermal and mechanical stabilities of the oxygen carriers over long-term redox cycling in a thermogravimetric analyser and a laboratory-scale fluidised bed reactor.
- Model the intrinsic kinetics of the oxygen release reaction of the oxygen carriers to aid with the scale-up of chemical looping reactors.
- Investigate the formation mechanism of the Cu-Mg-Al layered double hydroxides by varying the co-precipitation *pH* value during co-precipitation.
- Assess the effect of the *pH* value during co-precipitation on the structure of the layered double hydroxides and oxygen carriers, as well as the performance of the oxygen carriers in chemical looping processes.

1.3 Structure of the thesis

This thesis is comprised of eight chapters.

Chapter 2 provides a literature review of chemical looping processes for power generation with inherent CO_2 capture and the desired characteristics of oxygen carriers in terms of their thermodynamic properties and thermal, mechanical and chemical stability requirements over long-term redox cycling. The chapter then provides an overview of oxygen carrier materials, including the most commonly used transition metal oxides and their typical performance characteristics and more novel materials, such as combined metal oxides and non-stoichiometric materials (*e.g.* perovskites). The chapter also compares common preparation methods of oxygen carriers, highlighting layered double hydroxides as a promising design strategy for producing oxygen carriers for chemical looping processes. A review of common preparation methods used to synthesise layered double hydroxides is included to identify key synthesis parameters and their effect on the characteristics of layered double hydroxides.

Chapter 3 introduces the main experimental procedures and apparatus used throughout the thesis for material synthesis, characterisation and testing. The general operating conditions are provided in this chapter, with the specific conditions for each investigation supplied in the relevant chapters.

Chapter 4 investigates the introduction of Mg into the Cu-Al layered double hydroxide system prepared *via* co-precipitation using different molar ratios of Cu:Mg:Al and different co-precipitating agents. A range of characterisation methods was used to investigate the structure and properties of the layered double hydroxides and oxygen carriers.

Chapter 5 reports the results of the thermal, chemical and mechanical stability tests of the oxygen carriers. Experiments were carried out in a thermogravimetric analyser and fluidised bed reactor to assess the long-term performance of the oxygen carriers. The materials were also characterised after cycling to investigate the effect of redox cycling on the material characteristics.

Chapter 6 models the intrinsic kinetics of the oxygen release reaction of the oxygen carriers using an effectiveness factor-based model. The kinetic model was modified for the oxygen release reaction and accounts for the internal mass transfer resistance of the oxygen carriers and the mass transfer resistances of the measurement system.

Chapter 7 investigates the effect of co-precipitation *pH* on the material characteristics of Cu-Mg-Al layered double hydroxides. The layered double hydroxides were co-precipitated for 300 min using an automated co-precipitation rig that was used to supply a constant flow rate of the metal solution to a reaction vessel, with the alkaline solution flow rate varied to maintain a constant *pH*. A range of material characterisation techniques was used to explore the changes in layered double hydroxide structure during synthesis at different co-precipitation *pH* values. The effect of co-precipitation *pH* on the performance of the oxygen carriers was also investigated using a thermogravimetric analyser at 900°C.

Chapter 8 summarises the overall conclusions and suggests areas for future work.

Chapter 2

Literature review

2.1 Introduction

This chapter provides an overview of chemical looping processes for power generation with inherent CO₂ capture. The processes were initially developed for gaseous fuels and later adapted for solid fuels. Solid-fuelled processes often exhibit poor performances using conventional oxygen carriers, requiring oxygen carriers with special properties to overcome these limitations. In this chapter, the desired characteristics of oxygen carriers are presented in terms of their thermodynamic properties and thermal, mechanical and chemical stability requirements over long-term redox cycling. Additionally, safety and environmental risks are briefly considered. The chapter then provides an overview of oxygen carrier materials, including traditional transition metal oxides and their typical performance characteristics, and more novel materials, such as combined metal oxides and non-stoichiometric materials (*e.g.* perovskites). Due to their low cost and high availability, oxygen carriers derived from natural ore sources were considered and compared to higher-cost synthetic oxygen carriers. The chapter also compares common preparation methods of oxygen carriers, highlighting layered double hydroxides (LDHs) as a promising design strategy for producing mixed metal oxides (MMOs) for chemical looping processes. A review of the preparation methods used to synthesise LDHs is included to identify key synthesis parameters and their effect on the characteristics of LDHs.

2.2 Chemical looping processes

2.2.1 Chemical looping combustion

The fundamental chemical looping concept was demonstrated by Lewis et al. in 1951²⁷ and patented by Lewis and Gilliland in 1954²⁸ for the production of pure CO₂ by contacting a carbonaceous fuel (e.g. methane, coke or natural gas) with a CuO oxygen carrier in a fluidised bed reactor (FBR) at temperatures between 800 and 1000°C. The reduced oxygen carrier was withdrawn, re-oxidised with air back to CuO in a separate air reactor and then returned to the fuel reactor (**Figure 2-1**). Later, Richter and Knoche proposed a fuel oxidation reaction scheme to reduce the irreversibility of the conventional combustion process (higher exergetic efficiency).²⁹ The reaction scheme separated the conventional fuel combustion reaction into two intermediate redox reactions linked by a metal oxide oxygen carrier. The process was later named chemical looping combustion (CLC) by Ishida *et al.* in 1987³⁰ and was first suggested as an option for efficient CO₂ capture in 1994.³¹

From **Figure 2-2**, research in CLC has accelerated since the early 2000s, driven by the growing interest in CCS technologies for climate change mitigation. Compared to other CO₂ capture technologies, CLC has a significant advantage in terms of process efficiency penalties because the total heat evolved over the two reactors is the same as conventional combustion and CO₂ capture is inherent to the process. Although initially developed for power decarbonisation, the chemical looping reaction scheme has also shown potential for areas beyond combustion, including hydrogen production, methane reforming and the production of chemicals such as methanol, ethylene and ammonia.^{20,32}

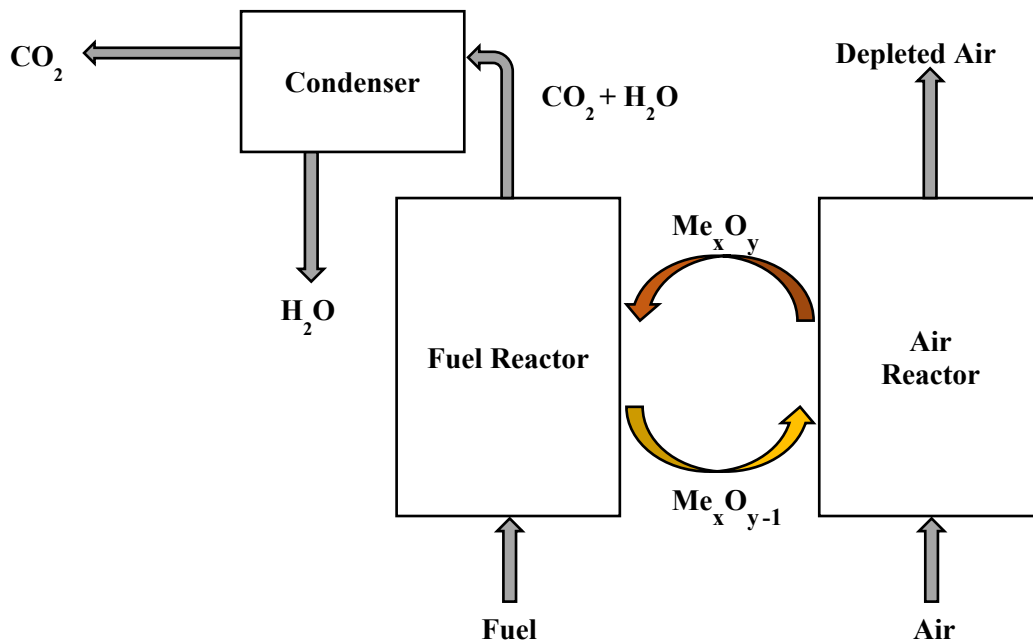


Figure 2-1: The CLC process, where Me_xO_y and Me_xO_{y-1} denote the oxidised and reduced oxygen carrier, respectively.

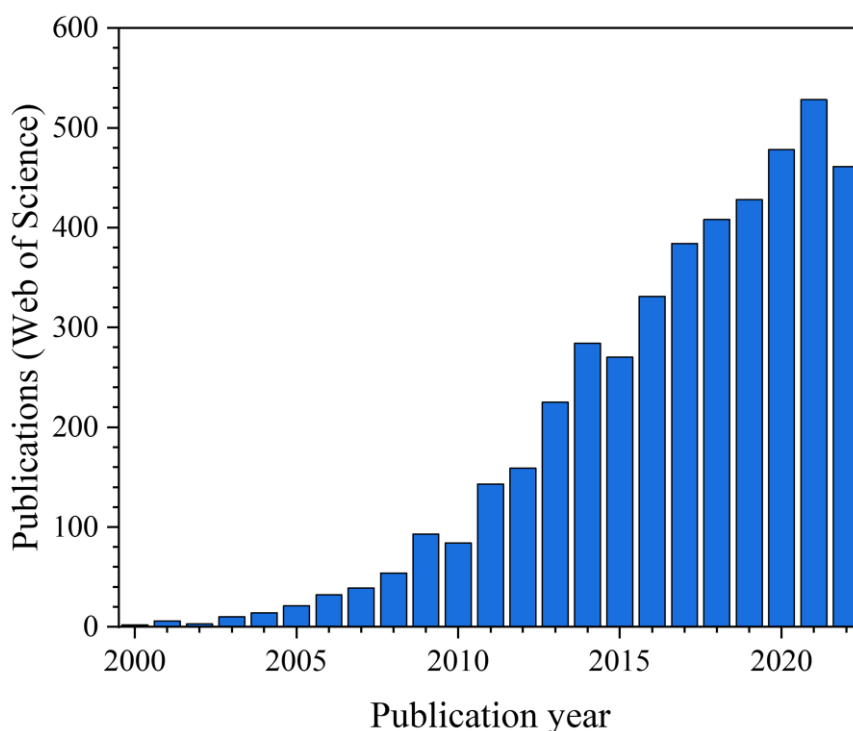


Figure 2-2: Annual publications containing the keyword “chemical looping” since 2000. Data from Clarivate Web of Science. © Clarivate 2023. All rights reserved. The decline in publications for 2022 could be related to the impact of the COVID-19 pandemic.

A general scheme of the CLC process is shown in **Figure 2-1**. The reactor system is typically based on two interconnected reactors: an air reactor and a fuel reactor. In the fuel reactor, the fuel reacts with the oxygen carrier to produce CO_2 and H_2O . The oxygen carrier, typically based on a transition metal oxide, is a critical part of the process and is used to cycle oxygen between the air and fuel reactors, preventing direct contact between the fuel and air. Since nitrogen dilution is avoided, a pure stream of CO_2 is obtained after simple steam condensation, demonstrating the main advantage of CLC over other CO_2 capture technologies. The reduced oxygen carrier is then reoxidised in the air in the air reactor and recirculated to the fuel reactor to complete a cycle, or “loop”. Two interconnected FBRs is the most commonly proposed reactor configuration for CLC,³³ although chemical looping systems based on fixed³⁴ and moving bed reactors³⁵ have also been proposed.

The CLC process is highly fuel flexible. Early research focussed on gaseous fuels, *e.g.* natural gas and syngas, since these fuels are straightforward to use and can be easily introduced to the system with the fluidising gas.^{33,36–39} The current challenges for the scale-up of CLC technology for gaseous fuels are a lack of dynamic modelling, the need for highly reactive and stable oxygen carriers over long-term redox cycling and operating the system under pressure (1-3 MPa⁴⁰) to increase the net electrical efficiency of the process using a combined cycle.^{41–43} The use of liquid fuels is a more recent development, driven by limited studies reported on heavy fuel oils and heavy vacuum residues produced during crude oil

refining.⁴⁴⁻⁴⁶ In the medium-long term, coal is expected to remain a key global energy source and coal-fuelled CLC could play a role in future CO₂-restrictive energy scenarios.⁴⁷ Most types of solid fuels have been studied, including hard coals, pet cokes, solid wastes and biomass.^{21,48,49} Biomasses are generally more reactive than coals and the combination of bioenergy with CCS, or BECCS, has been identified as essential to keep the rise in global temperature below 2°C above pre-industrial levels.² Combining bioenergy and CCS opens up the possibility of power generation with negative emissions, *i.e.* decreasing the atmospheric concentration of CO₂ while producing power.

Solid-fuelled CLC can be further classified depending on whether the fuel is directly or indirectly introduced to the reactor:

Indirect: the solid fuel is converted to an intermediate syngas which is then combusted in a CLC unit developed for gaseous fuels. An external gasification unit and air separation unit are required to produce the syngas because the syngas must be free of nitrogen.²¹

Direct: the solid fuel is introduced directly to the fuel reactor. This approach is further classified based on the behaviour of the oxygen carrier: in-situ gasification CLC (iG-CLC) and chemical looping with oxygen uncoupling (CLOU).

The direct solid fuel option is preferred because it avoids the energy penalty for producing oxygen and the capital costs associated with the gasification and air separation units required to produce the syngas.

2.2.2 *In-situ gasification chemical looping combustion (iG-CLC)*

The iG-CLC reaction scheme is shown in **Figure 2-3**. The solid fuel is added directly to the fuel reactor, where it is devolatilised to produce volatile matter, char and ash (reaction (2-1)). The char is then gasified by reactions (2-2) or (2-3) depending on whether CO₂ or steam is used as the gasifying agent, respectively. Direct reduction of the oxygen carrier by the volatile matter and gasification products (mainly CO and H₂) occurs *via* reactions (2-4) and (2-5). The reduced oxygen carrier is then transported to the air reactor, where it is re-oxidised *via* reaction (2-6).

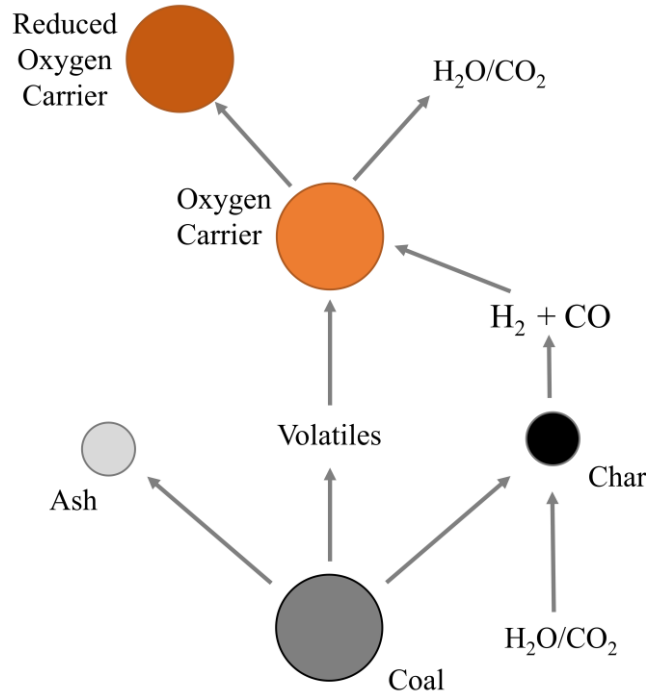
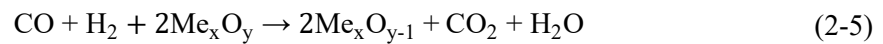
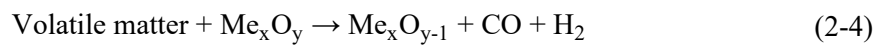
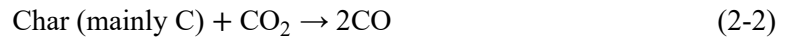
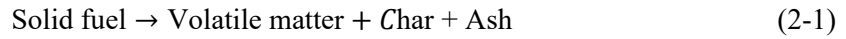


Figure 2-3: iG-CLC fuel reactor scheme. Coal is used as a representative solid fuel, adapted from Adanez et al.⁵⁰



Reaction (2-5) is very fast at high temperatures, and fuel gasification (reactions (2-2) and (2-3)) is generally considered to be the rate-limiting step in the fuel reactor.^{51,52} If char gasification is incomplete, some char will be transported to the air reactor with the reduced oxygen carriers. In the air reactor, any unconverted char will react with air to produce CO₂ that cannot be captured, reducing the overall CO₂ capture efficiency of the process. The higher volatile content of biomasses in comparison to high-rank coals is advantageous in this respect because a greater proportion of the fuel can directly reduce the oxygen carrier through reaction (2-4).

A carbon stripper has been proposed to separate any unconverted char exiting the fuel reactor from the oxygen carriers and feed it back to the fuel reactor.^{53,54} Unreacted volatiles and gasification products have also been observed at the outlet of the fuel reactor in bench- and pilot-scale studies, indicating incomplete combustion.^{55,56} An oxygen polishing step has been suggested to convert these unburnt products to CO₂ using highly concentrated oxygen.^{57,58} However, these additional downstream processing steps can significantly increase the cost of CO₂ capture.¹⁹ To overcome these challenges related to incomplete fuel conversion, research has shifted towards using materials with oxygen uncoupling capabilities.

2.2.3 Chemical looping with oxygen uncoupling (CLOU)

Since its proposal in 2009 by Mattisson *et al.*,²¹ the CLOU process has become a significant research area within the chemical looping community. This approach involves the release of gaseous oxygen from the oxygen carriers at high temperatures, which can react directly with the char and volatiles in the fuel reactor. In comparison, in iG-CLC, lattice oxygen in the metal oxide oxygen carriers reacts indirectly with the char *via* its gasification by-products.

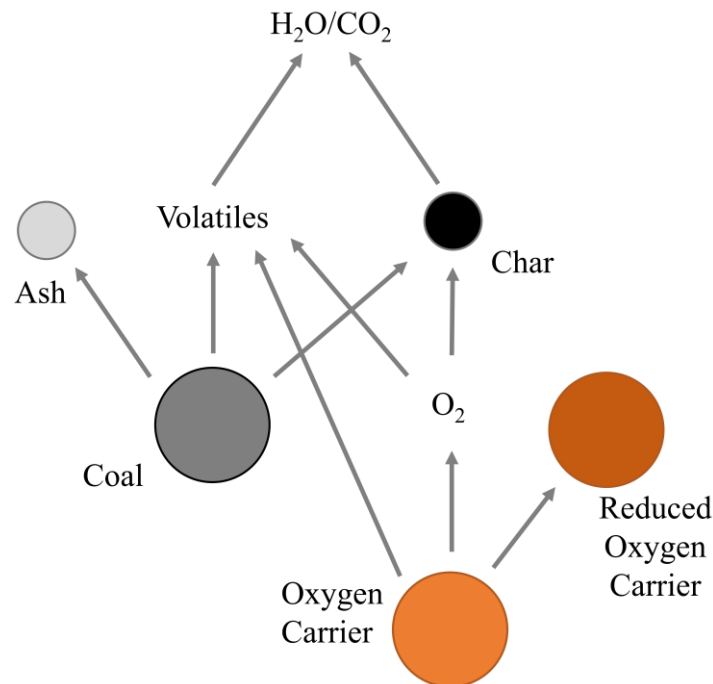
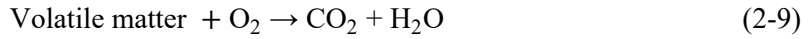


Figure 2-4: CLOU fuel reactor scheme. Coal is used as a representative solid fuel, adapted from Adanez *et al.*⁵⁰

The CLOU reaction scheme is shown in **Figure 2-4**. As with iG-CLC, the solid fuel is devolatilised in the fuel reactor to produce volatile matter and char (reaction (2-7)). Combustion of the volatiles and char occurs through reactions (2-9) and (2-10), respectively, using the gaseous oxygen released by the oxygen carriers with suitable thermodynamics for CLOU (reaction (2-8)). The reduced oxygen carrier is then transferred to the air reactor, where it is re-oxidised *via* the reverse of the reaction (2-8).



2.2.4 Comparison of iG-CLC and CLOU processes

Oxygen carriers with CLOU capabilities have been shown to significantly improve the performance of CLC units using solid fuels. A key advantage of CLOU over iG-CLC is the large reduction of oxygen carrier and fuel residence times because the fuel conversion rates are much higher with gaseous oxygen⁵⁵; this is particularly useful for low-reactivity fuels. Combustion efficiencies close to 100% and lower oxygen carrier inventories than equivalent iG-CLC units have also been reported.²² The steam requirement to the fuel reactor and carbon stripper for gasification can also be avoided using CLOU and recirculated CO₂ can be used as the sole fluidising gas.¹⁹ Pérez-astray *et al.* carried out a comparative study of biomass-fuelled CLC under both iG-CLC and CLOU modes.⁵² The tar species and concentrations at the fuel reactor outlet were extremely different under the two combustion modes. For the same process conditions, the amount of tar generated under iG-CLC was significantly higher and of a different type than was found in CLOU. The findings were attributed to the release of gaseous oxygen by the CLOU oxygen carriers.

However, the reactor temperatures must be more strictly controlled in CLOU. The thermodynamics of the oxygen release and re-oxidation reactions for each specific CLOU oxygen carrier constrain the operating temperatures of the fuel and air reactors.⁵³

Another important consideration is the cost of the oxygen carrier. Oxygen carriers from mineral sources, such as ilmenite⁵⁹ and industrial waste materials⁶⁰ can be used for iG-CLC, whereas synthetic oxygen carriers are mainly considered for CLOU, which increases the cost of oxygen carrier production. Therefore, the cost of the oxygen carrier make-up stream required due to the periodic purging of fuel ash is also higher for synthetic oxygen carriers, which increases the overall cost of CO₂ capture.

2.3 Oxygen carrier requirements

Developing oxygen carriers that can withstand extended redox cycling in chemical looping processes remains a critical challenge to advancing the technology. In a review published in 2016, Nandy *et al.*³⁶

estimated that over 1000 different oxygen carriers had been tested. This number has likely risen to at least 2000, considering the rise in studies published after 2016 citing the keyword “chemical-looping” (Figure 2-2). This section will discuss the different requirements of oxygen carriers.

2.4 Thermodynamics

Modified Ellingham diagrams have been used to screen for potential oxygen carrier materials.⁶¹ These diagrams plot the Gibbs free energy of the fuel oxidation and oxygen carrier oxidation reactions against temperature (Figure 2-5). For a reaction to occur, it must be thermodynamically favourable. Therefore, the Gibbs free energy of the fuel combustion reaction must have a more negative value than the oxidation reaction of the metal oxide. Potential oxygen carrier materials were identified by Jerndal *et al.* using thermodynamic analyses of different metal oxides with CH₄, H₂ and CO.⁶² Transition metal oxides of Cu, Mn, Ni, Fe and Co were identified as the metal oxides with the greatest potential for CLC.

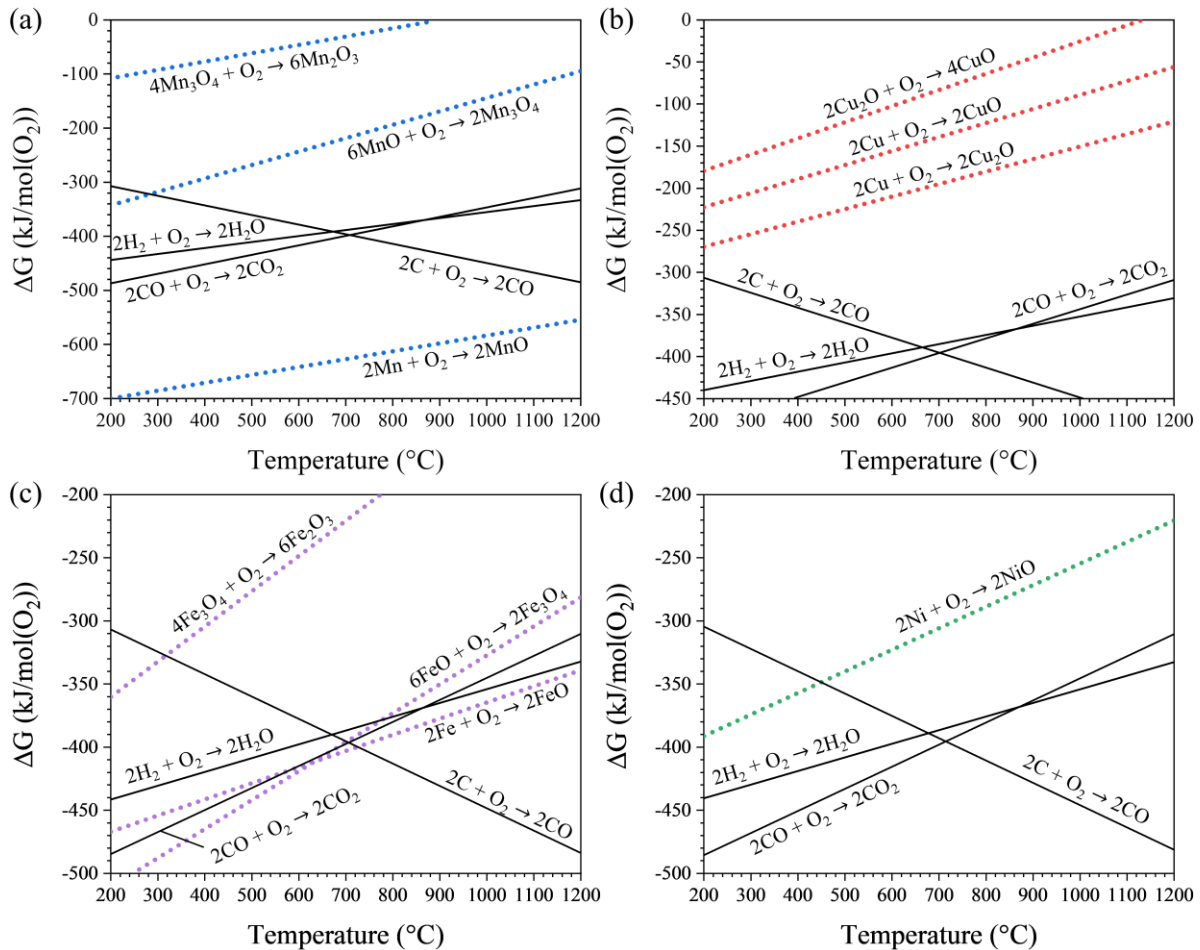
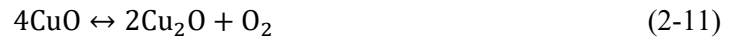


Figure 2-5: Modified Ellingham diagrams for (a) Mn oxides, (b) Cu oxides, (c) Fe oxides and (d) Ni oxides. Data from FactSage.⁶³

During the initial screening of potential oxygen carriers for basic CLC, the metal oxides CuO, Mn₂O₃, and Co₃O₄, were found to release oxygen at high temperatures (under atmospheric pressure). Consequently, these materials were initially deemed unsuitable for CLC, and the use of their reduced

forms (Cu_2O , Mn_3O_4 and CoO , respectively) was recommended unless the process was performed at lower temperatures or higher system pressures.⁶² However, Mattisson and Lyngfelt used this oxygen release behaviour as the fundamental principle for CLOU.²¹ Oxygen carriers for CLOU must have suitable equilibrium oxygen partial pressures ($p_{\text{O}_{2\text{eq}}}$) at relevant combustion temperatures (800 to 1200°C) to release gaseous oxygen in the fuel reactor. This additional thermodynamic requirement limits the selection of metal oxides for CLOU. Oxygen carriers that release gaseous oxygen are typically single or mixed metal oxides based on Cu, Mn and Co.^{62,64} The metal oxides CuO , Mn_2O_3 and Co_3O_4 release oxygen *via* reactions (2-11), (2-12) and (2-13), respectively:



The $p_{\text{O}_{2\text{eq}}}$ as a function of temperature for reactions (2-11), (2-12) and (2-13) is shown in **Figure 2-6**. It is crucial to select oxygen carriers with the appropriate $p_{\text{O}_{2\text{eq}}}$ for suitable operation of the fuel and air reactors. If the $p_{\text{O}_{2\text{eq}}}$ is too low, not enough gaseous oxygen will be released for CLOU, and the oxygen carriers will behave as conventional oxygen carriers for CLC. If the $p_{\text{O}_{2\text{eq}}}$ is too high, excessive oxygen will be released, requiring a larger oxygen carrier inventory and contaminating the CO_2 stream from the fuel reactor with unreacted oxygen. The maximum operating temperature of the air reactor can be determined from **Figure 2-6** for $p_{\text{O}_{2\text{eq}}} = 0.21$. For higher $p_{\text{O}_{2\text{eq}}}$, the oxygen carriers would decompose in air. Maximum operating temperatures of ~1030, 890 and 830°C were determined for CuO -, Mn_2O_3 - and Co_3O_4 -based oxygen carriers, respectively.

In reality, the outlet oxygen concentration of the air reactor flue gas should be as low as possible to avoid large gas flows and accompanied thermal losses that reduce the overall plant efficiency.⁶⁵ An outlet oxygen concentration of 5% has been set as a target in the literature,⁶⁶ equivalent to an excess air ratio of 20%, which is comparable to what is used in circulating fluidised-bed boilers.⁶⁷ The equilibrium temperature corresponding to this outlet concentration of oxygen determines the maximum operating temperature of the air reactor. For $p_{\text{O}_{2\text{eq}}} = 0.05$ bar, maximum operating temperatures of ~960, 825 and 780°C were determined for CuO -, Mn_2O_3 - and Co_3O_4 -based oxygen carriers, respectively, using **Figure 2-6**.

The maximum operating temperatures of the air reactor using Co_3O_4 - and Mn_2O_3 -based oxygen carriers are much lower than the CuO -based system. Therefore, the redox rates of Mn_2O_3 -based oxygen carriers

have been observed to be much slower than the CuO-system at their respective equilibrium temperatures.⁶⁸

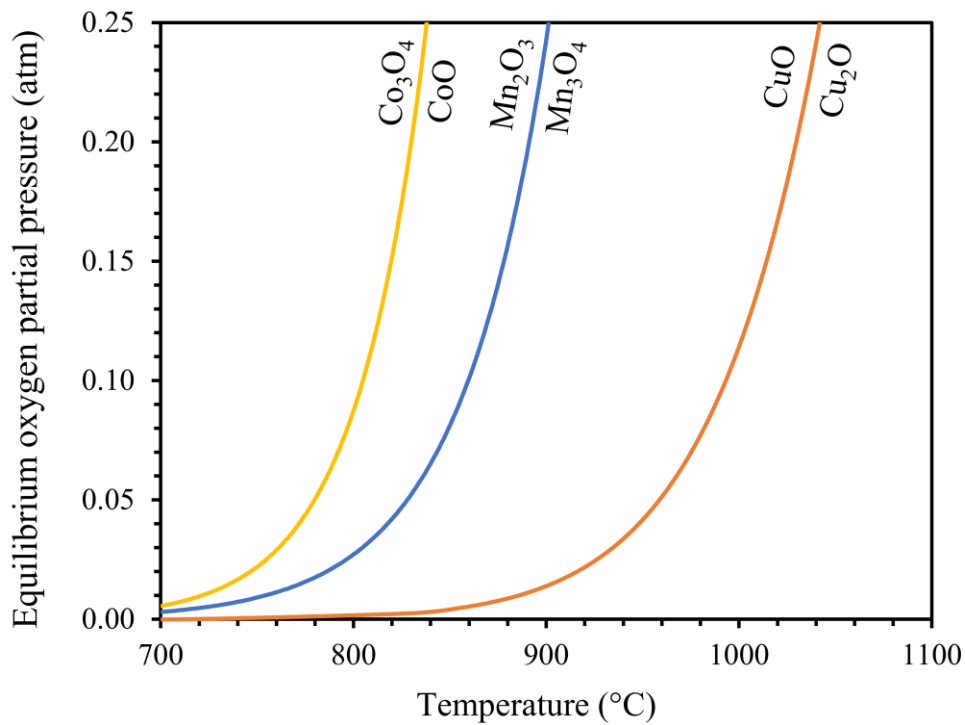


Figure 2-6: Equilibrium oxygen concentrations of Cu₂O/CuO, Mn₂O₃/Mn₃O₄ and CoO/Co₃O₄ systems as a function of temperature. Determined using FactSage.⁶³

In addition to stoichiometric metal oxides such as CuO, oxides possessing a perovskite structure have recently been used for chemical looping processes.^{69–72} The general crystal structure of perovskites is AMO₃, where A is an alkaline earth or rare metal cation and M is a transition metal cation. Perovskites have unique properties where oxygen can be released at high temperatures while maintaining their crystal structure. For example, the oxygen release reaction for a perovskite, AMO₃:



where the oxygen non-stoichiometric coefficient, δ , depends on the temperature and the oxygen partial pressure, p_{O_2} .

The resulting AMO_{3- δ} structure is stable and contains transition metal cations with mixed valences and oxygen non-stoichiometry. Further release of oxygen from the perovskite AMO_{3- δ} may occur through the phase transition to a brownmillerite phase, AMO_{2.5+ δ} , depending on the temperature and p_{O_2} in the reactor. The perovskite structure is highly tuneable, and the choice of A (e.g. La and Sr) and M (e.g. Fe, Cu and Co) can be optimised for different properties, such as p_{O_2eq} .

2.4.1 Oxygen capacity

The oxygen storage capacity, R_{OS} , is a critical parameter in the design of CLC units. The R_{OS} determines the amount of oxygen that can be transported from the air reactor to the fuel reactor. The R_{OS} value quantifies the amount of oxygen that can be transferred per unit mass of the oxygen carrier (g_{O_2}/g_{OC}). The parameter can be measured experimentally by calculating the difference between the mass of the fully oxidised (m_{ox}) and fully reduced (m_{red}) oxygen carrier, shown in equation (2-15). For oxygen carriers with multiple oxidation states, the extent of reduction and oxidation (and hence R_{OS}), depends on the reactor conditions. The oxygen release capacity, R_{OR} , is the amount of gaseous oxygen that can be released in the fuel reactor by a CLOU oxygen carrier and is calculated by determining the difference between m_{ox} and the fully oxygen released ($m_{O_2,release}$) oxygen carrier, shown in equation (2-16).

$$R_{OS} = \frac{(m_{ox} - m_{red})}{m_{ox}} \quad (2-15)$$

$$R_{OR} = \frac{(m_{ox} - m_{O_2,release})}{m_{ox}} \quad (2-16)$$

The oxygen capacities of some commonly used oxygen carriers are shown in **Table 2-1**. Using oxygen carriers with high R_{OS} and R_{OR} is advantageous because it enables the transport of a greater amount of oxygen between the two reactors for a smaller oxygen carrier inventory, thereby reducing the reactor volumes.

Table 2-1: Oxygen capacities of commonly studied oxygen carrier systems.

Oxygen carrier system (Oxidised/Reduced)	Oxygen capacity (gO ₂ /gOC)
CuO/Cu	0.201
CuO/Cu ₂ O	0.101
Mn ₂ O ₃ /Mn ₃ O ₄	0.034
Mn ₂ O ₃ /MnO	0.101
Co ₃ O ₄ /CoO	0.066
Fe ₂ O ₃ /Fe ₃ O ₄	0.033
Fe ₂ O ₃ /FeO	0.100
Fe ₂ O ₃ /Fe	0.301
NiO/Ni	0.214

2.4.2 Thermal stability

Oxygen carriers with high melting temperatures are needed to avoid the agglomeration of bed particles during operation. The melting temperature of the oxidised and reduced metal oxides (**Table 2-2**) should be above the reactor operating temperature to prevent operational issues. For processes using solid fuels, it is important to consider any low-melting eutectics that may form due to interactions of the oxygen carriers with ash species after devolatilisation. These eutectics can occur well below the melting temperature of the oxygen carrier and cause agglomeration of the bed material.^{73,74} In a fluidised system, particle agglomeration can cause localised defluidisation, increasing the local bed temperature, which can trigger more severe melting and further agglomeration.⁷⁵ Garcia-Labiano *et al.* developed a particle reaction model to study temperature variations within supported Cu-, Co-, Fe-, Mn- and Ni-based oxygen carrier particles (40 wt% active material) during redox cycling.⁷⁶ They found a maximum temperature variation of 15°C for any reaction of any oxygen carrier, although this will depend on particle size and loading of active metal oxide. The Tammann temperature is the temperature at which atoms in the bulk exhibit mobility, *i.e.* the onset of sintering, and is typically approximated as half of the melting temperature of a material. For CuO, the fuel and air reactors are likely to operate close to the melting temperature and above the Tammann temperature of Cu oxides. Therefore, effective stabilisation of the metal oxide is needed to prevent sintering, agglomeration and deactivation of the oxygen carrier during operation.⁷⁷

Table 2-2: Melting point and Tammann temperature of commonly investigated oxygen carriers.⁷⁸

Material	Melting point (°C)	Tammann temperature (°C)
CuO	1026	526
Cu ₂ O	1235	481
Cu	1083	405
Mn ₂ O ₃	1080	677
Mn ₃ O ₄	1564	919
MnO	1650	1150
Co ₃ O ₄	895	455
CoO	1935	970
Fe ₂ O ₃	1560	1105
Fe ₃ O ₄	1538	1094
FeO	1420	631
NiO	1955	841
Ni	1452	590

2.4.3 Mechanical stability

In a fluidised CLC unit, particle degradation is caused by a combination of thermal, mechanical and chemical stresses.^{79,80} Thermal stresses result from rapid temperature changes, causing particles to expand and contract. Mechanical stresses are due to particle-particle or particle-wall collisions. Chemical stresses occur due to the redox cycling of the oxygen carriers, whereby the lattice structure is forced to change rapidly.⁸¹ To improve the mechanical stability of the oxygen carrier, the active metal oxide is often combined with an inert support.^{50,81,82} The support material must be inert under relevant reactor conditions and have high mechanical strength. Commonly used materials to support metal oxides for CLC include TiO₂, SiO₂, ZrO₂, Al₂O₃ and MgAl₂O₄.³³ Patzschke used the microhardness of the support material to evaluate potential improvements to the mechanical stability of the oxygen carrier.⁸³ The average microhardness of the active metal oxides was ranked as: Cu₂O < CuO < NiO < Mn₃O₄ < Fe₃O₄ < Fe₂O₃. The average microhardness of the inert support was as follows: MgO < TiO₂ < ZrO₂ (CaO stabilised) < SiO₂ < MgAl₂O₄⁸⁴ < Al₂O₃.

Increasing the mechanical strength of an oxygen carrier particle can reduce the rate of attrition and increase the lifetime of the particle,⁸⁵ requiring lower make-up rates and improving process economics.⁸⁶ A commonly used screening tool to predict the mechanical performance of an oxygen carrier in a fluidised system is the single particle crushing strength test.^{87,88} For each test, a force gauge is lowered on a particle and the final force before the particle fractures is the crushing strength. In theory, the higher the crushing strength, the greater the stress the oxygen carrier particles can withstand in the fluidised system. Although this method is easy to use, the results may not accurately represent the true resistance towards mechanical stresses in-situ because the crushing force is not measured at relevant reactor conditions, nor in a reacting environment; and the relationship between the mechanical resistance of a particle and attrition is highly complex.⁸⁹

Attrition in a fluidised system can occur *via* a combination of surface abrasion or fragmentation.⁷⁹ Surface abrasion typically takes place in the dense region of the fluidised bed where the particles are subjected to friction or collisions at low velocity, generating a lot of very fine particles due to the wearing of the particle surface. In contrast, particle fragmentation occurs near the gas distributor, where the collision energy is higher due to the high velocity fluidising gas jets. Attrition can cause a loss of bed material due to the generation of fines which are elutriated from the reactors. The particle size distribution of the bed may undergo a significant change, which can affect the heat and mass transfer coefficients and reaction rates in the reactor.⁹⁰ The mode of attrition may vary from pure abrasion to total fragmentation.

The particle breakage mechanism that occurs during single particle crushing measurements is more representative of the fragmentation mode of attrition than surface abrasion. Attrition rate measurements using attrition rigs have been shown to provide a better indication of the rate of attrition in an industrial-scale fluidised system.⁸⁹ Rydén *et al.* used a jet cup to measure the attrition resistance of 25 oxygen carrier materials.⁸⁹ A jet cup is a device designed to simulate the effects of jet attrition and cyclone attrition, typically considered to be the two main contributors to mechanical attrition in circulating fluidised bed combustion.⁸⁹ No strong correlation between single particle crushing strength tests and attrition resistance measured in the jet cup could be established. However, it was clear that particles that recorded a crushing strength above 2 N in single particle tests demonstrated a higher attrition resistance in the jet cup.

2.4.4 Chemical stability

The reactivity of an oxygen carrier affects the solids residence time, oxygen carrier inventory and the size of the air and fuel reactors.⁹¹ The choice of metal oxide, support and particle preparation method can influence the reactivity of the oxygen carrier.^{19,92,93} Potential oxygen carriers are often screened using a thermogravimetric analyser (TGA)^{87,94} or bench-scale FBR^{95,96} and simulating chemical looping

conditions by alternating between oxidising and reducing gases at high temperatures. The TGA system requires only small amounts of oxygen carriers to be produced, while FBRs require larger amounts of materials but better simulate the actual process conditions and assess the mechanical strength and reactivity of the oxygen carrier over extended redox cycles. Discontinuous FBR experiments are useful as initial screening methods; however, tests in pilot plant facilities are required to gain a deeper understanding of the oxygen carrier performance.⁵⁰

Unsupported metal oxides have been shown to deactivate quickly during high-temperature operation due to sintering and agglomeration. Active metal oxides are usually combined with a support material to improve their chemical stability. The dispersion of an active metal oxide in a support can also provide a higher surface area for reaction and improve the mechanical stability of the oxygen carrier during redox cycling.^{50,81} However, some supports may chemically interact with the active material phase, which can have negative or positive effects on the performance of an oxygen carrier. **Figure 2-7** shows the main interactions between the main metal oxides and support materials commonly reported in the literature. Studies investigating metal oxides supported by ZrO_2 or MgAl_2O_4 generally report limited interaction between the support and active metal oxide. However, metal oxides supported by TiO_2 , SiO_2 or Al_2O_3 tend to show high interaction, leading to the formation of undesired solid-state reaction products, loss in reactivity and agglomeration at high temperatures.

The chemical interactions between the active metal oxide and the support can have a positive or negative effect on the performance of an oxygen carrier. For example, one of the most researched oxygen carriers is CuO supported on Al_2O_3 . However, at high temperatures, the interaction between CuO and Al_2O_3 can result in the loss of active CuO through the formation of a CuAl_2O_4 spinel phase, which is relatively stable to decomposition under CLOU conditions and reduces the oxygen release capacity of the particle.⁹⁷ Conversely, Fe_2O_3 supported on TiO_2 can form FeTiO_3 , which has been observed to enhance oxygen ion diffusion in the oxygen carrier and increase the oxygen carrier reactivity.⁹⁸ Therefore, it is important to have a strong understanding of the support and the metal oxide system to predict the solid phases that may form within the oxygen carrier and the impact of these phases on the performance and lifetime of the particle over long-term high-temperature redox cycles.

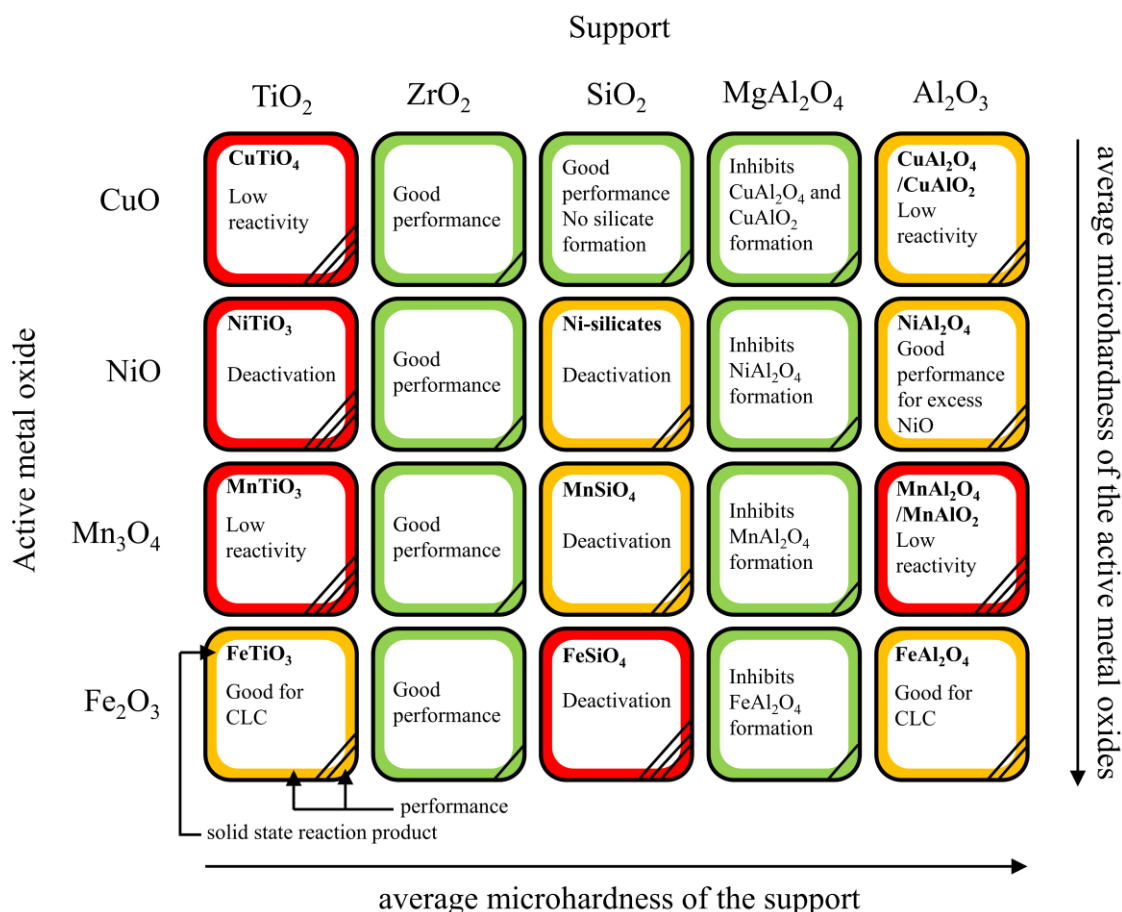


Figure 2-7: Interactions of commonly used active phase and support combinations. Each tile indicates the possible solid-state reaction products and their effect on the reactivity and performance of the oxygen carriers. Green (or one diagonal line) and red outlines (or three diagonal lines) indicate good and bad performance, respectively. The performance of the tiles with orange outlines (or two diagonal lines) depends on the reactor conditions and amount of support incorporated in the oxygen carrier, adapted from De Vos *et al.*⁸²

2.4.5 Safety and environmental impacts

It is also important to consider the health, safety and environmental risks of oxygen carriers used in chemical looping processes. Idziak *et al.* published a review of the safety and environmental risks of using Ni-, Co-, Cu-, Mn- and Fe-based oxygen carriers.⁹⁹ The study determined that Ni- and Co-based materials showed the most significant health risks due to their possibly carcinogenic properties. In contrast, Fe and Mn-based materials were considered non-toxic and posed little risk. Cu-based materials had considerably lower risks than Ni and Co, with the greatest risk associated with their impact on aquatic life.

2.5 Oxygen carrier materials

Transition metal oxides of Ni, Cu, Co, Fe and Mn have been extensively studied for the development of oxygen carriers due to their oxygen storage capacities and suitable thermodynamic properties.^{62,100} Initially, oxygen carrier development focused on monometallic oxides, but later research focused on the use of supported single metal oxides, binary metal oxides and non-stoichiometric materials, such as perovskites. This section provides an overview of the characteristics of common oxygen carrier materials.

2.5.1 Supported single metal oxides

Copper

CuO-based oxygen carriers have been extensively studied due to their excellent chemical looping properties, such as high oxygen storage capacities, fast kinetics, a low tendency towards carbon deposition, low costs and low toxicity.¹⁰¹ In addition, CuO is a CLOU material that can rapidly release gaseous oxygen through its decomposition to Cu₂O at temperatures above 850°C (at atmospheric pressure), resulting in high fuel conversion rates and CO₂ capture efficiencies.¹⁰² However, CuO-based oxygen carriers have two major drawbacks, low mechanical strength and a low melting point. These issues can lead to agglomeration of the oxygen carriers and defluidisation of the bed during operation.^{101,103} Despite the low melting temperature of Cu materials, successful operation of supported CuO-based oxygen carriers in fluidised systems has been reported for CLOU at 950°C.¹⁰⁴ However, oxygen carriers used in pilot facilities are usually restricted to low loadings of CuO (<40 wt%).^{105,106} To improve their mechanical stability, CuO is often supported on Al₂O₃.^{106–108} However, the active CuO can react with Al₂O₃ to form CuAl₂O₄, and upon oxygen release, CuAlO₂.¹⁰⁹ The formation of CuAlO₂ is detrimental to the performance of the oxygen carrier because the rate of re-oxidation back to CuAl₂O₄ has been shown to proceed much slower than the re-oxidation of Cu₂O to CuO.¹¹⁰

The addition of Mg to the Cu-Al system has been shown to stabilise the oxygen release capacity by inhibiting the formation of CuAl₂O₄ through the preferential formation of a MgAl₂O₄ support phase.^{107,111} Adánez-Rubio *et al.* investigated the oxygen release of CuO/MgAl₂O₄ oxygen carriers prepared using spray drying in an FBR.¹¹² The oxygen carriers exhibited the appropriate characteristics for CLOU and did not agglomerate during operation. However, a considerable amount of fines were generated after 40 h of continuous operation. Arjmand *et al.* produced CuO/MgAl₂O₄ oxygen carriers *via* freeze granulation and reported stable reactivity for CLOU and similarly reported a low crushing strength of only 0.5 N.¹¹³ Therefore, CuO/MgAl₂O₄ appears to be a suitable oxygen carrier for the CLOU process, but improvements in mechanical strength are necessary to improve their lifetime for use in scaled-up processes.

Manganese

Mn₂O₃-based oxygen carriers are a non-toxic and lower-cost alternative to CuO. However, they have lower oxygen capacities and generally demonstrate a lower reactivity with fuels than CuO-based oxygen carriers.⁸⁸ In addition, Mn₃O₄ can form stable metal oxides with most support materials, such as Al₂O₃, SiO₂ and TiO₂ (**Figure 2-7**), that are resistant to reduction and therefore represent a loss of active material and oxygen release capacity.^{87,100,114} Mn₂O₃-based oxygen carriers for CLOU have also shown slow re-oxidation kinetics from Mn₃O₄ to Mn₂O₃ at the low temperatures required for full re-oxidation in the air reactor (**Figure 2-6**). Mixed oxides of Mn with other transition metals have been produced to overcome these thermodynamic and kinetic limitations.¹¹⁵

Iron

Fe₂O₃ is a cheap, abundant, non-toxic and environmentally benign oxygen carrier with a high theoretical oxygen storage capacity ($R_{OS} = 0.30$ for reduction to metallic Fe).¹¹⁶ Fe₂O₃-based oxygen carriers undergo three transitions states to metallic Fe, Fe₂O₃ → Fe₃O₄, Fe₃O₄ → FeO, and FeO → Fe. The reduction and re-oxidation rates between Fe₂O₃ and Fe₃O₄ are generally fast; however, the Fe₃O₄ → FeO and FeO → Fe transitions are slow.⁶² Therefore, despite having a large potential oxygen storage capacity, the most common Fe₂O₃-based redox cycle used for CLC is Fe₂O₃ ↔ Fe₃O₄, with a much lower R_o of 0.04. Serious sintering and rapid deactivation of Fe₂O₃-based oxygen carriers have been reported in the literature.^{117,118} The metal oxide is often supported on Al₂O₃,¹¹⁹ MgAl₂O₄,¹²⁰ SiO₂,¹²¹ TiO₂⁹⁸ and ZrO₂¹²² to reduce deactivation over extended redox cycling. Chemical interactions of Fe₂O₃ with some supports, such as TiO₂, have also been shown to produce positive effects.⁹⁸ However, more research is required to produce Fe₂O₃-based oxygen carriers with high loadings of active metal oxide, high sintering resistance and high redox rates between Fe₃O₄, FeO and Fe.

2.5.2 Combined metal oxides

Combined metal oxides, e.g. CuMnO₂, consist of solid solution phases of multiple metal oxides, which have different thermodynamic and kinetic properties than their individual parent oxides. By tuning the ratio of metals in the oxygen carrier, mixed metal oxides can overcome some of the limitations associated with the constituent single metal oxides. Various Mn metal oxides, including Mn-Mg, Cu-Ni, Mn-Ni and Mn-Fe, have been synthesised and tested.¹¹⁴ The mixed Mn-oxides were found to overcome the restrictive low equilibrium temperatures required in the air reactor and enabled re-oxidation at higher temperatures where the rates are more appreciable.¹²³ In addition, Cu-Mn metal oxides have also demonstrated good oxygen release kinetics and overcome the stability and low melting point issues of Cu-based oxygen carriers and the low reactivity of Mn-based oxygen carriers.¹²⁴ A Cu-Mn oxide developed by Adánez-Rubio *et al.* was tested in a 1.5 kW_{th} continuous unit using biomass as fuel.¹²⁵ No unburnt compounds were present in the fuel reactor outlet, even at the lowest temperature studied (775°C), and high CO₂ capture (>95%) and combustion efficiencies (100%) were achieved with

no agglomeration. Fe and Mn have been widely studied as single metallic oxides with different support materials.¹²⁶ Fe-Mn binary oxides have been reported with the ability to release gaseous oxygen with good resistance to impurities such as sulphur.¹²⁷ However, X-ray studies of the phase evolution during redox cycling showed phase segregation during reduction,¹²⁸ and the de-alloying of Mn-Fe combined oxides during cycling reduces the synergistic effect of combining the two metal oxides.¹¹⁴

2.5.3 Perovskites

Oxygen carriers based on perovskite-type (AMO_3) materials have recently been explored in the literature. These materials are extremely tuneable and can be customised for different chemical looping applications. Some materials that have been tested in chemical looping processes include those based on A site metals Ca, La and Sr, *e.g.* $\text{CaMnO}_{3-\delta}$,¹²⁹ $\text{LaFeO}_{3-\delta}$,¹³⁰ and $\text{SrFeO}_{3-\delta}$,¹³¹ and it is also possible to introduce different cations for the M sites, *e.g.* $\text{CaMn}_{1-x}\text{B}_x$ (where B = Al, Fe, Co and Ni).⁷⁰ Perovskites can also have multiple metals for both A and M sites, *e.g.* $\text{La}_{1-x}\text{Sr}_x\text{Co}_{1-y}\text{Fe}_y\text{O}_{3-\delta}$.¹³⁰

The high tunability of perovskite materials means specific properties, such as $p_{\text{O}_2\text{eq}}$ and oxygen release capacity, can be optimised for different chemical looping applications. Lau *et al.* used in silico screening to screen 5501 potential materials for chemical looping air separation (CLAS), a variant of CLOU, which requires materials with high $p_{\text{O}_2\text{eq}}$ at low temperatures.¹³² Three perovskite materials were identified as the most promising candidates based on the perovskite to brownmillerite reaction and were synthesised and tested for CLAS. $\text{SrFeO}_{3-\delta}$ demonstrated large and stable oxygen release at low temperatures (600°C). In future studies, the in-silico screening method could be expanded to include quaternary and doped perovskite materials. Furthermore, Marek *et al.* investigated $\text{SrFeO}_{3-\delta}$ for CLC.¹³¹ During reduction, $\text{SrFeO}_{3-\delta}$ was converted to SrO and metallic Fe and converted back to a perovskite structure $\text{SrFeO}_{3-\delta}$ upon re-oxidation. The material showed remarkably high stability despite the severe change in structure beyond the perovskite to brownmillerite ($\text{SrFeO}_{2.5}$) phase transition. As a result, the material demonstrated a much higher oxygen storage capacity than expected. Although more cycles are required beyond the 30 cycles performed in this study, these results are very promising.

The €10M EU-FP7 SUCCESS (Scale-up of Oxygen Carrier for Chemical Looping Combustion using Environmentally Sustainable Materials) project focused on the scale-up of manufacturing and fabrication of two oxygen carriers using large-scale equipment and industrially available raw materials for use in demonstration-scale (10 MW_{th}) CLC reactors.¹⁰⁴ One of the oxygen carriers investigated for SUCCESS was $\text{CaMn}_{1-x}\text{Ti}_x\text{O}_{3-\delta}$. The perovskites were prepared at lab-scale by mixing stoichiometric quantities of MnO_2 , Ca(OH)_2 , MgO and TiO_2 in deionised water and homogenised using an attrition mill prior to spray drying. The material prepared at industrial-scale required Ca(OH)_2 to be substituted by CaCO_3 and minor changes to the spray drying process. The industrial-scale oxygen carriers demonstrated a much lower oxygen release capacity compared to the lab-scale materials and had

variable crushing strength and density. This was attributed to incomplete mixing, unreactive CaO remaining in the oxygen carriers and the low purity of the perovskite phase, attributed to an inhomogeneous calcination temperature.¹³³ Testing in a 10 kW pilot plant found that the fuel conversion using the industrial-scale oxygen carriers was significantly lower than the lab-scale materials.¹³⁴ Marek *et al.* prepared nearly phase-pure $\text{SrFeO}_{3-\delta}$ material by mechanical mixing of inexpensive Fe_2O_3 and SrCO_3 powders followed by calcination.¹³¹ The mechanical mixing technique is easily scalable compared to other synthesis methods for oxygen carrier preparation. However, the SUCCESS project found that the preparation of these materials at the ton scale was challenging and further optimisation was required to achieve a homogeneous sintering temperature during calcination.¹³³

A comparative study of Fe_2O_3 -, CuO -, and $\text{SrFeO}_{3-\delta}$ -based oxygen carriers for CLC of biomass char determined that the burnout time of 0.1 g char particles at 1168 K followed the trend $\text{CuO} < \text{SrFeO}_{3-\delta} < \text{Fe}_2\text{O}_3$.¹³⁵ The faster burnout of char using CuO than $\text{SrFeO}_{3-\delta}$ was attributed to the higher amount of oxygen released from CuO . Similar burnout times between CuO and $\text{SrFeO}_{3-\delta}$ were observed when the amount of CuO was reduced to match the oxygen released from $\text{SrFeO}_{3-\delta}$.

2.6 Natural ores and synthetic materials as oxygen carriers

Both natural ores and synthetic oxygen carriers have been used in pilot-scale CLC systems. While the choice of metal oxide in CLC has a substantial effect on the overall efficiency of energy production, the cost of oxygen carrier replacement can affect the overall economic feasibility of a scaled-up CLC process.¹³⁶ Oxygen carriers must withstand harsh operating conditions, including high temperatures and impurities from the gaseous and solid fuels used for CLC. The process conditions cause unavoidable loss of the oxygen carrier due to attrition, deactivation and oxygen carrier-ash separation.⁹⁴ A trade-off exists between the use of synthetic oxygen carriers with high fuel conversions, higher costs and often superior lifetimes and cheaper natural ores that require minimal conditioning.

2.1.1 Natural ores

The use of natural ores as oxygen carriers have been extensively researched due to their availability and low cost.^{137–139} These ores contain metal oxides that are naturally bound to other metal oxides in the ore, such as Al_2O_3 , TiO_2 and ZrO_2 , much like supported synthetic oxygen carriers. As a result, natural ores are a viable option for low-cost oxygen carriers, as they only require simple pre-treatment steps such as crushing, sieving and calcination. Natural ores have a lifetime of only a few hundred hours, which is sufficient considering their low cost. In contrast, synthetic materials are typically much more expensive and require a significant increase in lifetime to achieve comparable costs to ores.

A literature review of natural Cu ores used in chemical looping processes is presented in **Table 2-3**. The primary sources of Cu ore are from China, Chile, Peru and the United States.¹³⁷ For the Chinese

ores studied in **Table 2-3**, sulfuration and flotation are used to increase the Cu concentration in the ore, converting natural Cu and Fe to CuS and CuFeS, respectively.¹⁴⁰ A calcination process is used to oxidise the Cu concentrates to produce the oxygen carrier material. The average composition of the oxygen carriers based on refined Chinese Cu ore is 21 wt% CuO and 70 wt% CuFe₂O₄, with minor amounts of 6 wt% SiO₂ and 1 wt% CaSO₄. These oxygen carriers have high theoretical oxygen capacities but showed poor stability over extended redox cycling due to sintering.

Wen *et al.* studied three Cu ores using a TGA and FBR.¹⁴¹ All three Cu ores showed high reactivity and cyclic stability in a TGA. However, the ores with higher Cu contents experienced severe agglomeration during operation in an FBR. Despite the lower cost of natural ores compared to synthetic oxygen carriers, the lower Cu content required for the ore would require a substantial solid recirculation rate and solid inventories, and hence larger reactors, increasing capital costs.

Table 2-3: Cu ores used as oxygen carriers in CLC systems, adapted from Matzen *et al.*¹³⁷

Material	Cu content (wt%)	Process	Number of cycles	Performance	Reference
Chrysocolla, Cuprite, Malachite	CuO: 64.4, 15.7, 15	CLC: coal and methane, TGA	30	Stable conversion, no agglomeration, some loss of mechanical strength	Tian <i>et al.</i> ¹⁴²
Three copper ores	CuO: 87.3, 63.3, 5.8	CLOU, TGA and FBR	20	Higher Cu content ores agglomerate, stable reactivity	Wen <i>et al.</i> ¹⁴¹
Refined Chinese copper ore	CuO: 21 CuFe ₂ O ₄ : 70	CLC: coal, TGA and FBR	5	Slight agglomeration and sintering, stable performance after 1 cycle	Zhao <i>et al.</i> ¹³⁹
Refined Chinese copper ore	CuO: 21 CuFe ₂ O ₄ : 70	CLC: syngas, TGA and FBR	18	Decrease in activity stabilises after 10 cycles	Yang <i>et al.</i> ¹⁴³
Refined Chinese copper ore	CuO: 21 CuFe ₂ O ₄ : 70	CLC: pine sawdust, TGA and FBR	21	Stable O ₂ transport capacity, slight sintering, good fluidisation	Guo <i>et al.</i> ¹⁴⁴
Refined Chinese copper ore	CuO: 21 CuFe ₂ O ₄ : 70	CLC: coal, TGA and FBR	5	Some agglomeration at 950°C	Wang <i>et al.</i> ¹⁴⁵
Refined Chinese copper ore	CuO: 21 CuFe ₂ O ₄ : 70	CLC: syngas with H ₂ S, TGA and FBR	10	Cu ₂ S and FeS formation	Wang <i>et al.</i> ¹⁴⁶
Refined Chinese copper ore	CuO: 21 CuFe ₂ O ₄ : 70	CLC: syngas and coal, TGA and FBR	20	Sintering, decrease of O ₂ transport and methane conversion	Tian <i>et al.</i> ¹⁴⁷
Refined Chinese copper ore	CuO: 23 CuFe ₂ O ₄ : 57	CLC: methane, TGA	20	Sintering, decrease of O ₂ transport and methane conversion	Gu <i>et al.</i> ¹⁴⁸

2.1.2 Synthetic oxygen carriers

Table 2-4 presents the standard methods used to prepare oxygen carriers in the literature, including mechanical mixing, impregnation and co-precipitation. The preparation of oxygen carriers involves two main steps: mixing of the precursors and the formation of particles. Although there has been significant progress in the development of oxygen carriers, the large amounts of oxygen carriers required for large-scale continuous CLC reactors require laboratory-scale preparation methods to be suitable for scale-up without compromising material characteristics. Currently, oxygen carriers prepared using freeze granulation,¹⁴⁹ spray drying^{104,150} and impregnation¹⁰⁴ methods have been demonstrated in pilot-scale CLC units (<10 MW_{th}). The preparation conditions, active metal loading, crushing strength and performance of synthetic CuO-based oxygen carriers supported on Al₂O₃ or MgAl₂O₄ published in the literature are shown in **Table 2-5**.

Table 2-4: Common preparation methods used to synthesise oxygen carriers for chemical looping processes.¹⁵¹

Preparation method	Principle
Mechanical mixing	Mechanical mixing of metal oxide powders, usually carried out in a ball mill. The materials can be formed into oxygen carrier particles through pelletisation or extrusion followed by calcination, or the milled material can be calcined, crushed and sieved to the desired size fraction.
Mechanical mixing with spray-drying	Mechanical mixing followed by the addition of ~5 wt% of an organic solvent, <i>e.g.</i> isopropanol. The slurry is then milled and sprayed through a nozzle into a drying chamber where the droplets dry instantaneously.
Mechanical mixing with freeze-granulation	Mechanical mixing of metal oxide powders followed by the addition of ~5 wt% of an organic solvent, <i>e.g.</i> isopropanol. The slurry is then homogenised using a mill and sprayed through a nozzle into liquid nitrogen, where the droplets freeze instantaneously. The particles are then dried by freeze-drying.
Impregnation	Deposition of an active metal precursor on a support material by immersing an inert support in a metal salt solution. The mixture is then aged, followed by the removal of the liquid by drying. The material may undergo several impregnations to increase the loading before the material is calcined to convert the impregnated metal salts into metal oxides.
Co-precipitation	Mixing of a metal cation solution and precipitating agent in a reaction vessel to form a precipitate which is then washed and dried. The dried precipitate is calcined, crushed and sieved to the desired size fraction.

Table 2-5: Preparation and testing of CuO/Al₂O₃ and CuO/MgAl₂O₄ oxygen carriers for CLC and CLOU.

CuO content (wt%)	Support material	Preparation method	Crushing strength (N)	Calcination conditions	Process (cycles)	Performance	Reference
14	Al ₂ O ₃	IM	2.0	850°C, 1 h	CLC (65 h), FBR	Decrease of crushing strength from 3 to 2 N over 60 h	Izquierdo <i>et al.</i> ¹⁵²
15	Al ₂ O ₃	IM	2.5	850°C, 6 h	CLOU, TGA	Initial low reactivity, further decreased over cycling	Adánez-Rubio <i>et al.</i> ¹⁰³
15	Al ₂ O ₃	IM	4.6	850°C, 6 h	CLOU, TGA	Initial low reactivity, further decreased over cycling	Adánez-Rubio <i>et al.</i> ¹⁰³
33	Al ₂ O ₃	IM	3.0	850°C, 6 h	CLOU, TGA	Initial low reactivity, further decreased over cycling	Adánez-Rubio <i>et al.</i> ¹⁰³
42	Al ₂ O ₃	IM	0.9	950°C, 6 h	CLOU (5), TGA	Agglomeration at high temperatures	Song <i>et al.</i> ¹⁵³
80	Al ₂ O ₃	MM	2.6	1100°C, 6 h	CLOU, TGA	Low reactivity	Adánez-Rubio <i>et al.</i> ¹⁰³
82.5	Al ₂ O ₃	CP	3.0	950°C, 2 h	CLC (18), FBR	No agglomeration	Chuang <i>et al.</i> ⁹⁷
15	MgAl ₂ O ₄	IM	2.1	850°C, 1 h	-	-	Adánez-Rubio <i>et al.</i> ¹⁰³
21	MgAl ₂ O ₄	IM	0.8	850°C, 1 h	-	-	Adánez-Rubio <i>et al.</i> ¹⁰³
40	MgAl ₂ O ₄	SD	1.4	1100°C, 4 h	CLOU (3), FBR	No defluidisation	Jing <i>et al.</i> ¹⁵⁴
60	MgAl ₂ O ₄	MM-P	1.9	1100°C, 6 h	CLOU, FBR	No agglomeration, high attrition rates (20 h lifetime)	Adánez-Rubio <i>et al.</i> ¹⁰³
60	MgAl ₂ O ₄	MM-P	2.2	1100°C, 12 h	CLOU, FBR	No agglomeration, lower attrition rate (500 h lifetime predicted)	Adánez-Rubio <i>et al.</i> ¹⁰³
60	MgAl ₂ O ₄	SD	2.4	1100°C, 24 h	CLC (34), FBR	No agglomeration, maintain reactivity	Adánez-Rubio <i>et al.</i> ¹⁵⁵
60	MgAl ₂ O ₄	FG	<0.5	1050°C, 6 h	CLC (16), FBR	No agglomeration	Arjmand <i>et al.</i> ¹⁰⁷

Footnote: MM = mechanical mixing; MM-P = mechanical mixing following by pelletising by pressure; FG = freeze-granulation; IM = impregnation; SD = spray-drying

From **Table 2-5**, comparison of the performance of oxygen carriers prepared using different synthesis techniques is difficult due to differences in calcination temperatures and durations, CuO loadings and testing conditions. However, a few trends were observed from the literature review. The average crushing strength of the Al₂O₃-supported oxygen carriers was 2.7 N compared to 1.6 N for the MgAl₂O₄ oxygen carriers, which is consistent with the microhardness of the supporting materials. The average crushing strength for the MgAl₂O₄ oxygen carriers is below the 2 N threshold recommended by Rydén *et al.* for durability in fluidised systems.⁸⁹ Therefore, additional considerations are needed to increase the mechanical characteristics of these oxygen carriers. The performance of the Al₂O₃-supported materials in FBRs is generally characterised by severe agglomeration and sintering unless low CuO loadings are used. In comparison, the MgAl₂O₄-supported materials showed no defluidisation or agglomeration due to the effective stabilisation of CuO in the inert support.

Chuang *et al.* compared the performance of three CuO/Al₂O₃ oxygen carriers for CLC prepared using mechanical mixing, wet impregnation and co-precipitation synthesis methods.⁹⁷ The oxygen carriers prepared *via* co-precipitation performed significantly better than those prepared by mechanical mixing and impregnation. The poor performance of the mechanically mixed and impregnated oxygen carriers was attributed to the poor dispersion of active metal in the support, which resulted in severe sintering and agglomeration. From **Table 2-5**, the oxygen carriers prepared by impregnation are often limited to low loadings. The active metal is generally deposited on the surface of the support rather than the homogenous dispersion of the active metal in the support observed for co-precipitated materials. The synthesis *pH* was found to be a significant synthesis parameter for co-precipitation. The oxygen carriers derived from co-precipitation at a higher *pH* value of 9.7 were less porous with higher mechanical stability than those produced at *pH* 7.1, which were more porous and had lower strength and showed poor performance in the FBR. The results of this study highlight the importance of achieving a high degree of dispersion of CuO within an inert support for the long-term stability of the oxygen carrier.

2.1.3 Preparation of structured oxygen carriers

CuO-based oxygen carriers prepared using traditional synthesis techniques (*i.e.* those based on mechanical mixing and impregnation) often fail to provide the high degree of dispersion required to prevent sintering and agglomeration over extended redox cycling at high temperatures. To overcome these issues and use the favourable oxygen carrier properties of CuO, researchers have investigated producing structured oxygen carriers with a high degree of dispersion of active CuO within a stable support.

Song *et al.* prepared Cu-Al oxygen carriers from layered double hydroxides precursors synthesised *via* co-precipitation.¹⁵⁶ LDHs are a class of two-dimensional nanostructured anionic clays that consist of brucite-like layers formed of divalent and trivalent metal cations, with the general formula

$[M^{2+}_{1-x}M^{3+}_x(OH)_2]_x^+(A^{n-})_{x/n} \cdot yH_2O$, where M^{2+} and M^{3+} are di- and trivalent cations and A^{m-} is the balancing anion in the interlayer. The use of LDHs as a precursor enabled the homogeneous mixing of metals at the molecular level, giving a high degree of dispersion of the active material within the support after calcination. Na originating from co-precipitation leads to the formation of dawsonite, which tends to react with Al_2O_3 and form a variety of species (*i.e.* $Na_xAl_yO_z$) after calcination.¹⁵⁶ Therefore, MMOs of well-dispersed CuO nanoparticles in an amorphous Na–Al–O support were produced after calcination. The reactivity and stability of the oxygen carriers were determined over 100 CLOU cycles in an FBR. The presence of Na was effective in inhibiting the formation of $CuAl_2O_4$ due to the formation of $NaAl_2O_4$. Owing to the high dispersion of elements at the molecular level in the LDH precursor and Na-stabilisation, the active Cu phase in the calcined product remained highly dispersed and showed strong resistance to sintering.

Further testing of the LDH-derived Na-stabilised Cu–Al oxygen carrier was carried out for CLC of solid fuels (*i.e.* cycling between CuO and Cu_2O) and gaseous fuels (*i.e.* cycling between CuO and Cu).¹⁵⁷ The oxygen carriers demonstrated high thermal stability, which was attributed to the high degree of dispersion of the active Cu phases in the support. The Na-containing phases stabilised the Cu phases in the support and inhibited the formation of copper aluminates. However, it remains challenging to precisely control the content of Na-containing species, which originate from the co-precipitating agent during co-precipitation. Evaporation of Na at high temperatures would result in a loss of this stabilising agent, which might cause the material to fail over extended redox cycles. Other LDHs that have shown successful performance are oxygen carriers derived from Fe–Ni–Al LDHs for chemical looping gasification¹⁵⁸ and Ca–Fe–Mg LDHs for chemical looping reforming.¹⁵⁹ For both cases, the use of the structured precursor generated oxygen carriers with a fine dispersion of Fe_2O_3 . The high dispersion of active metal in a support reduced the prohibitive sintering commonly experienced by Fe_2O_3 -based oxygen carriers in chemical looping systems.^{117,118} The preparation of LDHs is covered in detail in the next section.

Core-shell structured oxygen carriers have also been developed for chemical looping processes. Typically used for catalysis,¹⁶⁰ core-shell designs are used to limit the sintering of metal oxides by encapsulating metal oxide cores within an inert or functional support material shell.¹⁶¹ The metal oxide core acts as a source of lattice oxygen and the shell is designed to prevent direct contact between the fuels and the core by facilitating lattice oxygen migration through the shell.¹⁶² The shell layer increases mass transfer resistances, but this can be partially overcome by doping and control of the particle dimensions, *e.g.* core size and shell thickness.¹⁶³ The core-shell design has been mainly applied to Fe_2O_3 -based oxygen carriers due to the serious sintering and rapid deactivation reported in the literature.^{117,118} Park *et al.* developed a $Fe_2O_3@SiO_2$ oxygen carrier for CLC using methane.¹⁶⁴ They observed that the encapsulation of a Fe_2O_3 core by the SiO_2 shell enhanced the sintering resistance of

the oxygen carrier at 700°C in an FBR. Ma *et al.* prepared a $\text{Fe}_2\text{O}_3@\text{CeO}_2$ oxygen carrier with a core-shell structure and a composite $\text{Fe}_2\text{O}_3/\text{CeO}_2$ oxygen carrier as a reference material.¹⁶⁵ They studied the performance of the oxygen carriers in a fixed bed reactor using steam as the oxidant to produce hydrogen at 850°C. The $\text{Fe}_2\text{O}_3@\text{CeO}_2$ showed much higher reactivity and hydrogen yields compared to the composite $\text{Fe}_2\text{O}_3/\text{CeO}_2$ oxygen carrier, which was observed to deactivate due to sintering over 15 cycles. A comparison of the Fe_2O_3 crystallite sizes found that the size of the $\text{Fe}_2\text{O}_3/\text{CeO}_2$ increased after 15 cycles. In contrast, the crystallite sizes of Fe_2O_3 and CeO_2 in the $\text{Fe}_2\text{O}_3@\text{CeO}_2$ oxygen carrier decreased, demonstrating the sintering resistance benefits of the core-shell design approach.

For CuO-based oxygen carriers, Xu *et al.* reported the synthesis of a core-shell $\text{Al}_2\text{O}_3@\text{TiO}_2\text{-CuO}$ oxygen carrier supported by Al_2O_3 and stabilised by TiO_2 for CLC and CLOU.¹⁶⁶ Unlike typical core-shell oxygen carriers reported in the literature, the active metal oxide CuO was in the shell with TiO_2 and the core was formed of Al_2O_3 . A modified sol-gel process was used to prepare the oxygen carrier precursor. Initially, an electrostatic self-assembly process was used to form a core of Al_2O_3 microparticles and a shell of TiO_2 nanoparticles (prepared by flame synthesis technology) by altering the *pH* of the solution. Cu nitrate and urea were added to the solution and stirred to form a sol-gel. The mixture was dried and calcined in air to produce a CuO-based crystalline layer deposited on a nanostructured shell of TiO_2 . The final chemical composition of the oxygen carrier was 78 wt% CuO, 17.5 wt% Al_2O_3 and 5 wt% TiO_2 . The oxygen carriers were cycled under CLOU conditions in a TGA and CLC conditions in an FBR. The oxygen carrier showed high reactivity and oxygen release and storage capacities over 10 to 15 redox cycles. The TiO_2 was found to be an effective barrier to prevent the formation of deleterious CuAl_2O_4 and CuAlO_2 and inhibited the sintering of CuO. However, characterisation of the oxygen carrier post-cycling was carried out on the samples cycled for 15 CLOU cycles in a TGA and not reported for oxygen carriers cycled for 10 CLC cycles in the FBR. The oxygen carriers maintained their mechanical strength over 15 cycles in the FBR. However, since CuO is a soft transition metal oxide, further testing is required to investigate the mechanical evolution of the particles using Al_2O_3 as the core material instead of the shell. It also needs to be determined if a small amount of TiO_2 sufficiently stabilises the CuO shell to prevent agglomeration over long-term redox cycling due to the low melting temperatures of Cu, Cu_2O and CuO. If CuO were used as the core material, then agglomeration may be prevented by effective encapsulation, but this would result in lower rates of oxygen release due to the higher mass transfer resistances for gaseous oxygen diffusion from the core through the shell to the bulk.

2.1.4 Cost

The cost of the oxygen carrier adds to the cost of CO_2 captured by the process. Lyngfelt and Leckner investigated the scale-up of CLC to the 1000 MW_{th} scale and introduced the parameter cost per tonne of CO_2 captured caused by the oxygen carrier, CCC_{OC} , given by equation (2-17).⁵⁷ The cost of safe

disposal of residues generated during synthesis was not considered, nor was recycling spent oxygen carriers to recover material.

$$CCC_{OC} = \frac{C_{OC} \text{ SI}}{SE \eta_{CO_2} t_{lifetime}} \quad (2-17)$$

where CCC_{OC} is in € / tonne CO_2 captured, C_{OC} is an estimated cost of oxygen carrier in € / tonne, SI is the solids inventory in tonne / MW_{th}, SE is the specific emission of the fuel in tonne CO_2 / MW_{th}, $t_{lifetime}$ is the average lifetime of the oxygen carrier, and η_{CO_2} is the CO_2 capture efficiency

The production of low-cost oxygen carriers is crucial for the scale-up of chemical looping applications. As shown by equation (2-17), the CCC_{OC} inversely depends on the particle lifetime. Therefore, any increase in cost due to the synthesis procedure must be compensated by an increase in particle lifetime. The cost of an oxygen carrier is the sum of several factors, including the cost of the metal oxide, the inert support, and synthesis method.⁵⁷ Production costs are lower if pure metal oxides are used; however, pure metal oxides generally have low reactivity and poor thermal and mechanical stabilities.¹⁰⁰ Abad *et al.* found the impact of oxygen carrier cost on process economics depends primarily on the lifetime of the particles.¹⁶⁷ Ideally, the oxygen carrier would be able to be redox cycled infinitely; however, a makeup flow of new particles is necessary to compensate for the loss of oxygen carrier by elutriation, attrition, and fouling during process operation.¹⁶⁸ Abad *et al.* found a particle lifetime of 300 h (based on impregnated Fe_2O_3/Al_2O_3 and NiO/Al_2O_3 oxygen carriers) was cost equivalent to the makeup of amine in a commercial MEA adsorption plant for CO_2 capture.¹⁶⁷ In addition, particles with a lifetime of 100 h were still found to fulfil the target range of \$ 20-30 per tonne of CO_2 avoided, the metric proposed for CO_2 capture processes.

The cost of producing the oxygen carrier increases with each additional synthesis step and modification of the oxygen carrier. For the structured materials, the LDHs are produced *via* simple co-precipitation, which is widely applied in research laboratories and industry at large scales to produce precursors for catalysts and catalyst supports.¹⁶⁹ Materials such as core-shell catalysts have a more complex synthesis route with more steps and reactants. The synthesis process for the core-shell CuO-based oxygen carrier supported by Al_2O_3 and stabilised by TiO_2 oxygen carrier reported by Xu *et al.* involves a multi-step sol-gel process.¹⁶⁶ The modified sol-gel process also has multiple temperature, *pH* and mixing requirements which may require additional efforts to yield a homogenous oxygen carrier precursor in a scaled-up synthesis process. The use of TiO_2 nanoparticles, produced *via* flame synthesis technology, used to stabilise the CuO phase would be more expensive than the intrinsic stabilisation of the CuO due to the LDH structure reported by Song *et al.*, prepared by mixing metal nitrate and alkaline (NaOH and Na_2CO_3) solutions at room temperature while maintaining a constant *pH*.¹⁵⁶

2.7 Layered double hydroxides

LDHs, also known as hydrotalcite-like compounds, are a class of two-dimensional nanostructured anionic clays composed of brucite-like layers formed of divalent and trivalent metal cations. The general formula is $[M^{2+}_{1-x}M^{3+}_x(OH)_2]_x^+(A^{n-})_{x/n} \cdot yH_2O$, where M^{2+} could be Mg, Cu, Ni, Co, etc., and M^{3+} could be Al, Fe, Mn etc. and A^{n-} is the charge balancing anion that exists in the interlayer with interlayer water molecules (**Figure 2-8**). The chemical composition of the LDH can be represented by the mole fraction of trivalent cations, x , or the molar ratio of divalent to trivalent cations, M^{2+}/M^{3+} . The value of x is generally limited to between 0.2 to 0.33 due to Pauling's rule of cation avoidance, which corresponds to an M^{2+}/M^{3+} ratio of 4 and 2, respectively.¹⁷⁰ Therefore, the most commonly studied LDH compositions are within this range.¹⁷¹ Values of x beyond these limits may result in the formation of metal hydroxide impurity phases. Calcination of the LDHs results in the formation of MMOs which have shown excellent catalytic properties for many processes due to the high dispersion of metals in the precursor structure.¹⁷² The most well-known naturally occurring LDH is the mineral hydrotalcite, $Mg_6Al_2(OH)_{16}CO_3 \cdot 4H_2O$, and others are shown in **Table 2-6**. The variety of transition metals that can be incorporated into the LDH structure make them tuneable for many applications beyond catalysis, such as CO_2 adsorbents¹⁷³ and as oxygen carrier precursors for high-temperature chemical looping processes.^{156,157}

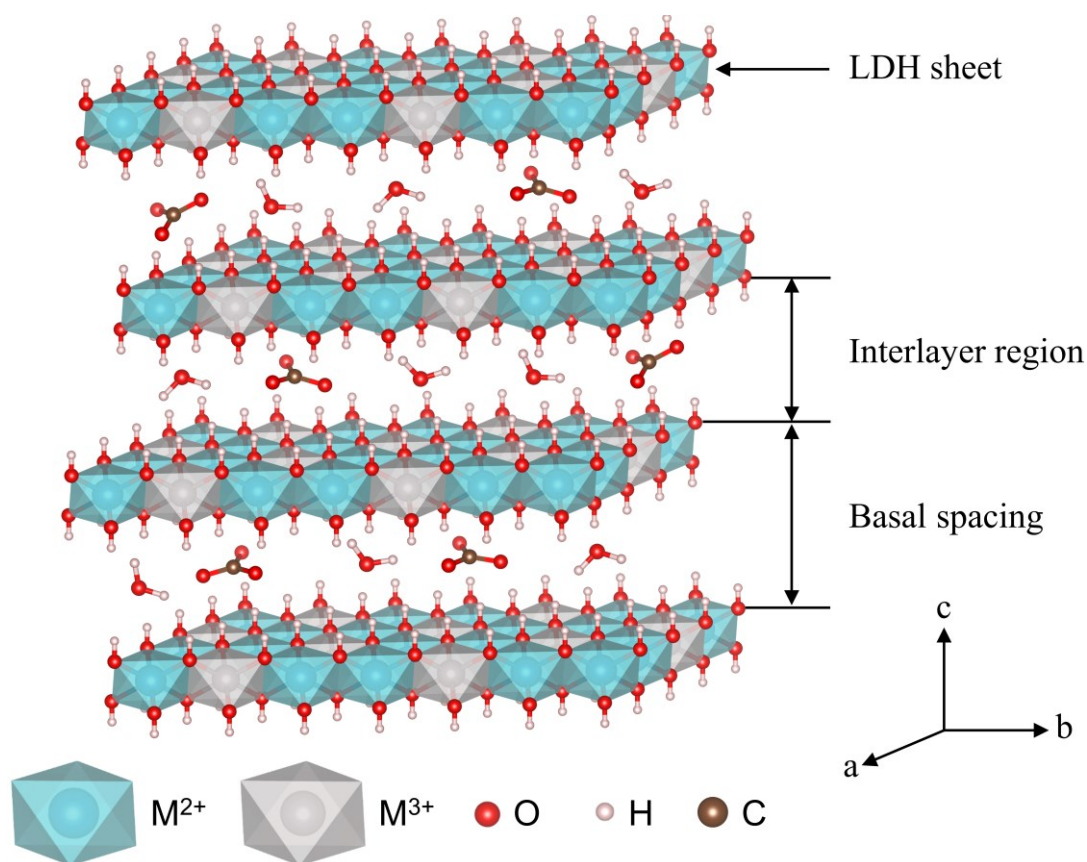


Figure 2-8: Idealised structure of Cu-Mg-Al LDHs produced using GSAS-II.¹⁷⁴

Table 2-6: Chemical formulae of naturally occurring hydrotalcites.¹⁷⁵

Name	Chemical Formula
Hydrotalcite	$\text{Mg}_6\text{Al}_2(\text{OH})_{16}\text{CO}_3 \cdot 4\text{H}_2\text{O}$
Manasseite	$\text{Mg}_6\text{Al}_2(\text{OH})_{16}\text{CO}_3 \cdot 4\text{H}_2\text{O}$
Pyroaurite	$\text{Mg}_6\text{Fe}_2(\text{OH})_{16}\text{CO}_3 \cdot 4.5\text{H}_2\text{O}$
Stichtite	$\text{Mg}_6\text{Cr}_2(\text{OH})_{16}\text{CO}_3 \cdot 4\text{H}_2\text{O}$
Takovite	$\text{Ni}_6\text{Al}_2(\text{OH})_{16}\text{CO}_3 \cdot 4\text{H}_2\text{O}$
Reevessite	$\text{Ni}_6\text{Fe}_2(\text{OH})_{16}\text{CO}_3 \cdot 4\text{H}_2\text{O}$
Desautelsite	$\text{Mg}_6\text{Mn}_2(\text{OH})_{16}\text{CO}_3 \cdot 4\text{H}_2\text{O}$

The LDH formation process is highly complex and not entirely understood.¹⁷⁶ Some factors thought to affect the stability of LDHs include the thermodynamic stabilities and *pH* of formation of the constituent metal hydroxides¹⁷⁷ and the synthesis method. The most widely used methods to prepare LDHs are co-precipitation¹⁷⁸ and urea hydrolysis.¹⁷⁹

2.7.1 Preparation via co-precipitation

Co-precipitation is a simple ‘one-pot’ method used to prepare LDHs by mixing a metal cation solution containing the chosen M^{2+} and M^{3+} cations with an alkaline solution that contains the desired interlayer anions. The metal cation solution is generally prepared by dissolving metal nitrate or chloride salts in water and the alkaline solution usually contains an ionic compound of the anion, *e.g.* Na_2CO_3 . Co-precipitation is carried out under supersaturation conditions by controlling the *pH* using a strong base, *e.g.* NaOH . If the *pH* value is too low, then complete precipitation of all metallic cations may not be possible depending on the solubilities of the metal hydroxides, while a *pH* value that is too high may result in the leaching of metallic ions into solution.^{180,181} Two co-precipitation methods are used depending on the method of addition of the strong base, the constant *pH* method at low supersaturation conditions and the variable *pH* method at high supersaturation conditions.

For the constant *pH* method at low supersaturation conditions, the metal cation solution is added to a reaction vessel containing the alkaline solution of the desired interlayer anion. A second alkaline solution containing the strong base is co-added to maintain a constant *pH*. An alternative scheme of this process is adding the metal cation solution to a reaction vessel containing water and co-adding an alkaline solution containing the desired interlayer anion and strong base, *e.g.* a solution of Na_2CO_3 and NaOH . The flow rate of the alkaline solution is adjusted to maintain a constant *pH*. LDHs synthesised using this method have been reported to have high crystallinity due to the low rate of nucleation at low supersaturation conditions resulting in a high crystal growth rate.¹⁸²

For the variable *pH* method carried out at high supersaturation conditions, a metal cation solution is added to a reaction vessel containing an alkaline solution containing the desired interlayer anion and strong base. The *pH* of the reaction vessel continuously changes throughout the addition of the metal ion solution. If the metal cation solution is added to the alkaline solution, the reaction vessel *pH* decreases over the synthesis time and is named the decreasing *pH* method. If the alkaline solution is added to an acid solution, the solution *pH* increases and is termed the increasing *pH* method. Under high supersaturation conditions, the rate of nucleation is high and a large number of primary LDH particles are formed with low crystallinity^{182,183} and the undesired M^{2+}/M^{3+} ratio¹⁷⁵ due to the formation of impurity hydroxide phases.¹⁸⁴

Yun *et al.* prepared Mg-Al LDHs with a molar Mg/Al ratio of 2, 3 and 4 *via* co-precipitation at low and high supersaturation conditions.¹⁸⁵ They reported LDHs with Mg/Al ratios close to their target ratios for both preparation methods. The LDHs prepared by the variable *pH* method were smaller, with higher surface areas and rougher surfaces than the LDHs prepared using the constant *pH* method. The pore size distribution of the LDHs also changed with the co-precipitation method. The variable *pH* materials reported narrower pore size distributions centred at a pore diameter of ~40 nm, determined using N₂ adsorption. In contrast, the materials produced using the constant *pH* method were larger with smoother surfaces and broader pore size distributions centred at higher pore diameters (ca. 100 nm).

Table 2-7 provides a summary of the synthesis conditions, observed Mg/Al ratio and XRD phases of Mg-Al LDHs reported in the literature prepared using the constant *pH* method. **Table 2-8** presents the effects of some of the main synthesis parameters that affect the final characteristics of the LDHs. The co-precipitation *pH* value was found to significantly impact the final Mg/Al ratio of the LDHs. Wang *et al.* investigated the LDH formation mechanism prepared using the constant *pH* method by increasing the co-precipitation *pH* value for each synthesis from 6.5 to 14 for Mg-Al LDHs with a target Mg/Al ratio of 3.¹⁸⁶ They observed an Mg/Al ratio of 0.6 at *pH* 7, which increased to 1.5 at *pH* 8 and 2.3 at *pH* 9 before stabilising around the target value of 3.1 at *pH* 10. Between *pH* 6.5 and 9, the authors observed the formation of an Al(OH)₃ phase with the Mg²⁺ remaining in the solution. Seron & Delorme investigated the formation mechanism of Mg-Al LDHs with a target Mg/Al ratio of 3 using the increasing *pH* method and measuring the Mg/Al ratio during co-precipitation.¹⁸⁷ Below a *pH* value of 8.5, they observed the formation of an Al species, likely Al(OH)₃.¹⁸³ At a *pH* value of 8.5 they observed the formation of an Mg-deficient LDH species, which incorporated more Mg until the target Mg/Al ratio was achieved at a *pH* of 10. The results of these studies show that the formation mechanism of the LDHs may depend on the co-precipitation method used. However, regardless of the co-precipitation method, a co-precipitation *pH* value close to 10 was necessary for the complete precipitation of Mg-Al LDHs, as shown in **Table 2-7**.

Table 2-7: Preparation conditions and material characteristics of Mg-Al LDHs synthesised *via* co-precipitation at constant *pH*.

Target Mg/Al molar ratio	Temperature	[Metal]	[Alkaline]	Aging time	pH	Observed Mg/Al molar ratio	XRD Phases	Reference
2	70	0.25	1 M NaOH*	24	10	2.7	LDH	Cheah <i>et al.</i> ¹⁸⁸
3	70	0.25	1 M NaOH*	24	10	3.0	LDH	Cheah <i>et al.</i> ¹⁸⁸
4	70	0.25	1 M NaOH*	24	10	4.0	LDH	Cheah <i>et al.</i> ¹⁸⁸
2	40	1	2 M NaOH 1 Na ₂ CO ₃ **	40	10	2.2	LDH	Yun <i>et al.</i> ¹⁸⁵
3	40	1	2 M NaOH 1 Na ₂ CO ₃ **	40	10	3.3	LDH	Yun <i>et al.</i> ¹⁸⁵
4	40	1	2 M NaOH 1 Na ₂ CO ₃ **	40	10	4.1	LDH	Yun <i>et al.</i> ¹⁸⁵
3	RT	1	3.4 M NaOH*	24	6.5	0.5	Poorly crystalline LDH	Wang <i>et al.</i> ¹⁸⁶
3	RT	1	3.4 M NaOH*	24	7	0.6	Poorly crystalline LDH	Wang <i>et al.</i> ¹⁸⁶
3	RT	1	3.4 M NaOH*	24	8	1.5	Poorly crystalline LDH	Wang <i>et al.</i> ¹⁸⁶
3	RT	1	3.4 M NaOH*	24	9	2.3	LDH	Wang <i>et al.</i> ¹⁸⁶
3	RT	1	3.4 M NaOH*	24	10	3.1	LDH	Wang <i>et al.</i> ¹⁸⁶
3	RT	1	3.4 M NaOH*	24	11	3.1	LDH	Wang <i>et al.</i> ¹⁸⁶
3	RT	1	3.4 M NaOH*	24	12	3.2	LDH	Wang <i>et al.</i> ¹⁸⁶
3	RT	1	3.4 M NaOH*	24	13	3.2	LDH	Wang <i>et al.</i> ¹⁸⁶
3	RT	1	3.4 M NaOH*	24	14	3.2	LDH	Wang <i>et al.</i> ¹⁸⁶

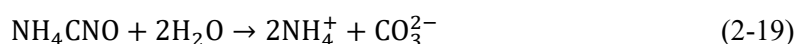
Footnote: RT = room temperature; metal and alkaline solutions * added to a reaction vessel containing Na₂CO₃ solution; ** added to water

Table 2-8: Main synthesis parameters for LDH prepared *via* co-precipitation

Parameter	Influence
Co-precipitation pH	Degree of supersaturation, formation of pure LDH phase, crystallite size and crystallinity
Temperature	Crystallinity, impurity phases
Aging time	Crystallite size and crystallinity
Ratio of metal cations	Formation of pure LDH phase
Solution concentration	Degree of supersaturation, crystallite size and size distribution

2.7.2 Preparation via urea hydrolysis

LDHs can also be prepared *via* urea hydrolysis. This technique is similar to co-precipitation but is generally considered to be a different preparation method. Urea is a very weak Brønsted base ($pK_b = 13.8$) which gradually hydrolyses in water at high temperatures. The hydrolysis reactions occur through equations (2-18) to (2-21), where urea decomposes to form ammonium cyanate, which reacts to produce ammonium carbonate. The process starts at a low pH , and the presence of ammonia and carbonate ions gradually releases hydroxide ions to raise the pH value to around 7 to 9. Due to the slow release of hydroxide ions, the precipitation is very finely controlled, resulting in very large and highly crystalline LDHs.^{179,183,189} The hydrolysis rate is highly temperature sensitive and increases significantly by around 200 times with a temperature increase from 60 to 100°C. Therefore, the release of hydroxide ions and control of the pH can be achieved by adjusting the temperature.



A summary of the synthesis conditions, observed Mg/Al ratios and XRD phases of Mg-Al LDHs reported in the literature prepared *via* urea hydrolysis is presented in **Table 2-9**. As for the increasing pH co-precipitation method, LDHs synthesised *via* urea hydrolysis have been reported to have lower Mg/Al ratios than their target ratios, indicating incomplete co-precipitation of Mg^{2+} . Cheah *et al.* prepared Mg-Al LDHs with target Mg/Al ratios of 2, 3 and 4 using the urea hydrolysis and constant pH co-precipitation methods.¹⁸⁸ The LDHs synthesised at a constant pH of 10 successfully formed LDHs with Mg/Al ratios close to their target values of 2, 3 and 4. In contrast, LDHs produced *via* urea hydrolysis had Mg/Al ratios of 0.9, 0.8 and 1.7 for target Mg/Al ratios of 2, 3 and 4, respectively. Adachi-Pagano *et al.* prepared LDHs *via* urea hydrolysis and observed the formation of $\text{Al}(\text{OH})_3$ during the early stages of the reaction at low pH values. As the reaction progressed, the pH of the solution gradually increased and Mg^{2+} was slowly incorporated into the solid hydroxide. The final Mg/Al ratio was reported to be much lower than the target ratio of 3. As previously discussed, the formation of Al-rich (or Mg-deficient) LDHs was also observed for Mg-Al LDHs synthesised *via* the increasing pH co-precipitation method.^{186,187} Therefore, the pH during the early stages of urea hydrolysis is too low for the Mg^{2+} to be co-precipitated with Al^{3+} . Many authors also report that a final pH value of 9 is achieved using urea hydrolysis. However, from **Table 2-9**, the final pH after urea hydrolysis is between 7 and 8,

which is likely too low for the complete incorporation of Mg into the initially formed $\text{Al}(\text{OH})_3$, resulting in LDHs with Mg/Al ratios below their target values.

The solution temperature during urea hydrolysis is an important synthesis parameter as it controls the rate of hydrolysis to ammonia and carbonate and, therefore, the release of hydroxide ions into solution.¹⁷⁹ A final *pH* value of 9 is targeted in the literature to precipitate a large range of metal hydroxides. The solution *pH* also depends on the urea concentration to metal ion concentration ratio ($[\text{urea}]/[\text{metal ion}]$). To investigate this parameter, Zeng *et al.* prepared Mg-Al LDHs with an Mg/Al molar ratio of 4 and varied the $[\text{urea}]/[\text{NO}_3]$ ratios from 1 to 6.¹⁹⁰ Although the authors did not report the Mg/Al ratio of the final materials, it could be inferred by the yields. The yields were reported to increase from approximately 15, 40, 70 to 90% for $[\text{urea}]/[\text{NO}_3]$ ratio equal to 1, 2, 3 and 4, respectively. Further increase of the $[\text{urea}]/[\text{NO}_3]$ ratio did not significantly improve the yield. The increased yield for the higher ratios of $[\text{urea}]/[\text{NO}_3]$ was attributed to a greater increase of the solution *pH* due to the larger amount of hydroxide ions released into the solution.

From **Table 2-9**, an increase in synthesis time was also found to result in Mg-Al LDHs with Mg/Al ratios closer to their target values. Berber *et al.* found that the Mg/Al ratio of the materials increased with synthesis time from 3 to 12 h.¹⁹¹ The urea hydrolysis reaction is relatively slow; therefore, the longer synthesis time allowed the solution *pH* to reach a value sufficient for the precipitation of the Mg^{2+} . In general, the synthesis time for urea hydrolysis must be chosen to ensure sufficient amounts of hydroxide ions are released into the solution to raise the *pH* value.

The effect of metal ion concentration was investigated by Oh *et al.*, where Mg-Al LDHs were prepared using extremely long reaction times of 672 h using metal ion concentrations between 0.065 and 0.87 M while keeping all other synthesis parameters constant.¹⁸⁹ The LDH particle size was found to increase with decreasing metal ion concentration, from 1170 nm at 0.87 M to 4470 nm at 0.065 M. The effect of the metal ion concentration on the particle size was explained using the classical crystal growth mechanism, where the supersaturation ratio is proportional to the metal ion concentration. Therefore, higher concentrations resulted in a larger number of primary nuclei and lower crystal growth during the precipitation process.

Table 2-9: Preparation conditions and material characteristics of Mg-Al LDHs synthesised *via* urea hydrolysis.

Mg/Al ratio	Temperature (°C)	[Metal] (M)	[Urea] / [Metal]	Synthesis time (h)	Observed Mg/Al ratio	XRD Phases	Final pH	Reference
2	90	0.25	3.3	48*	0.9	LDH	7-8	Cheah <i>et al.</i> ¹⁸⁸
3	90	0.25	3.3	48*	0.8	LDH	8	Cheah <i>et al.</i> ¹⁸⁸
4	90	0.25	3.3	48*	1.7	LDH	8	Cheah <i>et al.</i> ¹⁸⁸
3	100	0.1	3.3	36	2.8	LDH (l)	-	Costantino <i>et al.</i> ¹⁷⁹
5	100	0.5	4	36	3.1	LDH (fg)	-	Costantino <i>et al.</i> ¹⁷⁹
4	100	0.5	2	36	2.4	LDH (g)	-	Costantino <i>et al.</i> ¹⁷⁹
4	100	0.5	3.3	36	3.1	LDH (vg)	-	Costantino <i>et al.</i> ¹⁷⁹
4	100	0.5	4	36	2.9	LDH (m)	-	Costantino <i>et al.</i> ¹⁷⁹
3	100	0.5	2	36	2.6	LDH (g)	-	Costantino <i>et al.</i> ¹⁷⁹
3	100	0.5	3.3	36	2.9	LDH (vg)	-	Costantino <i>et al.</i> ¹⁷⁹
3	100	0.5	4	36	2.9	LDH (vg)	-	Costantino <i>et al.</i> ¹⁷⁹
3	100	0.5	6	36	2.8	LDH (m)	-	Costantino <i>et al.</i> ¹⁷⁹
2.5	100	0.5	4	36	2.5	LDH (vg)	-	Costantino <i>et al.</i> ¹⁷⁹
3	100	1	3.3	36	2.8	N/A	-	Costantino <i>et al.</i> ¹⁷⁹
2	120	1	0.5	24	0.6	No LDH	5.4	Berber <i>et al.</i> ¹⁹¹
2	120	1	1	24	0.9	No LDH	6.0	Berber <i>et al.</i> ¹⁹¹
2	120	1	1.5	24	1.5	LDH	7.1	Berber <i>et al.</i> ¹⁹¹
2	120	1	2	3	1.0	No LDH	6.6	Berber <i>et al.</i> ¹⁹¹
2	120	1	2	6	1.7	LDH	7.3	Berber <i>et al.</i> ¹⁹¹
2	120	1	2	12	2.0	LDH	7.5	Berber <i>et al.</i> ¹⁹¹
2	120	1	3	12	2.0	LDH	7.9	Berber <i>et al.</i> ¹⁹¹
2	120	1	3.5	12	2.0	LDH	8.2	Berber <i>et al.</i> ¹⁹¹
2	120	1	2	18	2.0	LDH	7.8	Berber <i>et al.</i> ¹⁹¹
2	120	1	3	18	2.0	LDH	8.2	Berber <i>et al.</i> ¹⁹¹
2	120	1	3.5	18	1.9	LDH	8.3	Berber <i>et al.</i> ¹⁹¹

Footnote: g = good; m = medium; l = low; f = fairly; v = very

2.7.3 Hydrothermal treatment

A post-synthesis hydrothermal treatment step is often used to improve the characteristics of the LDHs.^{192,193} Hydrothermal treatment is generally performed in an autoclave with water at elevated temperatures and pressures. Hickey *et al.* reported that hydrothermal treatment of LDHs produced *via* co-precipitation at constant *pH* 10 resulted in LDHs with larger particle sizes.¹⁹² They also found that treatment in water rather than in the mother liquor resulted in a material with greater crystallinity. These effects may be explained by the Ostwald ripening phenomenon, in which smaller LDH particles dissolve back into solution and deposit on larger particles. Labajos and Rives reported that hydrothermal treatment of unwashed LDHs increased the Mg/Al ratio in the LDHs.¹⁹⁴

2.8 Concluding remarks

CLC technology has successfully been applied to gaseous fuels, such as natural gas. The use of CLC for solid fuels, such as biomass and coal, is more complicated due to the additional gasification step required to overcome the slow reactions between the solid oxygen carrier and fuel char. CLOU is a variant of CLC that has been proposed to overcome the char gasification step by using oxygen carriers that can release gaseous oxygen in the fuel reactor. The gaseous oxygen can react with the char directly, increasing the fuel conversion rate. Therefore, the key advantages of CLOU over iG-CLC are the large reduction of oxygen carrier and fuel residence times, lower oxygen carrier inventories, combustion efficiencies close to 100% and higher CO₂ capture efficiencies.

Oxygen carriers for CLOU must have suitable equilibrium oxygen partial pressures at relevant combustion temperatures (800 to 1200°C) to release gaseous oxygen in the fuel reactor. This additional thermodynamic requirement limits the selection of metal oxides for CLOU. Oxygen carriers capable of releasing gaseous oxygen are typically single or mixed metal oxides based on Cu, Mn and Co.

Of the potential oxygen carrier candidates, CuO-based oxygen carriers have received a great deal of attention due to their high reactivity, high oxygen storage capacity and absence of thermodynamic limitation for the complete combustion of fuels. In addition, CuO/Cu₂O has a high oxygen capacity for the release of gaseous oxygen (0.101 g_{O2}/g_{OC}). Despite these attractive features, CuO-based oxygen carriers are prone to sintering and tend toward agglomeration due to the low CuO, Cu₂O and Cu Tammann temperatures of 526, 481 and 405°C, respectively. In practice, sintering of pure CuO oxygen carriers can occur at temperatures as low as 800°C. Therefore, CuO requires stabilisation on a support material.

Many CuO-based oxygen carriers have been synthesised in the literature using Al₂O₃ as a support due to its abundance and low cost. However, CuO and Al₂O₃ can form the spinel CuAl₂O₄ during high-

temperature calcination and redox cycling. This spinel is relatively stable to decomposition during CLOU and, therefore, reduces the oxygen release capacity of the oxygen carrier.

In order to stabilise CuO, a high degree of dispersion within the support is required. The preparation of oxygen carriers using conventional methods is limited to low loadings of active metal oxides due to its poor dispersion in the support. Oxygen carriers with poor dispersions of CuO perform poorly during operation due to sintering and agglomeration over long-term redox cycling. Chaung *et al.* showed that oxygen carriers prepared *via* co-precipitation achieved better dispersion of active material and support.⁹⁷ Co-precipitation is a widely applied technique for synthesising catalysts and catalyst supports at an industrial scale.

To use CuO as a high-performance oxygen carrier, researchers have investigated using structured materials to target a high degree of dispersion of active CuO within a stable support. Song *et al.* synthesised Cu-Al oxygen carriers from LDH precursor materials synthesised *via* co-precipitation.¹⁵⁶ The use of LDHs as a precursor enabled homogeneous mixing at the molecular level, giving the active material a high degree of dispersion within the support after calcination. The reactivity and stability of the oxygen carriers were maintained over 100 cycles in FBR experiments. It was found the presence of Na was effective in inhibiting the formation of CuAl_2O_4 due to the formation of NaAl_2O_4 . However, it remains challenging to precisely control the content of Na species which originate from the precipitation agent used for co-precipitation. Evaporation of the Na at high temperatures will result in a loss of this stabilising agent, which could lead to the formation of copper aluminate phases and the deterioration of the materials over extended redox cycles. Therefore, it is desirable to tune the synthetic chemistry of the LDH precursors to minimise the formation of Na-containing impurities to achieve a more stable long-term cycling performance.

The most commonly used methods for synthesising LDHs are co-precipitation and urea hydrolysis. A review of the literature was carried out to identify the main synthesis parameters affecting the final material characteristics of the Mg-Al LDHs. The review found that LDHs produced using the constant *pH* co-precipitation method had Mg/Al ratios much closer to their target values than those prepared *via* the varying *pH* co-precipitation method and the urea hydrolysis method. The *pH* was determined to be a crucial synthesis parameter for achieving the desired Mg/Al ratio.

The addition of Mg to the Cu-Al system has been shown to stabilise the oxygen release capacity by inhibiting the formation of CuAl_2O_4 through the preferential formation of a MgAl_2O_4 support phase. Therefore, this thesis investigates the preparation of $\text{CuO}/\text{Al}_2\text{O}_3$ and $\text{CuO}/\text{MgAl}_2\text{O}_4$ oxygen carriers derived from the calcination of Cu-Al and Cu-Mg-Al LDHs, respectively, prepared *via* co-precipitation at constant *pH*.

Chapter 3

Experimental methods for material synthesis, characterisation and testing

3.1 Introduction

In this chapter, the experimental procedures and apparatus used throughout this thesis are presented. The methods are separated into those for preparing the LDHs and MMOs, material characterisation, and testing of the oxygen carriers in chemical looping processes using bench-scale equipment. The general operating conditions are provided in this chapter, with the specific conditions for each investigation provided in the relevant chapters.

3.2 Material synthesis

3.2.1 Co-precipitation of layered double hydroxide precursors

The LDHs were prepared via co-precipitation at room temperature and atmospheric pressure using an automated co-precipitation rig (**Figure 3-1**). A 2 M metal nitrate solution was prepared by dissolving $\text{Cu}(\text{NO}_3)_2 \cdot 2.5\text{H}_2\text{O}$, $\text{Mg}(\text{NO}_3)_2 \cdot 6\text{H}_2\text{O}$, and $\text{Al}(\text{NO}_3)_3 \cdot 9\text{H}_2\text{O}$ in the desired molar ratio in de-ionised (DI) water. A 1 M NaOH and 1 M Na_2CO_3 alkaline solution was also prepared by dissolving appropriate amounts of NaOH and Na_2CO_3 in DI water. The chemical reagents used for co-precipitation are shown in **Table 3-1**. For each experiment, the reaction vessel was primed with a small amount of DI water (~10 ml). A control programme written in Agilent VEE was used to maintain a constant *pH* during co-precipitation, measured using a *pH* probe. Unless otherwise stated, the flow rate of the acidic solution was set at 10 ml min^{-1} . The flow rate of the alkaline solution was controlled by the Agilent VEE programme to maintain a constant *pH*. A three-point calibration was used to calibrate the *pH* probe (**Table 3-1**). The reaction vessel was stirred at 350 rpm by a magnetic stirrer.

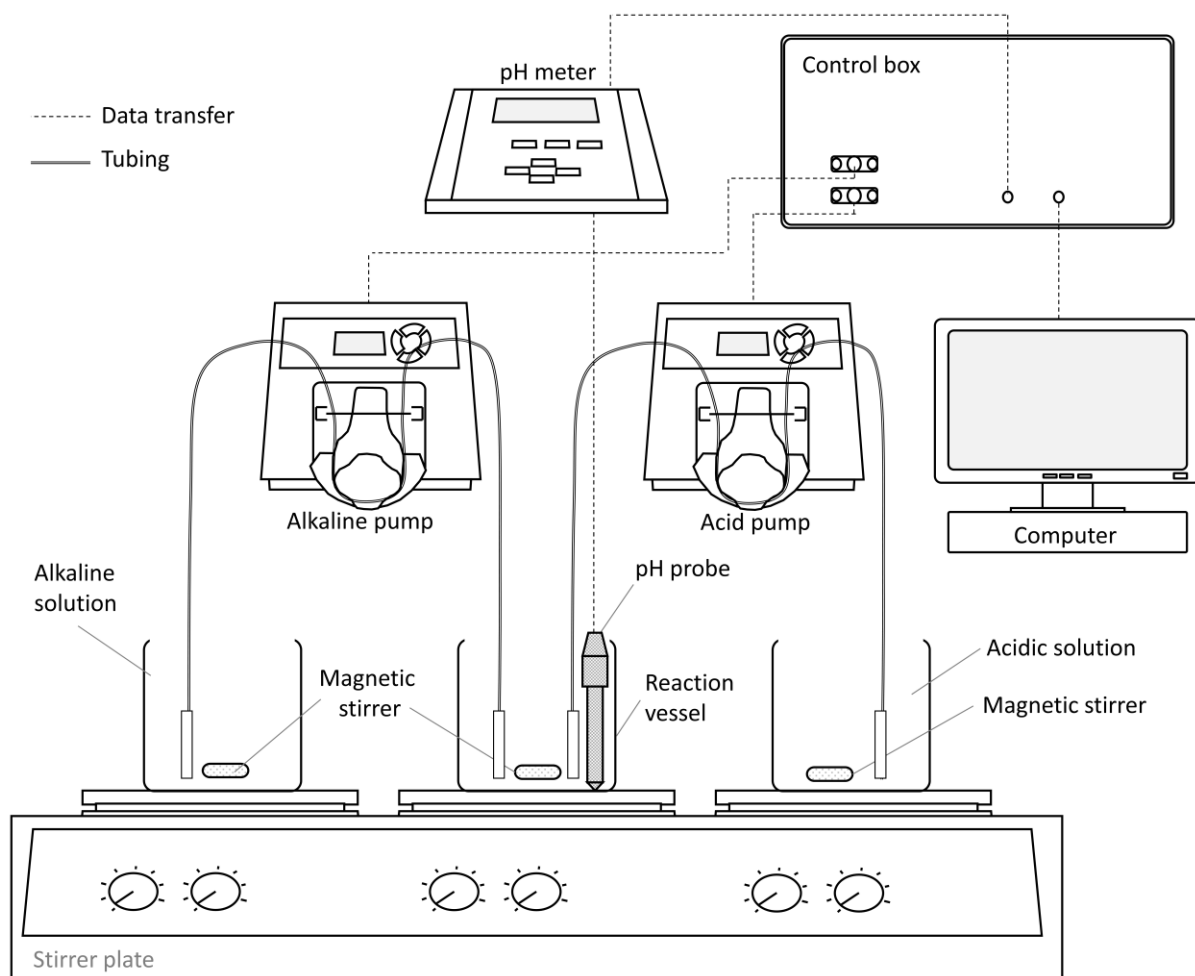


Figure 3-1: Schematic of the automated co-precipitation rig. The pH of the reaction vessel was maintained by controlling the rate of alkaline solution addition, adapted from Patzschke.¹¹⁵

Table 3-1: Reagents used for synthesis of the co-precipitated LDH precursors.

Reagent	Purity (mol%)	Supplier
$\text{Cu}(\text{NO}_3)_2 \cdot 2.5\text{H}_2\text{O}$	98	Alfa Aesar
$\text{Mg}(\text{NO}_3)_2 \cdot 6\text{H}_2\text{O}$	98	Alfa Aesar
$\text{Al}(\text{NO}_3)_3 \cdot 9\text{H}_2\text{O}$	98	Alfa Aesar
NaOH	>97	VWR
Na_2CO_3	>99.6	ARCOS Organics
Buffer solution pH 4.0	-	Fluka
Buffer solution pH 7.0	-	Fluka
Buffer solution pH 11.0	-	Fluka

The materials were co-precipitated until complete depletion of the acid solution (or for a specified period of time in some cases). An example of the *pH* profile during co-precipitation using the automated rig is shown in **Figure 3-2**. After co-precipitation, the precipitate was aged for 30 min with no additional stirring. The precipitate was then washed with DI water to remove residual Na until the ionic conductivity of the wash water measured below 150 μ S. The washed precipitate was recovered by vacuum filtration and dried overnight at 50°C in a well-ventilated oven.

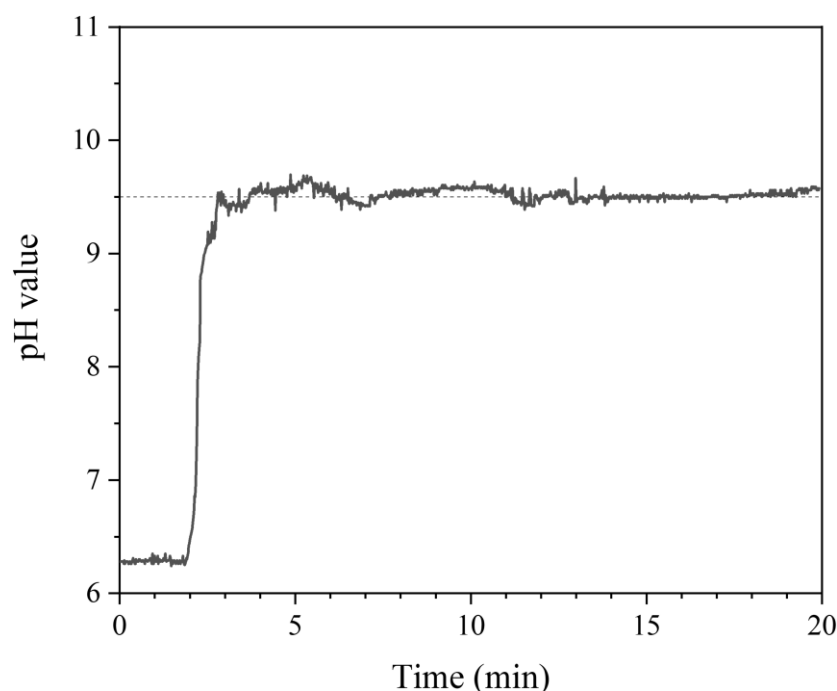


Figure 3-2: Example *pH* profile during LDH synthesis using the automated co-precipitation rig. Target constant *pH* value of 9 during co-precipitation.

From chapter 2, the literature review of LDH syntheses highlighted the co-precipitation *pH*, solution concentrations and aging time as critical synthesis parameters. This thesis builds upon previous work carried out by Song *et al.* to develop Cu-Al LDHs and MMOs for chemical looping processes.¹⁵⁶ Therefore, the synthesis conditions used in Song *et al.* were adopted as the initial conditions in this work, specifically, 2 M concentrations of metal nitrate and alkaline solutions, a co-precipitation *pH* of 9.5 and aging the precipitate for 3 h. The co-precipitation conditions were then partially optimised by varying each synthesis parameter and characterising the LDHs using the material characterisation techniques outlined in this chapter. The results presented in Appendix A1 show that the solution concentration (0.5, 1 and 2 M) did not significantly impact the structure of the precipitated materials. Therefore, a 2 M concentration was used for each solution to increase the amount of material synthesised per unit volume. The aging period after co-precipitation (30 min, 3 h and 6 h) also did not have a considerable impact on the characteristics of the precipitates. Therefore, an aging time of 30 min or 3 h was used. The co-precipitation *pH* (9.5, 10.5 and 11.5) was found to have a significant effect on

the XRD patterns and pore size distributions of the LDHs. Therefore, the effect of co-precipitation *pH* was investigated throughout this thesis, and a *pH* value of 9.5 was used for the initial co-precipitation experiments.

3.2.2 Preparation of mixed metal oxides

The MMOs were prepared by calcining the dried LDH precipitate in a horizontal tube furnace for 6 h at 975°C using a heating rate of 15°C min⁻¹ and an air flow rate of 2 L min⁻¹ (SATP). The MMOs were crushed and sieved to produce particles in the 300-425 µm size range for characterisation and testing as oxygen carriers for chemical looping processes in bench-scale reactors.

3.3 Material characterisation

3.3.1 Powder X-ray diffraction

Ex-situ powder X-ray diffraction (XRD) analysis was performed using an X'Pert PRO (PANalytical) under Bragg-Brentano orientation operating at 40 kV with a tube current of 20 mA, producing Cu-Kα radiation with a characteristic wavelength of 0.1541 nm. A diffractogram (the XRD pattern) is generated by plotting the intensities of the diffracted X-rays (measured in counts) against the Bragg angle, 2θ . The diffractogram contains several peaks (reflections) that are characterised by their position, intensity and profile. **Table 3-2** outlines the general information that can be obtained from each peak. By applying Bragg's law (equation (3-1)), the spacing between planes of atoms in the crystal lattice can be related to the position of the peaks and the wavelength of the incident X-ray.

$$2d\sin(\theta) = n\lambda \quad (3-1)$$

where d is the interplanar spacing, n is the diffraction order, θ is the angle between the incident X-ray and the diffracting plane, and λ is the wavelength.

Table 3-2: Insights from powder diffractogram peak features.¹⁹⁵

Peak feature	Cause	Insight
Position	Periodic arrangement of atoms	Qualitative phase analysis
	Wavelength of X-rays	Lattice parameters
	Instrument contributions	
Intensity	Crystal structure	Quantitative phase analysis
	Wavelength of X-rays	Crystal structure
	Sample preparation	Preferred orientation
	Instrument contributions	
Profile (shape)	Lattice distortions	Micro-strain
	Instrument contributions	Crystallite size

In a typical experiment, the sample was ground into a fine powder by manual grinding with a pestle and mortar and sieved to below 50 μm . The powdered sample was loaded onto a graphite disk slide mount sample holder and pressed with a glass slide to produce a matte finish. A typical program scanned in the 2θ -range from 5 to 85° using a step size of 0.0334° and a time per step of 85.1 s (scan speed = 0.05° per s). X'pert HighScore Plus software was used to identify the phases present in the diffraction pattern. The software compares the measured pattern with spectra from the International Centre for Diffraction Database (ICDD).

The crystallite size was estimated using Scherrer's equation (equation (3-2))¹⁹⁶ and the peak broadening used in the calculation was taken as the difference of the observed peak broadening and the instrument broadening. The instrument broadening was determined experimentally to be $2\theta = 0.144^\circ$ using the (111) peak of an Si standard.

$$L = \frac{K \lambda}{(B_{obs} - B_I) \cos(\beta)} \quad (3-2)$$

where K is the crystallite-shape factor (for LDH crystallites, $K = 0.886$ ¹⁹⁷), λ is the wavelength of the incoming Cu-K α radiation, β is the peak position, B_{obs} is the observed peak broadening of the sample equal to full width at half maximum (FWHM), and B_I is the peak broadening of the instrument calibration standard.

In-situ high-temperature XRD was performed using an Empyrean (PANalytical) under Bragg-Brentano orientation with Cu-K α radiation and within a hermitically sealed Anton-Paar HTK 1200N furnace

chamber (**Figure 3-1**). The gas flow rate (N_2 or air) was controlled at 50 ml min^{-1} using two digital mass flow controllers (Bronkhorst) and gas switching between air and N_2 controlled by the FlowView program (Bronkhorst). The phase changes during redox reactions at 900°C were investigated by switching gas flows between air and N_2 and repeatedly scanning the 2θ range 34 to 40° at a step size of 0.013° . Each scan had a duration of approximately 90 s once the goniometer had repositioned to the start angle.

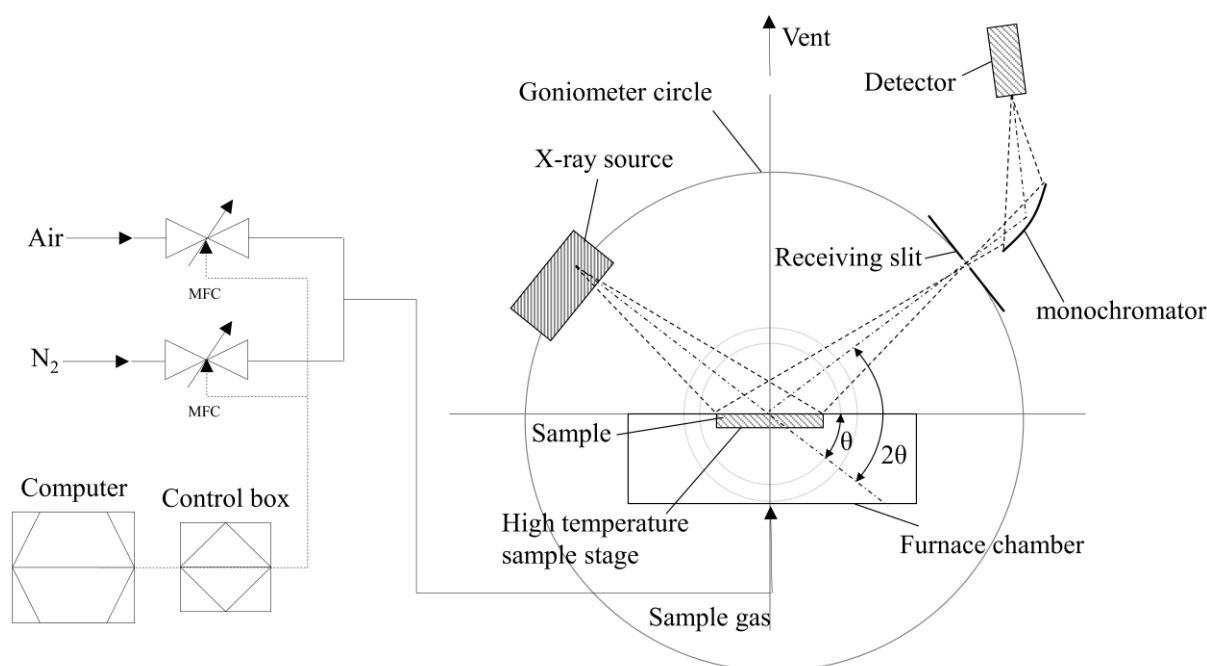


Figure 3-3: Simplified schematic of the in-situ XRD diffractometer used for high temperature XRD analysis. Adapted from Patzschke.¹¹⁵

3.3.2 X-ray fluorescence spectroscopy

X-ray fluorescence spectroscopy (XRF) was carried out using an Epsilon 3XLE X-ray Spectrometer (PANalytical). The Epsilon software was used for semi-quantitative analysis. XRF is an analytical technique used to identify and quantify the elements in a sample. The technique works on the principle of the excitation of individual atoms by high-energy X-rays which causes the atoms to emit secondary X-rays of a characteristic energy or wavelength. When an X-ray hits an atom in the sample, one of its inner-shell electrons may be ejected, resulting in a vacancy in the inner shell. An electron from the outer shell then moves to fill the inner shell vacancy and releases an X-ray of characteristic energy unique to the atom. The elements present in the sample can be identified and quantified by measuring the energies and intensities of the X-rays emitted by the sample.

In a typical experiment, 1-2 g of powdered sample (<50 μm) was tightly packed into a sample container sealed with a thin prolene film. XRF was conducted on each sample three times for analysis. The results of XRF analysis were converted from mass fractions of the elements to mass fractions of the oxides using the relative molecular weights of the compounds.

One limitation of using XRF for Cu-Mg-Al LDHs is that Mg and Al have relatively low atomic numbers. As a result, the X-ray emissions of Mg and Al are less intense than heavier elements. The equipment uses a He gas purge to improve the measured intensities of these low atomic number elements. However, the detection of these metals is still at the lower resolution limit of the equipment, and their low signal can lead to challenges in quantifying the amount of these metals in samples. To overcome this limitation, Mg and Al were calibrated using eight mechanically mixed samples of known oxide compositions. The mass fractions measured using XRF were plotted against the expected mass fractions to determine the calibration functions shown in **Figure 3-4**. For each metal, the R^2 for each calibration function is close to 1.

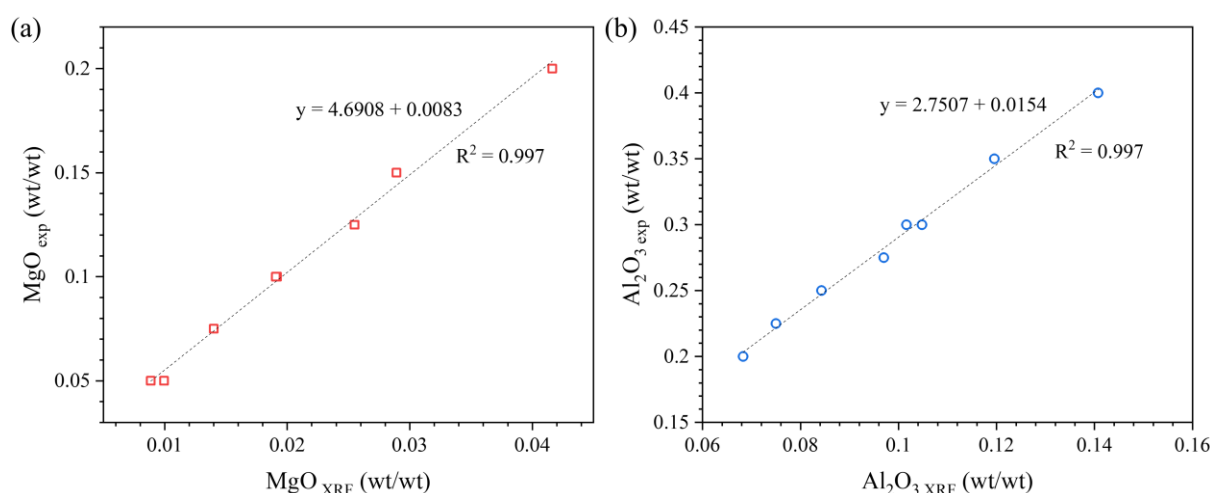


Figure 3-4: The results of the XRF calibration. Mass fractions measured by XRF against the actual mass fractions of the samples prepared via mechanical mixing for the determination of the (a) MgO and (b) Al₂O₃ calibration function.

3.3.3 Nitrogen adsorption

N₂ adsorption was performed using a TriStar 3000 (Micromeritics) gas adsorption analyser. N₂ adsorption analysis is used for the characterisation of porous material, e.g. measurement of the surface area, pore size distribution, pore structure and pore volume. The technique works on the principle of the physical adsorption of N₂ gas onto the surface of a material at cryogenic temperatures (~77 K). The amount of gas adsorbed onto the surface is measured as a function of increasing and decreasing pressure.

The adsorption/desorption volumes are then plotted at each pressure to generate an adsorption-desorption isotherm.

In a typical experiment, 200-300 mg of samples were degassed at 120°C under vacuum in a sample tube for at least 12 h to remove any moisture or volatile impurities on the surface of the materials. The sample tube was loaded into the instrument and cooled to 77 K. N₂ was then introduced into the sample chamber. The pressure was increased to the saturation pressure of N₂, then decreased to generate the adsorption and desorption isotherms. The Barrett–Joyner–Halenda (BJH) theory was used to determine pore size distributions and the pore volume of micropores, mesopores and small macropores below 200 nm in diameter. The BJH theory is based on a modified Kelvin equation using a correction for the multilayer thickness of N₂ to evaluate pore width from the filling pressure. It is known that the BJH method can significantly underestimate the pore volume of pores with diameters below 10 nm by 20 to 30%.¹⁹⁸ However, preliminary analysis suggests few pores exist with this diameter in the LDH and MMO materials.

3.3.4 Helium pycnometry

Helium pycnometry was carried out using an AccuPyc II 1340 (Micromeritics). This technique is non-destructive and measures the volume of gas displaced by He under high pressure to calculate the skeletal density, ρ_{sk} , of a sample.

To perform the measurements, a 1 cm³ sample holder was filled with an appropriate amount of sample. The sample holder was loaded into the instrument, which was then evacuated. After evacuation, helium gas was introduced into the chamber to rapidly fill pores as small as 1 Å in diameter and then expanded into a second chamber of known volume. By measuring the pressure difference before and after expansion, the ρ_{sk} was calculated using the mass of the sample. The ρ_{sk} values are the average of ten measurements.

3.3.5 MIP

Mercury intrusion porosimetry (MIP) was carried out using an AutoPore IV 9500 (Micromeritics) to measure the pore size distribution and pore volume of a sample. Mercury has exceptionally high interfacial tension and therefore behaves as a non-wetting fluid and will not spontaneously penetrate pores by capillary action – it must be forced into the pores by the application of external pressure. The required pressure is inversely proportional to the pore diameter. By measuring the volume of mercury that intrudes into the sample with each pressure change, the volume of pores at different stages of intrusion (and pore diameters) is known.

In a typical experiment, a penetrometer was filled with 200-300 mg of particles in the size range 300-425 µm and loaded into the instrument. After calibration of the pressure transducers, the stem of the

penetrometer was evacuated, and Hg was introduced at low pressures. As the pressure was slowly increased, the mercury first filled the inter-particle voids, followed by the pores on the surface of the particles and the pores within the particles. A total pressure range of 0.7 – 2275 bar was used for mercury intrusion, corresponding to a pore diameter range of 18 μm – 5 nm, respectively. However, only the pore volumes for the pore diameter range 5 to 10000 nm were used for further calculations (for further discussion see Appendix A2). MIP was used to analyse the pore size distribution of the materials beyond the resolution of N_2 adsorption.

The porosity, ε , of the materials was calculated by solving equations (3-3) and (3-4) iteratively by varying the envelope density, ρ_p .¹⁹⁹ The ρ_{sk} was taken from helium pycnometry and the pore volume, V_p , was found using MIP analysis.

$$\varepsilon = 1 - \frac{\rho_p}{\rho_{sk}} \quad (3-3)$$

$$\varepsilon = \rho_p V_p \quad (3-4)$$

3.3.6 FTIR

Fourier-transform infrared spectroscopy (FTIR) was carried out using an Elmer Spectrum 100 FTIR spectrometer (Perkin) equipped with an attenuated total reflectance (ATR) accessory. FTIR spectroscopy is based on the interaction of infrared radiation with the chemical bonds in a sample. When infrared radiation is absorbed, it causes the chemical bonds to vibrate and bend in a characteristic way to specific groups.

The samples were dried at 50°C for at least 12 h before analysis. A small amount of LDH sample was loaded into the sample cell and pressed into a disk for analysis. Infrared radiation was passed through a sample, and the resulting absorbance spectrum was measured. Sixteen spectra were collected per sample to obtain an averaged spectrum over the 500–4000 cm^{-1} infrared wavelength range with a resolution of 2 cm^{-1} . The FTIR spectra provide information about the vibrational modes of the metal-oxygen groups and species in the interlayer of the LDH.

3.3.7 Electron microscopy

The surface morphology of the materials was investigated using a scanning electron microscope (SEM) type LEO Gemini 1525 or Hitachi S5500. Prior to SEM analysis, the samples were dispersed onto a stub coated with a layer of electrically conductive carbon tape and sputter-coated with a thin conductive layer of gold (for 30 s at 20 mA). In the microscope, an electron gun was used to produce a beam of electrons that was accelerated towards an anode and focused through lenses. The electrons interact with

the atoms on the surface of the sample and produce signals, such as secondary and backscattered electrons. These signals are detected and processed to create an image of the sample surface to study the surface morphology of the sample.

The morphology and chemistry of the materials were further analysed by using a JEOL JEM-2100F TEM equipped with an EDX X-Max detector (Oxford Instruments) and carried out in collaboration with Dr Oriol Gavalda-Diaz. Samples were prepared on a carbon film on a gold TEM grid and imaged at an accelerating voltage of 200 kV.

3.3.8 *Thermal analysis*

Calcination of the LDHs in air was studied using a Q5000 TGA (TA Instruments). For each experiment, a platinum pan was loaded with 10 mg of the LDH sample (<50 μm) and heated to 50°C for 1 h. The temperature was then increased to 900°C using a heating rate of 10°C min⁻¹. Additionally, a TGA coupled with a mass spectrometer (Netzsch) was used for specific samples to identify the gases released from the LDHs during calcination under Ar.

3.3.9 *Crushing strength*

The crushing strength of an oxygen carrier refers to its capacity to withstand physical stresses without breakage and is an important parameter for screening oxygen carriers for fluidised bed systems. The mechanical strength of an oxygen carrier was determined by measuring the force required to break a single particle in the size fraction 300–425 μm using a 50 N Series 3 Force Gauge (Mark-10) operating at a sampling rate of 2000 Hz. For each experiment, the force gauge was manually lowered onto the particle as the MESURTM gauge software recorded the experimental results. A typical crushing force profile is shown in **Figure 3-5**. The crushing force reaches a certain value where the particle breaks (2.45 N in **Figure 3-5**), which results in a sudden decrease in the measured force. Measurements were carried out on 30 randomly chosen particles, and an average was calculated to obtain a reliable estimate of the crushing strength of the MMOs.

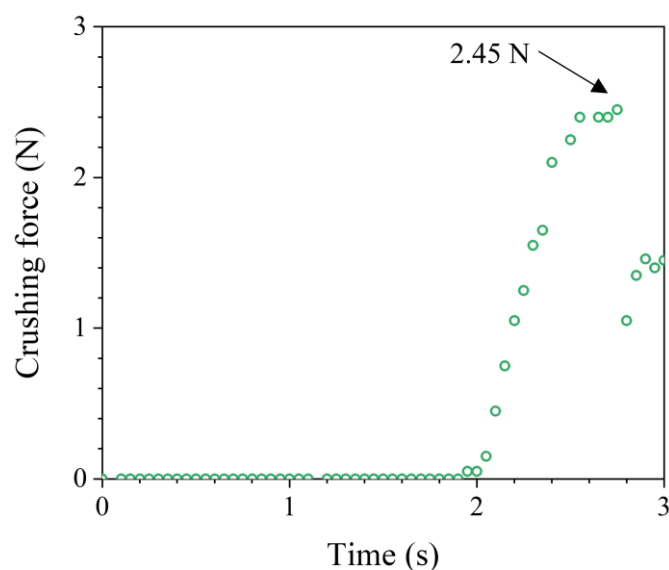


Figure 3-5: *Crushing force measurement of an MMO particle in the 300–425 μm size range. MMOs were calcined from LDHs co-precipitated at pH 11 for 300 min.*

3.4 Oxygen carrier testing

3.4.1 Thermogravimetric analyser

A Q5000 (TA Instruments) type TGA was used to investigate the long-term stability of the oxygen carriers over extended redox cycling under different chemical looping modes (CLOU and CLC). The experimental set-up of the TGA is presented in **Figure 3-6**. The TGA software could only control the flow rate of N_2 into the furnace via internal mass flow controllers (MFCs). Therefore, an external gas supply system was required to achieve the desired gas compositions and flow rates of the reducing and oxidising gases for the redox cycling experiments. Three MFCs (Brooks) controlled the external system using feed gases of CO/N_2 , N_2 and laboratory air, as indicated. The external MFCs were controlled via a separate computer programme written in the software Agilent VEE 9.0.

To synchronise the TGA programme with the external MFC control program written in Agilent VEE, a DAQ module was connected to the TGA. The cycling programme written in the TA software communicated with the Agilent VEE programme via a binary signal of the position of an external event switch (on/off). The Agilent VEE code interpreted the sequence of external events to supply the external gas flow rates required for each cycle phase. The gases supplied through the external gas mixing set-up and the N_2 controlled by the TGA were combined using a 3-way solenoid valve. To minimise the response time of gas switching, the flow rates were initialised by the Agilent VEE programme and vented for a few seconds before the TGA required them.

For CLOU cycling experiments, a two-phase programme was used, where the MMOs were placed in a platinum crucible (1.5 mm high and 9.8 mm in diameter) and exposed to n cycles of, for example,

- (i) decomposition in N_2 for a specified duration,
- (ii) re-oxidation in air for a specified duration.

For CLC cycling experiments, a four-phase programme was used, where the MMOs were exposed to n cycles of, for example,

- (i) reduction in 10% CO/N_2 for a specified duration,
- (ii) a N_2 purge for 1 min to prevent mixing of the oxidative and reductive atmospheres,
- (iii) re-oxidation in air for a specified duration,
- (iv) a N_2 purge for 1 min.

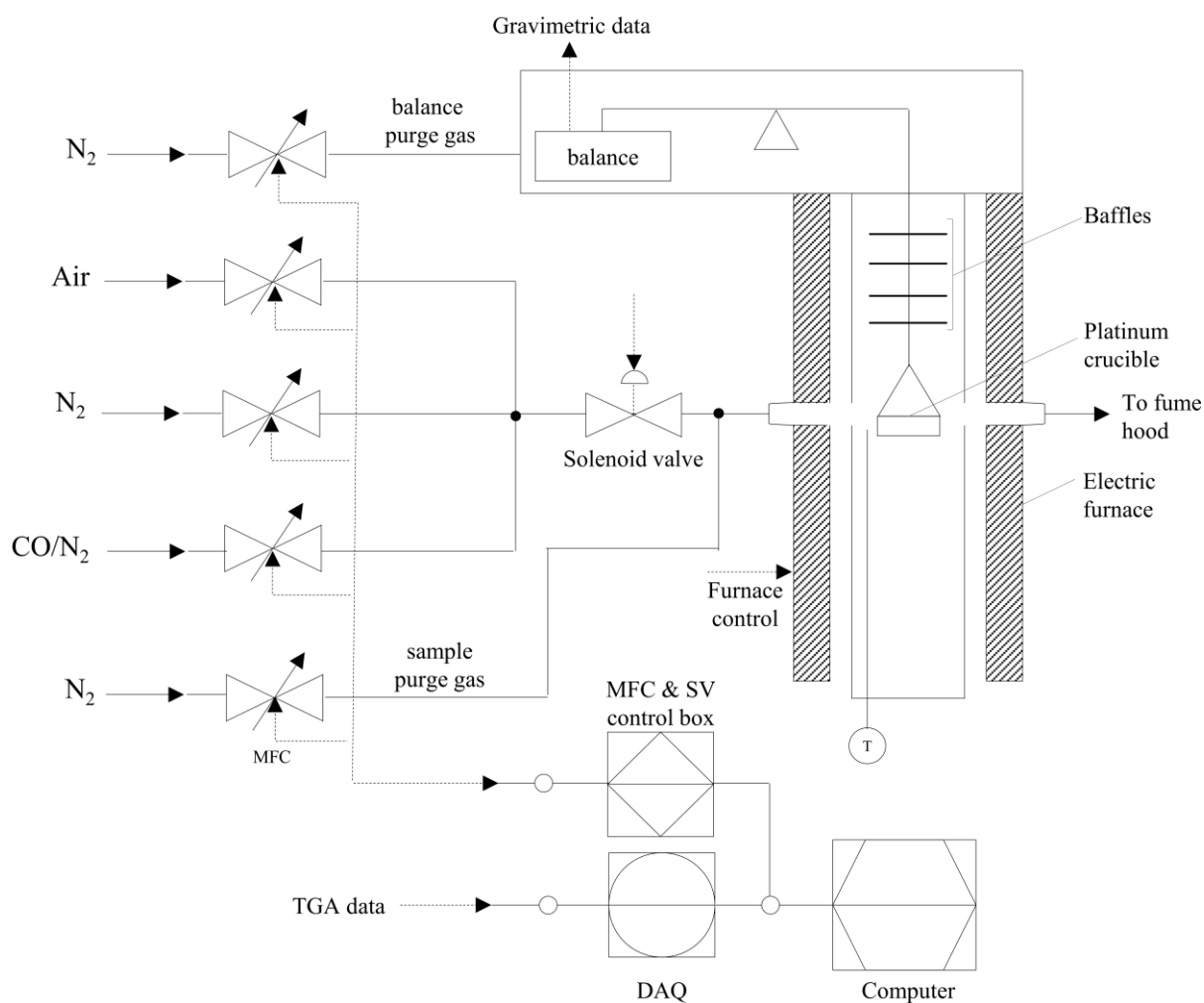


Figure 3-6: TGA and external gas supply set-up. Adapted from Patzschke.¹¹⁵

Minimising external mass transfer resistances in the TGA

The TGA was also used to study the kinetics of the oxygen release reaction in chapter 6. It is possible that the measured reaction rates during the TGA experiments could be affected by external mass transfer – despite using the maximum gas flow rate permitted by the instrument (200 ml min^{-1}) to sweep the oxygen released from the MMOs from the TGA pan to minimise these effects. In later chapters, the maximum rate of oxygen transfer from the particle surface to the bulk was calculated using equation (3-5)¹¹⁰,

$$N_{O_2} = C \cdot D \cdot \frac{\pi d_{pan}^2}{4h} \cdot \ln \left(\frac{1 - y_{O_2,b}}{1 - y_{O_2,s}} \right) \quad (3-5)$$

where N_{O_2} is the molar flow rate of oxygen, C is the molar gas concentration, D is the molecular diffusivity of O_2 in N_2 , d_{pan} and h are the diameter and height of the TGA pan, respectively, and y_s and y_b are the mole fractions of oxygen at the particle surface and in the bulk of the TGA, respectively.

The molecular diffusivity was calculated using the Chapman–Enskog theory²⁰⁰ (equation (3-6)),

$$D = \frac{1.86 \cdot 10^{-3} T^{3/2} (1/M_1 + 1/M_2)^{1/2}}{p \sigma_{12}^2 \Omega} \quad (3-6)$$

where T is the absolute temperature, M_i are the molecular weights of the gases, σ_{12}^2 and Ω are the collision diameter and collision integral, respectively and are characteristic molecular properties of the Chapman and Enskog theory. The σ_{12} was determined by the arithmetic average of the two species (equation (3-7)). The Ω depends on an integration of the interaction between the two species and is described by the Lennard–Jones 12-6 potential.²⁰⁰ The resulting integral varies with the temperature and the energy of interaction. This energy ε_{12} is a geometric average of contributions from the two species (equation (3-8)). Once ε_{12} is known, Ω can be found as a function of $k_B T / \varepsilon_{12}$ using the literature correlations.

$$\sigma_{12} = \frac{1}{2} (\sigma_1 + \sigma_2) \quad (3-7)$$

$$\varepsilon_{12} = \sqrt{\varepsilon_1 \varepsilon_2} \quad (3-8)$$

For comparison the molecular diffusivity was also calculated using an empirical correlation proposed by Fuller, Schettler and Gidding (equation (3-9)).²⁰¹

$$D = \frac{10^{-3} T^{1.75} (1/M_1 + 1/M_2)^{1/2}}{p[(\sum v)_1^{1/3} + (\sum v)_2^{1/3}]^2} \quad (3-9)$$

where $(\sum v)_i$ are the diffusion volumes of species i

The parameters used for the calculation of the molecular diffusivities are given in **Table 3-3**. For equation (3-6), Ω was found to be 0.72.²⁰² There was good agreement between the calculated molecular diffusivities using the two methods. The molecular diffusivity was calculated to be 2.16 cm² s⁻¹ using equation (3-6) and 2.27 cm² s⁻¹ using equation (3-9).

Table 3-3: Parameters for the calculation of molecular diffusivity in the TGA.

Parameter	O ₂	N ₂
M _i (g mol ⁻¹)	32	28
σ_i (Å) ²⁰²	3.467	3.798
ε_i/k_B (T) ²⁰²	106.7	71.4
$(\sum v)_i$ ²⁰³	16.3	18.5

3.4.2 Fluidised bed reactor

An FBR was also used to investigate the long-term cycling performances of the MMOs. In addition to the thermo-chemical stresses experienced in the TGA due to high-temperature chemical reaction, the MMO particles in the FBR are also exposed to additional mechanical stresses arising from collisions between oxygen carriers with other particles and the reactor walls.

The 1.5 kW_e FBR used for CLOU experiments is shown in **Figure 3-7**. Typically, FBRs have a distributor (a porous disk located near the inlet of the reactor) which create a bubbling fluidised bed within the reactor vessel. However, the FBR in this work is operated as a spouted bed reactor. The inlet gas is introduced into the reactor through a small opening at the bottom of the reactor liner, resulting in the formation of an open cylindrical cavity (or central lean solid phase) that extends to the surface of the bed, referred to as the spout. The solid particles are entrained by the gas flow in the spout region, while the remaining particles are in a dense downward solid phase surrounding the spout (annular region), shown in the inset of **Figure 3-7**. Compared to an FBR with a distributor, a spouted bed typically exhibits a lower pressure drop and better mixing, but the bed material suffers significant attrition in the spout region.²⁰⁴

The FBR was designed, built and used by previous PhD students in the Fennell group.²⁰⁵ The main body of the reactor is constructed from Incoloy® Alloy 800HT and positioned between two sets of flanges connected by eight stainless-steel bolts. A quartz liner tube (internal diameter = 30 mm) with an inverted cone-shaped base ($\theta_{\text{cone}} = 60^\circ$) was placed on top of a support disc and connected to the gas inlet tube. To ensure a tight fit between the quartz liner and the support disc, a layer of Superwool® 607Max blanket was used as a seal. A cylindrical counterweight was then placed on top of the quartz liner to compress the seal and fix the liner in place. Copper O-rings were positioned between the flanges and the reactor body at both ends to form a tight seal upon thermal expansion during heating. The reactor was heated using an electric furnace (Lenton) and the temperature inside the spouted bed and at the reactor wall were monitored using thermocouples.

An automated gas supply system was used to provide gases for each phase of the CLOU redox cycling (oxygen release and re-oxidation). The gas supply system consisted of four MFCs and two solenoid valves. The MFCs have a ramp-up period before reaching the set flow rate which could impact the stability of the spouted bed (*i.e.* cause defluidisation) and measurement of the reaction rate. Therefore, solenoid valves were used to minimise this effect by enabling the set points of the gas flow rates of the next cycle phase to be reached and vented to the exhaust for a few seconds before the end of the current phase. The solenoid valves were then switched from the vent to the inlet of the reactor to maintain the desired flow rate based on the minimum fluidisation velocity of the bed materials. The flow rates and duration of each cycle phase during redox cycling were controlled using an Agilent VEE programme.

The off-gas from the reactor was passed through a U-bend packed with glass wool to trap any fines generated by mechanical stresses in the reactor to preserve the integrity of the downstream equipment. The gas was then directed through a CaCl_2 trap to remove any moisture and split into a vent and sample gas stream. The sample gas stream was analysed by an MGA3000 Multi-Gas Analyser (ADC Gas Analysis), which used infrared gas analysis to measure the concentrations of CO_2 , CO and CH_4 . An electrochemical oxygen sensor built into the gas analyser was used to measure the concentrations of O_2 . To ensure accuracy, the O_2 sensor was calibrated before and after each experiment using N_2 , 10 vol% O_2 and air from BOC gas cylinders.

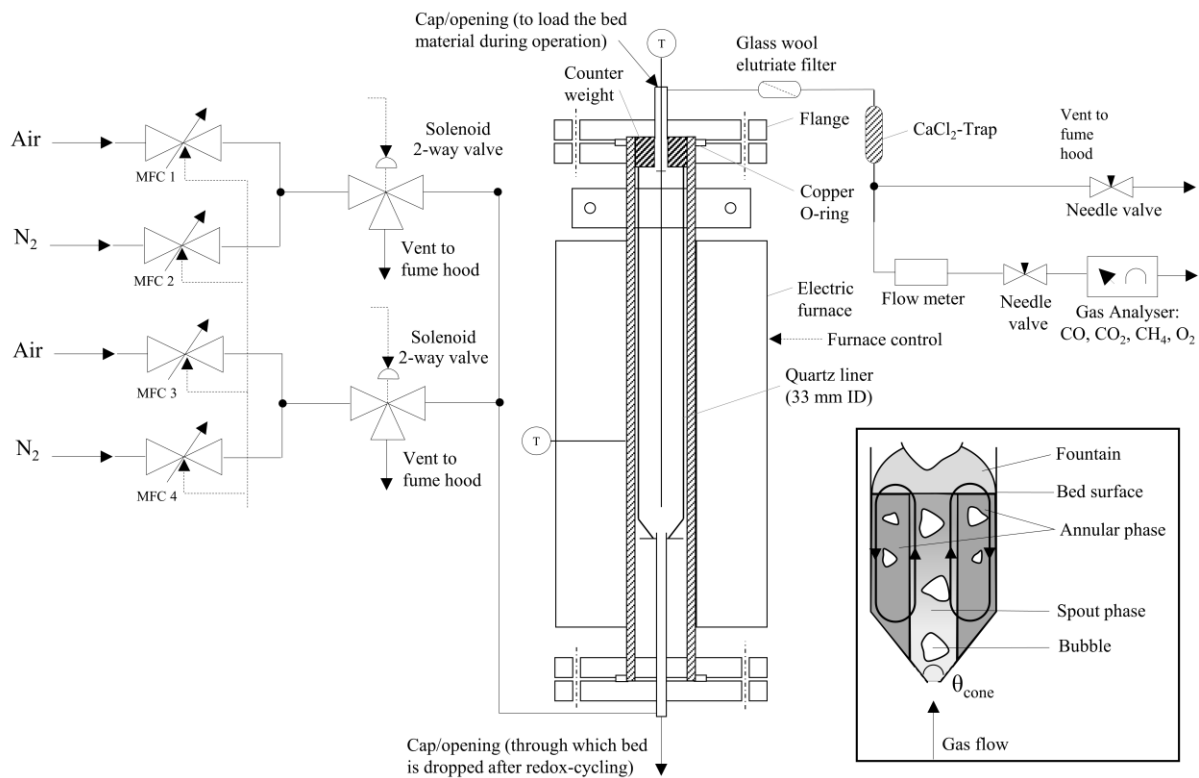


Figure 3-7: Set-up of the 3kW_e FBR, adapted from Patzschke.¹¹⁵ Inset shows the behavior of a bubbling spouted bed reactor, adapted from Zhang.²⁰⁵

A 3kW_e FBR was used for CLC experiments. The dimensions and set-up of the reactor were similar to the FBR used for the CLOU experiments. However, the heating was supplied by two sets of copper electrodes connected at the top and bottom of the reactor instead of an electric furnace. An electrical current was passed through the electrodes using a high-output transformer (2.5 V, 1600 A) to generate electrical resistance heating. An Agilent VEE code was used to control the gas flow rates, system pressure, as well as the wall and bed temperatures. The off-gas from the reactor was passed through a filter trap to remove particulates and a CaCl₂ trap to remove moisture before being split into two separate vent and sample gas streams. The sample gas stream was analysed by an MGA3000 Multi-Gas Analyser (ADC Gas Analysis). The CH₄ and CO signals were calibrated when required using BOC calibration gases.

Calculation of minimum fluidisation velocity

For operation of the FBRs, it was crucial to determine the appropriate gas inlet flow rate to fluidise the bed and ensure optimal gas-solids mixing. The minimum fluidisation velocity, u_{mf} , represents the lowest velocity required for fluidisation, where the bed of particles begins to exhibit fluid-like behaviour, and the upward drag on the particles balances the gravitational force. The u_{mf} depends on the properties of the fluidising gas and particles, and it can be calculated using equation (3-10),

$$u_{mf} = \frac{\mu_g Re_{mf}}{d_p \rho_g} \quad (3-10)$$

where μ_g and ρ_g are the viscosity and density of the fluidising gas mixture, d_p is the mean bed particle diameter, and Re_{mf} is the Reynolds number at minimum fluidisation and can be calculated using,

$$Re_{mf} = [\alpha_R^2 + \beta_R Ar]^{1/2} - \alpha_R \quad (3-11)$$

Where α_R and β_R are constants that have the value of 33.7 and 0.0408, respectively, and Ar is the Archimedes number as is given by,

$$Ar = \frac{d_p^3 \rho_g (\rho_p - \rho_g) g}{\mu_g^2} \quad (3-12)$$

where ρ_p is the density of the bed particle, g is the acceleration due to gravity.

The result of the u_{mf} calculation for sand ($\rho_p = 2600 \text{ kg m}^{-3}$) using N_2 as the fluidising gas at 900°C is shown in **Table 3-4**. The u_{mf} was used to determine the required hot fluidising flow rate ($v_{g,hot}$) and the MFC flow rates ($v_{g,SATP}$).

Table 3-4: Minimum fluidisation velocity calculation. Based on the envelope density of inert sand bed material (2600 kg m^{-3}).

T	ρ_g	μ_g	Ar	Re _{mf}	U _{mf}	$v_{g,hot}$	$v_{g,SATP}$
(°C)	(kg m ⁻³)	(kg m ⁻¹ s ⁻¹)	(-)	(-)	(m s ⁻¹)	(L min ⁻¹)	(L min ⁻¹)
900	0.291	4.61E-05	166	0.101	0.0440	1.864	0.474

Deconvolution of the measured gas analyser signal

The gas concentrations from a reaction in an FBR change during the path from the reactor exit to the gas analyser. It is important to account for these changes to ensure that the measured concentration profiles by the gas analyser are as close as possible to those during the reaction in the bed. Dead time is introduced by the finite rate at which the gas can be transported from the bed to the gas analyser through the piping. Additionally, mixing of gases may occur in the freeboard of the reactor and within the piping, which further convolutes the true concentration. The electrical and internal piping of the gas analysers also has an inherent response time to changes in concentration.

Deconvolution is a signal processing technique that reconstructs the input to a system from the measured output. Deconvolution was achieved by using a mathematical model of the system to create a transfer function to account for the convolution effects of the measurement system following a procedure developed by Fennell *et al.*²⁰⁶ The contributions from each component of the measurement system were modelled as a period of dead time (t_d) followed by two continuously stirred tank reactors (CSTRs) in series with residence times τ_{GM} and τ_{GA} to account for the convolution of the signal due to the gas mixing in the piping and the response time of the analyser, respectively.²⁰⁷

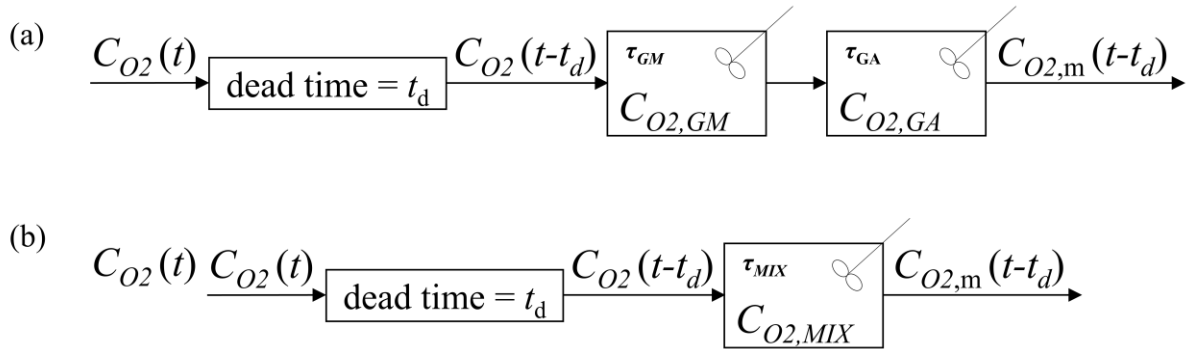


Figure 3-8: Diagram of the measurement system modelled as dead time and (a) series of CSTRs and (b) a single CSTR, adapted from Patzschke.¹¹⁵

The deconvolution model is shown in **Figure 3-8a** and given by equation (3-13) for the concentration of oxygen in the bed, C_{O_2} , and the measured oxygen concentration from the gas analyser, $C_{O_2,m}$.

$$C_{O_2}(t - t_d) = C_{O_2,m} + \tau_{GM} \frac{dC_{O_2,GM}}{dt} + \tau_{GA} \frac{dC_{O_2,GA}}{dt} \quad (3-13)$$

The total response time is approximately additive; therefore, the overall response time was modelled using a single CSTR with residence time τ_{MIX} (**Figure 3-8b**). C_{O_2} can then be estimated from the measured gas concentration using equation (3-14),

$$C_{O_2}(t - t_d) = C_{O_2,m} + \tau_{MIX} \frac{dC_{O_2,m}}{dt} \quad (3-14)$$

To calculate τ_{MIX} , the inlet gas entering the FBR was alternated between 10 vol% O_2 and N_2 . Around 40 g of inert sand was added as bed material to the FBR at 875°C. The inlet gas flow rate was 2.45 L min^{-1} (SATP), and the flow rate into the gas analyser was 300 ml min^{-1} (SATP). Gas switching was performed five times, and the profiles for the last three cycles were averaged. From **Figure 3-9**, t_d was determined to be approximately 14.5 s. After t_d , the measured molar fraction of oxygen decreased to zero and was compared to a step function. Then, the value of τ_{MIX} was adjusted to minimise the square error between the deconvoluted oxygen fraction (equation (3-14)). The deconvoluted signals for τ_{MIX}

equal to 3, 5 and 7 are shown in **Figure 3-9**. The results show that the deconvoluted signal more closely resembled the step function as τ_{MIX} increased. However, at high τ_{MIX} (i.e. 7), the measured signal was overcorrected and the deconvoluted signal went below 0. An optimal τ_{MIX} of 5.3 was determined for the experiment performed at 875°C. Inert cycles were performed for each FBR experiment carried out in this thesis to establish a baseline for gas switching in the absence of the oxygen carriers and τ_{MIX} was calculated to deconvolute the signal.

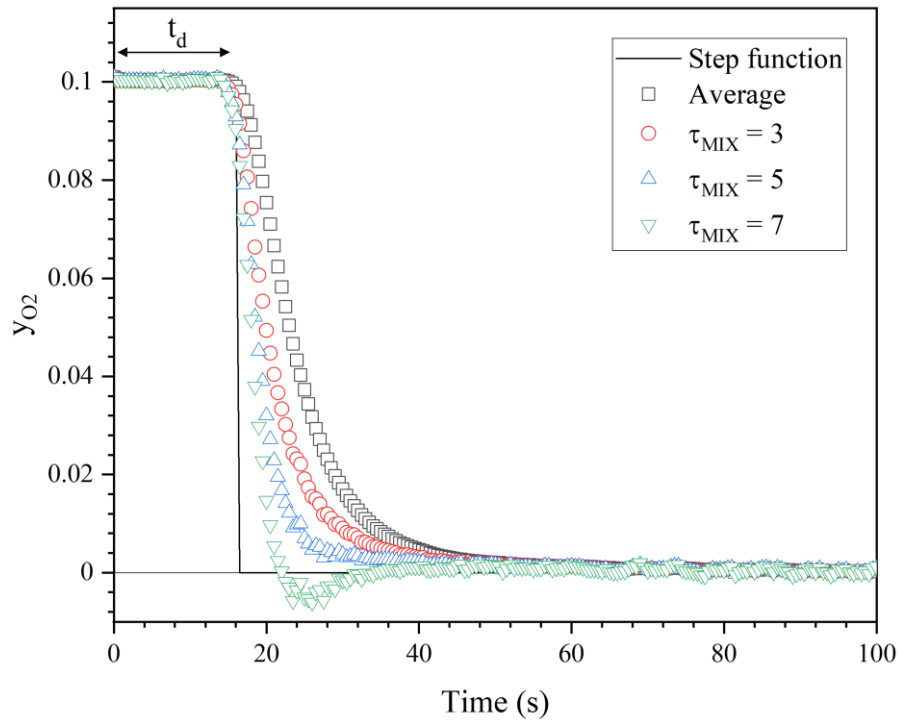


Figure 3-9: Measured and deconvoluted signal from the gas analyser. Gas switching between 10 vol% O_2 and N_2 at 875°C in the FBR ($u/u_{mf} = 4$) compared to a step function.

Chapter 4

Development of Cu-Mg-Al layered double hydroxides and derived oxygen carriers for chemical looping processes

4.1 Introduction

Although significant efforts have been devoted to the development of CuO-based oxygen carriers, an alternative approach is desirable to control the synthetic chemistry of the precursors for improved long-term reactivity and stability of their derived MMOs. The synthesis of Cu-Al LDH precursors and derived MMOs have been reported for chemical looping processes.¹⁵⁶ Although LDH chemistry and MMOs have been well studied for decades, especially for catalysis applications,^{208–210} the use of LDH-derived materials as oxygen carriers for high-temperature chemical looping processes is still an innovative approach.

Owing to the high dispersion of elements in the Cu-Al LDH precursors, the calcined MMOs consist of a highly dispersed active CuO phase within a support that have shown fast oxygen release rates and redox stability.¹⁵⁶ Furthermore, the residual alkaline species (Na or K) was previously found to effectively stabilise the MMOs during long-term thermochemical redox-cycling by reacting with Al_2O_3 to form a variety of species (*i.e.* $\text{Na}_x\text{Al}_y\text{O}_z$).¹⁵⁶ However, it remains challenging to precisely control the content of Na-containing species which originate from the co-precipitating agent used for co-precipitation. Evaporation of the Na at high temperatures may result in a loss of this stabilising agent, which could lead to material deterioration over extended redox cycling. Therefore, it is desirable to tune

the synthetic chemistry of the LDH precursors to minimise the formation of Na-containing impurities and achieve a more stable long-term cycling performance.

From chapter 2, the introduction of Mg into the Cu-Al system has been shown to stabilise CuO-based oxygen carriers over many cycles by inhibiting the formation of CuAl_2O_4 through the preferential formation of a MgAl_2O_4 support phase.^{107,211} In this chapter, the introduction of Mg into the Cu-Al LDH system was investigated. Cu-Mg-Al LDHs were prepared *via* co-precipitation using a molar ratio of Cu:Mg:Al equal to 3:x:2, where x varied from 0 to 1 in steps of 0.2. The effect of the co-precipitating agent on the LDH characteristics was investigated using two different co-precipitating agents, either (i) 1 M NaOH and 1 M Na_2CO_3 , or (ii) 2 M NaOH. Characterisation methods, including XRD, XRF, SEM and TEM, were used to investigate the effect of the co-precipitating agent on the structure and properties of the LDHs and calcined MMOs.

4.2 Incorporation of Mg into the Cu-Al layered double hydroxide system

4.2.1 Synthesis of LDHs using a co-precipitating agent of 1 M NaOH and 1 M Na_2CO_3

Cu-Mg-Al LDH precursors were synthesised *via* co-precipitation at constant *pH*. A metal nitrate solution with a total metal ion concentration of 2 M was prepared by dissolving appropriate amounts of $\text{Cu}(\text{NO}_3)_2 \cdot 2.5\text{H}_2\text{O}$, $\text{Al}(\text{NO}_3)_3 \cdot 9\text{H}_2\text{O}$, and $\text{Mg}(\text{NO}_3)_2 \cdot 6\text{H}_2\text{O}$ in the desired ratios in de-ionised water (DI water). An aqueous alkaline solution was prepared that contained 1 M NaOH and 1 M Na_2CO_3 . The metal nitrate solution and alkaline solution were mixed by dropwise addition of both solutions into a reaction vessel under constant stirring (at 300 rpm). A *pH* value of 9.5 ± 0.2 was maintained by adjusting the flow rate of the acidic and alkaline solutions. After the complete addition of the metal nitrate solution, the mixing was stopped, and the suspension was aged for 3 h at room temperature. Then, the supernatant was carefully decanted, and the precipitate was mixed with fresh DI water. This washing procedure was repeated until the conductivity of the wash water measured below $50\ \mu\text{S cm}^{-1}$. The precipitated solids were separated from the liquid phase first by decanting and then by vacuum filtration. The solids were then dried at 60°C for at least 12 h in a ventilated oven. After drying, the samples were calcined in a horizontal tube furnace at 950°C for 3 h in an airflow of about $1\ \text{L min}^{-1}$ at standard atmospheric temperature and pressure (SATP, *i.e.* 20°C and 101.3 kPa), using a heating rate of $15^\circ\text{C min}^{-1}$.

To investigate the effect of Na substitution by Mg in the LDH and derived MMO structure, the molar ratio of Cu:Mg:Al was varied from 3:0:2 to 3:1:2. The concentration of the metal ion and co-precipitating solutions were kept constant at 2 M.

4.2.2 XRD and chemical characterisation

A range of characterisation analyses were performed to understand the structure and properties of the LDH precursors. The X-ray diffraction patterns of the precursors (**Figure 4-1a**) contain the characteristic peaks of LDHs, for example, the (003) and (006) basal peaks at 2θ of 12° and 24° , respectively, and non-basal peak (110) at 2θ of 60° , which confirmed the formation of LDH structures for each synthesis. A comparison with reference patterns (drawn under the measured patterns) indicated that the structures are a hybrid between Cu-Al hydrotalcite and Mg-Al hydrotalcite, with the peaks matching best with CuAl hydrotalcite (JCPDS 46-0099), $\text{Cu}_6\text{Al}_2(\text{OH})_{16}\text{CO}_3 \cdot 4\text{H}_2\text{O}$ (JCPDS 37-0630) and $\text{Mg}_6\text{Al}_2(\text{OH})_{16}\text{CO}_3 \cdot 4\text{H}_2\text{O}$ (JCPDS 22-0700). With increasing molar Mg concentration, the basal peaks shift to lower Bragg angles, *i.e.* the material resembles decreasingly the CuAl LDH and increasingly the MgAl LDH. The crystallite size, L , of the LDHs was calculated using Scherrer's equation (**Table 4-1**). The height of the LDH crystallites (L_{003}) was estimated from the (003) peak at $\sim 11^\circ$ and the diameter of the LDH crystallites (L_{110}) was estimated from the (110) peak at $\sim 60^\circ$.

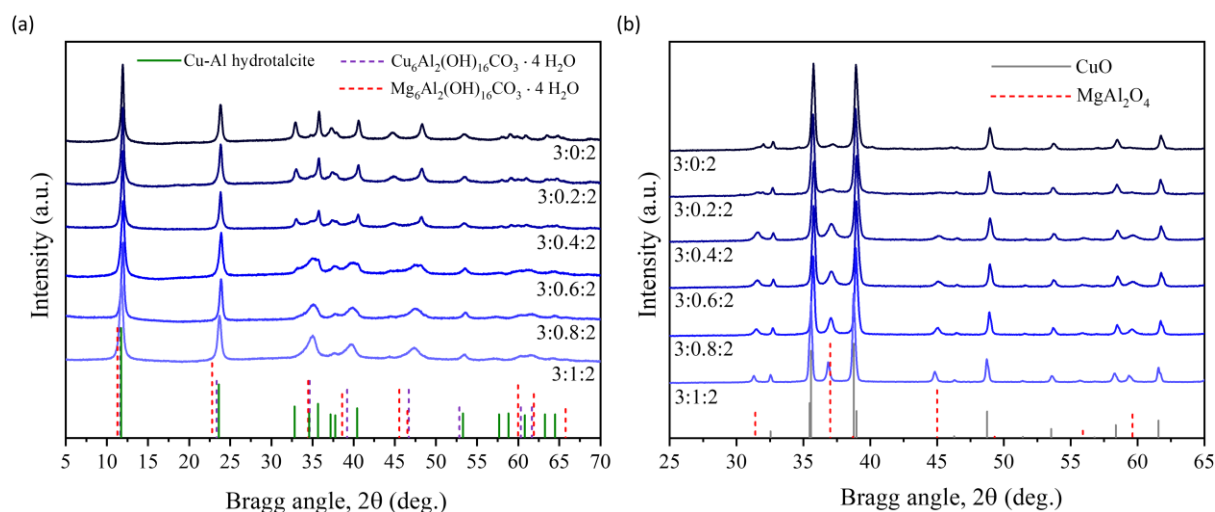


Figure 4-1: XRD patterns of Cu-Mg-Al LDH precursors and calcined mixed metal oxides prepared using 1 M Na_2CO_3 and 1 M NaOH . (a) XRD patterns of CuMgAl-LDHs and (b), CuMgAl-MMO. The crystalline pattern in (a) corresponds to CuAl hydrotalcite (JCPDS 46-0099, 37-0360; vertical lines), $\text{Cu}_6\text{Al}_2(\text{OH})_{16}\text{CO}_3 \cdot 4\text{H}_2\text{O}$ (JCPDS 37-0630) and $\text{Mg}_6\text{Al}_2(\text{OH})_{16}\text{CO}_3 \cdot 4\text{H}_2\text{O}$ (JCPDS 22-0700; vertical dashed lines). Crystalline patterns in (b) correspond to CuO (JCPDS 80-1268; vertical lines) and MgAl_2O_4 (JCPDS 73-1959, vertical dashed lines), respectively. The molar ratio of Cu:Mg:Al in the LDHs varies from 3:0:2 to 3:1:2, as indicated.

After calcination at 950°C for 3 h in air, the active phase of the MMOs consisted of CuO (JCPDS 80-1268) as analysed by XRD (**Figure 4-1**). Additionally, the samples with a molar composition of $3:x:2$ with $x \geq 0.2$ also showed peaks at positions corresponding to those of the reference for MgAl_2O_4 (JCPDS 73-1959), with their peak intensity increasing with an increase in the molar

concentration of Mg. When increasing the Mg loading, the crystallite size of MgAl_2O_4 also increased steadily from 16.6 ± 1.7 nm to 43.9 ± 8.8 nm, while the crystallite size of CuO remained relatively constant in the range of 37 to 54 nm. The results of the crystallite size calculation are presented in **Table 4-1**. The XRD patterns of the freshly calcined samples were compared with the reference pattern for CuAl_2O_4 (JCPDS 00-33-0448), which confirmed that synthesis using 1 M Na_2CO_3 and 1 M NaOH as the co-precipitating agent was effective in inhibiting the unfavourable formation of this spinel oxide in all samples.

Table 4-1: Crystallite size of the LDHs produced using 1 M NaOH + 1 M Na_2CO_3 , and crystallite size of the active and support phases of the calcined MMOs.

Molar ratio of Cu:Mg:Al	LDH		MMO	
	L_{003} (nm)	L_{110} (nm)	L_{CuO} (nm)	$L_{\text{MgAl}_2\text{O}_4}$ (nm)
3:0:2	27 ± 5	16 ± 3	37 ± 6	-
3:0.1:2	24 ± 2	13 ± 4	54 ± 13	-
3:0.2:2	27 ± 5	18 ± 5	39 ± 13	19 ± 2
3:0.5:2	22 ± 4	9 ± 3	44 ± 9	22 ± 2
3:0.8:2	22 ± 4	10 ± 3	44 ± 9	28 ± 4
3:1:2	22 ± 4	11 ± 3	39 ± 10	44 ± 9

Footnote: The crystallite size was calculated using Scherrer's equation ($L = K \lambda / (B \cos(\theta))$) with $K = 0.9$ and $\lambda = 0.15406$ nm. The peak broadening of the instrument was determined experimentally as 0.144 FWHM ($^\circ 2\theta$) using the (111) peak of a Si standard.

To study the composition of the LDH precursors and calcined oxides, XRF and ICP analyses were performed to quantify the content of Na and Mg. The results of ICP and XRF are presented in **Table 4-2**. **Figure 4-2** shows the mass fractions of Na and Mg in the LDH and MMO samples, which were converted to mass fractions of the oxides using stoichiometry and the relative molecular masses of the compounds. In previous work on Cu-Al LDHs, Na-containing species such as dawsonite ($\text{NaAlCO}_3(\text{OH})_2$) were formed when the co-precipitation was performed using Na_2CO_3 as a co-precipitating agent¹⁵⁶. The calcination of dawsonite led to the formation of Na aluminates (NaAlO_2 and other phases) during calcination and inhibited the undesired solid-state reaction of CuO and Al_2O_3 to CuAl_2O_4 . From **Table 4-2** and **Figure 4-2**, in the absence of Mg, significant amounts of Na were incorporated into the materials (XRF_{Na2O}: 3 wt%) due to the formation of dawsonite during co-precipitation of the Cu-Al LDHs. The measured mass fraction of Na_2O was observed to decrease with

an increase in the loading of Mg, indicating that the formation of dawsonite was suppressed during co-precipitation with Mg (**Figure 4-2**). The Mg is expected to perform a similar role as the Na-rich phases in the Cu-Al LDH by inhibiting the formation of deleterious CuAl_2O_4 upon calcination. A discussion of the inhibition of Na-containing species by the presence of Mg is given in section 4.3.

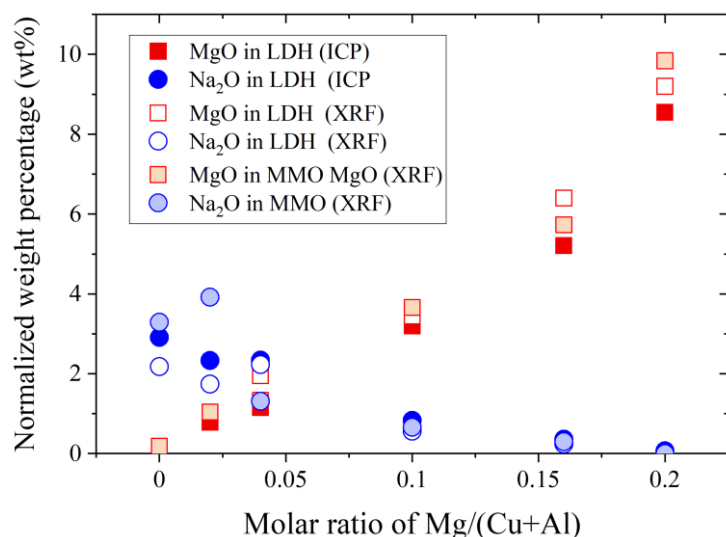


Figure 4-2: Normalised weight percentage of Na_2O and MgO in the LDH precursors and calcined MMOs calculated from ICP and XRF measurements.

Table 4-2: Composition of LDH precursors and derived MMOs prepared using 1 M NaOH + 1 M Na_2CO_3 , calculated from XRF and ICP measurements.

Molar ratio of Cu:Mg:Al	Theoretical (wt%)			LDH								MMO			
				ICP				XRF				XRF			
	CuO	MgO	Al ₂ O ₃	CuO	MgO	Al ₂ O ₃	Na ₂ O	CuO	MgO	Al ₂ O ₃	Na ₂ O	CuO	MgO	Al ₂ O ₃	Na ₂ O
3: 0: 2	70.1	0.0	29.9	69.5	0.0	27.6	2.9	64.9	0.2	32.8	2.2	61.8	0.2	34.7	3.3
3: 0.1: 2	69.2	1.2	29.6	69.0	0.8	27.9	2.3	62.8	1.0	34.4	1.7	62.7	1.0	32.4	3.9
3: 0.2: 2	68.4	2.3	29.2	70.7	1.2	25.9	2.3	64.1	2.0	31.7	2.2	69.4	1.3	27.9	1.3
3: 0.5: 2	66.2	5.6	28.3	70.4	3.2	25.5	0.8	67.3	3.5	28.7	0.6	66.7	3.7	29.0	0.7
3: 0.8: 2	64.0	8.7	27.3	69.0	5.2	25.4	0.4	61.5	6.4	31.9	0.2	65.9	5.7	28.1	0.3
3: 1.0: 2	62.7	10.6	26.8	66.1	8.6	25.3	0.1	60.9	9.2	29.9	0.0	61.3	9.8	28.9	0.0

Footnote: LDHs were synthesised at a *pH* of 9.5.

4.2.2 Morphological and structural characterisation

The LDH precursors and calcined MMOs were characterised using electron microscopy techniques to understand the morphological and structural evolution of the LDH precursors. Scanning transmission electron microscopy (STEM), high-angle annular dark-field (HAADF)-STEM, and energy dispersive spectroscopy (EDS) analysis (**Figure 4-3a-c**) confirmed the platelet-like structure and uniform elemental distribution in the LDH precursors. The SEM image of the Cu-Mg-Al LDH precursor (**Figure 4-3d**) showed a well-defined platelet-like structure with the longer dimension of the platelets measuring on average 110 ± 46 nm (the interval denotes the standard deviation when analysing 120 randomly selected platelets). Correspondingly, the average measured size for the shorter dimension of the platelets (*i.e.* their thickness) was 24.8 ± 4.8 nm. Upon calcination, the platelets coalesced to form larger, more spherical platelets, which have partially developed grain-like features (**Figure 4-3e**).

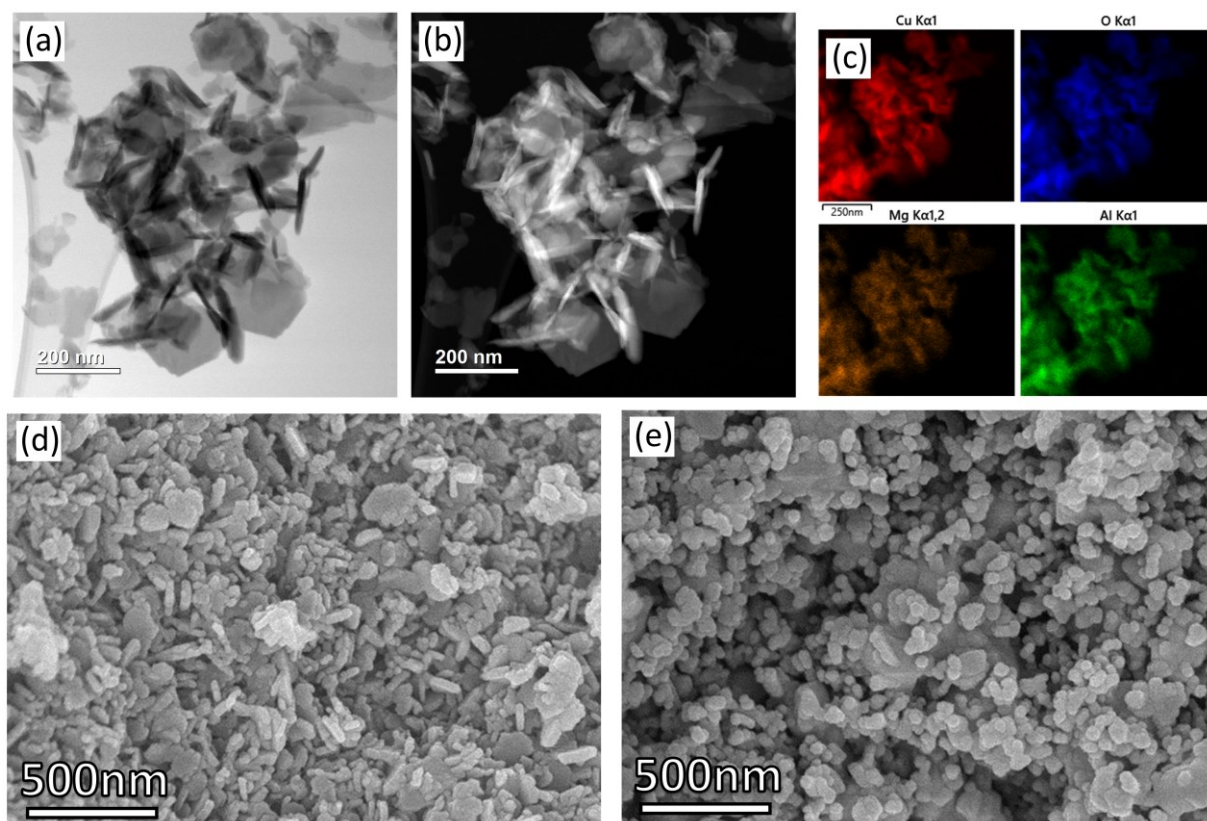


Figure 4-3: Characterisation of the Cu-Mg-Al LDH. (a) STEM and (b) HAADF-STEM images of the Cu-Mg-Al LDH precursor (c) element mapping of the Cu-Mg-Al-LDH precursor, Cu (red), Al (green), Mg (yellow), and O (blue); SEM images of the (d) Cu-Mg-Al LDH and (e) derived-MMO. The LDH precursor sample was prepared using a molar Cu:Mg:Al ratio of 3:1:2.

TEM images of the MMOs calcined at 800°C show highly dispersed CuO (10–20 nm) with a high dispersion in the support phase (**Figure 4-4d-e**). The fast Fourier transform (FFT) patterns of different regions suggest the formation of crystalline domains, however specific assignment of crystalline phases

could not be obtained, which might be due to defects in the CuO phases, interactions between CuO and the Mg-Al oxide support at their interfaces or partial incorporation of CuO into the support.

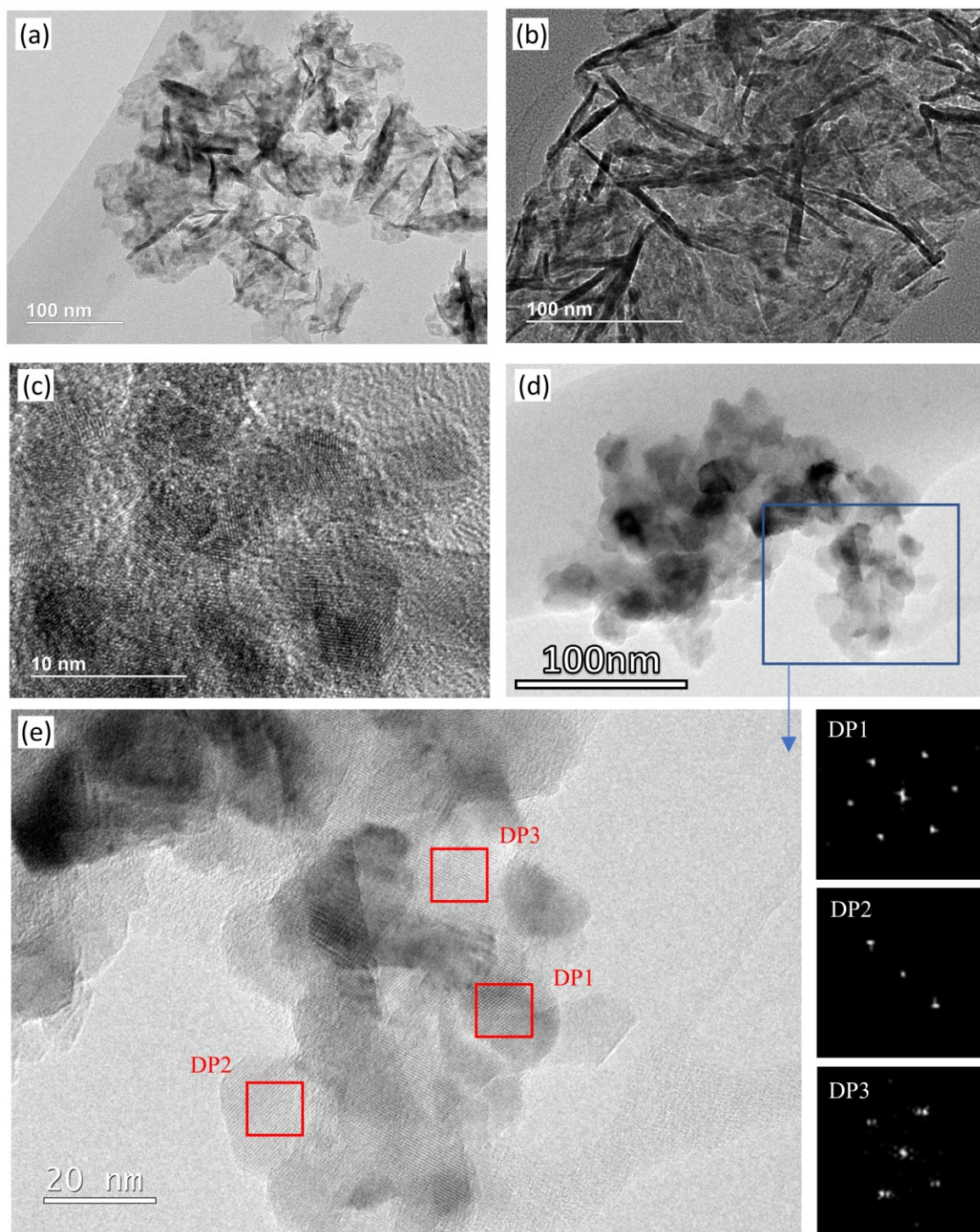


Figure 4-4: Characterisation of the Cu-Mg-Al MMO. (a-b) STEM image of the Cu-Mg-Al MMO; (c) HR-TEM images of the Cu-Mg-Al MMO; (d) STEM image of the calcined the Cu-Mg-Al MMO; (e) HR-TEM image of the Cu-Mg-Al MMO with insets showing the fast Fourier transform (FFT) patterns of different regions. The Cu-Mg-Al MMO sample was prepared by calcining up the CuMgAl-LDH (Cu:Mg:Al = 3:1:2) to 800°C and cooling down to room temperature.

4.3 Thermodynamic analysis of the inhibition of Na-containing species in Cu-Mg-Al layered double hydroxide precursors

The formation of dawsonite, $\text{NaAlCO}_3(\text{OH})_2$, plays an important role in the formation of Na-containing species in Cu-Al LDH precursors and derived MMOs. Thermodynamic calculations were carried out to investigate this relationship using SPANA (formerly MEDUSA),²¹² which is based on the procedures developed by Kakolowicz *et al.*²¹³ and Eriksson.²¹⁴ The calculations were performed for Mg-Al LDHs due to an absence of thermodynamic data for Cu-Mg-Al LDHs.

In the pH values range used during co-precipitation in this thesis (*i.e.* pH 9 – 11.5), the overall reaction for dawsonite formation is shown in equation (4-1)²¹², with its intermediates typically forming according to equations (4-2) to (4-4).



SPANNA was used to compare the predicted thermodynamic equilibrium in the presence and absence of Mg ions. A thorough screening of the available species in SPANA's standard database DATABASE found that relevant compounds, such as dawsonite and bimetallic LDHs, were not included in the standard database. Therefore, equilibrium constants for these compounds were found in the literature and added to DATABASE (**Table 4-3**).

Table 4-3: Values for the equilibrium constants (k_r) and structures for the compounds added to the dataset used for the thermodynamic calculations with SPANA.

Formula	Name	Log $k_{r,298\text{K}}^\circ$	Reference (Database)
$\text{Mg}_2\text{CO}_3(\text{OH})_2 \cdot 3\text{H}_2\text{O}$	Artinite	19.66	^{215,216} (EQ3/EQ6)
$\text{NaAlCO}_3(\text{OH})_2$	Dawsonite	4.35	^{215,216} (EQ3/EQ6)
$\text{Mg}_5(\text{CO}_3)_4(\text{OH})_2 \cdot 4\text{H}_2\text{O}$	Hydromagnesite	32.55	^{215,216} (MINTEQA2)
$\text{NaAlCO}_3(\text{OH})_2$	Dawsonite	4.35	^{215,216} (EQ3/EQ6)
$\text{Mg}_4\text{Al}_2(\text{OH})_{12}(\text{CO}_3) \cdot 2\text{H}_2\text{O}$	CO_3 -hydrotalcite	-51.14	²¹⁷⁻²¹⁹

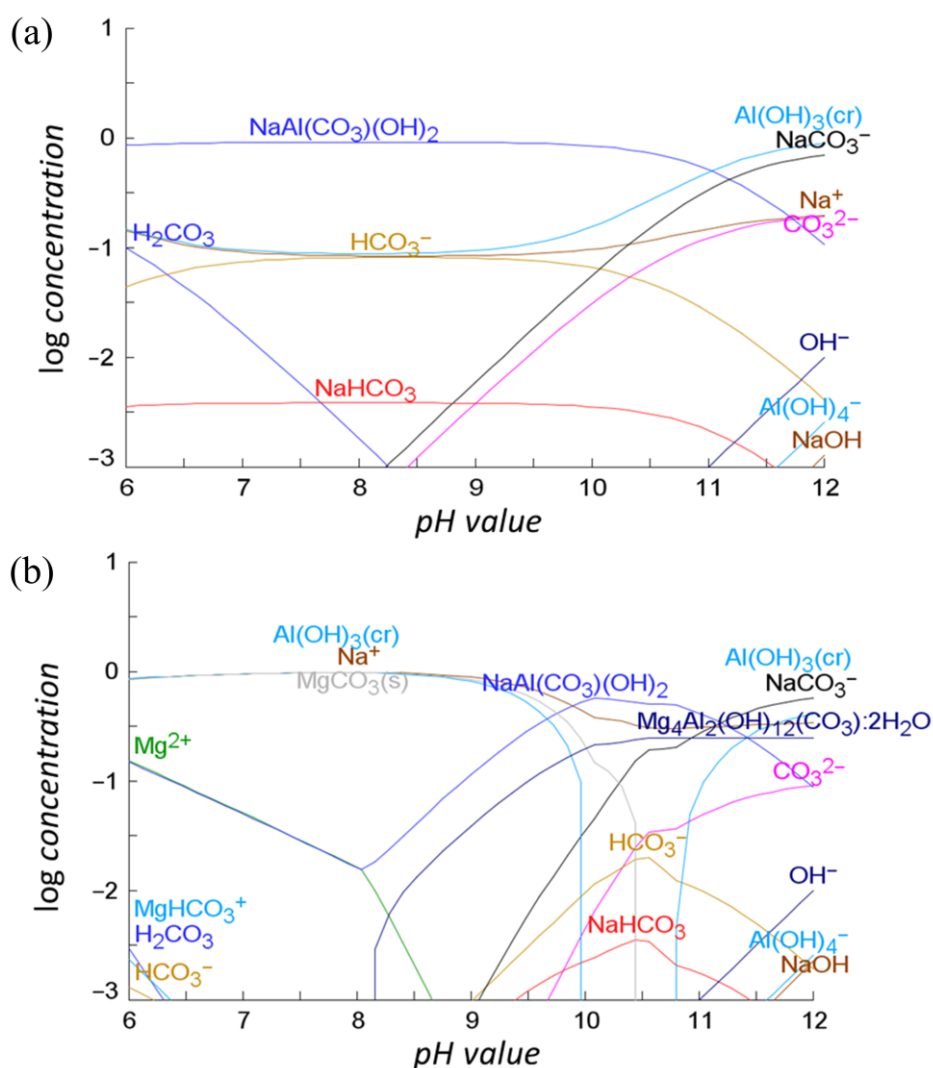
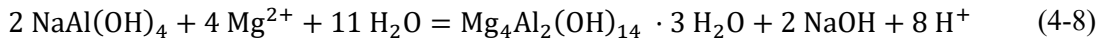


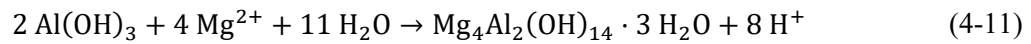
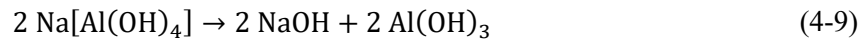
Figure 4-5: Plots of equilibrium compositions (a) in the absence and (b) presence of Mg ions as a function of the pH value. The plots were generated with SPANA (formerly MEDUSA) using data from DATABASE (formerly HYDRA),²¹² as well as literature values for the compounds listed in **Table 4-3**.

The results of the thermodynamic calculations using SPANA's standard database and additionally dawsonite and $\text{Mg}_4\text{Al}_2(\text{OH})_{12}(\text{CO}_3) \cdot 2\text{H}_2\text{O}$ with data from **Table 4-3**, in the presence and absence of Mg are presented in **Figure 4-5a-b**, respectively. From **Figure 4-5a**, the formation of dawsonite occurs over a wide pH range. However, when the calculation was repeated with Mg ions being present, as shown in **Figure 4-5b**, the presence of Mg thermodynamically suppresses the formation of dawsonite and favours the formation of intermediates required for the formation of Mg-Al LDHs (e.g. MgCO_3 and $\text{Al}(\text{OH})_3$) at moderate pH values (i.e. pH 6.0–9.5). At higher pH values (pH > 9.5), significant Mg-Al LDH formation was predicted (log concentration > 0.1). Though dawsonite is predicted to form over a wide pH value range, its equilibrium concentration is significantly lower when Mg is present. This thermodynamic suppression and fast kinetics of the formation of Mg-Al LDHs and its intermediates are likely to effectively inhibit dawsonite formation. Other Na-containing species remain dissolved or are soluble, allowing their removal from the system upon extensive washing of the precipitate.

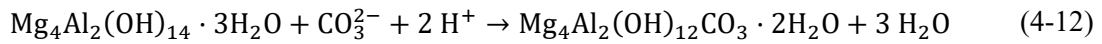
The formation of Mg-Al LDHs is possible *via* an ion exchange reaction with the NaAl(OH)₄, produced according the reactions shown in Equations (4-7) and (4-8):



Since hydrated sodium aluminate can also dissociate, a two-step reaction during which the dissociated aluminium hydroxide reacts with an Mg-ion is also a possible pathway:



In these reactions, Mg-species are likely to effectively scavenge carbonate groups and Al from either dawsonite or from the mix of ions required for dawsonite formation. In the final stage, the positively charged Al-Mg hydroxide forms two-dimensional layers while intercalating carbonate groups according to the reaction such as equation (4-12) as predicted by SPANA:



Following the formation of the Mg-Al-CO₃ layered double hydroxide, all the Na remains soluble in the solution as NaCO₃⁻ and Na⁺ (**Figure 4-5b**). These soluble Na-species are then separated from the precipitate and removed with the supernatant during the repeated DI-water washing step of the synthesis procedure.

In a binary Cu-Al LDH system, such as the one investigated by Song *et al.*,¹⁵⁶ the absence of Mg enabled the formation of dawsonite. The precipitation of dawsonite in the solid phase prevented the complete removal of the Na from the materials during the subsequent DI washing procedure, and therefore Na remained as a contaminant in the calcined MMOs.

The inhibiting effect of Mg on dawsonite formation has also been observed in natural subsurface dawsonite reservoirs in “Mg-poor environmental conditions”.²²⁰ In lab experiments, the authors reproduced potential dawsonite formation conditions and likewise observed an inverse relationship between the concentration of Mg and the formation of dawsonite.²²⁰

4.4 Effect of co-precipitating agent

4.4.1 Synthesis of layered double hydroxides using 2 M NaOH

To further investigate the influence of Mg on the composition of the MMOs, Cu-Mg-Al LDH were synthesised using an aqueous solution of 2 M NaOH as the co-precipitating agent. As for the LDHs synthesised using 1 M Na₂CO₃ and 1 M NaOH, the molar ratio of Cu:Mg:Al was varied from 3:0:2 to 3:1:2 while the concentration of the metal ion solution was kept constant at 2 M, and a constant *pH* value of 9.5 was maintained during co-precipitation.

4.4.2 XRD and chemical characterisation

A range of characterisation analyses were performed to understand the structure and properties of the LDH precursors. XRF and ICP analyses were performed to quantify the content of Na and Mg in the LDHs and calcined MMOs (**Table 4-4**). The results show that Mg was successfully incorporated into all the materials for each molar ratio of Cu:Mg:Al. However, in contrast with the materials synthesised using NaOH and Na₂CO₃, no Na₂O was detected in the materials synthesised using solely NaOH. From section 4.3, dawsonite formation requires the presence of CO₃²⁻ and no other insoluble Na species were predicted to form (**Figure 4-5b**). Therefore, any residual Na⁺ was removed from the materials during washing which was carried out until the wash water ionic conductivity measured below 50 $\mu\text{S cm}^{-1}$.

Table 4-4: The composition of LDH precursors and derived mixed metal oxides, prepared with 2 M NaOH calculated from XRF and ICP measurements.

Sample	Theoretical (wt%)			LDH								MMO			
				ICP results				XRF				XRF			
Cu: Mg: Al	CuO	MgO	Al ₂ O ₃	CuO	MgO	Al ₂ O ₃	Na ₂ O	CuO	MgO	Al ₂ O ₃	Na ₂ O	CuO	MgO	Al ₂ O ₃	Na ₂ O
3: 0: 2	70.06	0.00	29.94	74.85	0.00	25.15	0.00	70.02	0.26	29.71	0.01	68.52	0.40	31.08	0.00
3: 0.1: 2	69.24	1.17	29.59	76.16	0.00	23.84	0.00	65.75	1.33	32.89	0.03	68.62	1.18	30.19	0.00
3: 0.2: 2	68.44	2.31	29.24	72.92	1.98	25.10	0.00	64.36	2.46	33.18	0.00	71.68	1.96	26.36	0.00
3: 0.5: 2	66.15	5.59	28.26	68.08	4.64	27.28	0.00	63.66	4.94	31.40	0.00	62.18	5.65	32.18	0.00
3: 0.8: 2	64.01	8.65	27.35	67.01	7.02	25.97	0.00	65.74	6.84	27.42	0.00	57.53	9.52	32.95	0.00
3: 1.0: 2	62.65	10.58	26.77	65.11	9.16	25.73	0.00	64.39	8.75	26.86	0.00	58.29	11.04	30.68	0.00

Footnote: LDHs were synthesised at a *pH* of 9.5. Most of the variations are within a range of 5% measurement error.

The XRD spectra show low-crystallinity LDHs were produced using NaOH solely as the co-precipitating agent (**Figure 4-6a**), compared to the high-crystallinity LDHs produced when using NaOH + Na₂CO₃ (**Figure 4-9c**). The XRD results show that a significant amount of CuAl₂O₄ was formed in the Cu-Al MMO, while addition of the Mg (*i.e.* Cu-Mg-Al LDHs) limited the formation of CuAl₂O₄ (**Figure 4-6b**). The results of the crystallite size calculation of the MMOs are presented in **Table 4-5**. When increasing the Mg loading, the crystallite size of CuAl₂O₄/MgAl₂O₄ decreased steadily from 102 ± 11 nm to 70 ± 7 nm, while the crystallite size of CuO remained relatively constant in the range of 58 to 69 nm. The crystallite size of the aluminate and CuO phases of the MMOs derived from LDHs produced using NaOH were much larger than those precipitated using NaOH + Na₂CO₃ (**Table 4-1**).

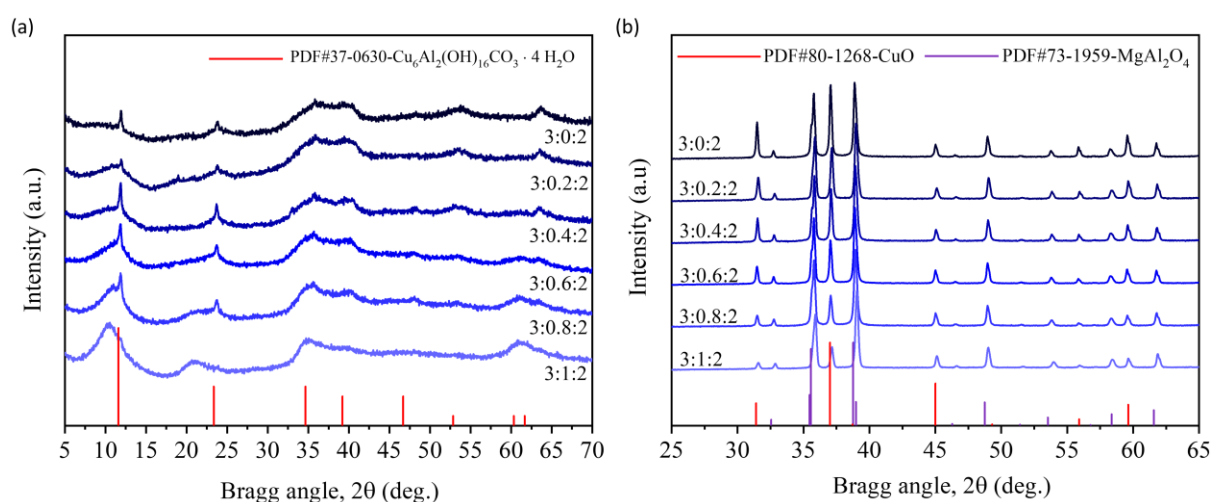


Figure 4-6: XRD patterns of Cu-Mg-Al LDH precursor and calcined MMOs prepared using 2 M NaOH. (a) XRD patterns of Cu-Mg-Al LDHs and (b) Cu-Mg-Al MMO. The crystalline patterns in (a) correspond to Cu-Al hydrotalcite (JCPDS 37-0360), and in (b) correspond to CuO (JCPDS 80-1268; vertical lines) and MgAl₂O₄ (JCPDS 73-1959, vertical dashed lines), respectively. The molar ratio of Cu:Mg:Al in the MMOs varies from 3:0:2 to 3:1:2, as indicated, and calcined at 950°C for 3 h for analysis.

Table 4-5: Crystallite size of the MMOs derived from LDHs produced using 2 M NaOH and 1 M NaOH + 1 M Na₂CO₃.

Molar ratio of Cu:Mg:Al	NaOH		NaOH + Na ₂ CO ₃	
	L_{CuO} [nm]	$L_{\text{MgAl}_2\text{O}_4}$ or $L_{\text{CuAl}_2\text{O}_4}$ [nm]	L_{CuO} [nm]	$L_{\text{CuAl}_2\text{O}_4}$ [nm]
3:0:2	63 ± 6	102 ± 11	37 ± 6	-
3:0.1:2	63 ± 13	98 ± 9	54 ± 13	-
3:0.2:2	63 ± 13	92 ± 7	39 ± 13	19 ± 2
3:0.5:2	64 ± 9	81 ± 5	44 ± 9	22 ± 2
3:0.8:2	58 ± 9	79 ± 7	44 ± 9	28 ± 4
3:1:2	69 ± 10	70 ± 7	39 ± 10	44 ± 9

Footnote: The crystallite size was calculated using Scherrer's equation ($L = K \lambda / (B \cos(\theta))$) with $K = 0.9$ and $\lambda = 0.15406$ nm. The peak broadening of the instrument was determined experimentally as 0.144 FWHM ($^\circ 2\theta$) using the (111) peak of a Si standard.

4.2.3 Morphological and structural characterisation

FTIR spectra for the LDHs co-precipitated using solely NaOH and NaOH + Na₂CO₃ are presented in **Figure 4-7a** and **Figure 4-7b**, respectively. Bands associated with interlayer NO₃⁻ (from the metal nitrate reagents) were observed at 1381 cm⁻¹ and 1039 cm⁻¹ in **Figure 4-7a** indicating that the interlayer anions of the LDHs synthesised using NaOH are a mixture of NO₃⁻ and CO₃²⁻, despite the co-precipitating agent containing no Na₂CO₃. This is likely due to the ingress of ambient CO₂ into the reaction vessel due to the strong affinity of the LDH for CO₃²⁻, as has been reported elsewhere.²²¹ The absence of the bands associated with NO₃⁻ in **Figure 4-7b** shows that the interlayers anions of the LDHs prepared using NaOH and Na₂CO₃ are primarily CO₃²⁻. The band at 1352 cm⁻¹ associated with CO₃²⁻ is much weaker for the precursors prepared with NaOH than for those prepared using NaOH and Na₂CO₃ (**Figure 4-7**). Despite the incorporation of some CO₃²⁻ into the interlayer, the absence of the shoulder at 630 cm⁻¹ indicates that the quantity of CO₃²⁻ in the interlayer is lower than in the samples precipitated with NaOH and Na₂CO₃.

The use of Na₂CO₃ for co-precipitation has been suggested to increase stacking in the *c*-direction, perpendicular to the LDH sheets, due to the stronger electrostatic bonds between CO₃²⁻ (*versus* NO₃⁻) and the brucite layers.^{222,223} As such, LDHs with NO₃⁻ as the interlayer anion have been observed to be less crystalline, less stable, more disordered, and form denser aggregates than LDHs with CO₃²⁻ as the interlayer anion.²²⁴ Therefore, the LDHs produced using solely NaOH possess lower crystallinity because the primary interlayer is NO₃⁻ and those produced using NaOH + Na₂CO₃ have higher

crystallinity because the primary interlayer is CO_3^{2-} , as observed by XRD (**Figure 4-1a** and **Figure 4-6a**, respectively) and SEM (**Figure 4-9**). The formation of a mixture of LDHs with different interlayer anions (CO_3^{2-} and NO_3^-) for the LDHs synthesised using solely NaOH could explain the mixture of sharp and broad peaks observed in the XRD spectra (**Figure 4-6a**) that are associated with LDHs with high and low crystallinity, respectively.

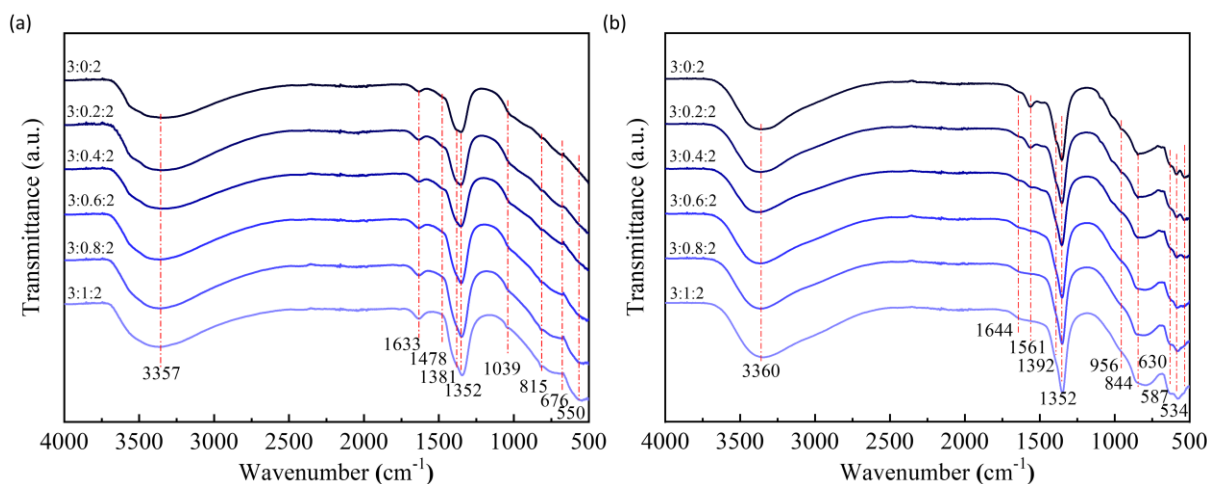


Figure 4-7: FTIR spectra of LDH precursors co-precipitated using (a) 2 M NaOH and (b) 1 M NaOH and 1 M Na_2CO_3 , with varying molar compositions of Cu:Mg:Al = 3 : 0 : 2 to Cu:Mg:Al = 3 : 1 : 2. All samples were prepared at a constant pH of 9.5.

The results of BET surface analysis from N_2 adsorption are shown in **Figure 4-8**. The LDHs and MMOs prepared using solely NaOH generally showed a lower surface area compared to those prepared using a mixture of NaOH and Na_2CO_3 . Analysis of the materials using SEM found the LDHs produced using solely NaOH were much smaller than those produced using NaOH and Na_2CO_3 and the aggregate structure was much denser (**Figure 4-9**).

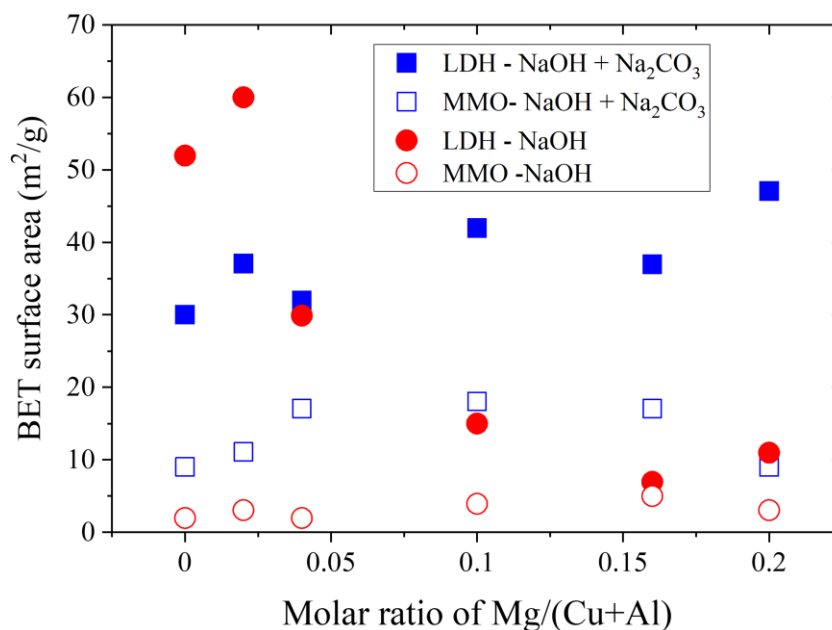


Figure 4-8: BET surface areas of the LDHs prepared using 2 M NaOH and 1 M NaOH and 1 M Na₂CO₃, and calcined MMOs for varying molar concentrations of Mg. All samples were prepared at a constant pH of 9.5.

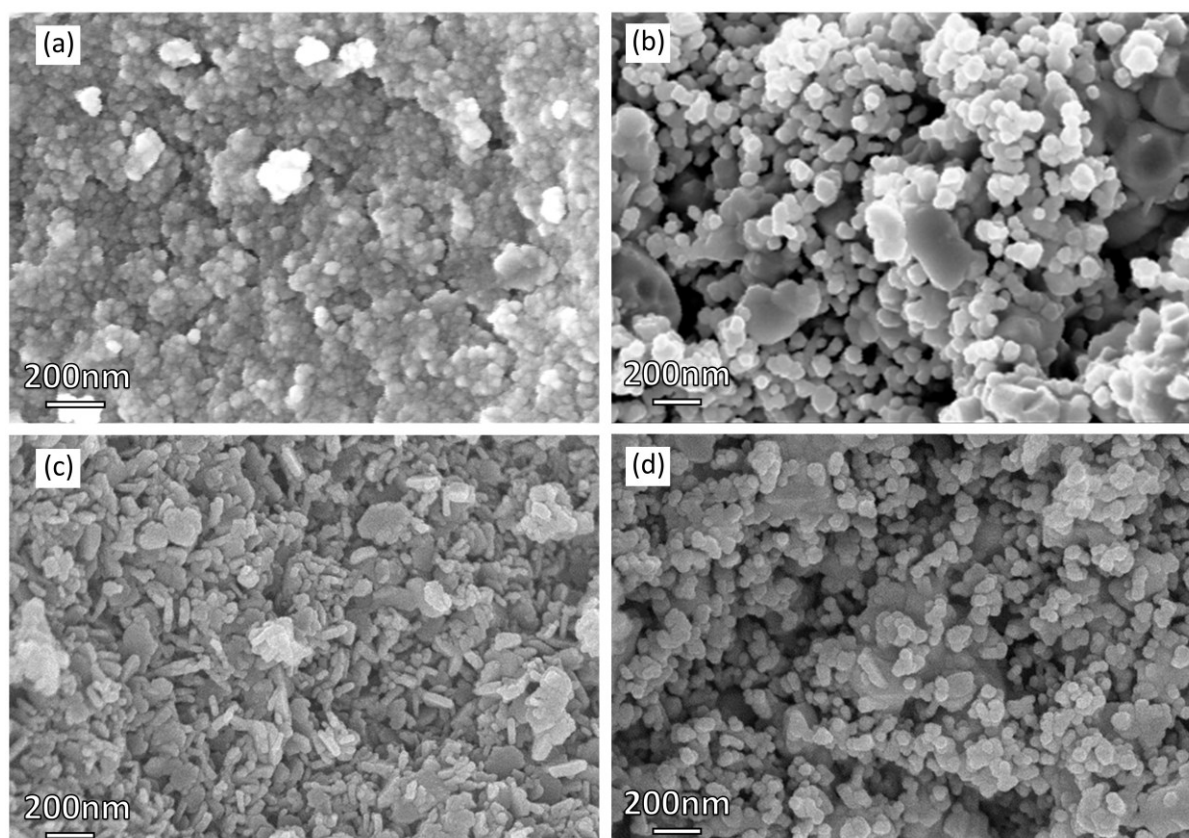


Figure 4-9: SEM images of LDH and MMO materials. (a) LDH precursor produced using 2 M NaOH and (b) derived MMO, and (c) LDH precursor produced using 1 M NaOH and 1 M Na₂CO₃ and (d) derived MMO. All samples were prepared at a constant pH of 9.5. All MMOs were calcined at 950°C for 3 h for analysis.

The degree of elemental dispersion in the MMOs critically determines their redox activity and thermal stability. To compare their elemental dispersion and morphology, HAADF-STEM imaging analysis and EDS elemental mapping were carried out for the following MMOs:

- Cu-Al MMOs, where Cu:Mg:Al = 3:0:2, prepared using 2 M NaOH
- Cu-Mg-Al MMO, where Cu:Mg:Al = 3:1:2, prepared using 2 M NaOH
- Cu-Al MMOs, where Cu:Mg:Al = 3:0:2, prepared using 1 M NaOH and 1 M Na₂CO₃
- Cu-Mg-Al MMO, where Cu:Mg:Al = 3:1:2, prepared using 1 M NaOH and 1 M Na₂CO₃

The Cu-Al MMO derived from Cu-Al LDH precipitated using NaOH showed a poorer dispersion of Cu and Al due to the phase separation of CuO and CuAl₂O₄ (**Figure 4-10**). Similarly, Cu-Mg-Al MMO calcined from low-crystallinity precursor precipitated using solely NaOH showed a dense aggregation of nanoparticles and the formation of large CuO particles (**Figure 4-11**). The formation of fine CuO nanoparticles dispersed in an amorphous matrix was observed for the Cu-Al MMO with residual Na prepared using a co-precipitating agent containing NaOH and Na₂CO₃ (**Figure 4-12**). In contrast, Cu-Mg-Al MMO calcined from high-crystallinity Cu-Mg-Al LDH with no residual Na showed homogeneous distribution of CuO (about 30–40 nm) at the nanometer scale (**Figure 4-13**). A higher degree of dispersion is expected to stabilise the CuO phase and improve the resistance to sintering, enabling higher redox activity and faster kinetics. A side-by-side comparison of the elemental mapping of each MMO is shown in **Figure 4-14** for easier comparison of the varying degrees of dispersion.

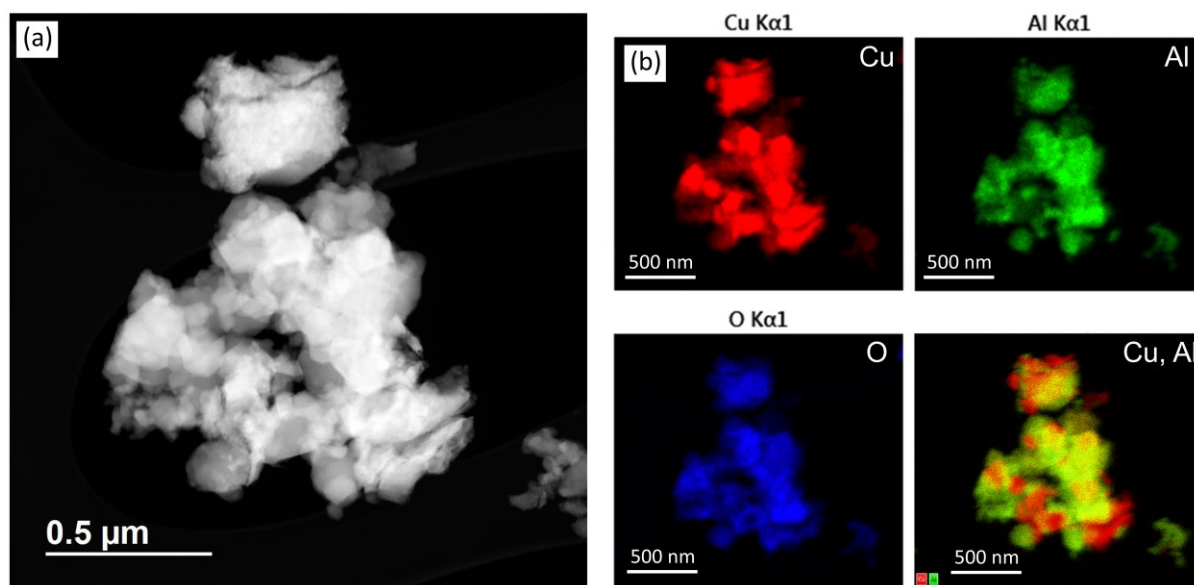


Figure 4-10: Characterisation of Cu-Al MMOs derived from Cu-Al LDH prepared by precipitation with 2 M NaOH without residual Na. (a) HAADF-STEM image of Cu-Al MMO calcined at 950°C. (b) EDS mapping showing the distribution of Cu (Red), Al (Green), and O (Blue), and overlay map of Cu and Al.

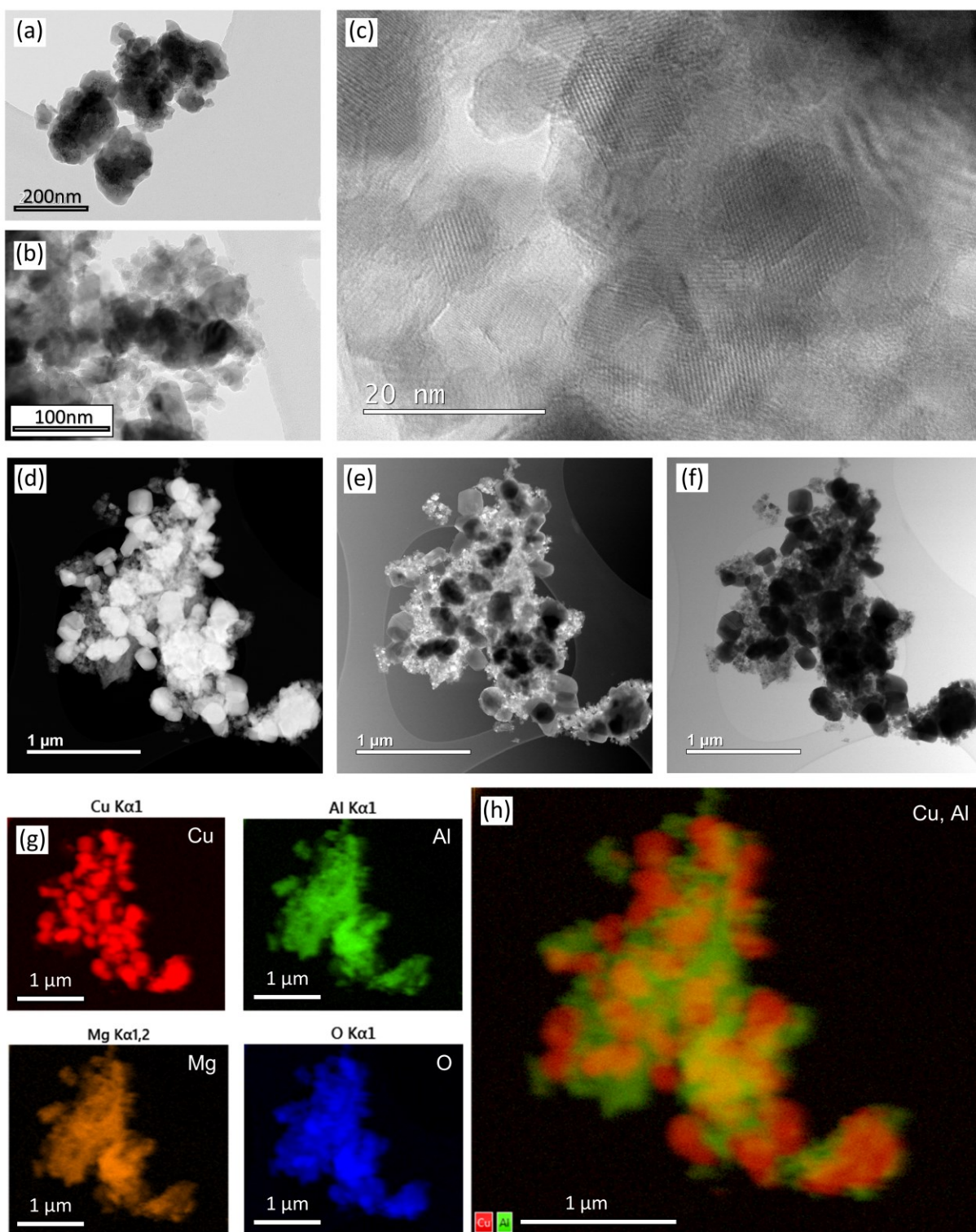


Figure 4-11: Characterisation of Cu-Mg-Al LDH precursor prepared by precipitation with 2 M NaOH and calcined MMOs. (a) STEM image of Cu-Mg-Al LDH precursor. (b) STEM image and (c) HRTEM image of Cu-Mg-Al MMOs calcined at 800°C for 3 h (Cu:Mg:Al = 3:1:2). (d) HAADF-STEM, (e) BF-STEM and (f) STEM images of Cu-Mg-Al MMO calcined at 950°C. (g) EDX mapping showing the distribution of Cu (Red), Al (Green), Mg (Yellow), and O (Blue), and (h) overlay of Cu and Al.

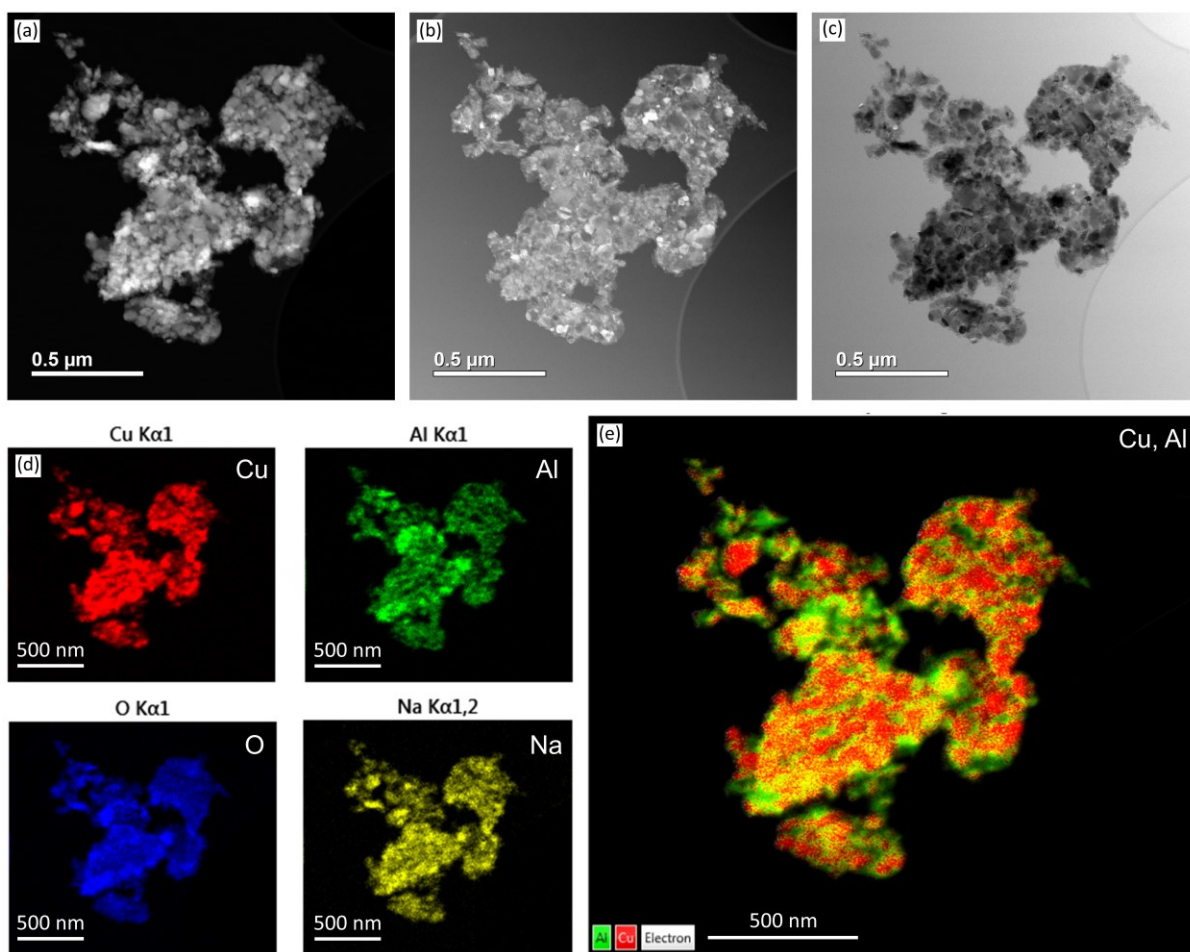


Figure 4-12: Characterisation of Na-stabilised Cu-Al MMOs derived from Cu-Al LDH prepared by precipitation with an aqueous solution containing 1 M NaOH and 1 M Na₂CO₃. (a) HAADF-STEM, (b) BF-STEM and (c) STEM images of Cu-Al MMO calcined at 950°C. (d) EDX mapping showing the distribution of Cu (Red), Al (Green), Na (Yellow), and O (Blue), and (e) overlay map of Cu and Al.

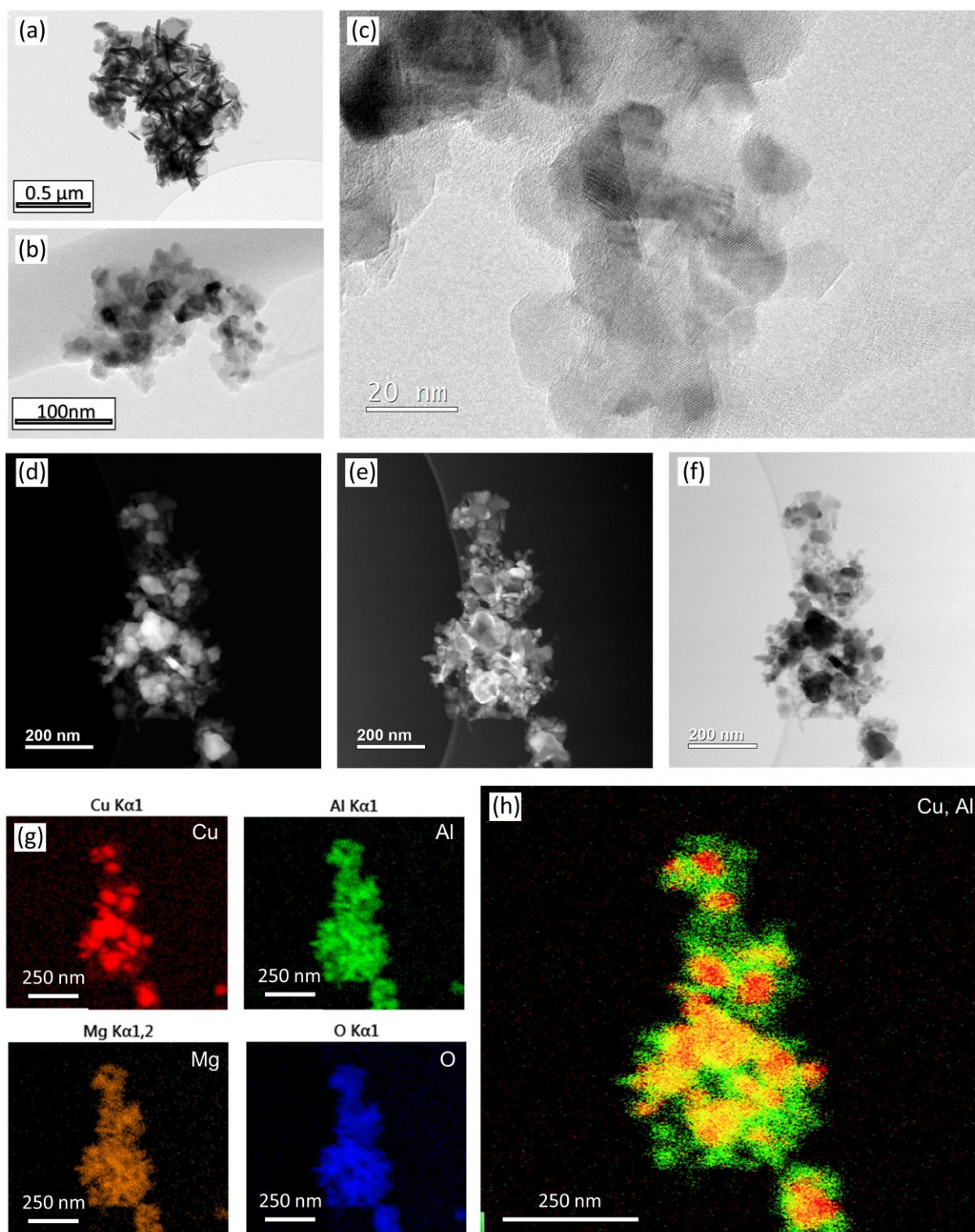


Figure 4-13: Characterisation of Cu-Mg-Al LDH precursor and calcined MMOs prepared by precipitation with 1 M NaOH and 1 M Na₂CO₃. (a) STEM image of Cu-Mg-Al LDH precursor. (b) STEM image and (c) HRTEM image of Cu-Mg-Al MMOs calcined at 800°C for 3 h (Cu:Mg:Al = 3:1:2). (d) HAADF-STEM, (e) BF-STEM and (f) STEM images of Cu-Mg-Al MMO calcined at 950°C. (g) EDX mapping showing the distribution of Cu (Red), Al (Green), Mg (Yellow), and O (Blue).

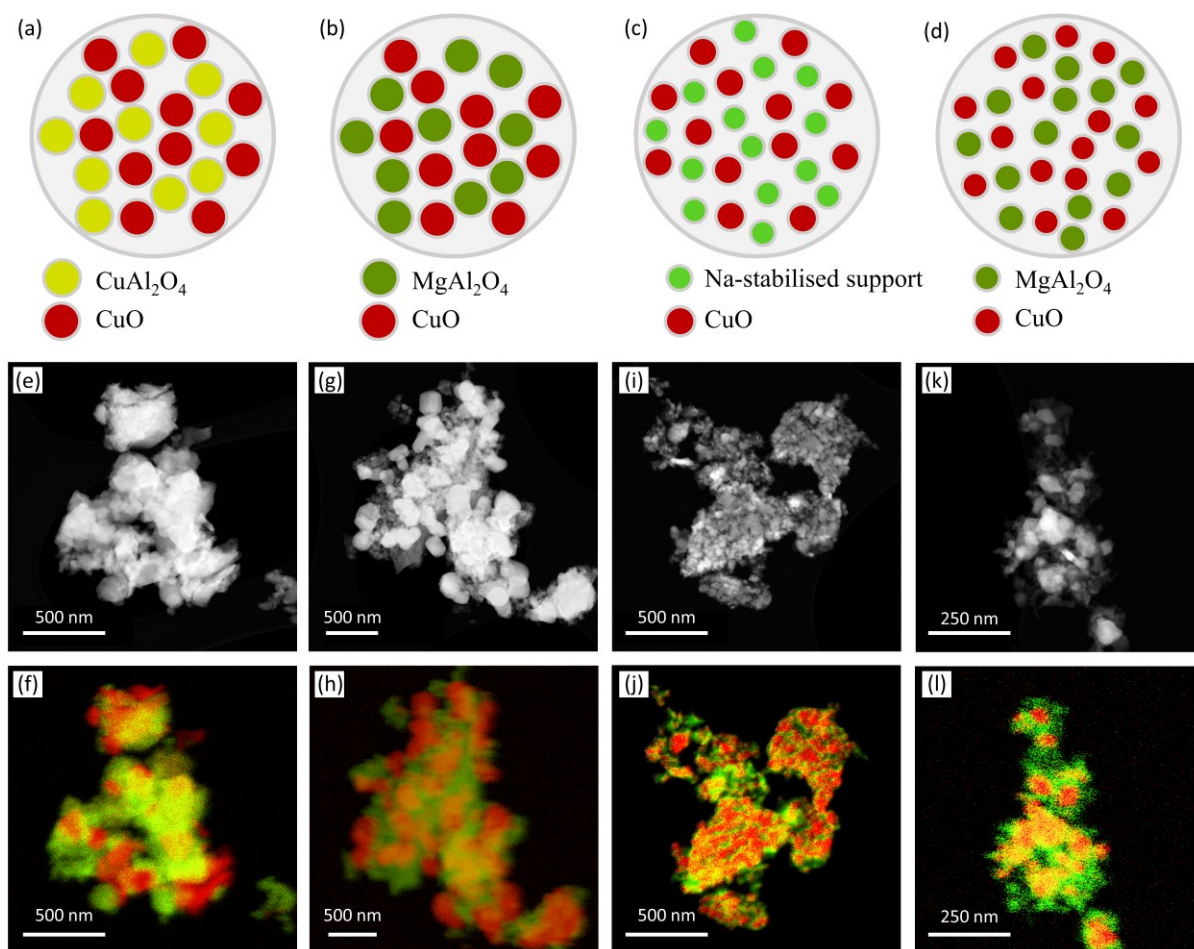


Figure 4-14: Comparison of the phase dispersion of the MMOs calcined from LDHs prepared using different synthesis conditions. Diagrams illustrating the composition and phase dispersion of the MMOs: (a) CuO/CuAl₂O₄ derived from Cu-Al LDH, (b) CuO/MgAl₂O₄ derived from low-crystallinity Cu-Mg-Al LDH, (c) CuO in Na-stabilised support, and (d) CuO in MgAl₂O₄ support derived from high-crystallinity Cu-Mg-Al LDH. (e) HAADF-STEM image and (f) element mapping of Cu-Al MMO synthesised from Cu-Al LDH, consisting of CuO/CuAl₂O₄. Cu:Al = 3:2, 2 M NaOH. (g) HAADF-STEM image and (h) element mapping of Cu-Mg-Al MMO derived from low-crystallinity Cu-Mg-Al LDH. Molar ratio of Cu:Mg:Al is 3:1:2, 2 M NaOH. (i) HAADF-STEM image and (j) element mapping of Cu-Al MMO derived from Cu-Al LDH with residual Na. The molar Cu:Al ratio is 3:2, 1 M NaOH + 1 M Na₂CO₃. (k) HAADF-STEM image and (l) element mapping of Cu-Mg-Al MMO calcined from high-crystallinity Cu-Mg-Al. Molar ratio of Cu:Mg:Al is 3:1:2, 1 M NaOH and 1 M Na₂CO₃. The combined element maps (f, i, l, o) only consist of Cu and Al. All the samples were calcined at 950°C for 3 h.

4.5 Thermodynamic analysis of the inhibition of CuAl₂O₄ by Mg

To predict the inhibiting effect of Mg on the active phase-support interactions, thermodynamic calculations were carried out using FactSage for the calcined system in the absence (Figure 4-15a-b) and presence (Figure 4-15c-d) of Mg.⁶³ The calculations were carried out at 600°C and 1000°C to cover a wide range of potential temperatures for CLC.

The equilibrium compositions have been plotted as a function of the oxygen concentration since the mechanisms of active phase-support interaction for the Cu-Al-O system (which is prone to these interactions) does not become apparent in the fully oxidised state (**Figure 4-15a and b** with x in $\text{Cu} + 2 \text{Al} + x \text{O}_2 = 2.0$). Here, CuO and Al_2O_3 are thermodynamically stable. These two species are also stable in the fully reduced state ($x = 1.5$). However, at intermediate oxidation states or upon oxygen removal during the thermal decomposition of CuO , a mixture of CuAlO_2 , Al_2O_3 and Cu or CuO is thermodynamically stable. This allows for the unfavourable Cu-Al oxide formation, which has been observed in the literature.^{225,226} For the trimetallic-system Cu-Al-Mg-O (**Figure 4-15c and d**), interactions between the active phase and the supporting phase are thermodynamically not favourable in the temperature range 600–1000°C and oxygen concentrations in the range occurring between full reduction and oxidation.²²⁰ Therefore, the thermodynamic calculations in the presence of Mg confirm that MgAl_2O_4 forms and remains stable while the formation of CuAl_2O_4 and CuAlO_2 is inhibited.

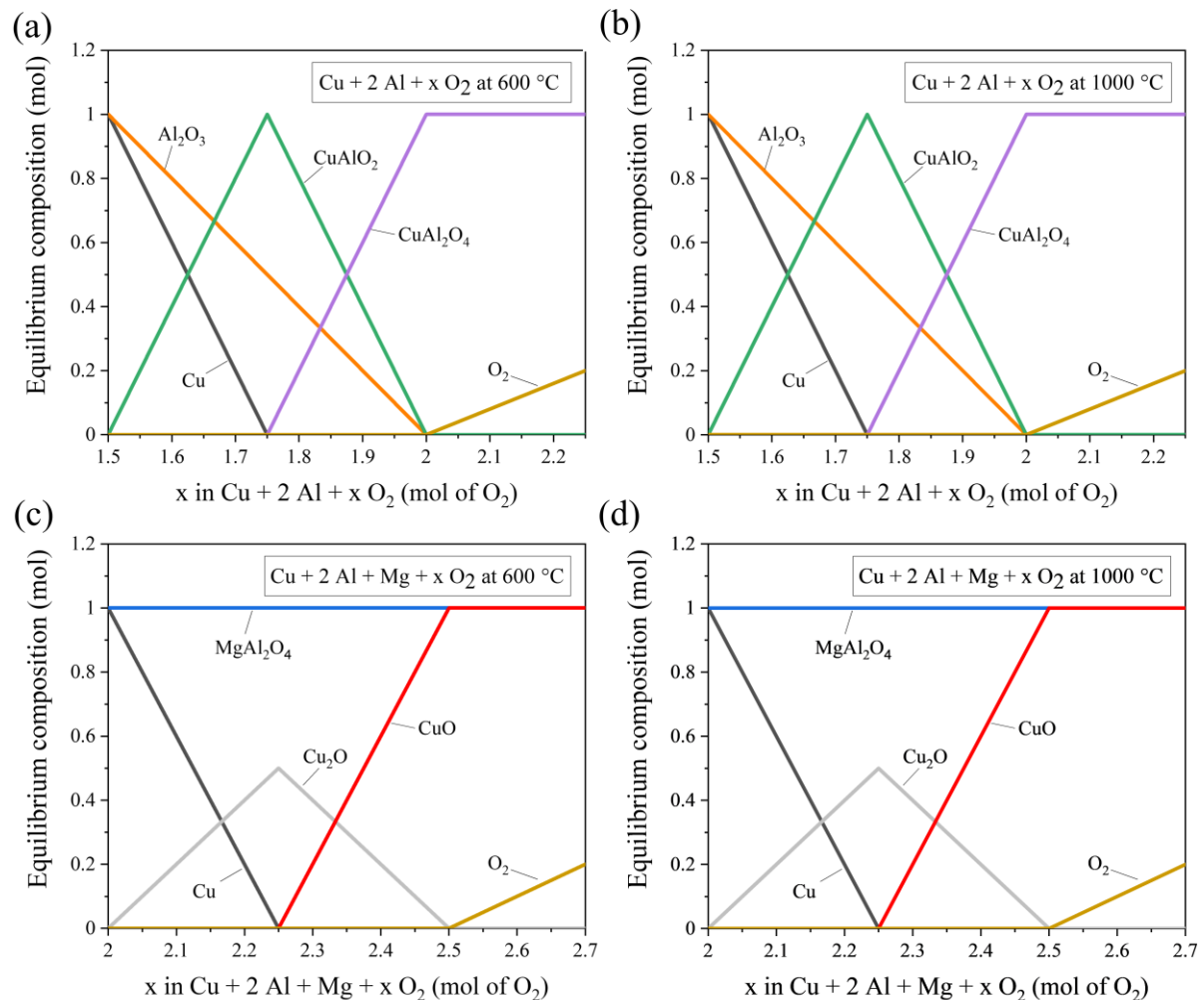


Figure 4-15: Plots of the thermodynamic equilibrium composition as a function of the oxygen concentration. (a, b) Cu-Al-O and (c, d) Cu-Al-Mg-O, and the temperatures (a, c) 600°C and (b, d) 1000°C. Data taken from FactSage and expanded with CuAl_2O_4 using Gibbs free energy data for the systems.

The phase evolution during calcination of the LDHs to MMOs was studied using ex-situ XRD (**Figure 4-16**). To prepare samples for XRD analysis, LDH precursors were calcined for 3 h at temperatures of 400, 600, 800 and 950°C using an air flow of 1 L min⁻¹. The LDH precursors synthesised using NaOH (**Figure 4-16a-b**) have a lower thermal stability than the precursors synthesised using NaOH and Na₂CO₃ (**Figure 4-16c-d**) as shown by the formation of crystalline CuO (sharper peaks) at lower temperatures. The Na-inhibition effect can be clearly seen for Cu-Al LDHs prepared using different co-precipitating agents. For Cu-Al LDHs prepared using NaOH and Na₂CO₃, (**Figure 4-16c**), the formation of CuAl₂O₄ was limited by the presence of Na-containing species, whereas the Cu-Al LDHs prepared using solely NaOH (**Figure 4-16a**), which contained no Na, recorded very intense peaks related to CuAl₂O₄. From the thermodynamic calculations in **Figure 4-15**, the formation of spinel phases is feasible at 600°C. However, no peaks associated with spinel phases were observable in the XRD patterns at this temperature. Although, these peaks may have been obscured by the broad peaks associated with CuO at this temperature. The peaks associated with spinel phases did appear in the XRD patterns for materials calcined at 800°C, which also contained sharper peaks associated with CuO.

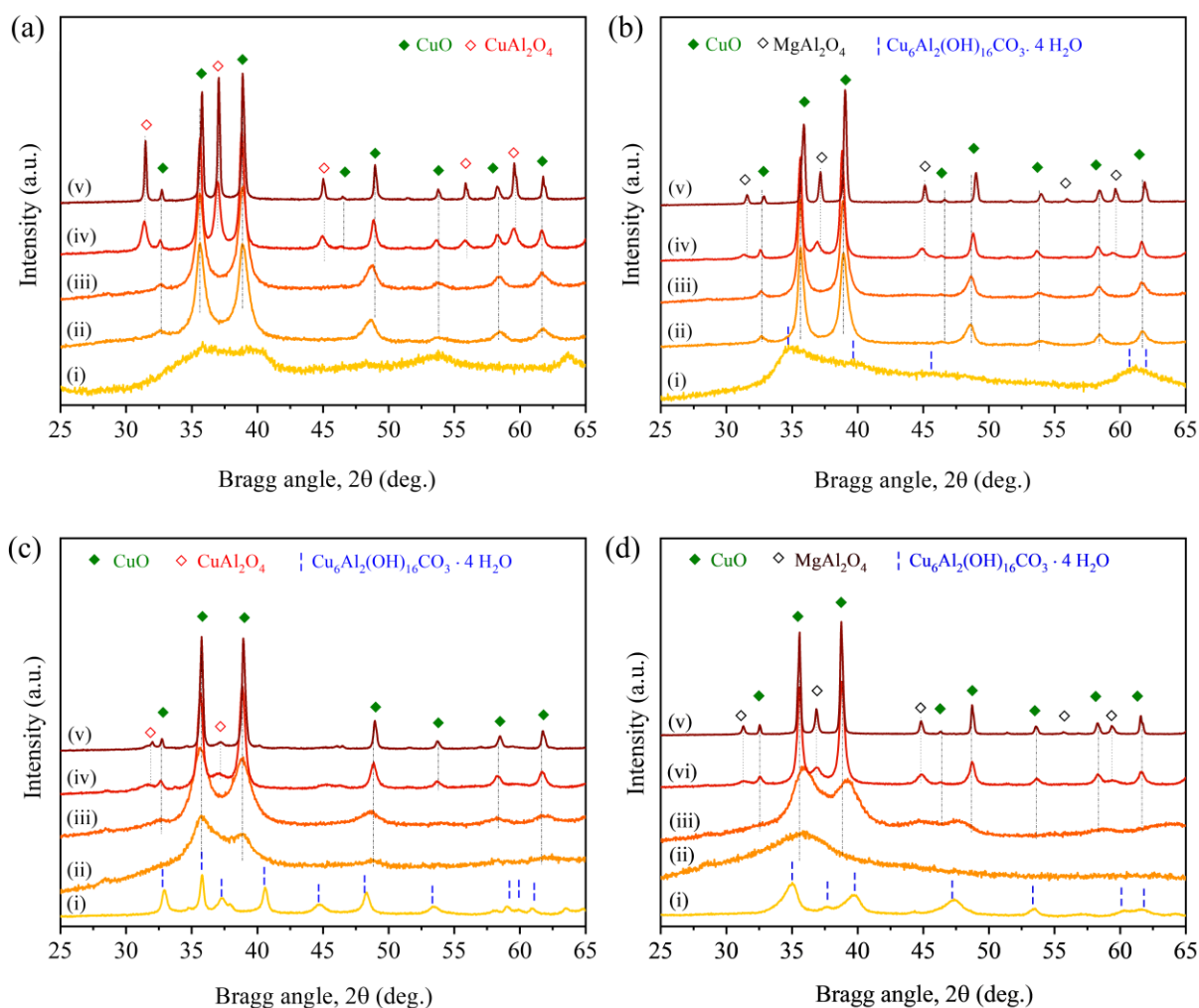


Figure 4-16: The phase composition as a function of the calcination temperature. (a) Cu-Al LDH with a Cu:Al molar ratio of 3:2, with co-precipitating agent of 2 M NaOH, (b) Cu-Mg-Al LDH with a Cu:Mg:Al molar ratio of 3:1:2, with co-precipitating agent of 2 M NaOH, (c) Cu-Al LDH with a Cu:Al molar ratio of 3:2, with co-precipitating agent of 1 M NaOH + 1 M Na₂CO₃; (d) Cu-Mg-Al LDH with a Cu:Mg:Al molar ratio of 3:1:2, with co-precipitating agent of 1 M NaOH + 1 M Na₂CO₃. The treatment temperatures were the following: (i) room temperature, (ii) 400°C, 3 h (iii) 600°C, 3 h (iv) 800°C, 3 h (v) 950°C, 3 h. The reference crystalline patterns are: CuO: JCPDS 80-1268, CuAl₂O₄: JCPDS 76-2295, MgAl₂O₄: JCPDS 73-1959, Cu₆Al₂(OH)₁₆CO₃·4H₂O: JCPDS 37-0630.

4.6 Concluding remarks

This chapter investigated the introduction of Mg into the Cu-Al LDH system. Two series of materials were produced, (i) LDHs co-precipitated using 1 M NaOH and 1 M Na₂CO₃, and (ii) LDHs co-precipitated using 2 M NaOH. For each series of materials, the molar ratio of Cu:Mg:Al was 3:x:2, where x varied from 0 to 1 in steps of 0.2, and a range of characterisation techniques was performed.

For all LDHs synthesised, the XRD spectra showed that the LDH structure was successfully obtained (**Figure 4-1** and **Figure 4-6**). For the LDHs produced using Na₂CO₃ and NaOH, the XRD spectra less closely resembled Cu-Al LDHs and more closely resembled Mg-Al LDHs with an increase in the loading of Mg. This indicates that Mg was successfully incorporated into the LDH structure (**Figure 4-1**). In addition, the Na content in the LDH precursors and derived MMOs was observed to decrease with increasing amounts of Mg (**Figure 4-2** and **Table 4-1**).

Thermodynamic calculations determined that the formation of insoluble Na species (i.e. dawsonite) was thermodynamically suppressed in the presence of Mg. The other possible Na species were either soluble or predicted to remain dissolved in the solution, which allowed for their removal from the system during washing. For the LDHs synthesised using solely NaOH, the results of ICP and XRF showed that no Na was retained in the material after washing. From the thermodynamic calculations, the formation of dawsonite requires the presence of CO₃²⁻. Therefore, Na was not retained in the LDH or MMOs for any Mg loading.

Ex-situ XRD was performed to study the evolution of the crystalline phases formed during the calcination of the LDHs to MMOs. The LDHs precipitated using NaOH (**Figure 4-16a-b**) were found to be less thermally stable than the precursors synthesised using NaOH and Na₂CO₃ (**Figure 4-16c-d**). The formation of significant quantities of deleterious CuAl₂O₄ spinel was observed in the temperature-evolved XRD patterns for the Cu-Al LDHs prepared using NaOH (**Figure 4-16c**) but not in the patterns of the Cu-Al LDH precursors produced using NaOH and Na₂CO₃ (**Figure 4-16a**) due to the Na stabilisation effect, as observed in the literature.¹⁵⁶

HAADF-STEM imaging analysis and EDS elemental mapping was carried out to compare the elemental dispersion and morphology of the MMOs prepared using different synthesis conditions (**Figure 4-14**). A summary of the findings for each LDH material synthesised in this chapter is shown in **Table 4-6**.

Table 4-6: Summary of findings regarding Cu-Al and Cu-Mg-Al LDHs prepared *via* co-precipitation using NaOH and Na₂CO₃ or NaOH.

MMO	Co-precipitating agent	Molar ratio of Cu:Mg:Al	Comments and observations
1	2 M NaOH	3:0:2	<ul style="list-style-type: none"> • XRF: zero Na content • XRD: low crystallinity LDH precursor • EDS: poor dispersion of Cu and Al due to the phase separation of CuO and CuAl₂O₄
2	2 M NaOH	3:1:2	<ul style="list-style-type: none"> • XRF: zero Na content • XRD: low crystallinity LDH precursor • EDS: dense aggregation of nanoparticles and the formation of large CuO particles.
3	1 M NaOH and 1 M Na ₂ CO ₃	3:0:2	<ul style="list-style-type: none"> • Previous work by Song <i>et al.</i>¹⁵⁶ • XRF: high Na content • XRD: high crystallinity LDH precursor • EDS: dense aggregation of nanoparticles and the formation of large CuO particles
4	1 M NaOH and 1 M Na ₂ CO ₃	3:1:2	<ul style="list-style-type: none"> • XRF: zero Na content • XRD: high crystallinity LDH precursor • EDS: fine CuO nanoparticles dispersed in an amorphous matrix

The Mg introduced into the Cu-Al LDH system is expected to perform a similar role as the Na-rich phases in the previously studied Cu-Al LDHs by inhibiting the formation of deleterious CuAl₂O₄ upon calcination and during redox cycling. Based on the observations in **Table 4-6**, the redox performance of MMOs derived from LDHs with a Cu:Mg:Al molar ratio of 3:1:2 synthesised using NaOH + Na₂CO₃ (**Table 4-6**, sample 4) will be investigated in the next chapter and compared against MMOs derived from LDHs with a Cu:Mg:Al molar ratio of 3:0:2 synthesised using solely NaOH (**Table 4-6**, sample 1).

Chapter 5

Long term redox cycling of Cu-Mg-Al layered double hydroxide-derived oxygen carriers in thermogravimetric and fluidised bed systems

5.1 Introduction

A challenge for chemical looping processes is the development of high-performance sintering-resistant oxygen carriers that can reversibly transfer oxygen over multiple redox cycles.²²⁷ CuO-based mixed oxides have been studied extensively owing to their high oxygen capacity (CuO/Cu: 0.201 gO₂/gCuO; CuO/Cu₂O: 0.101 gO₂/gCuO), fast rates of reaction, and absence of thermodynamic limitations for the complete combustion of fuels. To increase their mechanical strength, CuO is often supported on Al₂O₃.¹⁰⁸ However, the attrition and agglomeration of these materials leads to performance degradation.²²⁸ Furthermore, over extended periods of redox cycling, the CuO reacts with Al₂O₃ to form the CuAl₂O₄ spinel oxides.²²⁹ At typical CLOU operating temperatures, CuAl₂O₄ has a lower oxygen equilibrium partial pressure, slower oxygen release rates, and a lower oxygen release capacity than pure CuO.¹⁰⁹ Thus, it is desirable to develop a material that inhibits the formation of CuAl₂O₄. Co-precipitation has been used to prepare Cu-Al mixed oxides;⁹⁷ however, it remains difficult to control the Na content in the precursor for effective stabilisation of the CuO phase.

In this chapter, the long-term cycling performance of CuO-based MMOs developed from LDH precursors was studied using TGA and FBR systems. In chapter 4, LDH precursors were produced using different molar ratios of Cu:Mg:Al and co-precipitating agents. The chemical and structural evolution of these LDHs to MMOs upon calcination was investigated and two MMOs were selected for further testing and characterisation in this chapter. The MMOs selected for analysis are derived from

(i) LDHs with a Cu:Mg:Al molar ratio of 3:1:2 co-precipitated using 1 M NaOH and 1 M Na₂CO₃, and
(ii) LDHs with a Cu:Mg:Al molar ratio of 3:0:2 co-precipitated using 2 M NaOH. Upon calcination, the LDHs with a Cu:Mg:Al molar ratio of 3:1:2 and 3:0:2 form CuO/MgAl₂O₄ and CuO/CuAl₂O₄ MMOs, respectively. The MMOs were cycled under CLOU (oxygen release in N₂) and CLC (reduction in CO/N₂) modes to investigate their long-term chemical stability during redox cycling and the effectiveness of the Mg stabilisation strategy. The MMOs were also tested in an FBR. In addition to the thermal and chemical stresses experienced in a TGA, particles in a FBR are also exposed to mechanical stresses due to high-velocity collisions with other particles and the reactor wall. From the literature review conducted in chapter 2, the average crushing strength of the Al₂O₃-supported oxygen carriers was 2.7 N compared to 1.6 N for the MgAl₂O₄ oxygen carriers. The 1.6 N for the MgAl₂O₄ oxygen carriers is below the 2 N threshold Rydén *et al.* recommended for survivability in fluidised systems.⁸⁹ Therefore, the synthesis procedure was altered to increase the crushing strength of the oxygen carriers used in the FBR.

One promising application of CLC is for industrial gas purification. An example is argon recycling in the solar photovoltaic manufacturing industry, where a significant amount of high-purity argon gas is used in the fabrication of silicon wafers for solar panels. The exhaust gas stream usually contains contaminated gases such as CO and H₂ at several thousand ppm, along with traces of other combustible gases. Chemical looping combustive purification (CLCP) has been developed to remove these contaminants to below ppm levels. The oxygen carriers oxidise the combustible gases to CO₂ and H₂O, which are subsequently removed by molecular sieve sorbents. The reduced oxygen carriers are then regenerated by oxidation in air. CLCP has been successfully scaled up for argon or helium recovery and purification in industry.²³⁰ In a broad context, this principle can be applied to replace conventional regenerative thermal oxidisers operated at high-temperature for clean-up of low-concentration hydrocarbons, such as methane from landfills or volatile organic compounds, at lower temperatures. The performance of MMOs with a 3:1:2 molar ratio of Cu:Mg:Al as oxygen carriers for CLCP were investigated using an FBR and a feed gas of low concentrations of CO or CH₄.

5.2 Redox cycling in a thermogravimetric analyser

5.2.1 Methods

The MMOs initially investigated in this chapter were prepared from LDH precursors synthesised *via* co-precipitation at a constant *pH* value of 9.5. The Cu-Al MMOs (molar ratio 3:2) were synthesised using 2 M NaOH and the Cu-Mg-Al MMOs (molar ratio 3:1:2) were synthesised using 1 M NaOH and 1 M Na₂CO₃. After drying the precipitate, the LDHs were calcined in a horizontal tube furnace at 975°C for 6 h in an airflow of 1 L min⁻¹ using a heating rate of 15°C min⁻¹. After calcination, the solids were crushed and sieved into the desired particle size ranges.

Thermogravimetric analysis was carried out in a Q5000 (TA Instruments, set-up detailed in chapter 3) to evaluate the chemical stability of the MMOs. In a typical experiment, 3–4 mg of the calcined MMOs (size fraction 300–425 μm) were placed in a platinum crucible (1.5 mm high and 9.8 mm in diameter) and cycled for 100 redox cycles. For CLOU experiments, a two-step cycle was used,

- (i) Oxygen release in N_2 for 5 min,
- (ii) Re-oxidation in air for 3 min.

For CLC experiments, a four-step cycle was used,

- (i) Reduction in 5 vol% CO balanced with N_2 for 7 min,
- (ii) N_2 purge for 1 min to prevent gas mixing of the reducing and oxidising gases,
- (iii) Re-oxidation in air for 3 min,
- (iv) N_2 purge for 1 min.

All experiments were performed at 900 $^{\circ}\text{C}$, and the total gas flow rate was kept constant at 200 ml min^{-1} (SATP). The observed oxygen release capacity (CLOU) and oxygen storage capacity (CLC) were defined as the difference of the relative weights at the beginning and the end of the oxygen release or reduction period, respectively.

5.2.2 Result of long-term redox cycling in a thermogravimetric analyser

Isothermal redox reactions were performed in a TGA at 900 $^{\circ}\text{C}$ to investigate the chemical stability and reactivity of the MMOs. **Figure 5-1a** shows the weight change of the MMOs over 100 redox cycles between CuO and Cu_2O , which were performed by oxygen release in N_2 and re-oxidation in air (CLOU). The chemical stability of the MMOs was further investigated by cycling under CLC mode, with deep reduction of CuO to Cu under 5 vol% CO/ N_2 , followed by re-oxidation in air. The oxygen storage capacity of the MMOs over 100 CLC cycles is shown in **Figure 5-1b**. The first cycle weight profiles for CLOU and CLC cycling are shown in **Figure 5-1c** and **Figure 5-1d**, respectively.

From **Figure 5-1c**, the Cu-Mg-Al MMOs showed faster rates of oxygen release and oxidation than those observed for the Cu-Al MMOs (consisting of CuO and CuAl_2O_4). The Cu-Mg-Al MMOs showed almost no deactivation over 100 continuous redox cycles, with the oxygen release capacity remaining constant at 6.4 wt% (**Figure 5-1a**). In comparison, the Cu-Al MMOs were found to deactivate very quickly during CLOU redox-cycling, with the oxygen release capacity decreasing from an initial 5 wt% to 3.9 wt% after 100 cycles. The decline of the oxygen release capacity of the Cu-Al MMO can mainly be attributed to the formation of $\text{CuAl}_2\text{O}_4/\text{CuAlO}_2$, which have significantly slower rates of oxygen release and re-oxidation than $\text{CuO}/\text{Cu}_2\text{O}$,²³¹ as observed in **Figure 5-1c**. Interestingly, the oxygen storage capacity of each MMO tested under full reduction and re-oxidation (i.e. redox between CuO

and Cu) remained stable over 100 cycles (**Figure 5-1d**), *i.e.* ~14.1 wt% and 13 wt% for the Cu-Al and Cu-Mg-Al MMOs, respectively, and will be discussed in section 5.2.4.

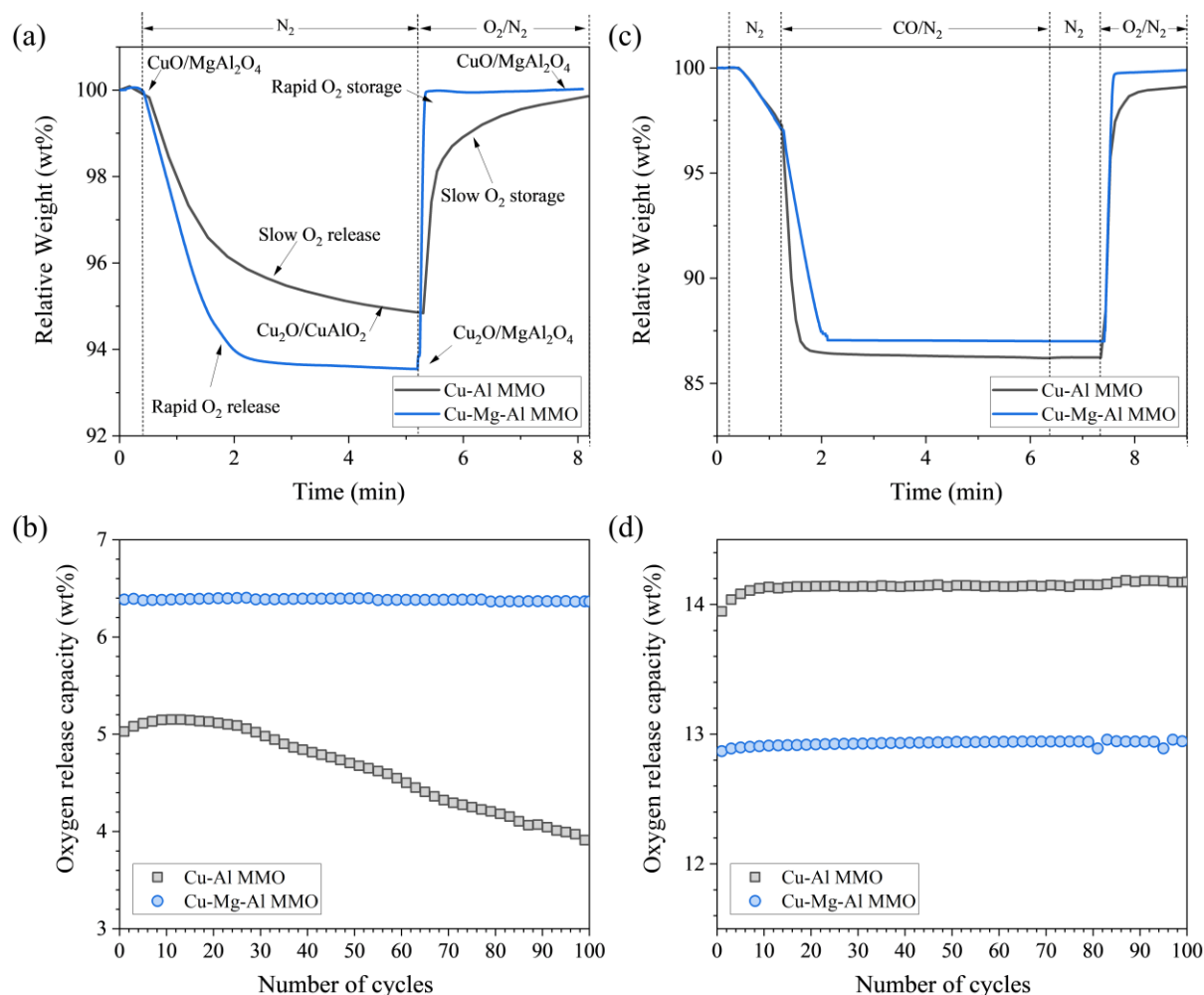


Figure 5-1: Redox cycling of Cu-Al MMO and Cu-Mg-Al MMO in a TGA at 900°C. (a) relative weight profiles for the first CLOU cycle, phase change between CuO and Cu_2O . The oxygen release was carried out under N_2 for 5 min, followed by re-oxidation in air for 3 min. (b) oxygen release capacities of the MMOs over 100 CLOU redox cycles. (c) relative weight profiles for the first CLC cycle, phase change between CuO and Cu. The reduction was carried out for 7 min in 5 vol% CO balanced with N_2 , followed by a 1 min N_2 purge. The samples were then re-oxidised for 3 min in air, followed by a further 1 min in pure N_2 . (d) oxygen storage capacities of the MMOs over 100 CLC redox cycles.

The Cu-Mg-Al MMOs were cycled for an additional 500 CLOU cycles at 900°C to further investigate the effectiveness of the $MgAl_2O_4$ stabilisation strategy. The first and last CLOU cycle profiles are shown in **Figure 5-2a**. The MMOs showed almost no deactivation over 500 continuous redox cycles, *i.e.* neither a significant reduction in observed rates (similar gradients of oxidation and reduction) nor in the

observed oxygen release capacity (6.4 wt%, **Figure 5-2b**). The variation in oxygen release between cycles 225 to 300 was attributed to disturbances in the external lab environment.

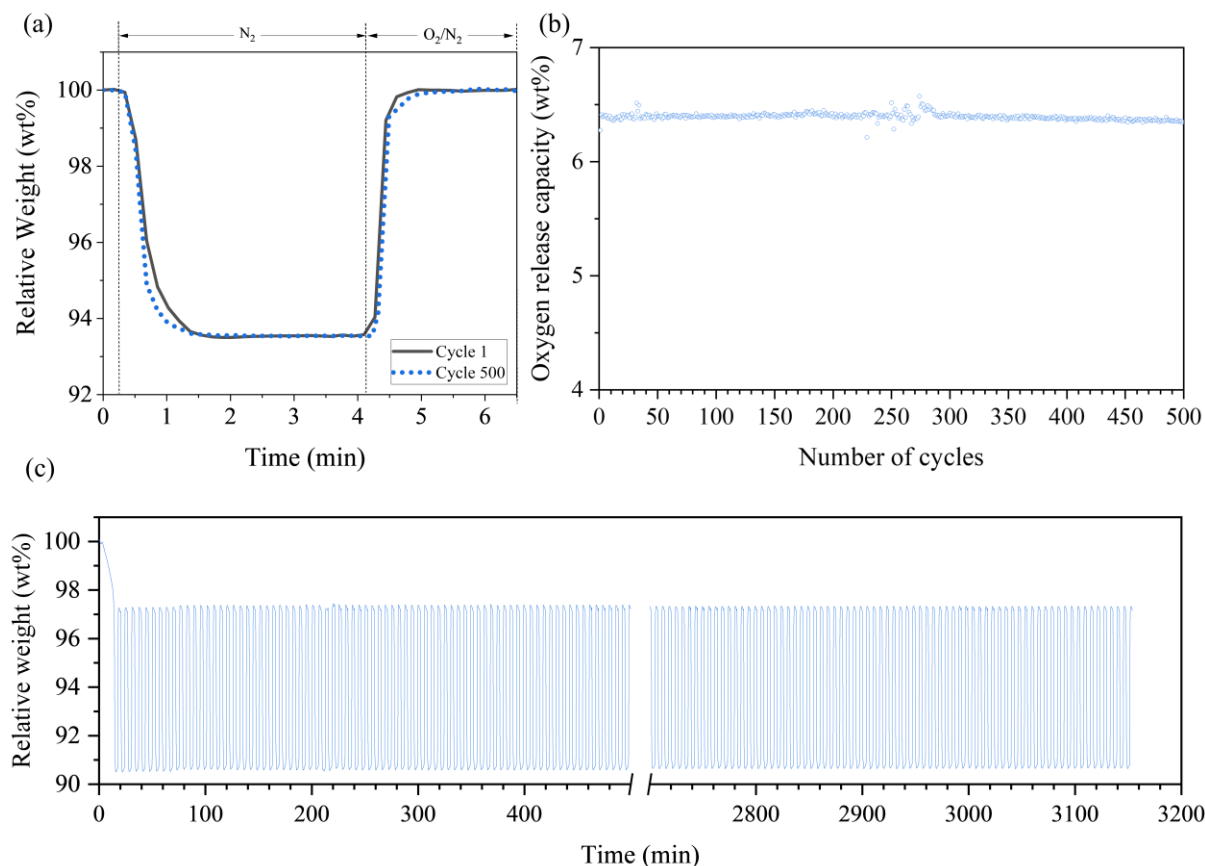


Figure 5-2: TGA profiles of long-term redox cycling of Cu-Mg-Al MMO. (a) relative weight profiles for the first and last CLOU cycle, phase change between CuO and Cu₂O. The oxygen release was carried out under N₂ for 4 min, followed by re-oxidation in air for 2.5 min **(b)** oxygen release capacity over 500 cycles of oxygen release and re-oxidation. **(c)** entire relative weight profile.

5.2.3 Material characterisation

Ex-situ XRD was used to track the phase changes of the Cu-Mg-Al and Cu-Al MMOs during CLOU cycling (**Figure 5-3a** and **b**, respectively). XRD analyses confirmed the chemical stability of CuO/MgAl₂O₄ in the Cu-Mg-Al MMOs during redox cycling (**Figure 5-3a**). Owing to the stabilisation by the MgAl₂O₄ support, CuO decomposed to Cu₂O and regenerated to CuO without forming CuAlO₂. In contrast, the formation of CuAlO₂ over extended redox cycling in the Cu-Al MMOs was confirmed in the cycled samples (**Figure 5-3b**). Interestingly, CuAlO₂ was not observed in the XRD profile of the oxygen release Cu-Al sample. The formation and re-oxidation of CuAlO₂ has been reported to be significantly slower than that of CuO.²³¹ Therefore, it is likely that the CuAlO₂ content in the MMOs

gradually increases over 100 cycles. The oxygen release and re-oxidation reaction mechanisms of the Cu-Al MMOs are discussed in section 5.2.4.

The phase changes of the Cu-Mg-Al and Cu-Al MMO during CLC cycling are shown in **Figure 5-3c** and **d**, respectively. The formation of Cu/MgAl₂O₄ upon reduction and solely CuO/MgAl₂O₄ upon re-oxidation confirmed the chemical stability of the Cu-Mg-Al MMOs during CLC cycling (**Figure 5-3c**). For both CLOU and CLC cycling, the XRD analyses show an increase in the intensity of the peaks associated with MgAl₂O₄ in the cycled sample compared to the fresh sample. This was attributed to the sintering of the MgAl₂O₄ phase. For the Cu-Al samples, XRD analyses confirmed the reduction of the MMO to Cu/Al₂O₃ and re-oxidation to CuO/CuAl₂O₄. Interestingly, the formation of CuAlO₂ was not observed in the cycled sample, which is discussed in section 5.2.4.

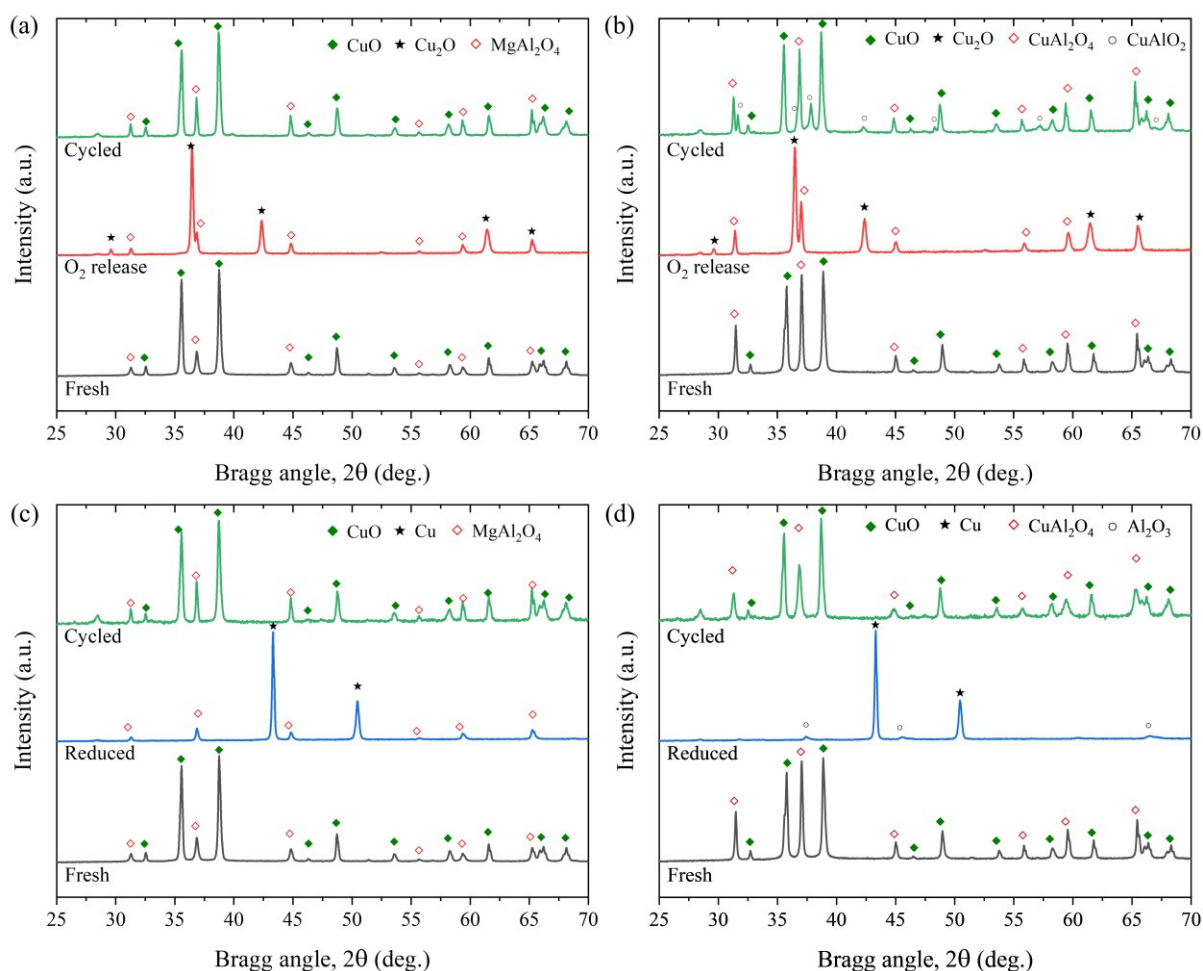


Figure 5-3: XRD patterns of fresh, oxygen released/reduced and cycled Cu-Al MMOs and Cu-Mg-Al MMOs. XRD patterns of (a) Cu-Mg-Al MMOs and (b) Cu-Al MMOs during CLOU cycling in a TGA. XRD patterns of (c) Cu-Mg-Al MMOs and (d) Cu-Al MMOs during CLC cycling in a TGA.

The phase changes of the MMOs during CLOU cycling were also studied using in-situ high-temperature XRD by exposing the MMOs to alternating N₂ and air gas streams at 900°C in a high temperature XRD stage (set-up detailed in chapter 3). The results show the CuO phase disappeared at a similar rate for each material. However, the XRD set-up did not permit the use of high gas flow rates. Therefore, the oxygen released from the sample may not have been effectively swept from the XRD stage, reducing the thermodynamic driving force for oxygen release and obscuring differences between the rates of oxygen release for the two samples. The intensity of the MgAl₂O₄ and CuAl₂O₄ phases remained relatively unchanged during cycling (**Figure 5-4**). However, any change in the intensity of the CuAl₂O₄ peak at $2\theta = 36.6^\circ$ may have been obscured by the growth of the Cu₂O phase (intense peak at $2\theta = 36.4^\circ$). In addition, the low gas flow rates may have resulted in an oxygen partial pressure across the stage that was too high for the formation of CuAlO₂ to occur.

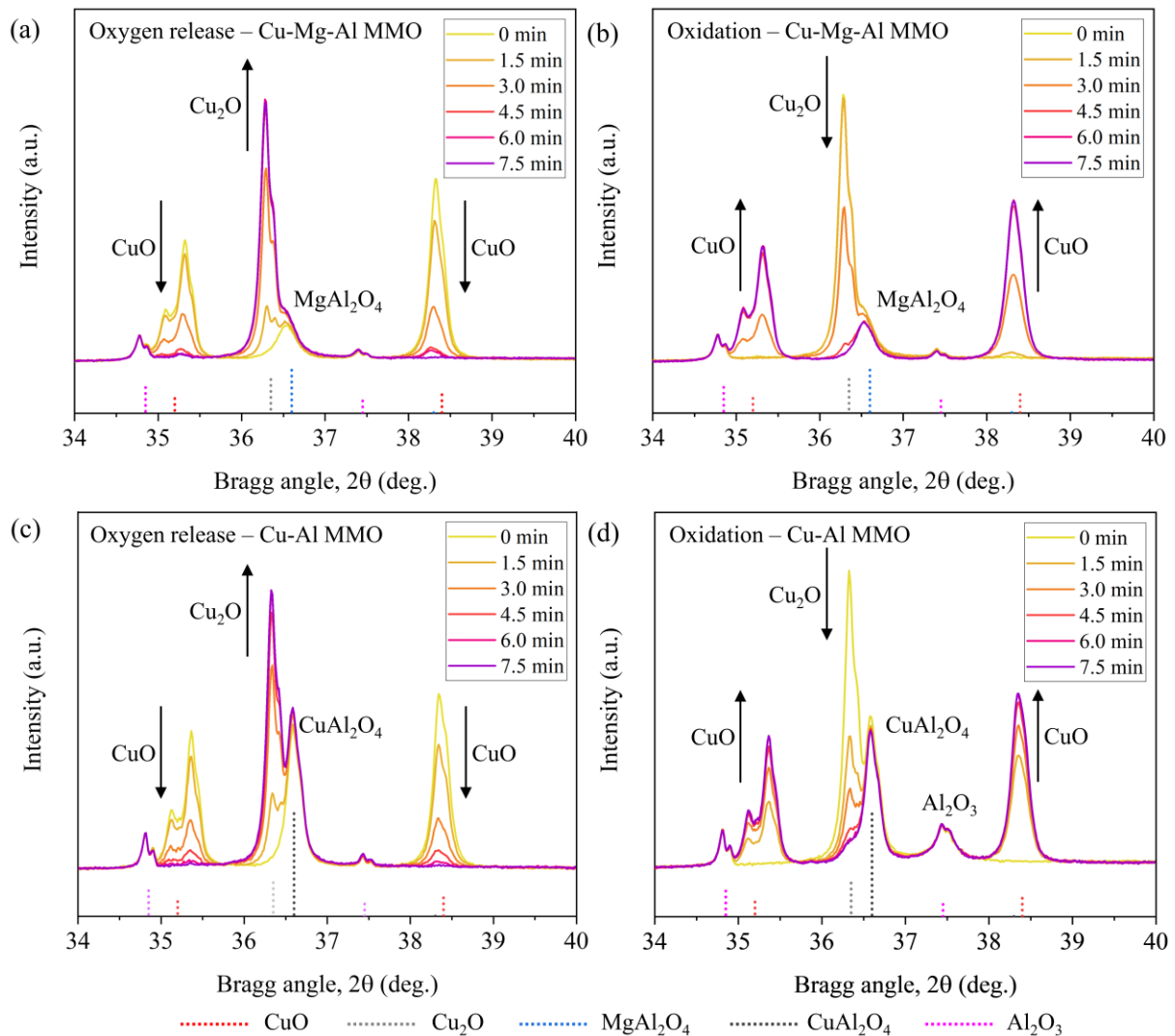


Figure 5-4: In situ high temperature XRD analyses. XRD profiles of Cu-Mg-Al MMO with (a) oxygen release in N₂ and (b) oxidation in air. XRD profiles of Cu-Al MMO, with (c) oxygen release in N₂ and (d) re-oxidation in air. All runs were performed at 900 °C.

5.2.4 Thermodynamic analysis of the Cu-Al MMO system

The thermodynamics of the Cu-Al-O system was studied to improve the understanding of the redox reactions of the Cu-Al MMO during cycling in the TGA. A phase diagram was produced using the Gibbs free energy data reported by Jacob & Alcock¹⁰⁹ for the Cu-Al system with a molar ratio of 1:1 (**Figure 5-5**).

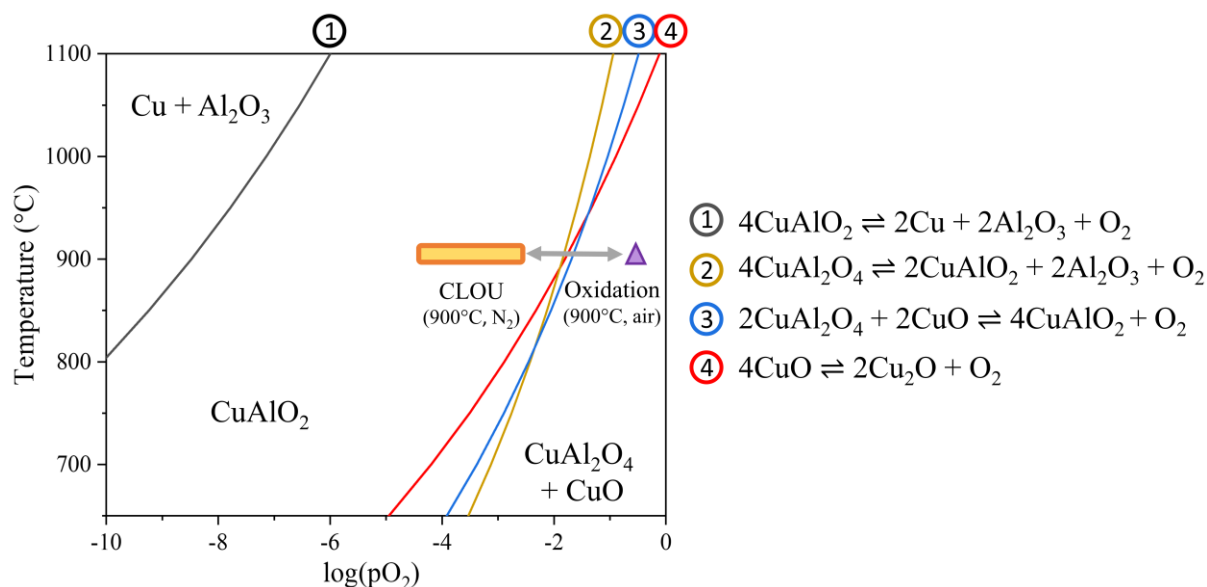


Figure 5-5: Cu-Al-O system equilibrium phase diagram for a 1:1 molar mixture of CuO and Al₂O₃. The region for oxygen release and re-oxidation during CLOU are demarcated, calculated using thermodynamic data from Jacob & Alcock.¹⁰⁹

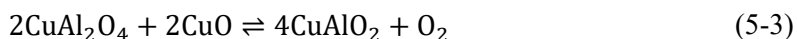
From **Figure 5-5**, calcination of Cu-Al LDH precursor in air at 975°C ($\log(p_{\text{O}_2})=0.68$) produces MMOs of CuO and CuAl₂O₄, formed through reaction (5-1), as confirmed by XRD analysis (**Figure 5-3b**, fresh).



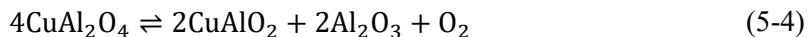
During redox cycling at 900°C, the oxygen partial pressure is sufficiently low (**Figure 5-5**, CLOU demarcation) for CuO to decompose to Cu₂O and oxygen through reaction (5-2),



The CuO can also react with CuAl₂O₄ to form CuAlO₂ and release oxygen through reaction (5-3),



The CuAl_2O_4 could also react to form CuAlO_2 and Al_2O_3 and release oxygen through reaction (5-4),



Although all three reactions are thermodynamically feasible, the rapid oxygen release of CuO (reaction (5-2)) observed in the in-situ XRD experiments (**Figure 5-4c**) suggests that the formation of CuAlO_2 is unlikely to occur *via* solid-solid reaction (5-3).²³¹ The absence of CuAlO_2 in the XRD pattern of the O_2 released sample (**Figure 5-3b**) and appearance in the cycled material pattern (**Figure 5-3b**) indicates that reaction (5-4) is kinetically limited. Therefore, oxygen release from the Cu-Al MMOs is likely to occur in two stages, (i) rapid oxygen release from $\text{CuO/CuAl}_2\text{O}_4$ *via* reaction (5-2), followed by (ii) oxygen release *via* the much slower reaction (5-4).

For re-oxidation, the CuAlO_2 peaks in the cycled material XRD pattern (**Figure 5-3b**) confirm some of the initial active CuO was not regenerated during re-oxidation. This is confirmed experimentally by the decrease in experimental oxygen release capacity observed over 100 redox cycles in a TGA (**Figure 5-1b**). The CuAlO_2 peaks in the cycled materials indicates that oxidation of CuAlO_2 is kinetically limited. Therefore, the active CuO and initial oxygen release capacity could be recovered if the time for re-oxidation was sufficiently increased. However, this would severely impact the operation and economics of the process.

While the oxygen release capacity of the Cu-Al MMOs was observed to decrease over 100 CLOU cycles, the oxygen storage capacity remained constant over 100 CLC cycles in a TGA (**Figure 5-1b**). In addition, no peaks associated with CuAlO_2 were observed in any of the XRD profiles (**Figure 5-3d**). The reduction of Cu-Al MMOs was found to produce solely Cu and Al_2O_3 , and the cycled samples contained CuO and CuAl_2O_4 . Therefore, it is likely that during re-oxidation, the formation of CuO occurred *via* the fast reactions, reaction (5-5) and the reverse of reaction (5-2), and the formation of CuAl_2O_4 occurred *via* reaction (5-1). The rates of these reactions are likely to occur at such a rate that the formation of any CuAlO_2 is inhibited, and therefore the re-oxidation rate and oxygen storage capacities were largely unchanged over long-term redox cycling in the TGA.



5.3 Redox cycling in a fluidised bed reactor

5.3.1 Methods

In addition to the redox experiments in the TGA, an FBR was used to investigate the long-term cycling performances of the MMOs (set-up detailed in chapter 3). In addition to the thermo-chemical stresses experienced in the TGA due to chemical reactions, the MMO particles in the FBR are also exposed to mechanical stresses owing to collisions of particles with other particles and the reactor walls. In a typical FBR experiment, 15 g of MMOs in the particle size range of 300–425 μm were used. Inert cycles were carried out by repeated automated gas switching between N_2 and air in the absence of the MMO particles to generate a baseline gas switching concentration profile. Then, the MMOs were added to the reactor and cycled for 100 redox cycles at 900°C. Two cycling modes were used to test the stability of the metal oxides: partial cycling and full cycling. Partial cycling comprised of five 20-cycle segments consisting of 19 short cycles where the oxygen release period (360 s) was not long enough to fully decompose the MMOs, followed by one longer cycle where the oxygen release period (1800 s) allowed complete oxygen release from the oxygen carriers. The full cycling mode consisted of 100 cycles of oxygen release and re-oxidation, where the time was sufficient for the complete oxygen release and re-oxidation during each cycle. The molar fraction of oxygen calculated from the gas analyser measurements of the gas leaving the reactor during inert cycles ($y_{\text{O}_2, \text{inert}}$) and during redox cycling of the oxygen storage materials ($y_{\text{O}_2, \text{sample}}$) were used to calculate the conversion by,

$$X_{\text{O}_2, \text{release}} = \frac{MW(\text{O}_2)}{m_{\text{OC}} R_{\text{OR}}} \int_0^t n_{\text{out}} (y_{\text{O}_2, \text{sample}} - y_{\text{O}_2, \text{inert}}) dt \quad (5-6)$$

where m_{OC} is the mass of oxygen storage materials loaded into the reactor (g); n_{out} is the molar flow rate of the effluent gas in mol s^{-1} ; $MW(\text{O}_2)$ is the relative molecular mass of oxygen (32 g mol^{-1}) and R_{OR} is the gaseous oxygen release capacity determined by thermogravimetric analysis (wt%).

The performances of the MMOs as oxygen carriers for CLCP were also analysed in an FBR. Two gaseous fuels were investigated, 1 vol% CH_4/N_2 at 800°C, and 2 vol% CO/N_2 at 400 and 800°C. Low volume fractions of the reactive gases were used to simulate industrial gases with low amounts of combustible contaminants.²³⁰ In a typical FBR experiment, 15 g of MMOs in the particle size range of 300–425 μm were used. Inert cycles were carried out by repeated automated gas switching between gaseous fuel, N_2 purge, air, and another N_2 purge without the presence of the samples. Then, the MMOs were added to the reactor and cycled for 20 redox cycles of reduction to Cu and re-oxidation to CuO . For CLCP cycling, one cycle consisted of a reduction period of 45 min, followed by an N_2 purge (2.5 min) to prevent the mixing of oxygen and the reducing gas, oxidation in 10 vol% O_2 (12 min), and another N_2 purge (2.5 min). The total gas flow rates were 2.25 L min^{-1} and 2 L min^{-1} at SATP for the CLCP experiments using CO at 400 and 800°C, respectively, and 1 L min^{-1} for CH_4 at 800°C. The

conversion of metal oxides (CuO to Cu) during the reduction period was calculated by the ratio of the total amount of oxygen reacted with gaseous fuel to the total amount of available oxygen in the oxygen carriers. The conversion of the MMOs for CO ($X_{red,CO}$) and CH₄ reduction (X_{red,CH_4}) are:

$$X_{red,CO} = \frac{MW(O_2)}{2m_{OC}R_{OS}} \int_0^t n_{out} y_{CO_{2,out}} dt \quad (5-7)$$

$$X_{red,CH_4} = \frac{2MW(O_2)}{m_{OC}R_{OS}} \int_0^t n_{out} y_{CO_{2,out}} dt \quad (5-8)$$

where R_{OS} is the oxygen storage capacity determined by thermogravimetric analysis (wt%). $y_{CO_{2,out}}$ is the mole fraction of CO₂ in the product gas.

5.3.2 Results of long-term redox cycling in a fluidised bed reactor

To assess their chemical, thermal and mechanical stabilities, Cu-Al MMOs and Cu-Mg-Al MMOs were tested for 100 cycles of partial oxygen release and re-oxidation in an FBR at 900 °C, with one cycle of full oxygen release and re-oxidation approximately every 20 cycles. The oxygen profiles during the full oxygen release and re-oxidation cycles for the Cu-Al MMOs are shown in **Figure 5-6a-b**, respectively, and the conversion over 100 cycles is shown in **Figure 5-6e**. The Cu-Al MMOs experienced severe attrition during the early stages of operation (<0.70 conversion during the first full oxygen release phase); therefore, the operation of the FBR ceased after 9 cycles to prevent fouling of the downstream equipment (*i.e.* the gas analysers). The oxygen profiles for the Cu-Mg-Al MMOs are shown in **Figure 5-6c-d**. The area between the inert and oxygen profiles for each cycle is proportional to the conversion of the oxygen carriers. From **Figure 5-6c**, the time required for full oxygen release of the MMO inventory decreases from around 1700 to 1100 s over 100 cycles. Accordingly, the calculated conversion during the full redox cycles decreased from 0.98 to ~ 0.83 over the first 30 cycles, where it remained stable until cycle 80, and the conversion again decreased to 0.62 at cycle 100 (**Figure 5-6e**). The decrease in overall conversion from 0.98 to 0.62 for the Cu-Mg-Al MMO was also attributed to the attrition of the oxygen carriers.

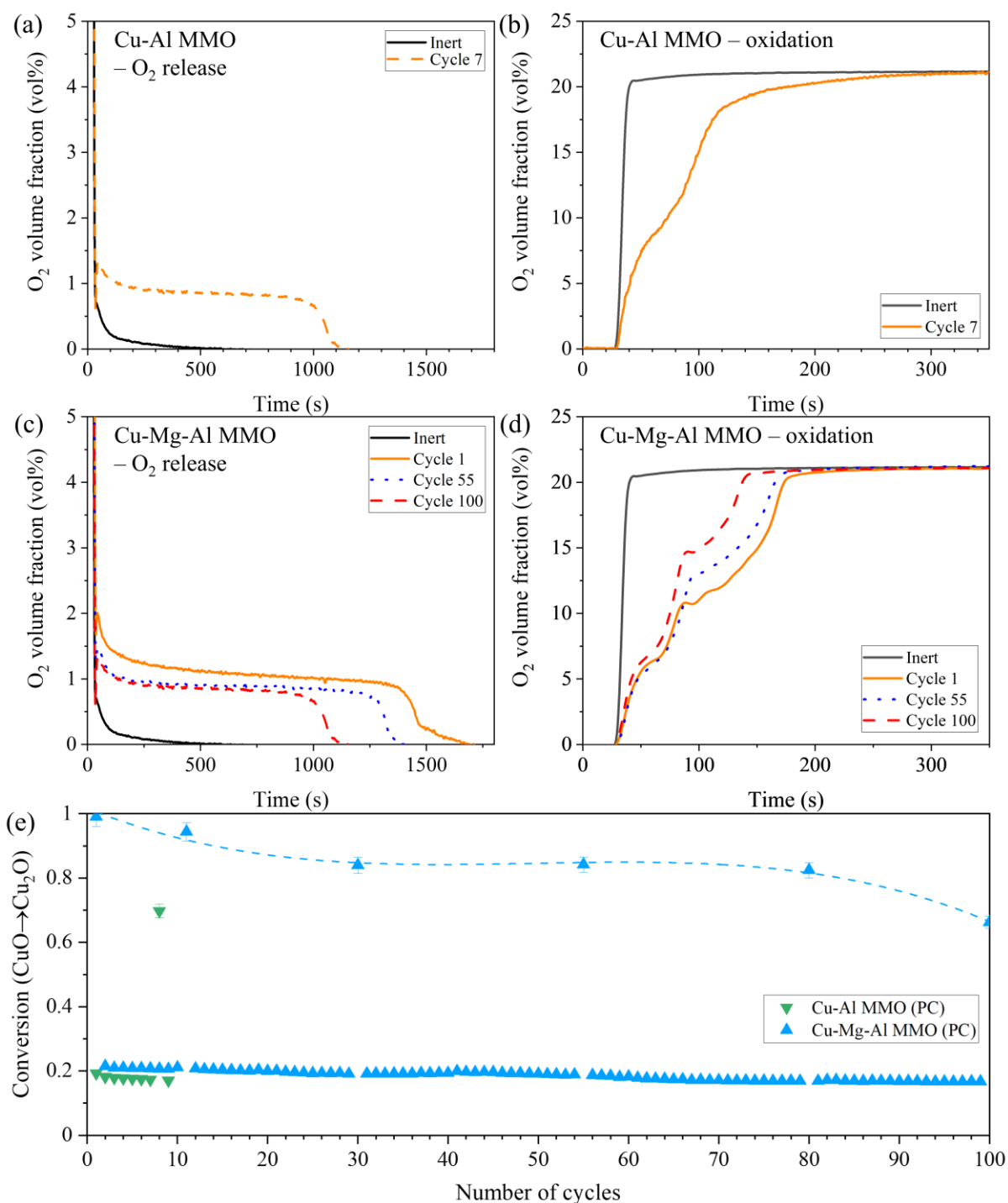


Figure 5-6: Redox cycling of Cu-Al and Cu-Mg-Al in an FBR at 900°C. Oxygen profiles during full cycle periods for (a) oxygen release and (b) oxidation of the Cu-Al MMOs. Oxygen profiles during full cycle periods for (c) oxygen release and (d) oxidation of the Cu-Mg-Al MMOs. (e) conversion of the MMOs. Where PC is partial cycling (100 cycles of partial oxygen release and oxidation with full cycles every 20 cycles), and FC is full cycling (100 cycles of full oxygen release and oxidation).

5.3.3 Optimisation of mechanical properties of the Cu-Mg-Al mixed metal oxides

The high attrition rate of the Cu-Mg-Al MMOs during operation in scaled-up fluidised chemical looping systems would be uneconomical considering the higher cost of the preparation procedure compared to other methods, such as spray drying. Furthermore, the large amounts of fines generated could cause damage to downstream process equipment. Therefore, the mechanical strength of the particles were optimised in order to use the LDH-derived MMOs as oxygen carriers in FBRs. Generally, there is an inverse correlation between the porosity and crushing strength of a particle. Therefore, MMOs with lower porosities were targeted to obtain particles with higher crushing strengths. New Cu-Mg-Al LDHs (Cu:Mg:Al molar ratio of 3:1:2) were synthesised using a higher *pH* value of 11 during co-precipitation using 1 M NaOH and 1 M Na₂CO₃ as the co-precipitating agent. The Cu-Mg-Al materials in this section will henceforth be referred to as “metals material-*pH*”, *i.e.* the Cu-Mg-Al MMOs synthesised from LDHs co-precipitated at *pH* 9.5 are referred to as Cu-Mg-Al MMO-9.5.

XRD analysis (**Figure 5-8a**), SEM imaging (**Figure 5-9b**) and STEM imaging (**Figure 5-9f**) confirmed the LDH structure and nanoplatelet morphology of the Cu-Mg-Al LDH-11 was obtained. Visual inspection of the platelets showed they were more densely aggregated compared to those of the precursors prepared at the lower *pH* value of 9.5 (**Figure 5-9**). From N₂ adsorption, the pore size distribution was found to narrow and shift to a lower average pore diameter with an increase in the *pH* value (**Figure 5-8b**). The shape of the two isotherms is similar and follows a Type IV hysteresis loop, characteristic of the N₂ physisorption between aggregates of platelets (**Figure 5-8b**).

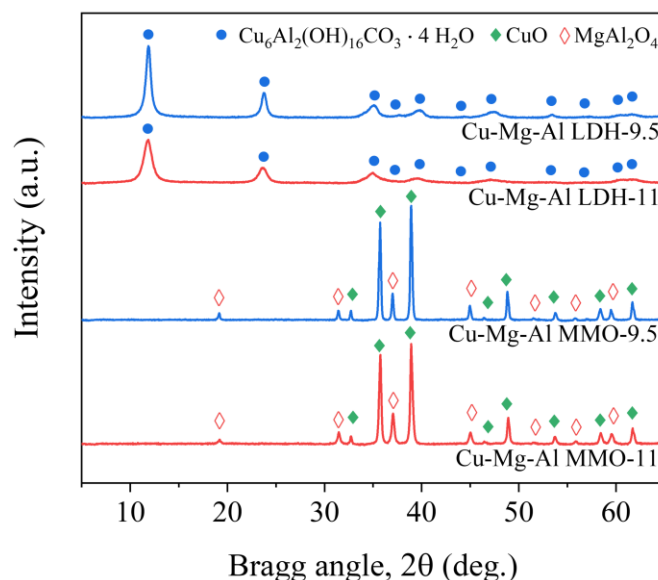


Figure 5-7: XRD patterns of the Cu-Mg-Al LDH precursors co-precipitated at *pH* 9.5 and 11 and derived MMOs.

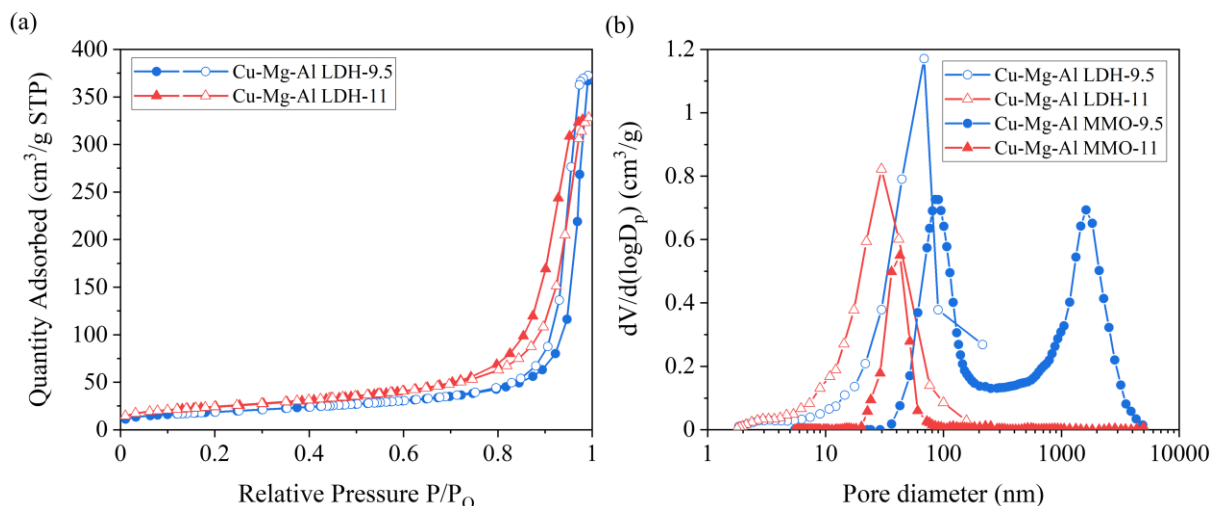


Figure 5-8: Characterisation of the pore structure of Cu-Mg-Al MMO-11. (a) The N_2 adsorption-desorption isotherms and (b) N_2 desorption and MIP pore size distributions for the Cu-Mg-Al LDH precursors and MMOs, respectively.

An increase of the pH value during precipitation from 9.5 ± 0.2 to 11.0 ± 0.2 resulted in the formation of smaller LDH platelets, which further aggregated into dense particles after calcination as observed by SEM (**Figure 5-9c-d**). The porosities of the MMOs were estimated by combining MIP (**Figure 5-8b**) and He pycnometry. The porosity was found to decrease from 74% to 38% when the co-precipitation pH was increased from 9.5 to 11. Furthermore, the crushing strength of the calcined particles increased from 2.3 ± 1.1 N to 5.7 ± 2.6 N.

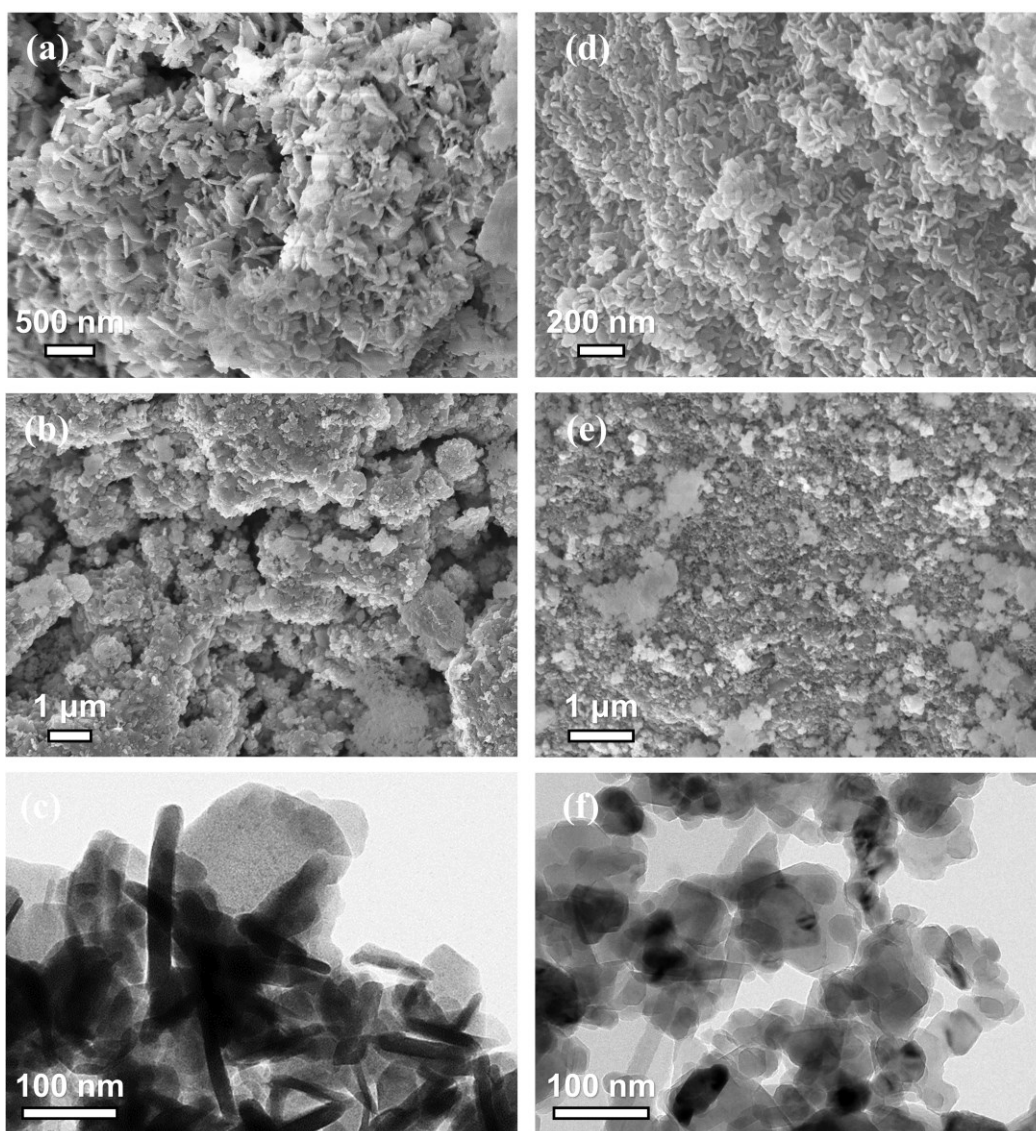


Figure 5-9: Shape and morphology evolution of Cu-Mg-Al LDHs and MMOs. (a) SEM image of the Cu-Mg-Al LDH-9.5. (b) SEM image of the freshly calcined the Cu-Mg-Al MMO-9.5. (c) STEM image of the Cu-Mg-Al LDH-9.5 precursor. (d) SEM image of the Cu-Mg-Al LDH-11. (e) SEM image of the freshly calcined the Cu-Mg-Al MMO-11. (f) STEM image of the Cu-Mg-Al LDH-11 precursor.

Isothermal redox reactions were performed in a TGA at 900°C to investigate the reactivity and stability of the Cu-Mg-Al MMO-11 as oxygen carriers. The results are shown in **Figure 5-10** and compared to those in **Figure 5-1**. Both Cu-Mg-Al MMOs showed faster rates of oxygen release and re-oxidation than those observed for the Cu-Al MMOs (consisting of CuO and CuAl₂O₄). The slightly slower rate of oxygen release and re-oxidation for Cu-Mg-Al MMO-11, compared to Cu-Mg-Al MMO-9.5, is likely a result of the lower porosity of the MMOs leading to greater intraparticle mass transfer effects. Overall, the highly stable oxygen release capacity (6.4 wt%, **Figure 5-1c**) and oxygen storage capacity (13.0 wt%, **Figure 5-1d**) over 100 redox cycles in a TGA demonstrate that the higher strength Cu-Mg-Al MMO-11 are good candidates for further testing in an FBR.

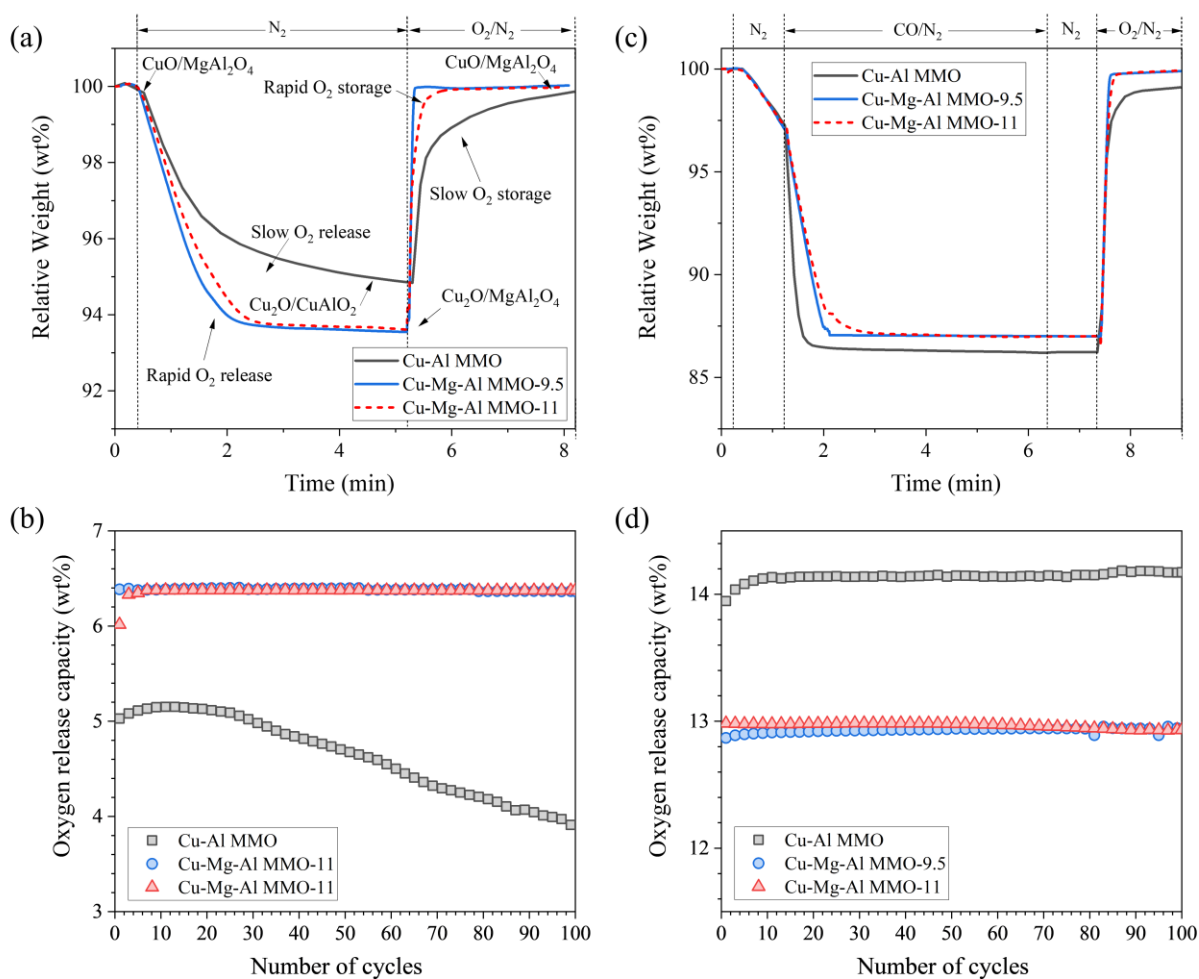


Figure 5-10: Redox cycling of Cu-Mg-Al MMO-11 in a TGA at 900°C. (a) oxygen release and storage profiles (CLOU), phase change between CuO and Cu₂O. The oxygen release was carried out under N₂ for 5 min, followed by re-oxidation in air for 3 min. **(b)** cyclic reduction and oxidation (CLC), phase change between CuO and Cu. The reduction was carried out for 7 min in 5 vol% CO balanced with N₂, followed by a 1 min N₂ purge. The samples were then re-oxidised for 3 min in air, followed by a further 1 min in pure N₂. **(c)** oxygen release capacities of the MMOs over 100 CLOU redox cycles. **(d)** oxygen storage capacities of the MMOs over 100 CLC redox cycles.

5.3.4 Results of long-term redox cycling of Cu-Mg-Al MMO-11 in an FBR

The oxygen carriers were tested for 100 cycles of partial oxygen release and re-oxidation in an FBR at 900°C to assess the chemical, thermal and mechanical stability of the Cu-Mg-Al MMO-11. The cycling scheme consisted of a repeating 20 cycle segment of 19 partial cycles of oxygen release and re-oxidation followed by one cycle of full oxygen release and re-oxidation. The oxygen profiles during the partial oxygen release and re-oxidation cycles for the Cu-Mg-Al MMO-11 are shown in **Figure 5-11a** and **b**, respectively, and the conversion over 100 cycles is shown in **Figure 5-11e**; the previously tested MMOs

are included for comparison. From **Figure 5-11e**, the conversion of the Cu-Mg-Al MMO-11 decreased from 0.97 to 0.82 over 100 cycles under the partial cycling mode, compared to a decrease of 0.98 to 0.62 for the Cu-Mg-Al MMO-9.5. The observed lower rate of attrition of the Cu-Mg-Al MMO-11 agreed well with the lower porosity and higher crushing strength determined for the oxygen carriers.

After the successful testing of the Cu-Mg-Al MMO-11 under the partial cycling mode, the oxygen carriers were rigorously tested in an FBR for 100 full oxygen release and re-oxidation cycles. The oxygen profiles for selected cycles of oxygen release and re-oxidation are shown in **Figure 5-11c-d**. As shown in **Figure 5-11e**, the conversion remained generally constant at 0.90 ± 0.05 (of the theoretical conversion) without significant attrition or agglomeration occurring over 65 h of operation. The slight decrease in conversion observed in the FBR may be attributed to three main factors:

- (i) loss of material when loading the bed,
- (ii) attrition suffered by the oxygen carriers during operation, and
- (iii) loss of active material due to the formation of CuAl_2O_4 .

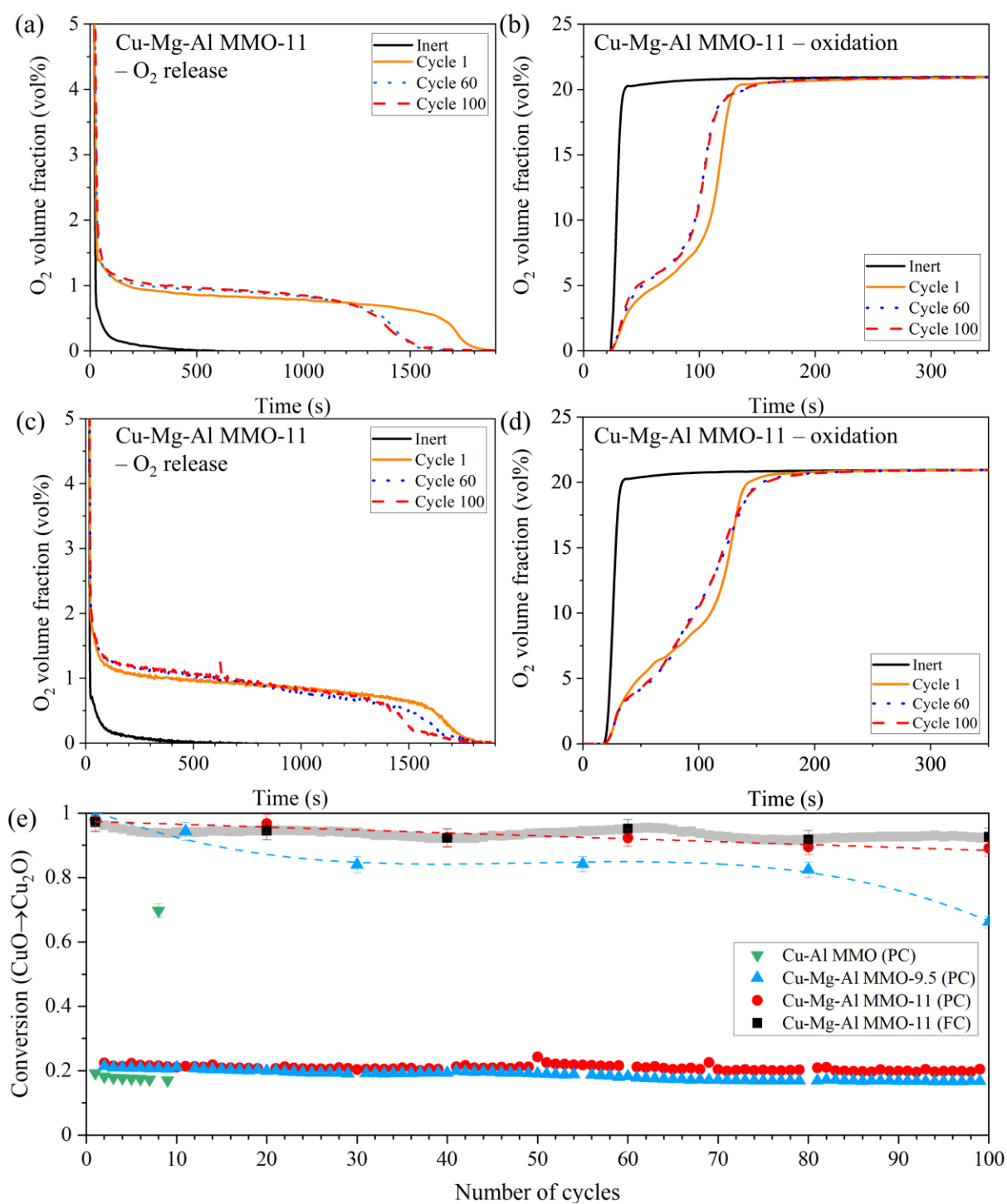


Figure 5-11: Redox cycling of Cu-Mg-Al MMO-11 in an FBR at 900°C. Oxygen profiles during full cycle periods for (a) oxygen release and (b) oxidation during partial cycling of Cu-Mg-Al-11. Oxygen profiles during full cycle periods for (a) oxygen release and (b) oxidation during partial cycling of Cu-Mg-Al-11. (e) conversion of the MMOs. Where PC is partial cycling (100 cycles of partial oxygen release and oxidation with full cycles every 20 cycles), and FC is full cycling (100 cycles of full oxygen release and oxidation).

5.3.5 Material characterisation

The Cu-Mg-Al MMO particles cycled in the FBR were collected and characterised to understand the structural evolution during redox cycling. The Cu-Mg-Al MMOs collected after FBR experiments were subjected to further TGA cycling to measure the oxygen release capacity (**Figure 5-12a**). The oxygen release capacity of the Cu-Mg-Al MMO-11 cycled under partial and full cycling modes corresponded with that of the fresh MMOs (6.4 wt%). Analysis of the XRD patterns of the cycled materials also show an absence of CuAl_2O_4 spinel oxide peaks (**Figure 5-12b**). These results confirm the decrease in conversion observed during redox cycling in the FBR was not due to the formation of CuAl_2O_4 .

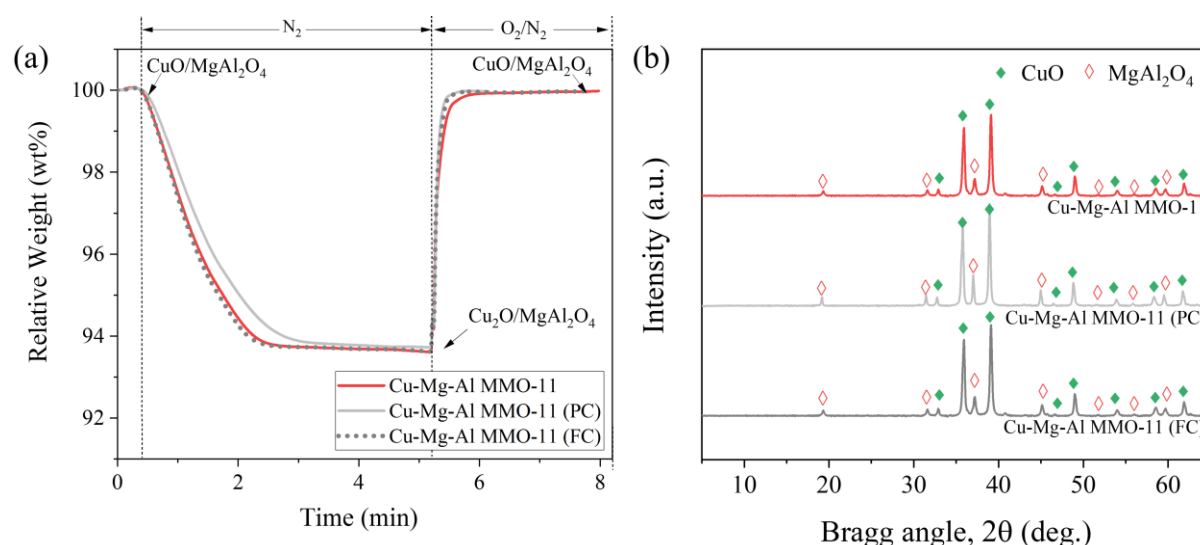


Figure 5-12: Post-cycling characterisation of the MMOs. (a) TGA profiles of freshly calcined particles, particles cycled for 100 cycles in an FBR with partial oxygen release (PC) and oxidation with full oxygen release every 20th cycle in an FBR; and particles cycled for 100 cycles with full oxygen release and oxidation in an FBR (FC) at 900 °C. **(b)** XRD patterns of fresh and cycled materials.

SEM images of the particles and particle surfaces before and after cycling are shown in (**Figure 5-13**). As shown in **Figure 5-13f** and **i**, the cycled particles maintained the initial shapes and sizes over 100 redox cycles. The surface morphology of the samples recovered after redox cycling was slightly smoother than the surface of the freshly calcined material, which indicated a small amount of surface attrition in the FBR. After 100 cycles of partial oxygen release and re-oxidation, the evolved surface morphology showed the aggregation of platelets into grains (**Figure 5-13g** and **j**).

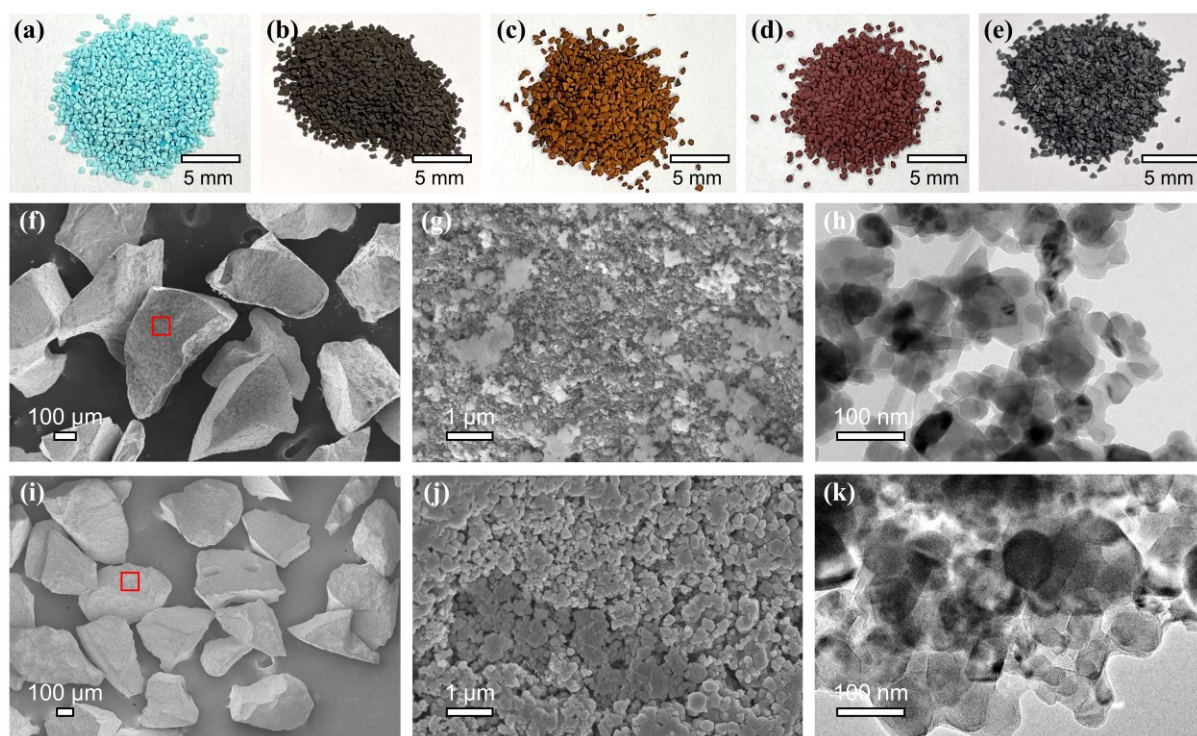


Figure 5-13: Morphological evolution of Cu-Mg-Al MMO-11 using imaging. Photos of Cu-Mg-Al LDH-11 precursors and derived MMOs in different states: (a) LDH precursor powders, (b) freshly calcined MMOs, (c) decomposed MMOs ($\text{Cu}_2\text{O}/\text{MgAl}_2\text{O}_4$), (d) reduced MMOs ($\text{Cu}/\text{MgAl}_2\text{O}_4$) reduction under 5 vol% CO balanced with N_2 , (e) MMOs after 100 cycles in the FBR. SEM image of the (f) freshly calcined MMOs and (g) their surface, and (h) STEM image. SEM image of the (i) cycled MMOs and (j) their surface, and (k) STEM image.

Using MIP (Figure 5-14a) and helium pycnometry, the porosity of the Cu-Mg-Al MMO-11 samples was found to decrease from 38 to 34% over 100 full cycles in the FBR. The results of MIP also indicate the change of pore size distributions for each material, showing the collapse of mesoporous pores and a shift towards larger pore diameters. The change of pore size distribution shows an increase in average pore diameter (towards the mesoporous range) for the Cu-Mg-Al MMO-11, but also a shift from uni-modal to bi-modal pore volume distribution. The change in porosity and pore size distribution of the Cu-Mg-Al MMO-9.5 was also investigated. The porosity decreased from 74 to 64%, and the pore size distribution similarly showed a shift towards large pore diameters and collapse of mesoporous pores. The greater rate of attrition of these materials during cycling was attributed to their higher porosity, larger pore diameters and lower crushing strengths than the Cu-Mg-Al MMO-11. The results of this study confirmed the high chemical stability and high thermal stability of the Cu-Mg-Al MMO-11 during redox cycling, although the mechanical properties of the materials may need to be improved using advanced particle engineering and manufacturing techniques in the future.

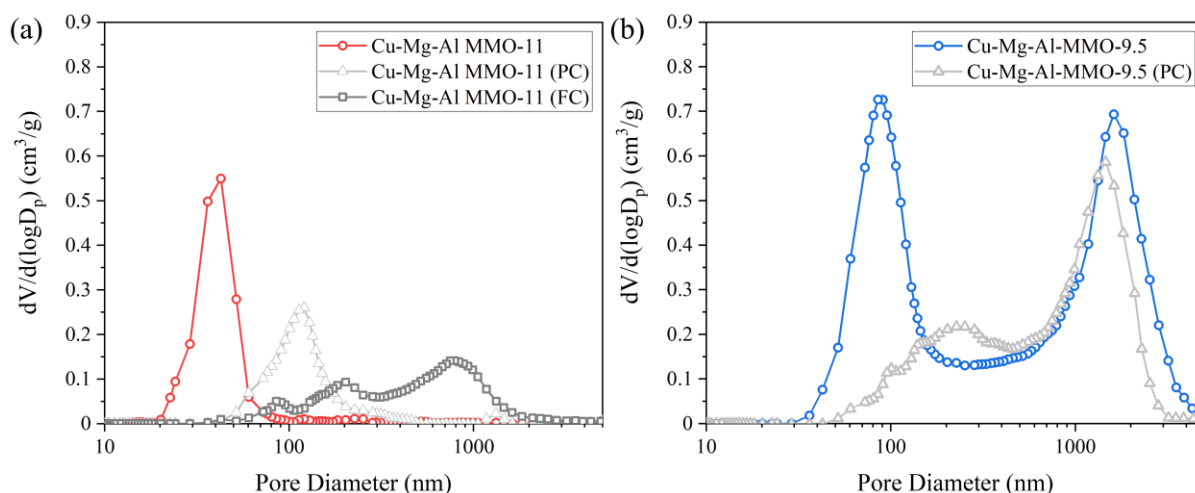


Figure 5-14: Pore size distributions of fresh and cycle MMOs from MIP analysis. (a) pore size distribution of fresh Cu-Mg-Al MMO-11 and cycled samples in FBR reactor derived from MIP, and **(b)** pore size distribution of fresh Cu-Mg-Al MMO-9.5 and cycled in FBR reactor derived from MIP

5.3.6 CLCP cycling of Cu-Mg-Al MMO-11 in a fluidised bed reactor

To further demonstrate the practical application of the Cu-Mg-Al MMOs as oxygen carriers, cyclic reduction and oxidation were performed using low concentrations of CO and CH₄, which is relevant to many industrial processes. The MMOs were tested during redox cycling with low concentrations of CO and CH₄ balanced with N₂ at low temperatures (400°C) and high temperatures (800°C) in the FBR.

The typical gas concentrations of the reactive gases during the reduction and oxidation stages are shown in **Figure 5-15a-c** (additional gas profiles are presented in **Figure 5-16**). As shown in **Figure 5-15a**, the Cu-Mg-Al MMO-11 can efficiently oxidise low concentrations of CO to CO₂ at 400°C. The CO and CH₄ conversions at 400°C and 800°C were between 0.6 and 0.7 (**Figure 5-15d**). To avoid coke deposition during the reduction of CH₄, the degree of conversion of CuO was controlled at about 60%. The materials demonstrated high stability for 20 cycles over 1000 min with no agglomeration of the oxygen carriers being observed (visually and by sieve analysis) in the samples withdrawn from the reactor. The XRD patterns of the materials cycled with CH₄ and CO (**Figure 5-17**) also found no peaks matching with Cu-Al oxides (CuAl₂O₄ or CuAlO₂), demonstrating the phase stability under CLCP conditions. These results confirmed the high reactivity and stability of the Cu-based redox sorbents, which have shown great potential for application in industrial processes, such as argon recovery and recycling in silicon manufacturing processes.²³⁰ Additional testing of these materials should be carried out to push the conversion of CuO to Cu to higher levels. Deeper conversion to Cu generates greater porosity within the oxygen carrier particle, which could cause the oxygen carriers to fail earlier.

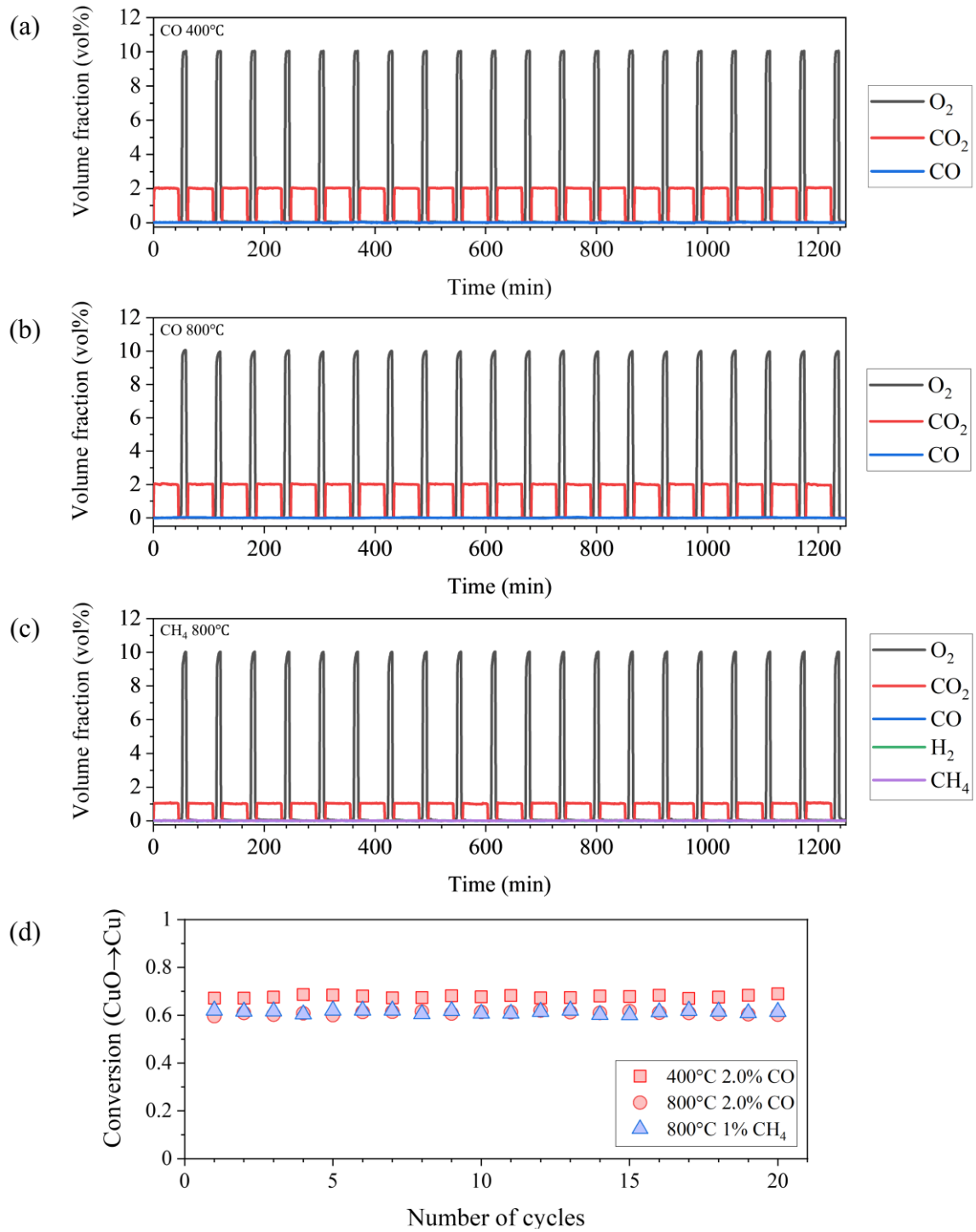


Figure 5-15: Gas concentration profiles of chemical looping combustive purification (CLCP) cycling of Cu-Mg-Al MMO-11 in FBR. (a) 2 vol% CO/N₂ used for the reduction and oxidation under 10 vol% O₂/N₂ at 400°C, (b) 2 vol% CO/N₂ used for the reduction and oxidation under 10 vol% O₂/N₂ at 800°C, (c) 1 vol% CH₄/N₂ used for the reduction and oxidation under 10 vol% O₂/N₂ at 800°C. (d) conversion profile for each testing mode over 20 CLCP cycles in an FBR.

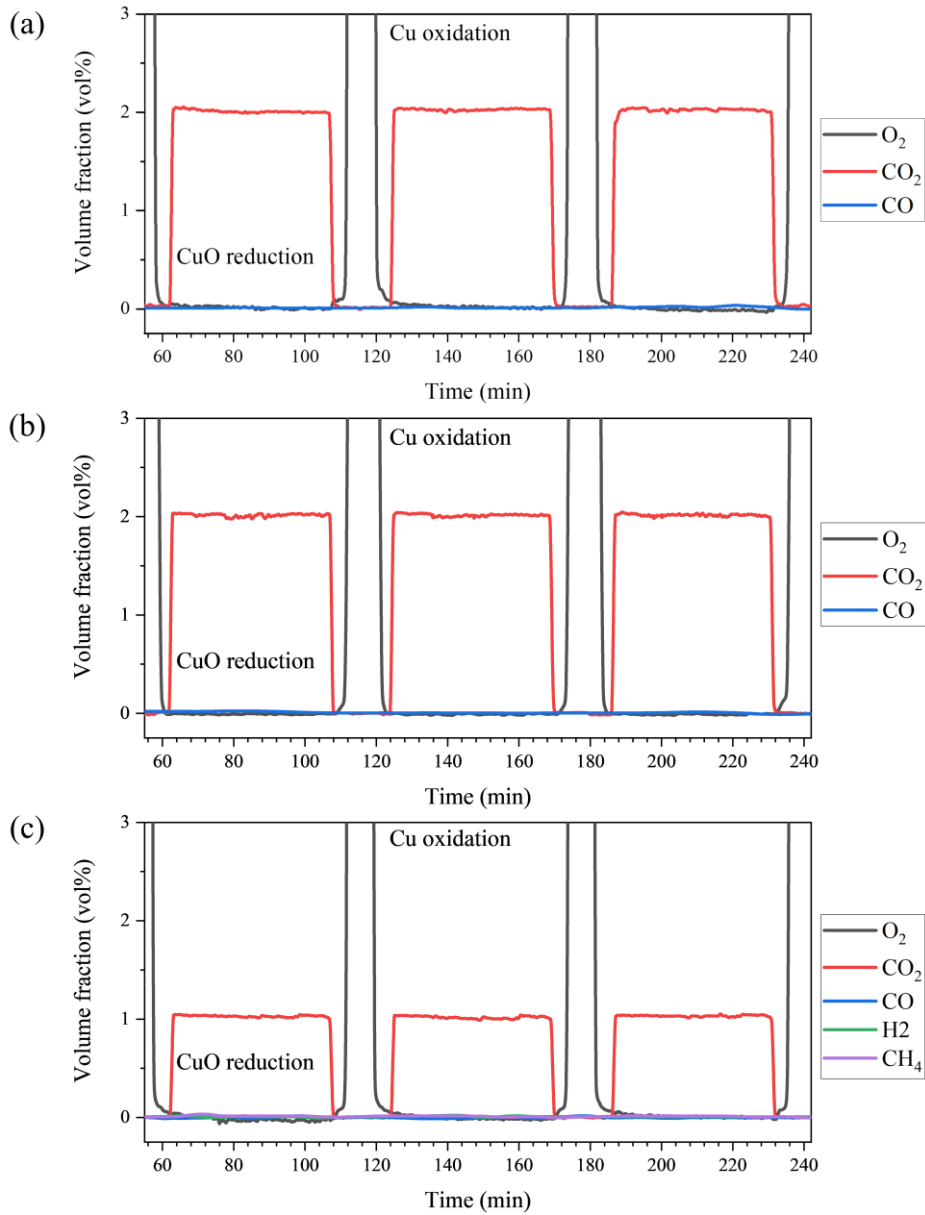


Figure 5-16: Enhanced gas concentration profiles of chemical looping combustive purification (CLCP) cycling of Cu-Mg-Al MMO in FBR. (a) 2 vol% CO/N₂ used for the reduction and oxidation under 10 vol% O₂/N₂ at 400°C, (b) 2 vol% CO/N₂ used for the reduction and oxidation under 10 vol% O₂/N₂ at 800°C, (c) 1 vol% CH₄/N₂ used for the reduction and oxidation under 10 vol% O₂/N₂ at 800°C. The intrinsic accuracy of the measurement is 1.0% of reading, and the detection limits of the MGA3000C Multi-Gas Analyser (ADC Gas Analysis) are 500 ppm for CO, CO₂ and CH₄ and 1000 ppm for oxygen.

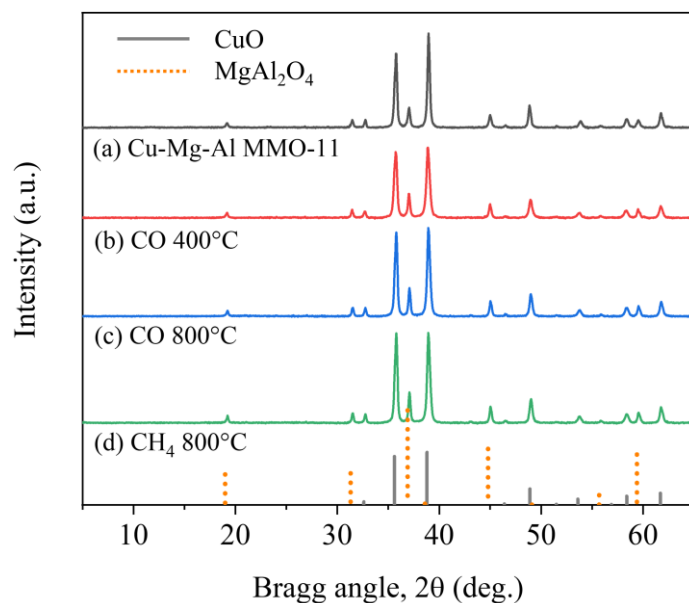


Figure 5-17: XRD patterns of fresh and cycled Cu-Mg-Al MMO-11 recovered after 20 redox-cycles in FBR. (a) fresh Cu-Mg-Al MMO-HS, (b) Cu-Mg-Al MMO-HS recovered after 20 CLC cycles in FBR at 400°C with 2 vol% CO/N₂ for the reduction and oxidation under 10 vol% O₂/N₂, (c) Cu-Mg-Al MMO-HS recovered after 20 CLC cycles in FBR at 800°C with 2 vol% CO/N₂ for the reduction and oxidation under 10 vol% O₂/N₂, (d) MMO recovered after 20 CLC cycles in FBR at 800°C with 1 vol% CH₄/N₂ for the reduction and oxidation under 10 vol% O₂/N₂.

5.4 Synthesis of Cu-Mg-Al layered double hydroxides and mixed metal oxides with higher Cu contents

5.4.1 Synthesis of layered double hydroxides and mixed metal oxides

The CuO loading of the MMOs was increased by changing the molar ratio of M²⁺/M³⁺ cations in the LDH precursor structure to test the effectiveness of the LDH-MMO design strategy. Naturally occurring LDHs typically have a molar ratio of M²⁺/M³⁺ equal to 2 (e.g. Quintinite, [Mg₄Al(OH)₁₂](CO₃)·3H₂O), or 3 (e.g. Hydrotalcite, [Mg₆Al₂(OH)₁₂](CO₃)·4H₂O) due to the local ordering of M²⁺ and M³⁺ that prevents the formation of M³⁺ clusters.²³² Therefore, LDHs with a target molar ratio of M²⁺/M³⁺ of 3 were prepared, increasing the loading of active CuO in the MMOs from 63 to 74 wt%. The 5:1:2 LDHs were synthesised *via* co-precipitation at two different *pH* values of 9.5 and 11 to investigate whether increasing the *pH* would result in LDHs and calcined MMOs with lower porosities, as observed previously for lower loading materials.²¹¹ From **Figure 5-18a**, XRD analysis confirmed the formation of the LDH structure at both *pH* values and the formation of CuO and MgAl₂O₄ upon calcination. The content of Cu, Mg and Al in the MMOs was quantified using XRF; the target ratio of metals was achieved in the materials synthesised at each *pH* value (**Table 5-1**).

Table 5-1: XRF results for the LDH-512s.

Synthesis pH	CuO (wt%)	MgO (wt%)	Al ₂ O ₃ (wt%)
9.5	73.4	7.3	19.3
11	74.0	7.5	18.5
(Target)	73.6	7.5	18.9

The pore size distributions and porosity of the LDHs and MMOs were determined using MIP and helium pycnometry (**Figure 5-18**). The porosity of the LDHs decreased from 64% to 47% when the co-precipitation *pH* value was increased from 9.5 to 11. Accordingly, the LDH platelet size was observed to decrease with increasing *pH* from 9.5 to 11 using SEM (**Figure 5-19**). The smaller platelets aggregated into denser particles with lower porosities. Upon high temperature calcination, the porosity of the materials decreased from 64% to 52% and 47% to 34% for the MMO-512-9.5 and MMO-512-11, respectively. The pore size distributions of the LDHs were found to shift toward larger pore diameters upon calcination to MMOs, likely due to sintering of smaller pores (**Figure 5-18b**). The average crushing strength of the calcined particles were 1.7 ± 1.0 N and 4.5 ± 1.6 N for the MMO-512-9.5 and MMO-512-11, respectively. An increase of co-precipitation *pH* from 9.5 to 11 resulted in LDHs and MMOs with lower porosities and MMOs with higher mechanical strength than those produced at *pH* 9.5, while achieving the desired loading of CuO in the oxygen carrier.

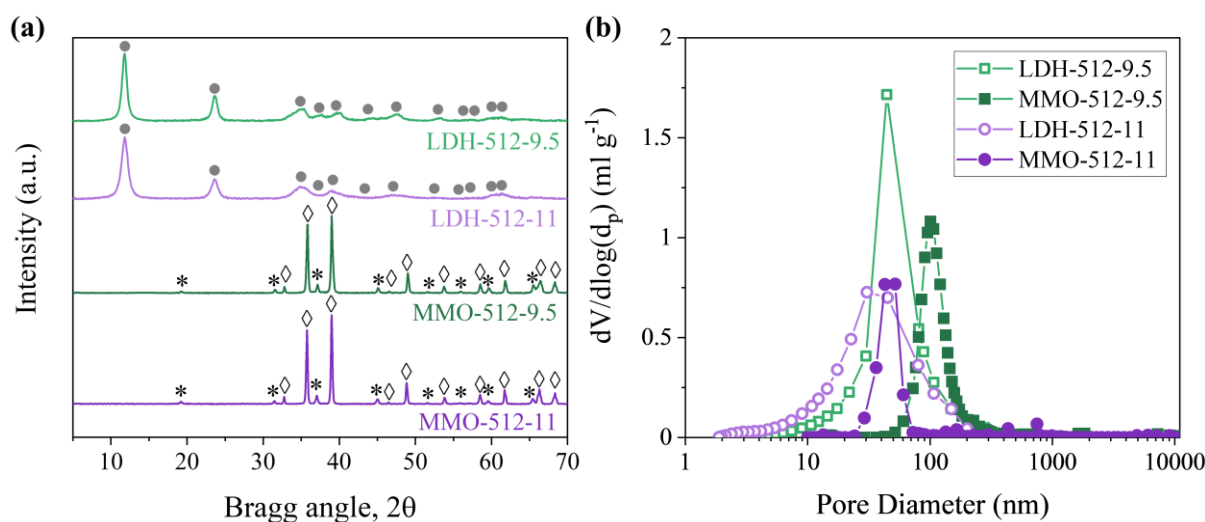


Figure 5-18: Characterisation of LDH-512s (a) XRD patterns of LDHs and MMOs, crystalline patterns correspond to ● $\text{Mg}_6\text{Al}_2(\text{OH})_{16}\text{CO}_3 \cdot 4\text{H}_2\text{O}$ (JCPDS 22-0700), ◇ CuO (JCPDS 80-1268) and * MgAl_2O_4 (JCPDS 73-19.59); (b) N_2 adsorption and MIP pore size distributions of LDH-512s and MMO-512s.

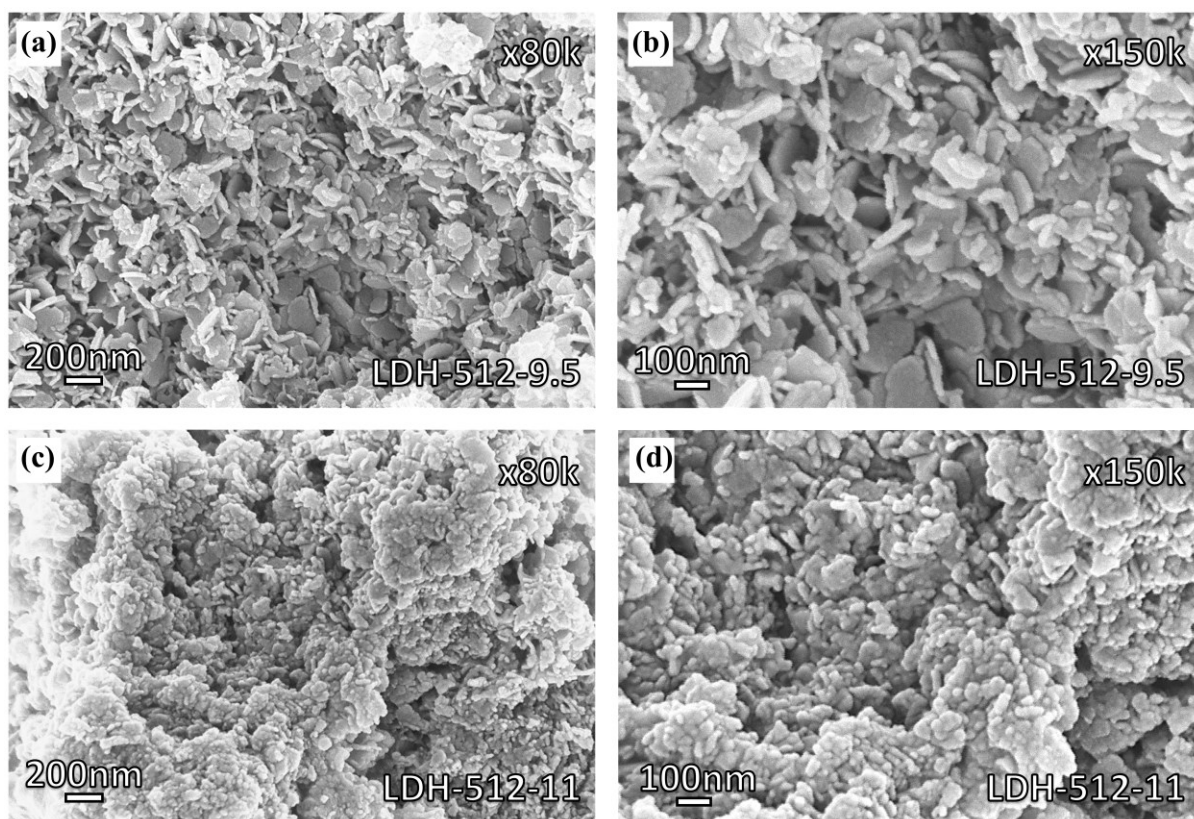


Figure 5-19: SEM images of LDH-512s. SEM images of LDH-512-9.5 particles (a) at 80k magnification and (b) 150k magnification; SEM images of LDH-512-11 particles at (c) 80k magnification and (d) 150k magnification.

5.4.2 Long-term cycling of Cu-Mg-Al mixed metal oxides in a fluidised bed reactor

Isothermal redox cycling was performed in a TGA to investigate the reactivity and stability of the MMOs. **Figure 5-20a** shows the first and last cycles of oxygen release and re-oxidation profiles for the MMO-512s. The slower rate of oxygen release of the MMO-512-11 compared to the MMO-512-9.5 (*i.e.* longer time required for total oxygen release) was attributed to the higher intraparticle mass transfer resistances of the lower porosity MMO-512-11s. Both MMOs showed stable oxygen release capacities over 100 cycles, close to the theoretical capacity of 0.074 g_{O2}/g_{MMO} (**Figure 5-20b**).

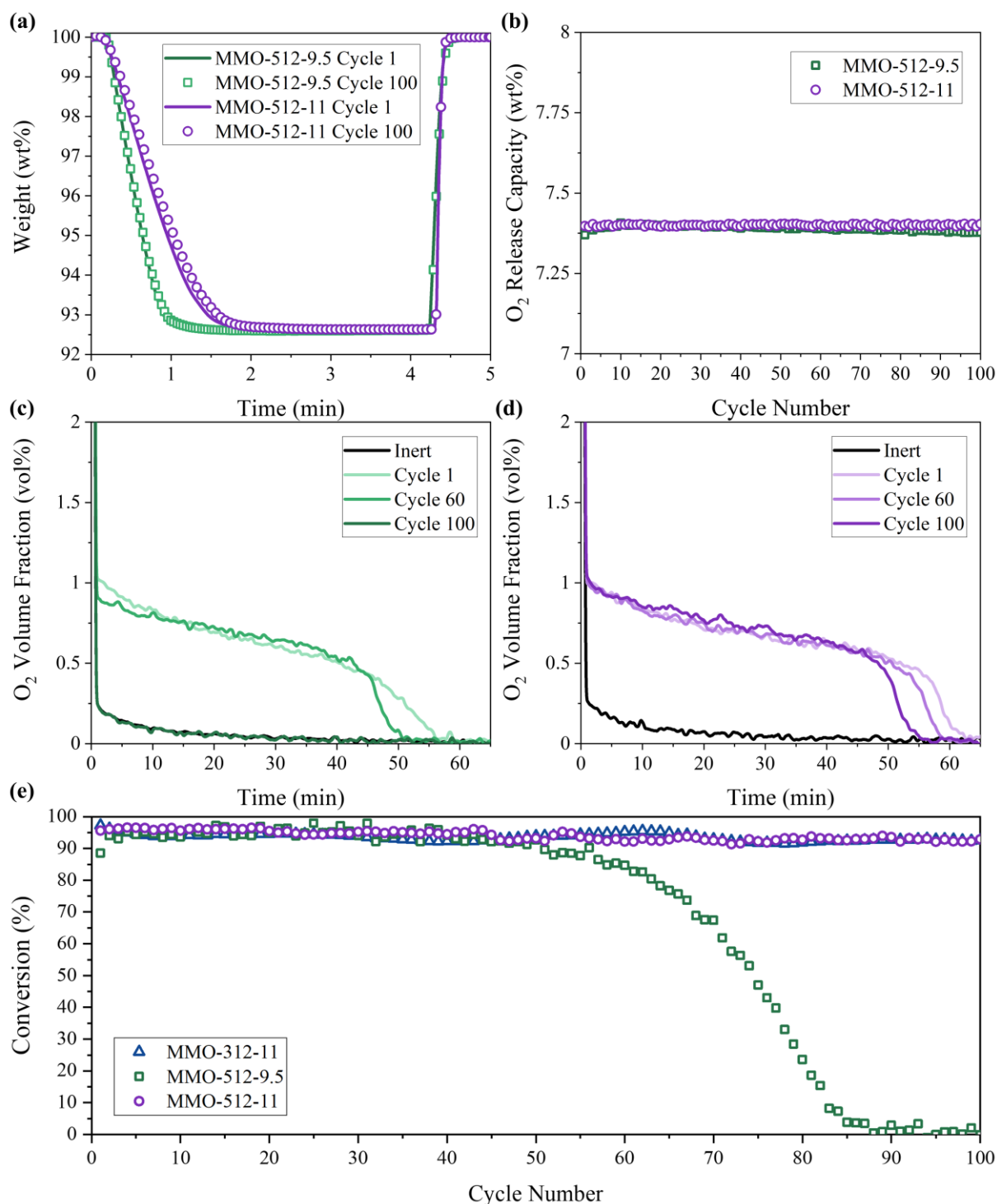


Figure 5-20: (a) oxygen release and storage profiles of the MMOs in a TGA at 900°C; (b) oxygen release capacities over 100 redox cycles in a TGA at 900°C; (c,d) oxygen release profiles for cycles 1, 60 and 100 in an FBR at 900°C for (c) MMO-512-9.5 and (d) MMO-512-11; (e) conversion of MMO-312-11,²¹¹ MMO-512-9.5 and MMO-512-11 over 100 cycles of full oxygen release and oxygen storage in an FBR at 900°C.

The three largest pilot facilities for chemical looping processes use interconnected fluidised bed systems (Alstom, 3 MW_{th},²³³ Chalmers University of Technology, 2-4 MW_{th},²³⁴ Technische Universität Darmstadt, 1 MW_{th}²³⁵) where attrition of oxygen carriers is a significant barrier to commercialisation. While oxygen carriers performing redox reactions at high temperatures experience chemical and thermal stresses, which can induce structural changes due to sintering, the fluidised system inflicts additional physical stresses on the particle due to collisions with other particles and reactor walls, leading to particle breakage. Therefore, the MMOs were tested for 100 redox cycles in the FBR at 900°C to assess the mechanical stability of the higher loading MMOs.

The oxygen release profiles for cycles 1, 60 and 100 are shown in **Figure 5-20c-d**. The overall conversion decreased from 94% to 0 over 88 cycles for the MMO-512-9.5, and from 96% to 93% over 100 cycles for the MMO-512-11 (**Figure 5-20e**). The observed decrease in conversion was due to severe attrition of the oxygen carriers during operation, not agglomeration of the oxygen carriers. The increased attrition of the MMO-512-9.5 compared to the MMO-512-11 is consistent with the higher porosity and lower crushing strength of the material. No agglomeration was observed in the MMO-512-11 samples withdrawn from the reactor after cycling. The conversion profile of the previously studied MMO-312-11 over 100 cycles in the FBR is shown in **Figure 5-20e**. The near-constant conversion of MMO-512-11, similar to the MMO-312-11, confirms the stabilisation design strategy was effective at higher loading of active CuO. The CuO loadings of these MMOs are much higher than the 13.8 wt% CuO oxygen carriers investigated in the EU-FP7 funded SUCCESS (Scale-up of oxygen carrier for chemical looping combustion using environmentally sustainable materials) project. The use of these MMOs could significantly reduce the required solids inventory for full fuel conversion.¹⁰⁴ The results indicate that Cu-Mg-Al MMOs are promising candidates for further development and scale-up for use in large-scale fluidised chemical looping systems.

5.5 Concluding remarks

In this chapter, the long-term cycling performance of the CuO/CuAl₂O₄ and CuO/MgAl₂O₄ MMOs developed in chapter 4 were studied using TGA and FBR systems. The Cu-Mg-Al MMOs demonstrated fast reaction rates, high oxygen capacity, and excellent stability against sintering over multiple cycles of reduction and oxidation between CuO-Cu₂O-Cu in a TGA (**Figure 5-1**). The MgAl₂O₄ phase remained inert during calcination and cycling and effectively inhibited the formation of CuAl₂O₄. In contrast, the Cu-Al MMOs consisting of CuO/CuAl₂O₄ were characterised by slower oxygen release and re-oxidation rates and were observed to deactivate over 100 CLOU cycles.

The relationship between the precursor chemistry and structure and properties of the MMOs in redox cycles was also investigated. The structural properties of the LDH precursors were found to govern the performance of the derived MMOs during redox cycling in FBRs. The synthesis *pH* was determined to

be an important parameter for tuning the mechanical properties of the MMOs. An increase in co-precipitation *pH* from 9.5 to 11 decreased the porosity and increased the crushing strength of the MMOs. The higher strength MMOs suffered much less attrition and retained high conversion over 100 full cycles of oxygen release and re-oxidation (over 65 h of operation in total). A similar trend was observed for Cu-Mg-Al MMOs synthesised from LDHs with higher contents of Cu in the structure. Although the CuO-based particles maintained their physical structures during testing, the mechanical properties and shapes of particles used in different types of reactors should be considered. For chemical looping processes using FBRs, attrition of particles is one of the most critical obstacles that limit commercialisation. The redox reactions at high temperatures generate significant chemical stresses, while thermal sintering generates additional mechanical and thermal stresses, which tend to induce structural changes and lead to a decline of the mechanical strength of the oxygen carriers in reactors. Advanced particle manufacturing technologies (that enable the production of near-spherical particles), such as spray drying and granulation, might further improve the mechanical strength and reduce attrition. For use in packed bed reactors, large-scale pelletising techniques could be used to prepare suitable particle shapes with enhanced mechanical strength. The effects of *pH* on the structure and performance of the LDH-derived MMOs are further explored in chapter 7.

The near-constant conversion confirmed the stability of the materials over extended redox cycling under CLOU conditions and highlights the potential of Cu-Mg-Al MMOs as promising candidates for further applications. The performance of the 3:1:2 Cu-Mg-Al MMO-11 under CLCP conditions was studied for 20 cycles in an FBR. The oxygen carriers showed stable redox-cycling over a wide temperature range (400–800°C) using low concentrations of combustible gases. This demonstrates the potential of the MMOs for gas purification, which may have important implications for the design of future industrial gas purifications systems for a wide range processes. The high thermal, chemical and mechanical stability of the lower-loading oxygen carriers under CLOU and CLC conditions indicates that these materials are suitable for further study. Therefore, the kinetics of oxygen release will be investigated in the next chapter to aid with fuel reactor design.

It remains challenging to fully understand the interfaces between the Cu phases and the support due to the difficulties characterising the sintering behaviour at high temperatures. In this chapter, the CuO nanoparticles were well dispersed in the support. Such embedding effects were observed for CuO/ZnAl₂O₄ catalysts derived from Cu-Zn-Al LDHs.²³⁶ According to thermogravimetric analysis (**Figure 5-1** and **Figure 5-10**) as well as ex-situ and in-situ XRD analysis (**Figure 5-3** and **Figure 5-4**), the gaseous oxygen is predominantly released from crystalline CuO, confirming that the content of CuAl₂O₄ or Mg(Cu)Al₂O₄ is negligible. Nevertheless, residual Cu species may be incorporated into the spinel support at the grain boundaries of the CuO nanoparticles and Mg-Al spinel support, which likely form reducible CuAl₂O₄ or Mg(Cu)Al₂O₄ overlayers, which in turn function as physical barrier layers

to separate CuO nanoparticles from sintering or further immobilise Cu phases in the support. These strong active phase-support interactions and the local electronic transfer merit further study in the future.

Although this chapter focuses on the applications of LDH-derived MMOs in chemical looping processes, the fundamental understandings of the precursor chemistry reported in this chapter have broad implications for other applications of LDHs and LDH-derived materials. In recent years, transition metal-based LDH materials have shown great promise as (photo-)electrocatalysts (or their precursors).^{237,238} For example, one recent work reported Cu-Al LDH-derived copper electrocatalysts that demonstrated promising acetylene electroreduction performance.²³⁹ The Cu-Al LDH was prepared using NaOH and Na₂CO₃ as co-precipitating agents, which would very likely lead to the formation of Na-containing species (*i.e.* dawsonite, NaAl(CO₃)(OH)₂) according to the findings of chapter 3 and previous work.^{156,157,240} However, the effect of the residual Na impurities on the structure of electrocatalysts and electrochemical reactions was poorly understood. This work shows that the fundamental understanding of precursor chemistry and the relationship with compositions and structures of MMOs could allow for a rational design of the materials, leading to significantly improved reactivity and stability.

In summary, this chapter demonstrates the precursor engineering of nanostructured oxygen carrier materials with significantly enhanced cycling stability for thermochemical looping applications. The LDH structure is extremely versatile and different combinations of metal ions can be used to produce novel MMOs with high dispersions of active metal oxides in active or inert supports. As a result, the synthesis strategy of this work may inspire the production of highly stable oxygen carriers, sorbents, and nano-catalysts for many emerging energy processes based on thermochemical looping processes, including chemical looping reforming of methane, CO₂ utilisation, hydrogen production, thermochemical energy storage, and redox catalysis.

Chapter 6

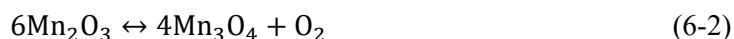
Kinetics of oxygen release from CuO-based mixed metal oxides derived from layered double hydroxides

6.1 Introduction

The use of solid fuels in CLC, such as biomass and coal, is more complicated than using gaseous fuel due to the additional gasification step required to overcome the slow reactions between the solid oxygen carrier and fuel char. This char gasification step is generally the rate-limiting step in the process.⁵³ CLOU is a variant of CLC that was proposed to overcome the slow char gasification step by using oxygen carriers that can release gaseous oxygen in the fuel reactor.²¹ The fast reaction between gaseous oxygen and char in CLOU reduces the size of the fuel reactor for a given heat duty and reduces the leakage of char into the air reactor which in turn increases the CO₂ capture efficiency of the process – as any char combusted in the air reactor is not captured by the process.^{52,241}

Oxygen carriers for CLOU require suitable equilibrium oxygen partial pressures, p_{O_2eq} , at the relevant process temperatures (800-1000°C) to release gaseous oxygen in the fuel reactor. Oxygen carriers capable of releasing gaseous oxygen are typically based on single or mixed oxides of Cu, Mn and Co.^{62,64} The metal oxides CuO, Mn₂O₃ and Co₃O₄ release oxygen *via* reactions (6-1), (6-2) and (6-3), respectively:





The $p_{\text{O}_2\text{eq}}$ as a function of temperature for reactions (6-1), (6-2) and (6-3) is shown in **Figure 6-1**. It is crucial to select oxygen carriers with the appropriate $p_{\text{O}_2\text{eq}}$ for the suitable operation of the fuel and air reactors. The maximum operating temperature of the air reactor can be determined from **Figure 6-1** for $p_{\text{O}_2\text{eq}} = 0.21$. Operation of the air reactor above this temperature (*i.e.* at higher $p_{\text{O}_2\text{eq}}$) would cause the metal oxide to decompose in air. A maximum air reactor operating temperature of $\sim 1030^\circ\text{C}$ was determined for CuO. In reality, the outlet oxygen concentration of the air reactor flue gas should be as low as possible to avoid thermal losses that reduce the overall plant efficiency.⁶⁵ An outlet oxygen concentration of 5% has been set as a target in the literature⁶⁶ which corresponds to an equilibrium temperature of $\sim 960^\circ\text{C}$ for CuO-based oxygen carriers. Therefore, CuO-based oxygen carriers have suitable partial pressure for oxygen release and storage at relevant operating conditions (800-1000°C). The low oxygen partial pressures of the CuO-based oxygen carriers at these temperatures should not be an issue since the oxygen released will be consumed immediately by fuel combustion. In addition, the CuO/Cu₂O redox pair has a higher oxygen release capacity of 0.101 g_{O2}/g_{OC} compared to the Mn₂O₃/Mn₃O₄ (0.034 g_{O2}/g_{OC}) and Co₃O₄/CoO (0.066 g_{O2}/g_{OC}) redox pairs. A material with a high oxygen release capacity is preferred as the system requires a smaller oxygen carrier inventory for the same amount of oxygen released, decreasing the fuel and air reactor sizes.

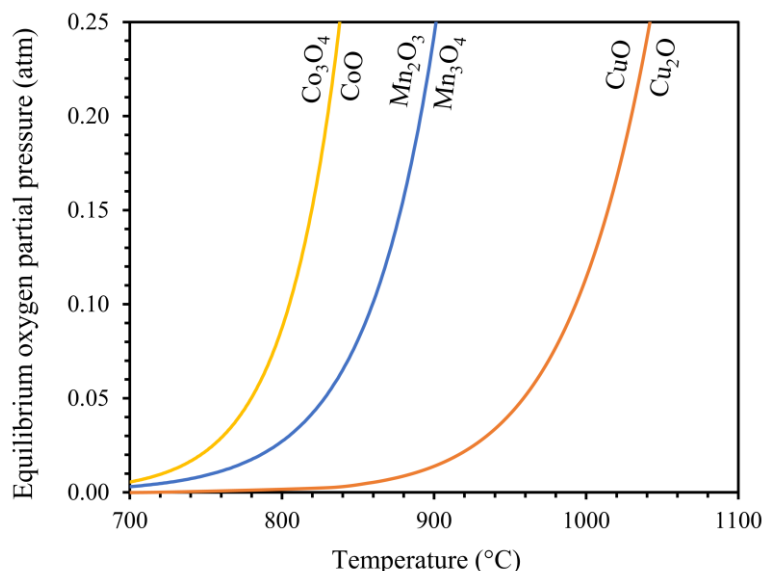


Figure 6-1: Equilibrium oxygen concentrations of Cu₂O/CuO, Mn₂O₃/Mn₃O₄ and CoO/Co₃O₄ systems as a function of temperature using FactSage.⁶³

Accurate knowledge of the oxygen release kinetics is critical because the rate of oxygen release from an oxygen carrier can limit the rate of fuel combustion in the fuel reactor.²⁴² Therefore, accurate oxygen release kinetics are needed for the proper design of the fuel reactor. **Table 6-1** summarises the results of the kinetic analyses of CuO-based oxygen carriers published in the literature. The kinetic parameters varied significantly and were obtained using different reactor systems (TGA and FBR). The large variations are primarily due to the different kinetic models used to determine the kinetic parameters, errors that were caused by measurement systems that are limited by mass transfer effects, and the different supports, active metal loading and preparation methods used to produce the oxygen carrier.^{243,244}

Table 6-1: Results of kinetic studies of CuO-based oxygen carriers for CLOU processes, adapted from Tian *et al.*²⁴⁴

CuO loading (wt%)	Support	Reactor	Temperature (°C)	Kinetic Model*	E _A (kJ mol ⁻¹)	Reference
18	SiO ₂	TGA	800–900	NNGM (N = 2)	315	Song <i>et al.</i> ²⁴³
			900–975		176	
20	Al ₂ O ₃	FBR	850–1100	SCM	81	Mean <i>et al.</i> ²⁴⁵
40	MgAl ₂ O ₄	FBR	850–900	Avrami-Erofeev (N=2)	139	Arjmand <i>et al.</i> ¹¹³
40	ZrO ₂	FBR	900–985	First order	20	Sahir <i>et al.</i> ²⁴⁶
45	ZrO ₂	TGA	775–925	First order	58	Clayton and Whitty ²⁴⁷
50	TiO ₂	TGA	800–900	First order	67	
60	Al ₂ O ₃ -CaO	TGA, FBR	850–950	SCM	60	Hu <i>et al.</i> ²⁴²
60	MgAl ₂ O ₄	TGA	875–1000	NNGM (N = 3/4)	270	Adáñez-Rubio <i>et al.</i> ²⁴⁸
70	SiO ₂	TGA	700–900	SCM	249	San Pio <i>et al.</i> ²²⁶

Footnote: *where NNGM is the nucleation and nuclei growth model; SCM is the shrinking core model

It is necessary to consider the kinetic and thermodynamic driving forces that contribute to the reaction rate to model the oxygen release rates from CuO-based oxygen carriers. The kinetic driving force is driven by the reaction temperature, while the thermodynamic driving force is determined by the difference between the equilibrium oxygen partial pressure (also temperature dependent) and the bulk oxygen concentration. Sahir *et al.* suggested that the high activation energies recorded in **Table 6-1** are global activation energies which combine the thermodynamic driving force and true activation energy

of the intrinsic kinetics.²⁴⁶ The true activation energy may be found by subtracting the thermodynamic driving force assumed to be equal to the standard enthalpy of oxygen release, $\sim 261 \text{ kJ mol}^{-1}$ (at 927°C).¹⁰⁹ Sahir *et al.* proposed two equations to determine the global and intrinsic oxygen release kinetics, given by reactions (6-4) and (6-5), respectively:

$$\frac{dX}{dt} = k_1 f(X) \quad (6-4)$$

$$\frac{dX}{dt} = k_2 (C_{O_2,eq} - C_{O_2,b})^n f(X) \quad (6-5)$$

where k_1 and k_2 are the global and kinetic rate constants, respectively, $f(X)$ is the conversion function, $C_{O_2,eq}$ and $C_{O_2,b}$ are the equilibrium and bulk concentrations of oxygen, respectively, and n is the reaction order with respect to oxygen.

Using equations (6-4) and (6-5), Sahir *et al.* determined global and kinetic activation energies of 281 and 20 kJ mol^{-1} , respectively, for a 40 wt% CuO-based oxygen carrier.²⁴⁶ Clayton and Whitty determined the kinetic activation energies of 45 and 50 wt% CuO-based oxygen carriers to be 58 kJ mol^{-1} and 67 kJ mol^{-1} , respectively, using equation (6-5). Similarly, Hu *et al.* found the activation energy of 67 kJ mol^{-1} for a 60 wt% CuO-based oxygen carrier. The rate of oxygen release also depends on the oxygen carrier conversion function, $f(X)$. As for other non-catalytic heterogeneous reactions, $f(X)$ depends on the solid reaction model used to describe the change in the specific surface area available for reaction as the reaction progresses.²⁰⁷ The reaction model is determined by fitting the experimental data and can offer insights into the reaction mechanism.⁸ However, several models may provide comparable fits of the predicted conversion with the experimental results, indicating that further discrimination between models may be necessary.

The rate equations (6-4) and (6-5) assume negligible mass transfer resistances during experiments to obtain the kinetic data. Therefore, any mass transfer effects in the sampling system that may influence the observed rate of reaction must be minimised to obtain reliable measurements. **Table 6-1** shows that a TGA is commonly used to study the kinetics of the oxygen release reaction. However, external mass transfer can significantly affect the kinetic data obtained using this instrument. A TGA is quick and easy to operate. The sample is loaded into a shallow cylindrical pan as a thin bed of particles with an inlet gas flow over the pan (**Figure 6-2a**). For the oxygen release reaction, the mass transfer steps in a TGA include oxygen diffusion out of the particle (intraparticle diffusion), oxygen diffusion through the bed of oxygen carrier particles (interparticle diffusion) and through a stagnant gas region above the bed of particles to the bulk flow over the pan (external diffusion).²⁴⁹

Mass transfer in a flow-through reactor, *e.g.* an FBR (**Figure 6-2b**), differs significantly from that in a TGA. In an FBR, the interparticle and external mass transfer effects can be significantly reduced by controlling the sample mass and increasing the gas flow rate. Sahir *et al.* used an FBR to determine the oxygen release kinetics of a 40 wt% CuO-based oxygen carrier.²⁴⁶ Pet coke particles were used to consume any oxygen produced to minimise the reduction of the thermodynamic driving force. A low activation energy of 20 kJ mol⁻¹ was reported and attributed to the slow reaction of the released oxygen with pet coke. The rate of oxygen release may have been enhanced by using a more reactive solid fuel. Arjmand *et al.* also studied the kinetics of a 40 wt% CuO-based oxygen carrier using an FBR.¹¹³ Devolatilised wood char was used to consume the gaseous oxygen released, and a global activation energy of 139 kJ mol⁻¹ was reported.

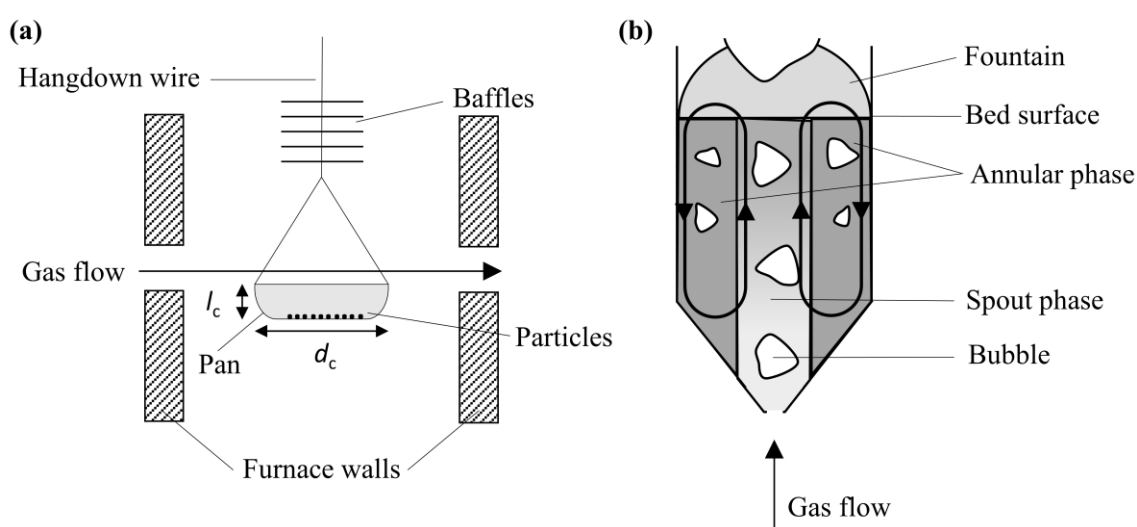


Figure 6-2: Gas flow in apparatus used to determine kinetics. (a) TGA (b) spouted-bed FBR.

Hu *et al.* developed a diffusion model to remove mass transfer effects from the rate parameters determined using a TGA and FBR.²⁴² In addition to minimising the mass transfer resistances, the combined kinetic-diffusion model determined an activation energy of 60 kJ mol⁻¹ for a 60 wt% CuO-based oxygen carrier. In this chapter, the intrinsic kinetics of oxygen release were investigated using an effectiveness factor-based model developed by Zhang *et al.* to determine the pseudo-intrinsic kinetics of the reduction of Fe₂O₃ by CO using an FBR.⁹⁶ The kinetic model was modified for the oxygen release reaction and accounts for both the internal and external mass transfer resistances.

6.2 Model to derive intrinsic oxygen release kinetics

A model developed to determine the pseudo-intrinsic kinetics of the reduction of Fe_2O_3 by CO using an FBR⁹⁶ and the kinetic parameters of CaO carbonation at elevated pressures²⁵⁰ was modified to extract oxygen release kinetics of the MMO-312-11 developed in chapter 5. The model assumes (a) the oxygen carrier particles were spherical; (b) the gas concentrations within the particles were pseudo-steady state; (c) the kinetics are first order.

The observed maximum rate of reaction, r , is given by equation (6-6),

$$r = k_o(C_{O_2,eq} - C_{O_2,b}) \quad (6-6)$$

where, $C_{O_2,eq}$ and $C_{O_2,b}$ are the equilibrium and bulk concentrations of oxygen, respectively, k_o is the observed reaction rate constant which incorporates the external and internal mass transfer effects, and is related to r_p , the mean radius of the particle, k_g , the external mass transfer coefficient, k_i , the intrinsic reaction rate constant, and η , the effectiveness factor, through equation (6-7),

$$\frac{1}{k_o} = \frac{r_p}{3k_g} + \frac{1}{\eta k_i} \quad (6-7)$$

$$C_{O_2,eq} = \frac{p_{O_2,eq}}{RT} \quad (6-8)$$

where $p_{O_2,eq}$ is the equilibrium partial pressure of oxygen, R is the molar gas constant and T is the temperature.

The extent to which the maximum rate of reaction is lowered due to intraparticle diffusion is characterised by η . For a sphere, η can be approximated using equation (6-9),

$$\eta = \frac{3}{\phi^2} (\phi \coth(\phi) - 1) \quad (6-9)$$

where ϕ is the Thiele modulus, a dimensionless quantity dependent on k_i and D_e using equation (6-10),

$$\phi = r_p \sqrt{\frac{k_i}{D_e}} \quad (6-10)$$

where D_e is the effective diffusivity which combines the effects of bulk diffusion, D_{AB} , and Knudsen diffusion, D_K , determined using equations (6-11) to (6-13),

$$D_e = \frac{\varepsilon}{\tau} \left(\frac{1}{D_K} + \frac{1}{D_{AB}} \right) \quad (6-11)^{251}$$

$$D_K = 194 \frac{\varepsilon}{S_A} \sqrt{\frac{T}{M_{O_2}}} \quad (6-12)^{251}$$

$$D_{AB} = \frac{0.00143 T^{1.75} \left(\frac{1}{M_A} + \frac{1}{M_B} \right)^{0.5}}{P \left[(\sum v)_A^{\frac{1}{3}} + (\sum v)_B^{\frac{1}{3}} \right]^2} \quad (6-13)^{201}$$

where ε is the particle porosity, τ is the fitted tortuosity factor, S_A is surface area measured using nitrogen adsorption, M_{O_2} is the molar mass of oxygen, M_A and M_B are the relative molecular masses, P is the pressure, and $(\sum v)_A$ and $(\sum v)_B$ are the diffusion volumes.

The external mass-transfer coefficient, k_g , was estimated from the Sherwood number, Sh , using equation (6-14). The Sherwood number was determined using equations (6-15) to (6-17) for the TGA, and equations (6-17) and (6-19) for the FBR systems.

$$Sh = \frac{k_g d_p}{D_{AB}} \quad (6-14)$$

$$Sh = 2 + 1.1(Re)^{\frac{1}{2}}(Sc)^{\frac{1}{3}} \quad (6-15)^{252}$$

$$Re = \frac{U d_p}{\nu} \quad (6-16)$$

$$Sc = \frac{\nu}{D_{AB}} \quad (6-17)$$

$$Sh = 2\varepsilon_{mf} + 0.69 \left(\frac{Re_p}{\varepsilon_{mf}} \right)^{1/2} Sc^{1/3} \quad (6-18)^{253}$$

$$Re_p = \frac{u_{mf} d_p}{\nu} \quad (6-19)$$

where Re is the Reynolds number, Sc is the Schmidt number, ν is the kinematic viscosity of the gas, ε_{mf} is the voidage of the particulate phase, d_p is the particle diameter, u_{mf} is the incipient fluidisation velocity estimated using the correlation by Wen and Yu.²⁵⁴

6.3 Methodology

6.3.1 Materials

This chapter investigates the kinetics of oxygen release by MMOs prepared from LDH precursors with a Cu:Mg:Al molar ratio of 3:1:2, which were synthesised *via* co-precipitation at constant a pH value of 11 (MMO-312-11). A 1 M NaOH and 1 M Na₂CO₃ alkaline solution was used during co-precipitation. After the precipitate was washed and dried, the LDHs were calcined in a horizontal tube furnace at 975°C for 6 h using an airflow of 1 L min⁻¹ and a heating rate of 15°C min⁻¹. The calcined solids were subsequently crushed and sieved to obtain the desired particle size ranges for testing in a TGA and FBR.

6.3.2 Oxygen release in a TGA to determine the fitted tortuosity factor

Thermogravimetric analysis was carried out in a TGA (**Figure 3-6**) to calculate the value of the fitted tortuosity parameter, τ , to determine D_e using equation (6-11). In theory, k_i and τ are independent of particle size and therefore their values were determined by measuring the oxygen release kinetics from six different particle size ranges and using equations (6-6) to (6-11). To obtain the value of k_i , the square error of k_i for a given mean particle radius and the average value of k_i was minimised by varying τ . A TGA was used to determine τ to keep the hydrodynamics of the system constant and avoid the elutriation of smaller size fractions from the FBR. The size fractions used in the TGA experiments to determine τ are given in **Table 6-2**.

Table 6-2: Particle size ranges used for the TGA experiments to determine τ .

Lower particle diameter (μm)	Upper particle diameter (μm)	Average particle diameter (μm)
125	212	168.5
212	300	256
300	425	362.5
425	500	462.5
500	710	605
710	1000	855

In a typical experiment, 5 mg of the calcined MMOs were placed in a platinum crucible (1.5 mm high and 9.8 mm in diameter) and cycled for 5 redox cycles under CLOU conditions. A two-step cycle was used,

- (i) oxygen release in N_2 for 10 min,
- (ii) re-oxidation in air for 5 min.

6.3.3 Identification of the optimal sample mass for kinetic experiments in the TGA

The amount of sample used for TGA experiments is an important experimental parameter. The amount of oxygen released in the TGA pan increases with increasing sample mass, which can lower the thermodynamic driving force and mask the true rates of the oxygen release reaction. To investigate the effect of sample mass on the observed kinetics of the oxygen release reaction, sample masses of 1, 2, 4, 8, 16, and 32 mg were tested at 900°C , and the results are presented in **Figure 6-3**. The data indicates that the sample mass had a significant impact on the maximum observed rate of oxygen release, with the rate decreasing from $0.046 \text{ mmol}(\text{O}_2)\text{s}^{-1}\text{g}_{\text{OC}}^{-1}$ for a sample mass of 1 mg to $0.004 \text{ mmol}(\text{O}_2)\text{s}^{-1}\text{g}_{\text{OC}}^{-1}$ for 32 mg, an order of magnitude lower (**Table 6-3**). In addition, the time required for the complete conversion of the oxygen carrier ($\text{CuO} \rightarrow \text{Cu}_2\text{O}$) increased from 150 to 700 s as the sample mass was increased from 1 to 32 mg. As shown in **Figure 6-3**, the TGA signal for the 1, 2, and 4 mg sample masses was unstable. Therefore, a sample mass of 5 mg was used for further redox cycling experiments in the TGA as a compromise between external mass transfer and signal-to-noise ratio and the sample pan containing enough particles in the pan to be representative of the particle size fraction.

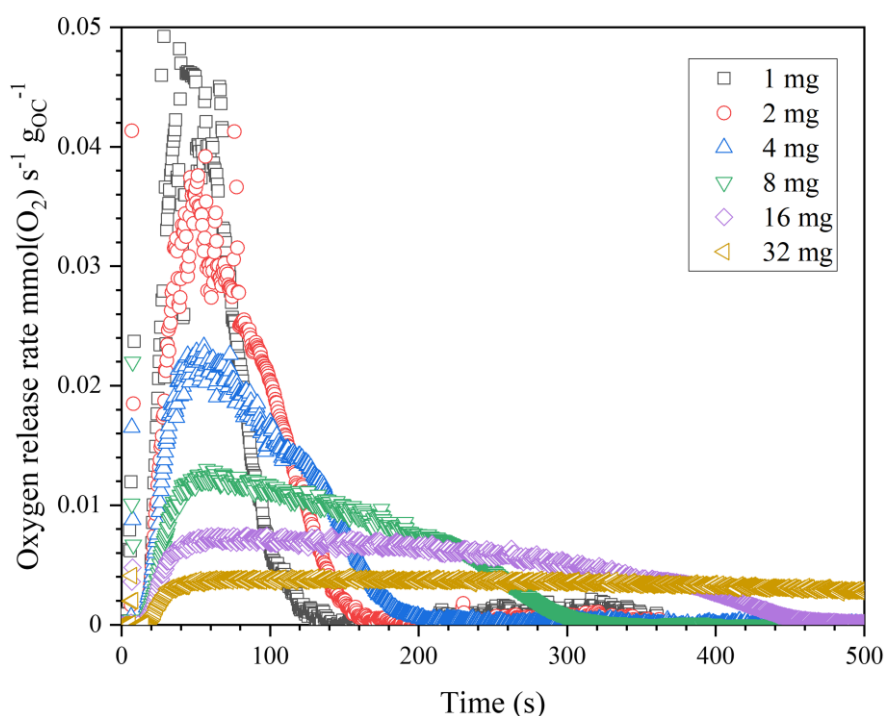


Figure 6-3: Observed oxygen release rates in the TGA at 900°C for different sample masses.

Table 6-3: Results of the sample mass experiments performed in a TGA at 900°C.

Mass (mg)	Maximum observed rate of oxygen release (mmol(O ₂)s ⁻¹ gOC ⁻¹)	Time required for full conversion (CuO → Cu ₂ O) (s)
1	0.046	150
2	0.036	178
4	0.022	220
8	0.013	310
16	0.007	475
32	0.004	700

6.3.4 Oxygen release in a fluidised bed reactor to determine kinetic parameters

A laboratory-scale FBR was used to study the oxygen release kinetics of the MMO-312-11 at high temperatures (850-962°C). A detailed description of the reactor set-up and control program written in Agilent Vee is given in chapter 3.

In a typical experiment, the reactor was heated to the set point temperature and 40 g of inert sand (300-425 µm) was added to create the fluidised bed. A three-point oxygen calibration was performed using N₂, a 10 vol% O₂/N₂ calibration gas and air. Three inert cycles of oxygen release and oxygen storage (*i.e.* without the presence of oxygen carriers) were carried out to provide baseline gas concentration profiles. On completion of the inert cycles, 0.5 g of the MMOs (300-425 µm) were added to the fluidised bed. The sample mass and particle size were carefully chosen to minimise the effects of external mass transfer and intraparticle diffusion while maintaining a good signal-to-noise ratio. High gas flow rates were also used to improve the quality of gas mixing in the bed. The signal from the gas analyser was deconvoluted using a method described in chapter 3. The rate of reaction was determined from the molar fraction of oxygen during redox cycling ($y_{O_2, \text{redox}}$) and leaving the reactor during inert cycles ($y_{O_2, \text{inert}}$) using equation (6-20),

$$r' \left[\frac{\text{mol}(\text{O}_2)}{\text{g}_{OC} \text{ s}} \right] = \frac{y_{O_2, \text{redox}} - y_{O_2, \text{inert}}}{dt} \cdot \frac{\dot{v}_{g, \text{out}}}{m_{OC} \cdot v_m} \quad (6-20)$$

where m_{OC} is the mass of oxygen carriers, v_m is the molar volume of the gas at standard ambient temperature and pressure (SATP), and $\dot{v}_{g, \text{out}}$ is the volumetric flow rate of the gas leaving the reactor determined using equation (6-21),

$$\dot{v}_{g,out} = \frac{\dot{v}_{g,in}}{1 - y_{O_2}} \quad (6-21)$$

where $\dot{v}_{g,in}$ is the volumetric flow rate of the gas entering the reactor. The conversion was calculated from the rate using equation (6-22),

$$X = \frac{MW(O_2)}{R_{OR}} \int_{t_0}^t r' \quad (6-22)$$

where $MW(O_2)$ is the molecular mass of oxygen and R_{OR} is the oxygen release capacity determined by thermogravimetric analysis.

The set point temperature of the FBR was varied between 850 and 962°C and the maximum rate of reaction at each temperature interval was calculated using equation (6-17). The intrinsic rate constant at each temperature interval was determined using the effectiveness-factor based kinetic model to extract the kinetic parameters of the oxygen release reaction.

6.3.5 Identification of the optimal sample mass for kinetic experiments in a fluidised bed reactor

The kinetics measured in an FBR can be significantly affected by the sample mass used in the experiments. Lower sample masses release lower amounts of oxygen which can be effectively removed using appropriate gas flow rates for good mixing and circulation of the particles in the reactor. Consequently, lower sample masses tend to yield higher observed reaction rates than larger sample masses. However, very low sample masses can negatively impact the accuracy and reliability of the kinetic measurements due to the low signal-to-noise ratio.

A range of sample masses were evaluated to determine the optimal sample mass for FBR experiments. The observed rate of oxygen release profiles at 875°C were compared for sample masses of 0.25, 0.5, 0.75, and 1.0 g. In a typical experiment, the reactor was heated to 875°C and 40 g of inert sand in the 300–425 µm size fraction was added to the reactor as bed material to provide a heat sink (absorb excess heat generated by the reaction) and improve the fluidisation characteristics of the bed, resulting in more reliable measurements. Inert cycles were carried out by repeated automated gas switching between N₂ and air. After the completion of inert cycling, MMOs in the particle size range 300–425 µm were added and cycled for ten CLOU cycles consisting of an oxygen release period of 600 s in N₂ followed by a re-oxidation period of 180 s in air. The oxygen concentration profiles over the last three cycles were averaged to determine the rate of the oxygen release reaction using equation (6-20).

The results presented in **Figure 6-4** show that the sample mass significantly impacted the observed rate of oxygen release. The observed oxygen release rate for the largest sample mass was half the $0.018 \text{ mmol(O}_2\text{) s}^{-1} \text{ g}_{\text{OC}}^{-1}$ rate observed for the smallest mass. A sample mass of 0.5 g was chosen as the optimal sample mass because the signal-to-noise ratio during experiments using 0.25 g sample masses at higher temperatures (*e.g.* 950°C), where the rate of oxygen release will be much higher, is expected to be too low.

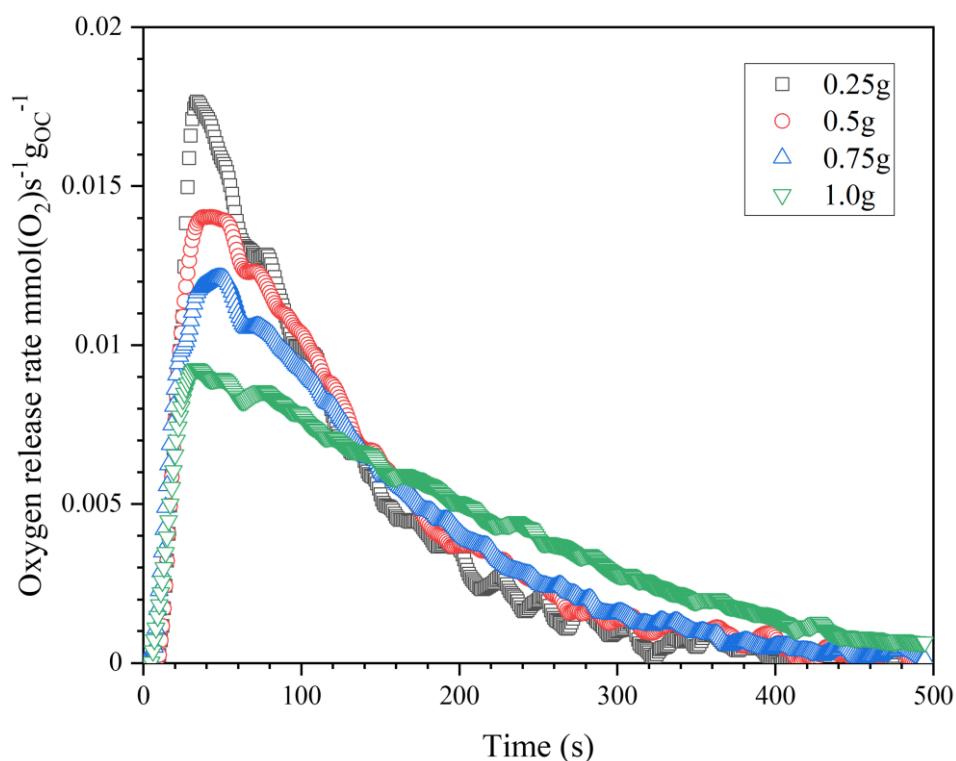


Figure 6-4: Observed oxygen release rates in the FBR at 875°C for different sample masses ($u/u_{\text{mf}} = 4$).

6.3.6 Identification of the optimal u/u_{mf} for kinetic experiments in a fluidised bed reactor

The fluidising flow rate is often expressed as the dimensionless parameter u/u_{mf} , as it provides an easy comparison of the actual gas velocity, u , to the u_{mf} . For the initial experiments, a baseline u/u_{mf} equal to 4 was taken from the literature.²⁵⁵ A comparison of the rate of oxygen release profiles between the TGA (mass = 5 mg) and FBR ($u/u_{\text{mf}} = 4$, mass = 0.5 g of oxygen carrier, 40 g of inert sand bed material) at 875°C is shown in **Figure 6-5**. The TGA exhibited a higher maximum rate of oxygen release than the FBR, which was unexpected given that TGAs typically experience lower rates of external mass transfer that are primarily controlled by diffusion through a thin boundary layer surrounding the sample, similar to a Stefan tube.²⁴² In contrast, the FBR using a low sample mass was expected to have higher rates of external mass transfer due to the better gas-solids mixing within the bed.

The u/u_{mf} was increased to 5, 6 and 7 to investigate the effect on the observed maximum rate of oxygen release. The results in **Figure 6-5** show that increasing the u/u_{mf} from 4 to 5 substantially increased the observed rate of reaction, and further increase of the u/u_{mf} to 6 and 7 did not change the rate of reaction significantly. Based on these findings, a u/u_{mf} of 5 was used for the kinetic experiments in this chapter. The gas flow rates used for each experiment were calculated using the procedure for minimum fluidisation velocity outlined in chapter 3. The gas flow rates for each temperature interval used to determine the intrinsic kinetics of the oxygen release reaction are provided in **Table 6-4**.

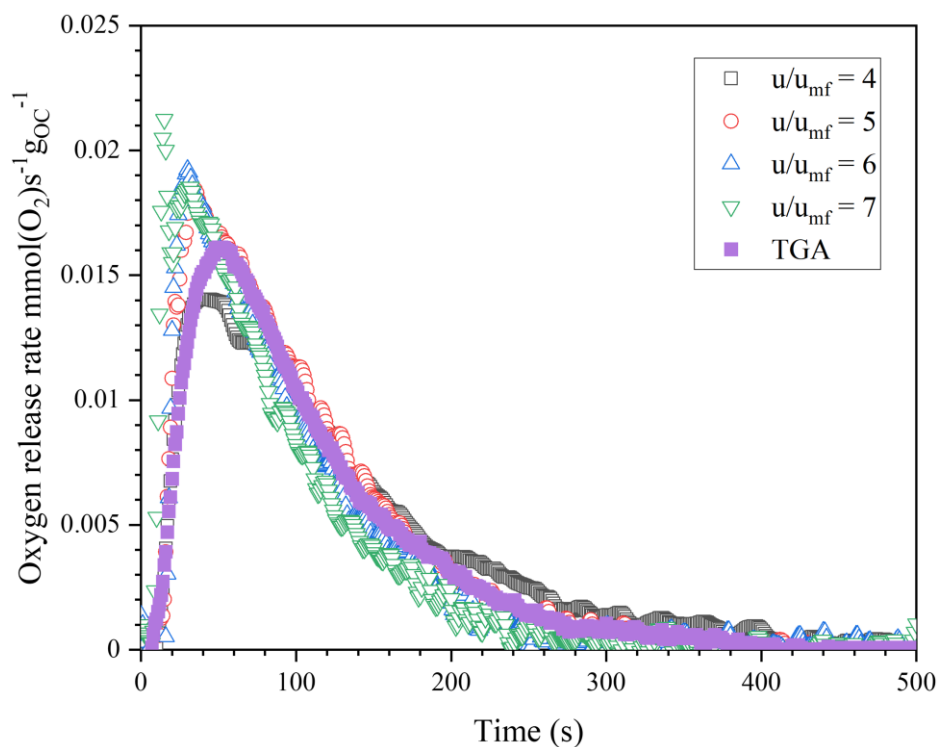


Figure 6-5: Observed oxygen release rates in the FBR at 875°C for different u/u_{mf} (sample mass = 0.5 g).

Table 6-4: Flow rates used for the kinetic experiments between 850 and 962°C in a TGA. Minimum fluidisation velocity calculations were based on the envelope density of inert sand bed material (300-425 µm, 2600 kg m⁻³).

T (°C)	ρ_g (kg m ⁻³)	μ_g (kg m ⁻¹ s ⁻¹)	Ar (-)	Re _{mf} (-)	U _{mf} (m s ⁻¹)	$v_{g,hot}$ (at u _{mf}) (L min ⁻¹)	$v_{g,SATP}$ (at u _{mf}) (L min ⁻¹)	$v_{g,SATP}$ (u/u _{mf} =5) (L min ⁻¹)
850	0.304	4.48E-05	183.9	0.1111	0.0452	1.92	0.509	2.54
862	0.301	4.51E-05	179.2	0.1084	0.0449	1.90	0.500	2.50
875	0.297	4.54E-05	174.8	0.1057	0.0446	1.89	0.491	2.45
887	0.294	4.58E-05	170.5	0.1031	0.0443	1.88	0.482	2.41
900	0.291	4.61E-05	166.4	0.1006	0.0440	1.86	0.474	2.37
912	0.288	4.64E-05	162.4	0.0982	0.0437	1.85	0.466	2.33
925	0.285	4.67E-05	158.5	0.0958	0.0434	1.84	0.457	2.29
937	0.282	4.70E-05	154.8	0.0936	0.0431	1.83	0.450	2.25
950	0.279	4.74E-05	151.2	0.0914	0.0428	1.81	0.442	2.21
962	0.276	4.77E-05	147.7	0.0893	0.0425	1.8028	0.4349	2.175

6.3.7 Calculation of the cross flow factor

The gas exchange efficiency between the bubble and particulate phase was estimated by calculating the cross flow factor, X_f , using a theoretical model developed by Davidson and Harrison.²⁵⁶ The quantity X_f is equivalent to the number of times a bubble has been swept out from its initial formation to the top of the bed. It can be calculated by dividing the total rate of exchange of gas between the bubble and particulate phases, W_s , by the flow rate of gas as bubbles ($u - u_{mf}$),

$$X_f = \frac{W_s}{u - u_{mf}} \quad (6-23)$$

where W_s can be determined using,

$$W_s = NQH \quad (6-24)$$

where N is the number of bubbles per unit volume, Q is an equivalent flow rate to and from the bubble, and H is the bed height.

The fluid flow ($u - u_{mf}$) is assumed to pass as bubbles through the particulate phase so that,

$$u - u_{mf} = NV_b u_A \quad (6-25)$$

where u_A is the absolute rising velocity of bubble, V_b is the bubble volume.

Therefore, X_f can be calculated by,

$$X_f = \frac{QH}{u_A V_b} \quad (6-26)$$

To calculate V_b , the bubble diameter, D_b , was calculated by,²⁵⁷

$$D_b = 1.295 \left[\frac{(u - u_{mf}) A_o}{g^{0.2}} \right]^{0.4} \quad (6-27)$$

where A_o is the cross-sectional area of the spout orifice.

The quantity u_A is estimated by equation (6-28) for $u \gg u_{mf}$,

$$u_A = u - u_{mf} + u_b \quad (6-28)$$

where u_b is the rising velocity of bubble in a stagnant fluid given by,

$$u_b = 0.71(gD_b)^{0.5} \quad (6-29)$$

where g is the acceleration due to gravity.

The quantity H was determined by,

$$\frac{H - H_{mf}}{H_{mf}} = \frac{u - u_{mf}}{u_b} \quad (6-30)$$

where H_{mf} is the bed height at minimum fluidisation given by,

$$H_{mf} = \frac{V_{bed}}{\varepsilon_{mf} A_c} \quad (6-31)$$

where V_{bed} the volume of the bed, A_c is the cross-sectional area of the reactor, and ε_{mf} is the voidage at minimum fluidisation, taken to be 0.42.²⁵⁵

The quantity Q was evaluated by,

$$Q = q + k_g S \quad (6-32)$$

where q is the rate of exchange between a bubble and the particulate phase, k_g is the mass transfer coefficient from a bubble to its surface, and S is the surface area of a rising bubble.

The quantity q was determined by,

$$q = \frac{3}{4} u_0 \pi d_b^2 \quad (6-33)$$

The quantity $k_G S$ is entirely theoretical and $k_G S$ was estimated using the correlation given by Davidson and Harrison,²⁵⁶

$$k_G S = \frac{0.91 \pi D_b^2 D_{AB}^{0.5} g^{0.25}}{D_r^{0.25}} \quad (6-34)$$

where D_r is the diameter of the reactor tube.

Table 6-5: Input and calculated parameters for the calculation of the cross flow factor at 875°C with a 40 g of inert sand bed material (300-425 μm , 2600 kg m^{-3}).

Parameter	Value
Reactor inside diameter, D_r (m)	0.030
Orifice diameter, D_o (m)	0.009
Minimum fluidisation velocity, u_{mf} (ms^{-1})	0.045
Fluidisation velocity, u_{mf} (ms^{-1})	0.22
Mean bubble diameter, D_b (m)	0.011
Absolute rising velocity of bubble, u_A (ms^{-1})	0.575
Bed height, H (m)	0.071
Flow rate to and from the bubble, Q ($10^4 \text{ m}^3 \text{ s}^{-1}$)	1.31
Cross flow factor, X_f (-)	22.5

A theoretical cross flow factor of 22.5 was found using equations (6-26) to (6-34). The high value of X_f indicates that there is a high degree of mixing in the bed. Therefore, the gas concentration in the bubble phase and particle phase are almost the same and limited gas bypasses the reactor without reacting.

6.4 Results

6.4.1 Fitted tortuosity factor

The oxygen release rates for the six different particle size fractions of 312-MMO-11 investigated in a TGA at 900°C are shown in **Figure 6-6**. The maximum observed rates of oxygen release are given in **Table 6-6**. The maximum rate of reaction decreased with increasing particle size fraction, which was expected due to increasing intraparticle diffusion resistance with particle size. **Figure 6-7** shows the variation of the observed rate constant, k_o , with average particle radius. To correct for mass transfer effects, the intrinsic rate constant, k_i , was recovered from k_o through an iterative process. In the first iteration, an effectiveness factor, $\eta = 1$ was assumed to calculate a k_i value using equation (6-7). The k_i value was then used to calculate the Thiele modulus, ϕ , using equation (6-10). This value was substituted into equation (6-9) for the calculation of a new η . These calculations were repeated until η converged. The final value of D_e (and therefore the value of k_i) was determined by minimising the square error of k_i for a given mean particle radius and the average value of k_i by varying τ in equation (6-11). An initial value of 4 was chosen for τ , the average of the 2 to 6 recommended by Satterfield for commercial catalysts.²⁵¹ The final value of τ after iteration was 3.1. The effectiveness factors for the different particle radii are shown in **Table 6-6**.

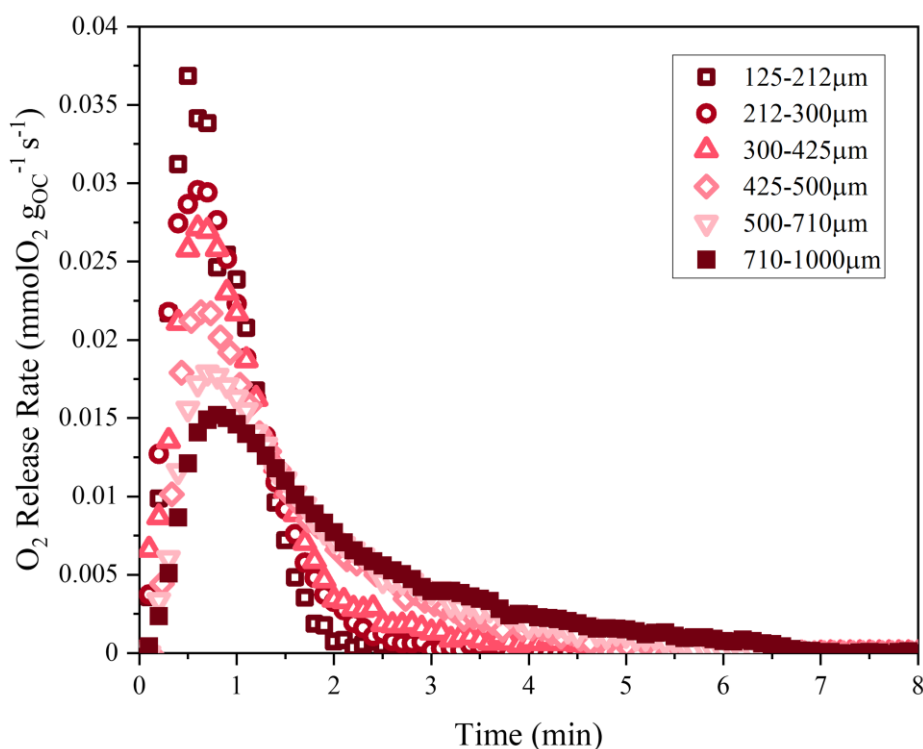


Figure 6-6: Rates of oxygen release for six particle size ranges using the averaged weight profile from cycles three to five in a TGA at 900°C.

Table 6-6: Effectiveness factors and maximum observed rates of oxygen release for each MMO-312-11 particle size fraction cycled in a TGA at 900°C.

Particle size range (μm)	Effectiveness factor (-)	Maximum observed rate of oxygen release ($\text{mmol}(\text{O}_2)\text{s}^{-1}\text{gOC}^{-1}$)
125-212	0.91	0.039
212-300	0.83	0.030
300-425	0.72	0.027
425-500	0.65	0.022
500-710	0.56	0.018
710-1000	0.42	0.015

The k_i determined for each particle radius using the iterative procedure are shown in **Figure 6-7**. The values deviate within 10% of the average intrinsic rate constant (1025 s^{-1}) calculated across all particle size ranges studied at 900°C. Despite taking measures to minimise the mass transfer effects across experiments by using the highest flow rate possible (200 ml min^{-1}) and the lowest mass for a good signal-to-noise ratio, irregularities may arise from:

- (i) Small variations in sample masses used for experiments, although efforts were made to maintain samples masses as close to 5 mg as possible.
- (ii) The placement of particles on the pan, as particles positioned close to each other can enhance mass transfer effects, and using smaller size fractions may result in a higher number of particles in the pan (and therefore a greater number of particles in contact resulting in higher interparticle mass transfer effects).

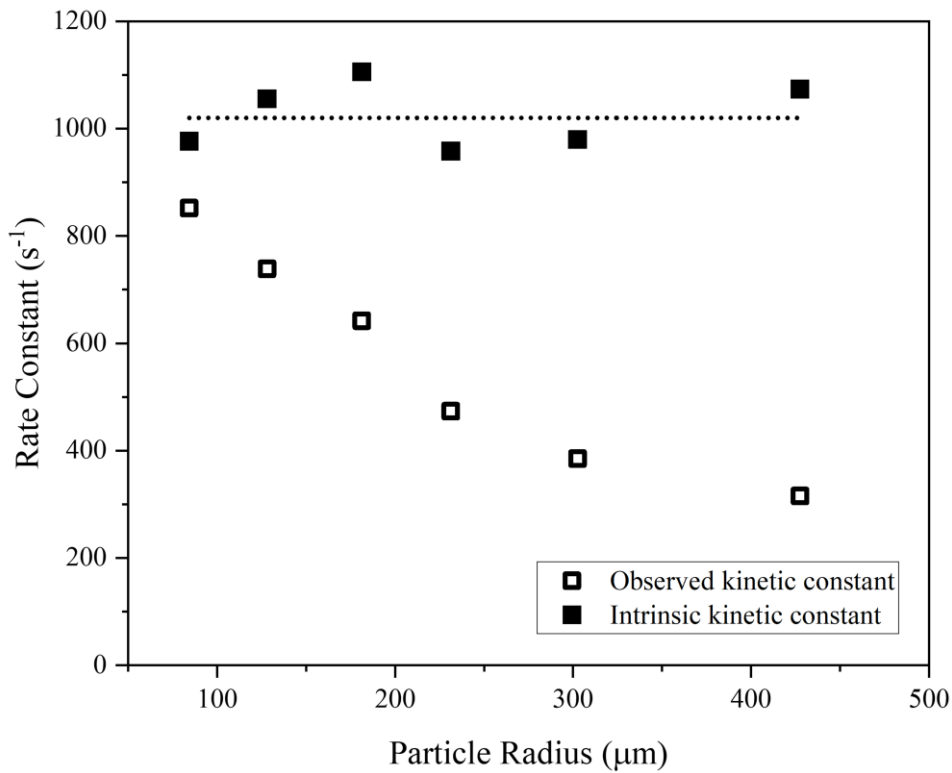


Figure 6-7: Observed and fitted rate constants for each MMO-312-11 particle size fraction cycled in a TGA at 900°C.

6.4.2 Kinetic parameters

A particle size fraction of 300-425 μm was selected for the kinetic experiments in the FBR based on the effectiveness factors calculated for the different particle size fractions cycled in the TGA to determine the fitted tortuosity factor. A reasonable effectiveness factor of 0.72 was determined for this size fraction at 900°C. The maximum rate of oxygen release with conversion for the temperature range of 850 to 962 is shown in **Figure 6-8**. As expected, the maximum observed rate increased with increasing temperature.

The temperature dependence of k_i was modelled using the Arrhenius equation (equation (6-35)), where: E_A is the activation energy and A is the pre-exponential factor. The value of k_i was recovered from the k_o measured at each temperature by applying the effectiveness factor-based kinetic model. An Arrhenius plot (**Figure 6-9**) was used to extract E_A (the slope) of $51 \pm 3 \text{ kJ mol}^{-1}$ and A (the intercept) of 0.0567 s^{-1} over the temperature range 850 to 962°C.

$$k_i = A \exp\left(\frac{E_A}{RT}\right) \quad (6-35)$$

The effectiveness factor was found to decrease from 0.75 at 850°C to 0.62 at 962°C, indicating that mass transfer effects were more significant at higher temperatures but should be accounted for by the model.

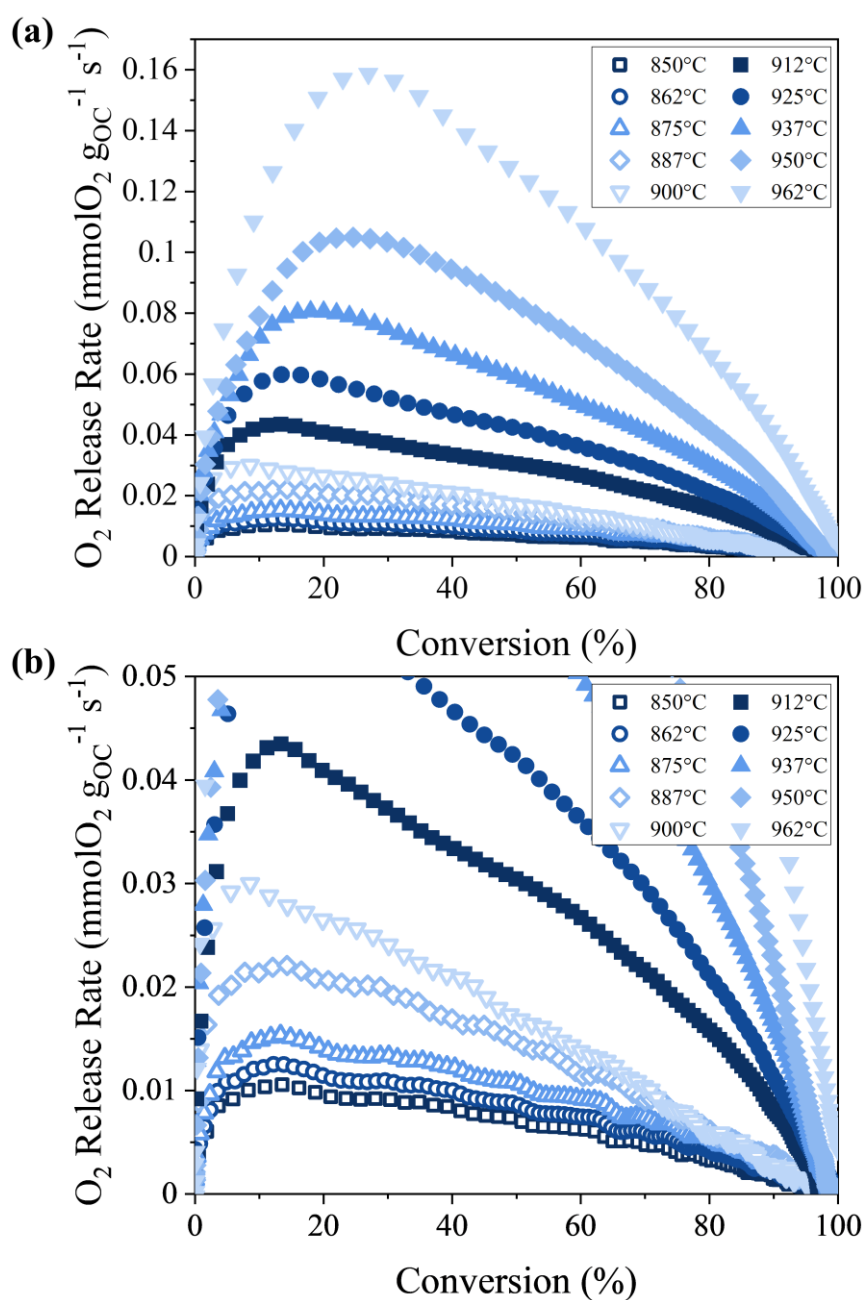


Figure 6-8: Oxygen release rates in the FBR. (a) rates of oxygen release of MMO-312-11 between 850 and 962°C, and **(b)** rates of oxygen release with an enhanced y axis.

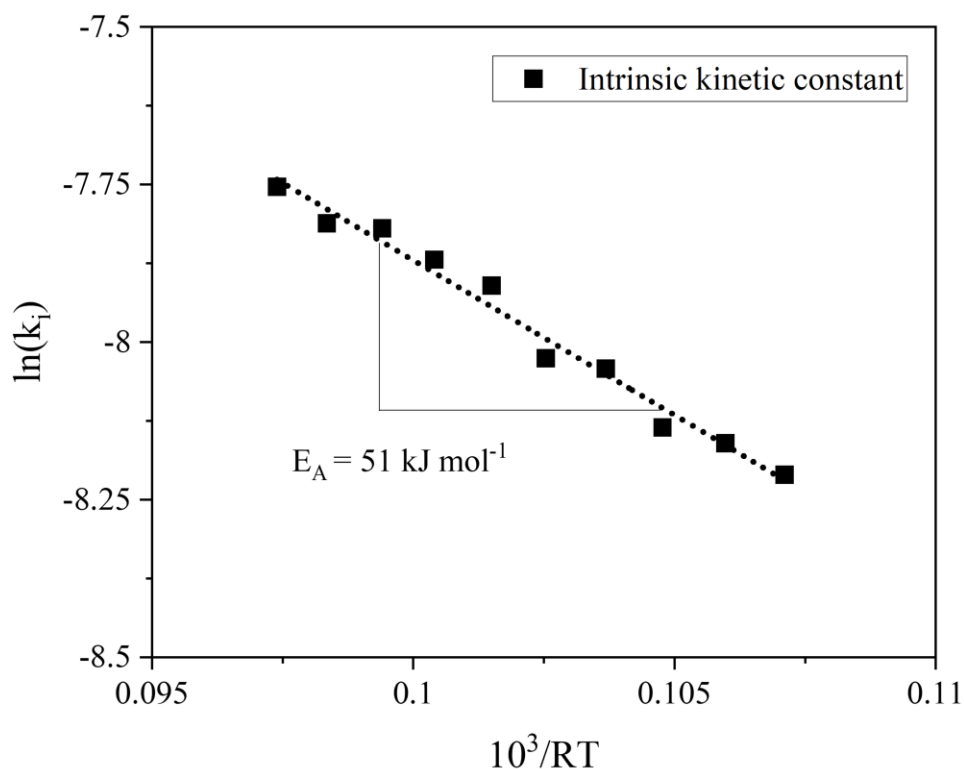


Figure 6-9: Arrhenius plot for the oxygen release from MMO-312-11s over the temperature range 850 to 962°C.

Table 6-7 compares the kinetic studies published in the literature for oxygen release from CuO-based oxygen carriers and the activation energy for the MMO-312-11 determined in this chapter. The activation energies vary significantly from 58 kJ mol⁻¹ to 315 kJ mol⁻¹. The activation energy calculated in this work (51 kJ mol⁻¹) compares well with those measured by Hu *et al.*,²⁴² who reported an activation energy of 60 kJ mol⁻¹ using a TGA and FBR, and Clayton and Whitty who reported activation energies of 58 kJ mol⁻¹ and 67 kJ mol⁻¹ for two different CuO-based oxygen carriers using a TGA.²⁴⁷

Table 6-7: Comparison of the activation energy recovered in this work with published kinetic studies for CuO-based oxygen carriers for CLOU. Adapted from Tian *et al.*²⁴⁴

CuO loading (wt%)	Support	Reactor	Temperature (°C)	Kinetic Model*	E _A (kJ mol ⁻¹)	Reference
18	SiO ₂	TGA	800–900	NNGM (N = 2)	315	Song <i>et al.</i> ²⁴³
			900–975		176	
20	Al ₂ O ₃	FBR	850–1100	SCM	81	Mean <i>et al.</i> ²⁴⁵
40	MgAl ₂ O ₄	FBR	850–900	Avrami-Erofeev (N=2)	139	Arjmand <i>et al.</i> ¹¹³
40	ZrO ₂	FBR	900–985	First order	20	Sahir <i>et al.</i> ²⁴⁶
45	ZrO ₂	TGA	775–925	First order	58	Clayton and Whitty ²⁴⁷
50	TiO ₂	TGA	800–900	First order	67	
60	Al ₂ O ₃ -CaO	TGA, FBR	850–950	SCM	60	Hu <i>et al.</i> ²⁴²
60	MgAl ₂ O ₄	TGA	875–1000	NNGM (N = 3/4)	270	Adánez-Rubio <i>et al.</i> ²⁴⁸
63	MgAl ₂ O ₄	TGA, FBR	850–962	First order	51	This work
70	SiO ₂	TGA	700–900	SCM	249	San Pio <i>et al.</i> ²²⁶

Footnote: *where NNGM is the nucleation and nuclei growth model; SCM is the shrinking core model.

The oxygen carriers in **Table 6-7** vary by CuO loading, support material and particle size. The large spread of reported activation energies could be due to interactions between CuO and different support materials and mass transfer effects due to the choice of preparation method, particle size and other testing conditions, such as whether a TGA or FBR was used to produce the experimental data. Sahir *et al.* suggested that the high activation energies recorded in **Table 6-7** are global activation energies which combine the thermodynamic driving force and true activation energy of the intrinsic kinetics.²⁴⁶ The effectiveness factor-based kinetic model used in this chapter accounts for the thermodynamic driving force by considering the equilibrium oxygen concentration in equation (6-5).

The activation energy calculated in this chapter corresponds with previously reported values in the literature (**Table 6-7**); however, it falls towards the lower end of the range. The higher rates of oxygen release at the higher temperatures investigated in this chapter may have been constrained by the gas-solid mixing in the FBR. Therefore, the rates of external mass transfer at higher temperatures were investigated to determine whether the experimental set-up limited the oxygen release rates. External

mass transfer in this case refers to that from the particle surface to the gas in the particulate phase in the FBR. The rate of mass transfer of oxygen from the surface of an oxygen carrier particle to the particulate phase was calculated using equation (6-36),

$$N_{O_2} = \frac{6k_g(C_{O_2,eq} - C_{O_2,b})}{d_p\rho_p} \quad (6-36)^{258}$$

The values of the external mass transfer coefficient were determined using those used in the kinetic model (equations (6-14) and (6-17) to (6-19)). The rate of external mass transfer was calculated for each temperature and compared to the measured rate of oxygen release, shown in **Table 6-8**. The maximum rate of mass transfer represents the maximum rate possible for the oxygen release reaction in the FBR if the diffusion of oxygen from the particle surface limited the rate. From **Table 6-8**, the ratio of mass transfer to oxygen release rates decreases as the temperature increases. The ratio at high temperatures is around 5, indicating that the rates of oxygen release at higher temperatures shown in **Figure 6-8** could be slightly inhibited by external mass transfer.²⁵⁹ The k_g was derived from the Sherwood number using the correlation in equation (6-18). Therefore, the rates of mass transfer may be higher or lower than the values in **Table 6-8** if an alternative correlation is used.

Table 6-8: Maximum observed rate of oxygen release and ratio of mass transfer/observed rates of oxygen release of MMO-312-11 cycled in an FBR between 850 and 962°C.

Temperature (°C)	Maximum rate of mass transfer (mmol(O ₂)s ⁻¹ gOC ⁻¹)	Ratio of mass transfer/observed rates of oxygen release
850	0.0745	7.1
862	0.0850	6.8
875	0.1028	6.7
887	0.1371	6.2
900	0.1853	6.2
912	0.2431	5.6
925	0.3243	5.4
937	0.4207	5.2
950	0.5544	5.2
962	0.7913	5.0

The Arrhenius parameters were extracted from a plot without the last two data points for 950 and 962°C to investigate whether the rates at higher temperatures were limited by external mass transfer (**Figure 6-10**). An E_A of $53 \pm 4 \text{ kJ mol}^{-1}$ and A of 0.0741 s^{-1} were determined over the temperature range 850 to 937°C. The new E_A for the temperature range 850 to 937°C is slightly higher than the $51 \pm 3 \text{ kJ mol}^{-1}$ determined for the temperature range 850 to 962°C, but not substantially.

A further consideration is the ability of the measurement system to respond to changes in gas concentration. The current measurement system samples the oxygen concentration at a frequency of two data points per s. From **Figure 6-10**, the rate of oxygen release from the MMO-312-11s at higher temperatures is very fast, with the maximum rate of oxygen release occurring at a conversion of 28% for the MMOs cycled at 962°C compared to closer to 10% for reactions below 900°C. Some authors have demonstrated that using alternative oxygen sensors, *i.e.* a universal exhaust gas oxygen sensor (UEGO), with higher sampling frequencies can more effectively capture the oxygen release kinetics in an FBR than existing experimental set-ups.²⁶⁰ Saucedo *et al.* demonstrated using a UEGO sensor with a sampling frequency of ~ 5 data points per s to measure oxygen concentrations during oxy-fuel combustion of a lignite char. Hu *et al.* also used an UEGO sensor for the measurement of kinetics of oxygen uncoupling to determine the activation energy of a 60 wt% CuO-based oxygen carrier to be 60 kJ mol^{-1} .²⁴²

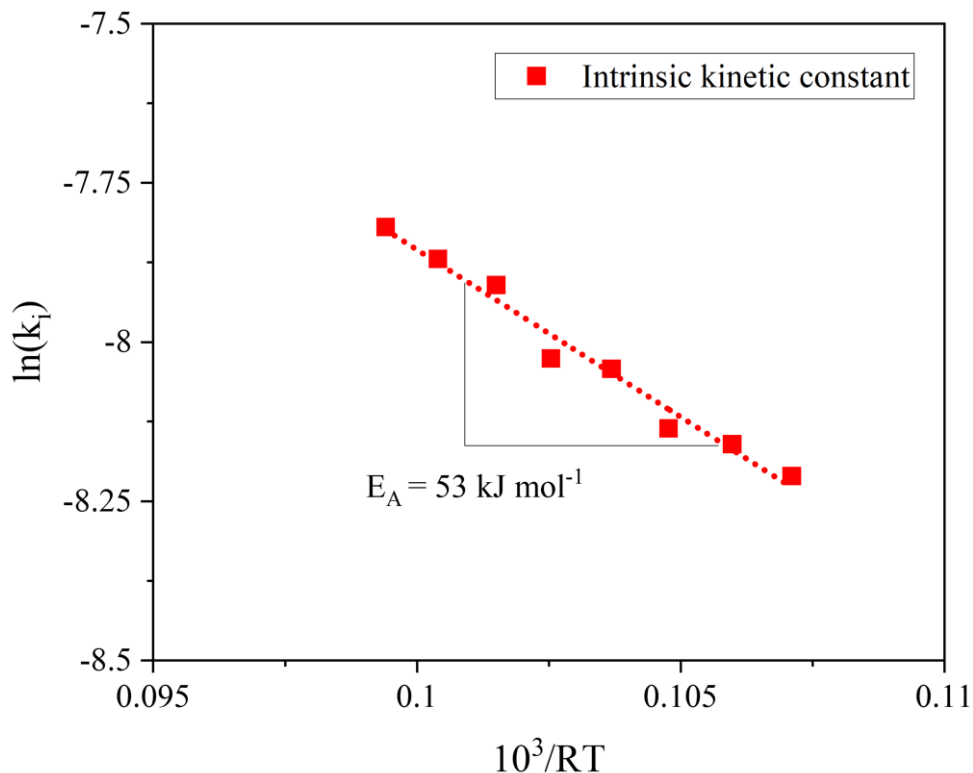


Figure 6-10: Arrhenius plot for the oxygen release from MMO-312-11s over the temperature range 850 to 937°C.

6.5 Concluding remarks

In this chapter, an adapted effectiveness factor-based kinetic model was used to determine the pseudo-intrinsic kinetics of oxygen release from the MMO-312-11. Experimental data was collected using a 1.5 kW_e FBR and TGA by selecting the appropriate sample masses and gas flow rates to minimise the effects of mass transfer. By modelling the internal and external mass transfer effects, the intrinsic rate constants for oxygen uncoupling were obtained for the temperature range 850-962°C. An activation energy of $51 \pm 3 \text{ kJ mol}^{-1}$ and a pre-exponential factor of 0.0567 s^{-1} were calculated for the oxygen release reaction using an Arrhenius expression.

The activation energy calculated in this chapter is consistent with previously reported values in the literature. However, the value determined in this work falls towards the lower end of the range. Therefore, the rates of external mass transfer were investigated to determine whether the experimental set-up limited the oxygen release rates at higher temperatures. The ratio of calculated external mass transfer rates to measured rates of oxygen release was around 5 at high temperatures. This suggests that the rates of oxygen release may have been limited by external mass transfer. However, the removal of data points at the high end of the temperature range did not significantly change the activation energy obtained by fitting the Arrhenius expression.

Another factor to consider is the ability of the measurement system to respond to changes in gas concentration. In future work, it may be more effective to use an alternative oxygen sensor with a higher sampling frequency, such as a UEGO, to capture the kinetics in an FBR as opposed to the gas analyser used in this chapter. In addition, the MMO-512-11s developed in the previous chapter could be investigated to explore the impact of CuO loading on oxygen release kinetics obtained using the effectiveness factor-based kinetic model developed in this chapter.

Chapter 7

Effect of co-precipitation pH on the growth of Cu-Mg-Al layered double hydroxides and the structure and performance of derived mixed metal oxides

7.1 Introduction

Co-precipitation is a simple ‘one-pot’ method used to prepare LDHs by mixing a metal cation solution containing the chosen M^{2+} and M^{3+} cations with an alkaline solution that contains the desired interlayer anions. From chapter 2, the pH value during co-precipitation was found to play a crucial role in the formation and characteristics of LDHs. During co-precipitation at constant pH , the pH of the solution can affect the degree of supersaturation and the solubility of the species present in the solution, which can affect the composition and crystal structure of the LDHs.^{182,186,187,223,224} The pH can also impact the morphology of the individual LDH platelets and bulk structure of the materials.¹⁸⁶ In general, at lower pH values and lower supersaturation, the nucleation rate is lower and increased growth of fewer crystallites leads to the formation of larger platelets.²⁶¹ At higher pH values and higher supersaturation, the rate of nucleation significantly increases, leading to the formation of a large number of smaller crystallites.²⁶² The shape of the platelet directly impacts the porosity of the materials, with larger crystals packing together less effectively, generating materials with higher porosities.

In chapter 5, the co-precipitation pH was determined to be an important synthesis parameter for tuning the structure of Cu-Mg-Al LDHs and the mechanical properties of the derived MMOs. An increase in co-precipitation pH from 9.5 to 11 was found to decrease the porosity of the LDHs and MMOs and

increase the crushing strength of the MMOs. The less porous MMOs experienced significantly lower rates of attrition in an FBR and retained high conversion over 100 full cycles of oxygen release and re-oxidation at 900°C.

In this chapter, the effects of *pH* on the material characteristics of Cu-Mg-Al LDHs were explored in detail. The LDHs were co-precipitated using an automated co-precipitation rig that was used to supply a constant flow rate of the metal solution to a reaction vessel, with the alkaline solution flow rate varied to maintain a constant *pH* between 9 and 11.5 for 300 min. The effect of *pH* on the morphology and performance of the LDH-derived MMOs in chemical looping processes using a TGA at 900°C was also investigated.

7.2 Methodology

7.2.1 Preparation of the layered double hydroxides and mixed metal oxides via co-precipitation

The Cu-Mg-Al LDHs were prepared *via* co-precipitation at room temperature and atmospheric pressure using an automated co-precipitation rig (**Figure 3-1**). A 2 M metal nitrate solution was prepared by dissolving $\text{Cu}(\text{NO}_3)_2 \cdot 2.5\text{H}_2\text{O}$, $\text{Mg}(\text{NO}_3)_2 \cdot 6\text{H}_2\text{O}$, and $\text{Al}(\text{NO}_3)_3 \cdot 9\text{H}_2\text{O}$ in a 3:1:2 molar ratio in DI water. A 1 M NaOH and 1 M Na_2CO_3 alkaline solution was also prepared by dissolving appropriate amounts of NaOH and Na_2CO_3 in DI water. The reaction vessel was primed with a small amount of DI water (~10 ml), and the flow rate of the metal nitrate solution was set at 5 ml min^{-1} . A control programme written in Agilent VEE was used to maintain a constant *pH* during synthesis by varying the flow rate of the alkaline solution using a variable-speed peristaltic pump. The reaction vessel was stirred at 350 rpm by a magnetic stirrer.

The LDHs were co-precipitated for 300 min, and samples were extracted at 5, 10, 15, 20, 30, 45, 60, 90, 120, 180 and 240 min intervals for characterisation. The samples and final precipitate (*i.e.* the precipitate in the reaction vessel after 300 min) were aged for 30 min with no additional stirring. After aging, the precipitate was washed in DI water until the ionic conductivity of the wash water measured below $150 \mu\text{S}$. The washed precipitate was recovered by vacuum filtration and dried overnight at 50°C in a well-ventilated oven. The dried precipitate was calcined in a horizontal tube furnace for 6 h at 975°C using a heating rate of $15^\circ\text{C min}^{-1}$ and an air flow rate of 2 L min^{-1} (SATP) to produce the MMOs. The MMOs were crushed and sieved to produce particles in the 300-425 μm size range for characterisation and testing as oxygen carriers.

The constant *pH* value during co-precipitation was varied from 9 to 11.5 in 0.5 steps to investigate the impact of synthesis *pH* on the structure of the LDHs and derived MMOs. The performance of the MMOs for CLOU and CLC was assessed using a TGA. In this chapter, the LDHs and derived MMOs are

referred to as LDH-pH and MMO-pH, respectively, and will refer to the materials produced after 300 min unless stated otherwise. For example, the materials produced after co-precipitation for 300 min at pH 9.5 are LDH-9.5 and MMO-9.5.

7.2.2 Thermogravimetric analysis

A TGA (**Figure 3-6**) was used for the thermogravimetric analysis of the MMOs. To investigate their chemical stability, MMOs in the 300-425 μm size range were placed in a platinum crucible (diameter: 1.5×10^{-3} m, height: 5×10^{-3} m) and reduced and oxidised repeatedly under different chemical looping cycling modes at 900°C.

For CLOU cycling experiments, ~3 mg of MMOs were exposed to 100 cycles of,

- (i) Oxygen release in N_2 for 2.5 min
- (ii) Re-oxidation in 10% O_2/N_2 for 2.5 min

The experimental oxygen release capacities and observed rate of oxygen release of the MMOs were determined using equations (7-1) and (7-2), respectively,

$$R_{OR} = 1 - \frac{m_{CLOU}}{m_{ox}} \quad (7-1)$$

$$r_{O_2} = -\frac{dm}{dt} \cdot \frac{1}{m_{ox}} \cdot \frac{1}{MW_{O_2}} \quad (7-2)$$

where, R_{OR} is the gaseous oxygen release capacity, m_{CLOU} is the mass of the sample after oxygen release, m_{ox} is the mass of the re-oxidised MMO, r_{O_2} is the rate of O_2 release and MW_{O_2} is the molecular weight of oxygen.

For CLC cycling experiments, ~5 mg of MMOs were exposed to 100 cycles of,

- (i) Reduction in 10% CO/N_2 for 2.5 min,
- (ii) N_2 purge for 1 min to prevent mixing of the oxidative and reductive atmospheres,
- (iii) Re-oxidation in 10 vol% O_2/N_2 for 4 min,
- (iv) N_2 purge for 1 min.

The experimental oxygen storage capacities of the MMOs were determined using equation (7-3),

$$R_{OS} = 1 - \frac{m_{CLC}}{m_{ox}} \quad (7-3)$$

where, R_{OS} is the oxygen storage capacity, and m_{CLC} is the mass of the sample after complete reduction to Cu.

For the extended CLC cycling experiments, ~3 mg of MMOs were exposed to 500 cycles of,

- (i) Reduction in 10% CO/N₂ for 2.5 min,
- (ii) N₂ purge for 1 min,
- (iii) Re-oxidation in 10 vol% O₂/N₂ for 2.5 min,
- (iv) N₂ purge for 1 min.

7.3 Synthesis of layered double hydroxide precursors

7.3.1 XRD characterisation

The XRD patterns of the samples co-precipitated for 300 min at constant pH values between 9 and 11.5 are shown in **Figure 7-1**. In each case, the diffraction patterns exhibit characteristic LDH reflections²⁶³. The reflections at Bragg angles (2θ) of 11.9°, 23.9°, 60.5° and 61.9° correspond to (003) and (006) basal planes and (110) and (113) non-basal planes, respectively. No crystalline impurity phases were detected in the patterns.

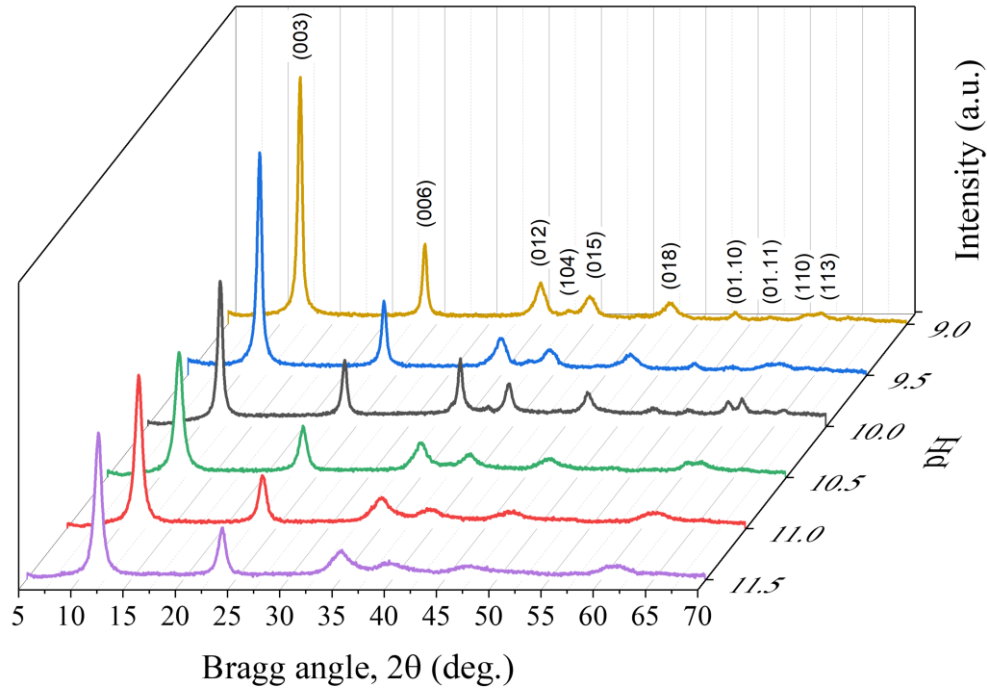


Figure 7-1: XRD patterns of the LDHs. The LDHs were co-precipitated for 300 min at constant pH values between 9 and 11.5 min using a constant flow rate of metal nitrate solution.

Most LDHs adopt a rhombohedral or hexagonal lattice system.²⁶⁴ By convention, the rhombohedral system is described by a triple hexagonal unit cell, where $a = b \neq c$, and $\alpha = \beta = 90^\circ$ and $\gamma = 120^\circ$, to facilitate direct comparison with hexagonal structures (**Figure 7-2**). The average cell parameters were calculated from the (003), (006) and (110) reflections according to Bragg's law, where $a = 2d_{(110)}$ and $c = 3d_{(003)} + 2d_{006}$.²⁶³ From **Figure 7-1**, the (003) and (006) reflections of the samples are well-defined, however, the (110) and (113) reflections overlap. Therefore, while cell parameter c could be determined reliably from the (003) (**Figure 7-11**) and (006) reflections, isolation of the a parameter required deconvolution of the reflections over 2θ range 55 to 67° using a peak fitting program. To improve the quality of the XRD patterns, the tube current was increased from 20 mA to 40 mA over 2θ 55 to 67° and the time per step was increased. The unit cell parameters are shown in **Table 7-1**. The average a and c cell parameters were ca. 3.057 \AA and 22.26 \AA , respectively. These results agree well with LDHs reported in the literature, where a and c cell parameters range from 3.04 to 3.11 \AA and 22 to 26 \AA , respectively.^{265,266}

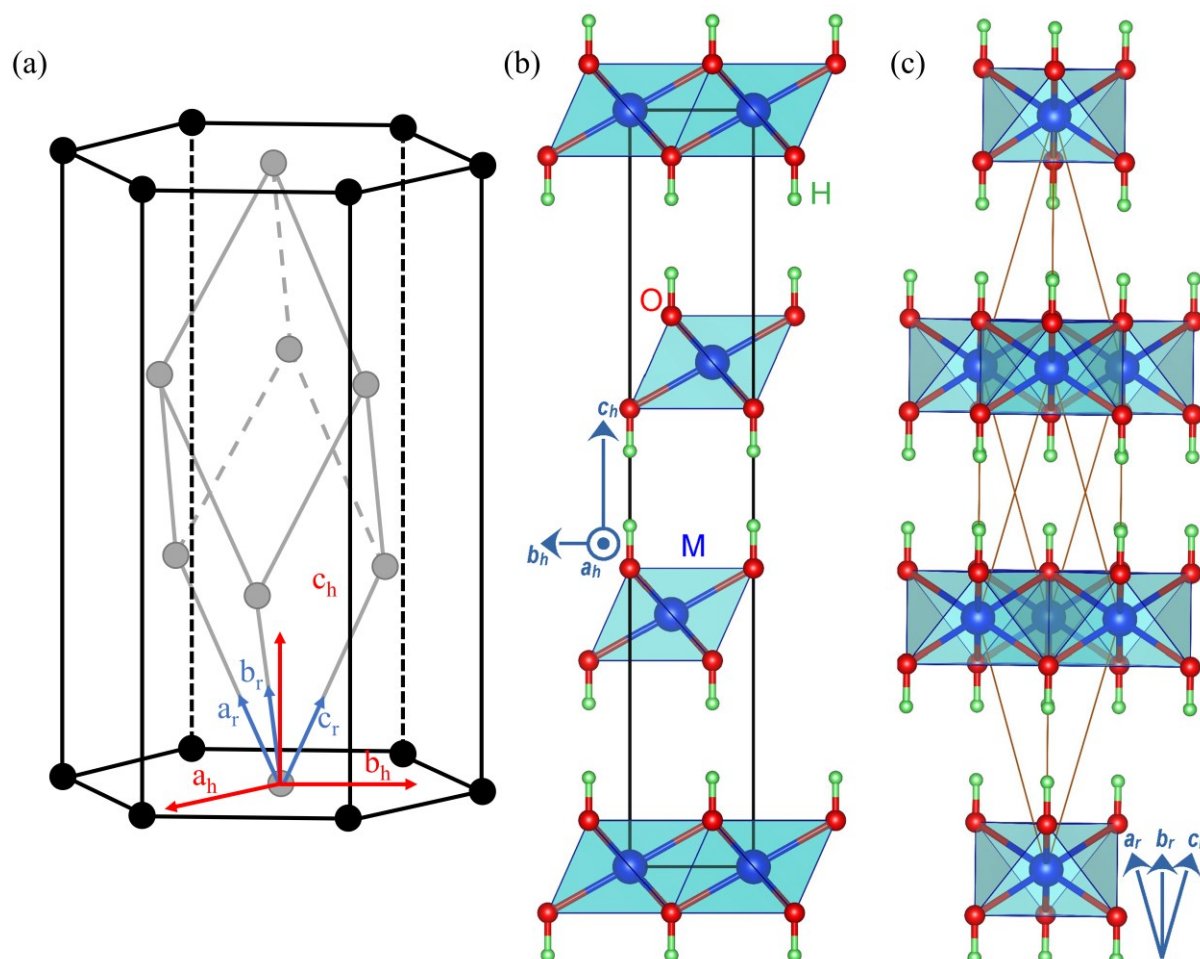


Figure 7-2: Unit cell of LDHs. (a) Relationship between the triple hexagonal cell to the primitive rhombohedral cell. The conventional cell of LDHs in (b) hexagonal representation with group $R\text{-}3m$ (space group 166) and (c) rhombohedral representation of the same structure, adapted from Mohammadi et al.²⁶⁷

Table 7-1: Unit cell parameters and elemental compositions of the LDHs co-precipitated at *pH* values between 9 and 11.5 for 300 min.

Material	a ¹ (Å)	c ² (Å)	3R1:2H1 ³ (%)	CuO ⁴ (wt%)	MgO ⁴ (wt%)	Al ₂ O ₃ ⁴ (wt%)	M ²⁺ /M ³ ratio (-)
LDH-9	3.052	22.293	90:10	61.5	7.2	31.3	1.55
LDH-9.5	3.057	22.342	91:9	62.5	10.3	27.2	1.95
LDH-10	3.056	22.360	84:14	62.6	10.4	27	1.98
LDH-10.5	3.054	22.376	78:22	62.7	10.5	26.8	1.99
LDH-11	3.056	22.399	66:34	62.9	10.5	26.5	2.02
LDH-11.5	3.057	22.432	58:42	63.2	10.6	26.2	2.06

Footnote: ¹a = 2d₍₁₁₀₎; ²c = 3d₍₀₀₃₎; ³ where the turbostratic disorder was 10% for each *pH*, except for *pH* 9 (5%); ⁴3:1:2 Cu:Mg:Al target molar ratio corresponds to 62.7 wt%, 10.6 wt% and 26.8 wt% on an oxide basis.

Inspection of the XRD patterns of the LDHs in **Figure 7-1** shows that the position and broadness of the diffraction peaks change with *pH* value during co-precipitation. Many authors assign these changes to a loss of crystallinity. However, the broadening of the low-angle ($2\theta = 5\text{-}25^\circ$) (003) and (006) and high-angle ($2\theta \sim 60^\circ$) (110) peaks arise from the decreasing size of the coherent crystallographic domain in the c and a directions, respectively. The additional non-uniform broadening (*i.e.* due to factors other than crystallite size) of the mid-angle ($2\theta = 25\text{-}60^\circ$) (*h*0*l*) and (0*kl*) reflections occur due to structural disorder within the LDHs.^{268–272}

LDHs contain two-dimensional positively charged brucite-like metal hydroxide layers, which comprise of hexagonal packed hydroxyl groups with the metal cations occupying alternative layers of octahedral sites. The brucite-like layers are separated by interlayer anions and water. The stacking sequence of the layers can give rise to different polytype structures. Bookin and Drits performed a comprehensive evaluation of potential two and three layer polytypes.^{263,273} In their work, the hydroxyl groups in the brucite-like layers (a-b plane perpendicular to the direction of layer stacking) can occupy an A, B or C position in the layer (**Figure 7-3a**). The corresponding metal cations can occupy an interstitial position a, b, or c. A single brucite-like layer can be represented as AbC (similar to the sites of spheres in close packing). The position of the cation can be omitted (*i.e.* AbC becomes AC) as it depends on the position of the hydroxyl groups. Stacking of two layers can result in the formation of two different interlayer geometries due to the position of the hydroxyls in the upper sheet of the lower layer and the lower sheet of the next layer. Assuming the bottom layer occupies positions AC, the lower sheet of hydroxyls in the next layer can either (i) position directly above the top sheet hydroxyls, *e.g.* AC=CA, forming a trigonal

prism interlayer region (P-type interlayer denoted by =; **Figure 7-3b**); or (ii) position in A or B sites, e.g. AC–AB and AC–BC, forming an elongated octahedra interlayer region (O-type interlayer denoted by –; **Figure 7-3c**). The two- and three-layer polytypes can be derived based on the hydroxyl sequence in the layers.

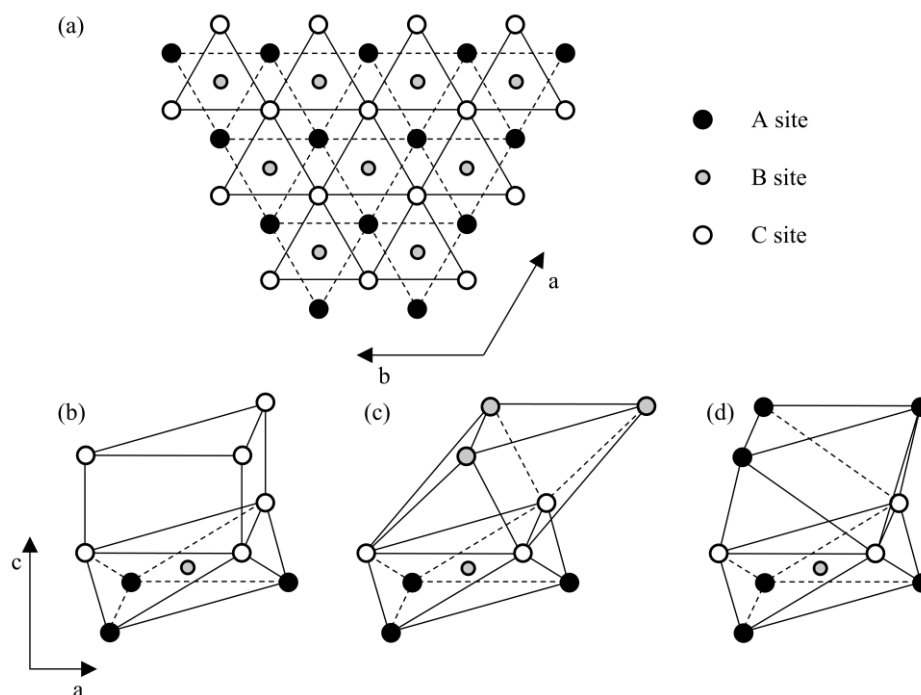
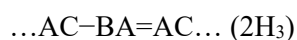
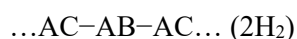
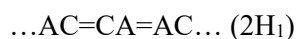


Figure 7-3: Structure of LDH materials. (a) hexagonally packed atom positions in the brucite-like layer; and stacking of layers with (b) trigonal P-type (e.g. AC=CA), and (c,d) octahedral O-type interlayer sites (e.g. AC–BA and AC–AC). Only the lower hydroxyl groups of the upper layer is shown. Large circles are hydroxyl groups, small circles are cations. Adapted from Bookin and Drits.²⁶³

The possible two-layer polytypes are presented in **Figure 7-4**. Structure 1 shows the simple one-layer polytype (AC repeating), structures 2 and 4 are structurally equivalent (only O-type interlayers), structures 3 and 6 are also structurally equivalent (alternating O-type and P-type interlayers), and structure 5 has only P-type interlayer regions. Therefore, for two-layer structures, only three different polytypes exist:



The 2H_1 polytype is the most commonly occurring two-layer polytype in naturally occurring and synthetic LDHs.²⁷⁴ The structural nomenclature developed by Bookin, Drits and Cherkashin refers to

the number of layers (2), symmetry (H, hexagonal), and numerical subscript for each unique polytype.^{263,273}

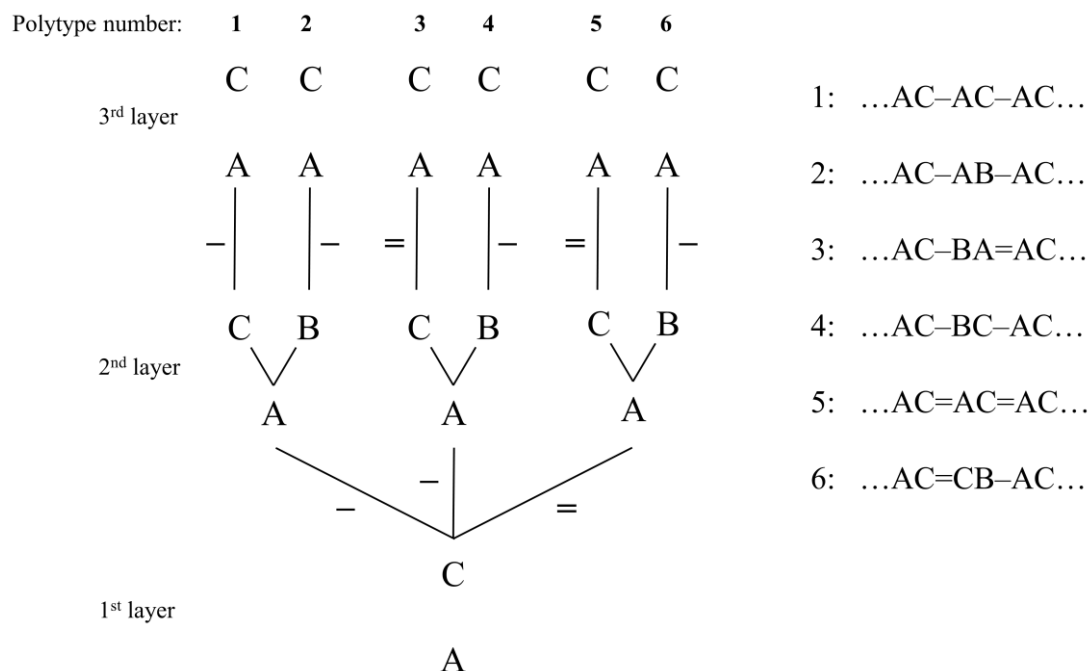


Figure 7-4: Scheme for derivation of two-layer polytypes. Adapted from Bookin and Drits.²⁶³

The possible three-layer polytypes can be derived using the same principle. For three-layer structures, nine possible polytypes exist. Polytypes containing only P-type or O-type interlayers are denoted 3R₁ and 3R₂, respectively.



Naturally occurring Mg-Al LDHs containing CO₃²⁻ as the interlayer anion form as either 2H₁ (hexagonal manasseite) or 3R₁ (rhombohedral hydrotalcite) polytypes.¹⁷⁶ Both polytypes contain only P-type interlayers, which facilitate the inclusion of interlayer carbonate anions.²⁷⁵ Synthetic LDHs containing interlayer carbonate have been found to form with an intergrowth of 3R₁ and 2H₁ polytypes,²⁷⁶ e.g. an LDH could have the stacking sequence ...AC=CB=BA=AB=BC=CA..., where a 2H₁ motif exists within a 3R₁ matrix (**Figure 7-5a**). The program DIFFaX (Diffracted Intensities from Faulted Xtals²⁷⁷) has previously been used to quantify the type and amount of polytypes in faulted LDH structures. In DIFFaX, LDHs are formed by stacking layers using stacking vectors. Each layer may be represented as AbCX, where A and C represent the hydroxyl group positions, b represent the metal cations and X represents the interlayer carbonate and water positions. The appropriate stacking vector can simulate the different polytypes. The 3R₁ polytype is obtained by translating the AC layer by stacking vector

(2/3, 1/3, 1/3). The 2H₁ polytype is obtained by defining a second layer, CA, and using stacking vector (0, 0, 1/2). A random mixture of these polytypes can be generated in DIFFaX by specifying the stacking probabilities of the polytypes to simulate the faulted structure. The XRD pattern of the crystal structure can then be simulated by DIFFaX. **Figure 7-5** demonstrates the broadening of (*h*0*l*) and (0*k**l*) reflections in the mid-angle region ($2\theta = 25\text{--}60^\circ$) arising from the random intergrowth of the 3R₁ and 2H₁ polytypes. Turbostratic disorder is another type of disorder that results in the non-uniform broadening of peaks. Turbostratic disorder arises from the random orientation of successive layers and is simulated using the random stacking vector (*x*, *y*, 1/3), where *x* and *y* are random.

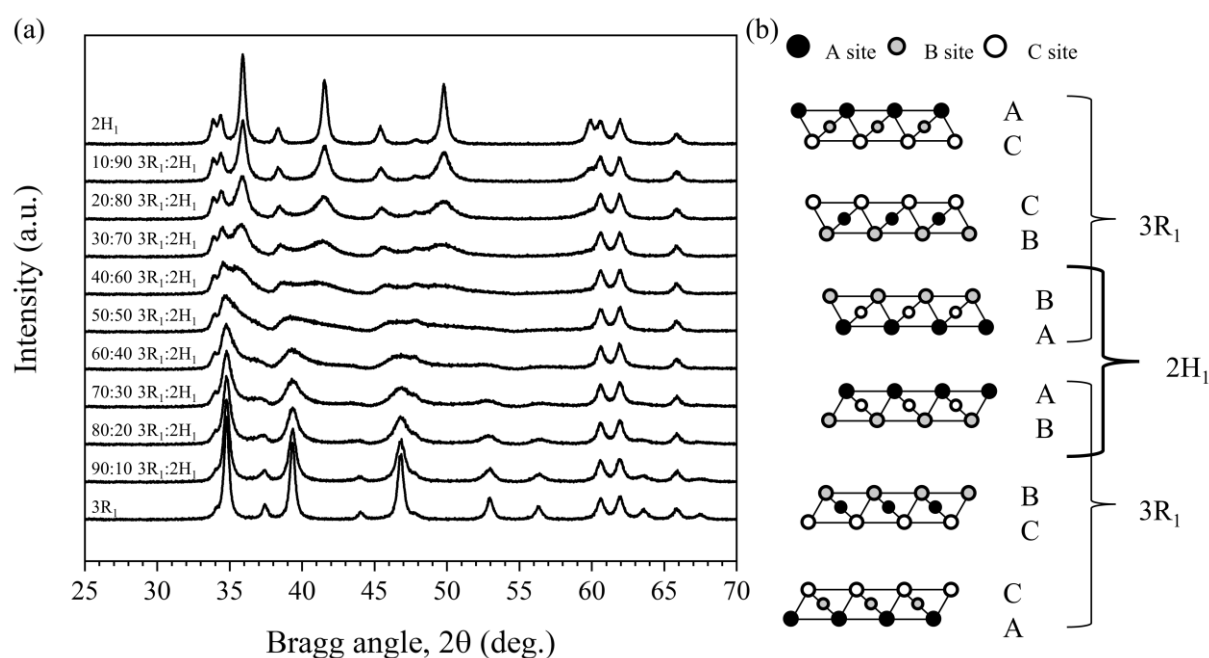


Figure 7-5: Simulation of stacking faults using FAULTS. (a) XRD patterns showing non-uniform broadening of mid-range peaks for increasing amounts of 2H₁ motif in 3R₁. (b) example of 2H₁ stacking fault in 3R₁ structure. Large circles are hydroxyl groups, small circles are cations.

In DIFFaX, the probabilities of stacking vectors are manually varied until a good visual fit between the simulated and observed patterns is achieved. In this chapter, the faulted structures were simulated using the program FAULTS,²⁷⁸ which is based on the DIFFaX formulation. In FAULTS, the probabilities of the stacking vectors can be refined by minimising the square error between the simulated and experimental XRD patterns. The AbCX layer was defined using the atomic position co-ordinates reported for hydrotalcite (ICSD no. 81963, **Table 7-2**). Unit cell parameters *a* and *c* were determined by peak fitting of the XRD patterns (**Table 7-1**) and the occupancy of the metal atoms were taken from the results of XRF (**Table 7-1**). Instrumental parameters *u*, *v*, *w* and *x* were determined from the refinement of a Si standard. The full width at half maximum (FWHM) of the (110) LDH peak is relatively unaffected by stacking faults; therefore, the simulated (110) peak was broadened to match the

experimental pattern to account for crystallite size effects and facilitate the fitting process.^{269,271,275} The probabilities of the stacking vectors (*i.e.* the ratio of 3R₁ to 2H₁) were determined using FAULTS for different amounts of turbostraticity incorporated into the structure (0 to 30% in steps of 5%).

Table 7-2: Co-ordinates and occupancies of atomic positions in the AbCX layer

Atom (position)	x	y	z	Occupancy
O (C)	0.6667	0.3333	-0.04383	1
Cu (b)	0	0	0	0.5000
Mg (b)	0	0	0	0.1667
Al (b)	0	0	0	0.3333
O (A)	0.3333	0.6667	0.04383	1
C	0.6667	0.3333	0.1667	0.0830
C	0	0	0.1667	0.0830
O	0.2408	0.4817	0.1667	0.1667
O	0.2408	0.7592	0.1667	0.1667
O	0.5183	0.7592	0.1667	0.1667
O	0.4258	0.8517	0.1667	0.1667
O	0.4258	0.5742	0.1667	0.1667
O	0.1483	0.5742	0.1667	0.1667

The simulated diffraction patterns in the 2θ region 30-65° are presented in **Figure 7-6**. The peak positions in the mid- 2θ region correlate well with those expected for the 3R₁ polytype, and the non-uniform broadening of lines was simulated by the random intergrowth of the 3R₁ and 2H₁ polytypes. The amounts of 3R₁ and 2H₁ are shown in **Table 7-2**. The amount of turbostratic disorder present in the materials was difficult to quantify. In general, a low amount of turbostratic disorder was found and was taken to be 10% for each *pH* except for *pH* 9.5, where a value of 5% was used. The incidence of 2H₁ stacking faults was determined to increase with increasing co-precipitation *pH*.

The effect of *pH* on the incorporation of stacking faults in LDHs is relatively unstudied. Radha *et al.* investigated the effect of synthesis *pH* on the incorporation of stacking faults in Co-Fe and Co-Al LDHs.²⁶⁹ For both LDH systems, the materials co-precipitated at a *pH* 10 incorporated a higher proportion of stacking faults (2H₁ motifs in 3R₁) than those synthesised at *pH* 7-8. Faour, Prévot and Taviot-Gueho also studied the effect of different synthesis routes on the faulted structure of Ni-Al LDHs.²⁷⁹ Three synthesis routes were considered, (i) co-precipitation at a constant *pH* value of 10, (ii)

co-precipitation under strong alkaline conditions (akin to synthesis at high pH), and (iii) urea hydrolysis (similar to slowly increasing the pH of the reaction medium during precipitation). From the XRD patterns of the materials, the authors determined that the LDHs synthesised *via* urea hydrolysis incorporated the lowest amount of stacking faults, followed by the LDHs prepared at constant pH and the high alkaline medium method. These results are consistent with the trends observed by Radha *et al.* and the analysis of the LDH materials in this work.²⁶⁹

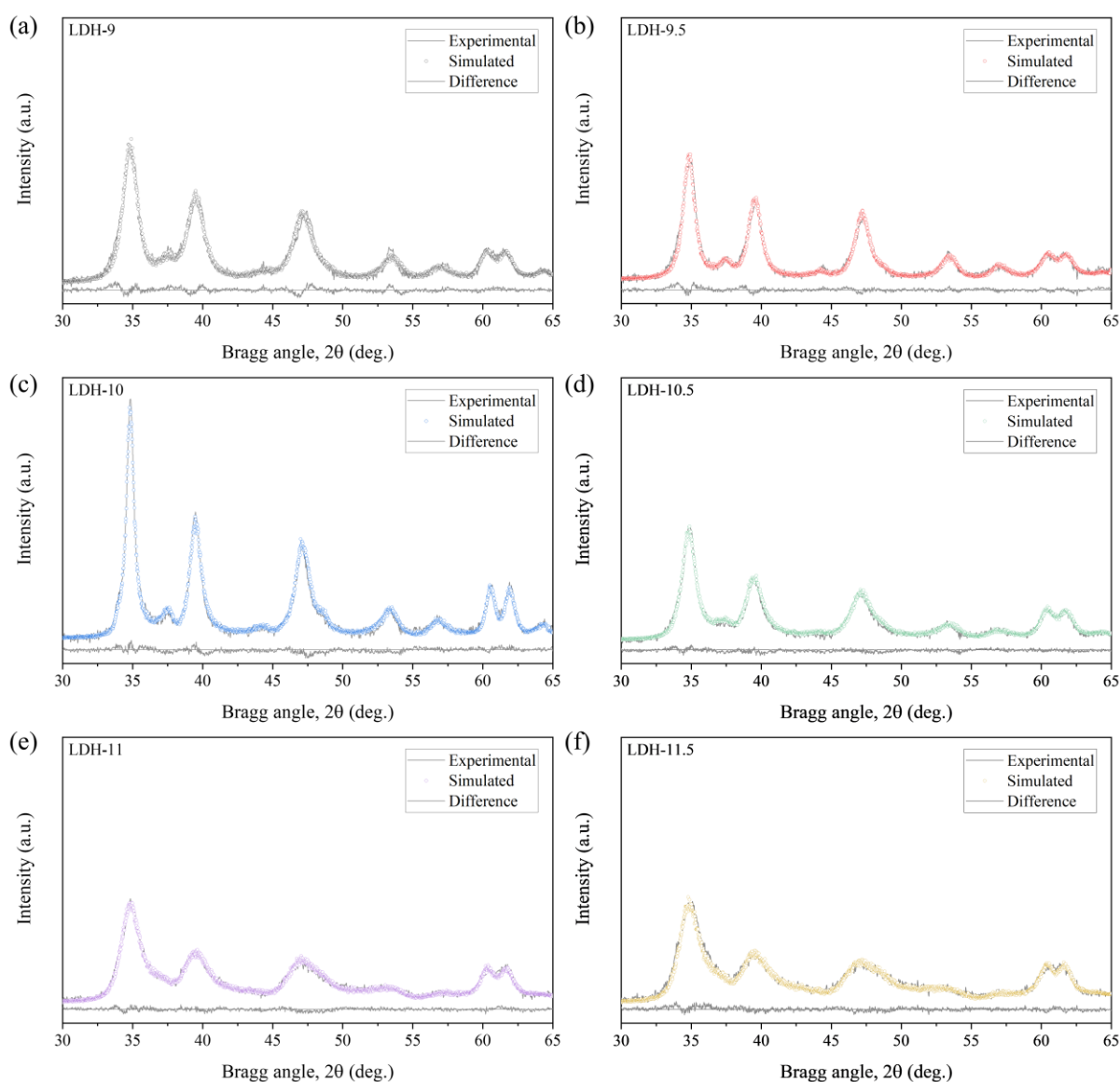


Figure 7-6: Results of FAULTS simulations to determine stacking faults in LDH structure. For LDHs co-precipitated at (a) pH 9, (b) pH 9.5, (c) pH 10, (d) pH 10.5, (e) pH 11, and (f) pH 11.5 for 300 min.

To understand the incorporation of stacking faults in LDHs, Radha *et al.* considered the thermodynamic stability of the different polytypes.²⁶⁹ The free energy of LDH formation is a function of enthalpy and

entropy, where the enthalpic component dominates, especially at low temperatures. Factors that affect the enthalpy of an LDH system include,

- (i) intra-layer bonding within the brucite-like sheet;
- (ii) bonding within the interlayer;
- (iii) ionic bonding between the positively charged brucite-like sheet and interlayer anions;
- and
- (iv) hydrogen bonding between the brucite-like sheet and the interlayer CO_3^{2-} and water molecules.

Polytypes are constructed using the same base brucite-like sheet and interlayer species. Therefore, the contributions from factors 1 and 2 can be assumed to remain the same for all polytypes. Factor 3 depends on the positive charge of the brucite-like layer, which depends on the ratio of divalent to trivalent metal cations. From **Table 7-1**, the LDHs co-precipitated at pH 9 incorporated a higher amount of trivalent cations than the other LDHs, and the ratio of divalent to trivalent metal cations is similar for the remaining LDHs co-precipitated at constant pH between pH 9.5 to 11.5. Therefore, the enthalpic contribution from factor 3 is constant for different polytypes for each pH (as the same layer and interlayer is used to construct the polytypes). Still, the magnitude of the enthalpic contribution for each pH is slightly different due to the small differences in layer composition. Hence, factor 4, the hydrogen bonding between the brucite sheet and the interlayer species, is thought to be the chief determinant of polytype selectivity.^{269,271} The carbonate anion is known to intercalate between the brucite-like layers in such an orientation that is compatible with P-type interlayer sites to maximise hydrogen bonding and the enthalpy of the system. Therefore, the $3R_1$ and $2H_1$ polytypes are expected to have comparable enthalpies. It follows that, the entropy of the system must be considered, which arises from disorders in the form of stacking faults. By increasing the entropy of the crystal while maintaining the enthalpy, stacking faults increase the thermodynamic stability of the system. In accordance with classical nucleation theory, the rate of nucleation is expected to increase with increasing pH ,¹⁸² and therefore, the incorporation of stacking faults into the LDH structure may arise due to the much larger number of initial nuclei stacking together at higher pH values. The effect of stacking faults on the properties of LDHs is relatively unstudied. Some authors have suggested that the electrochemical,²⁸⁰ thermal,²⁷¹ and mechanical²⁸¹ properties may be affected by stacking faults, but more research is needed in this area. Nevertheless, the results of the structural analysis performed using FAULTS show that the broadening of peaks observed in **Figure 7-1** can be assigned a combination of crystallographic size effects and stacking faults in the material structure, not a reduction in the crystallinity of the LDHs.

7.3.2 Chemical characterisation

The results of XRF are shown in **Table 7-1**. The Mg content of the LDH-9 is well below the target value of 10.3 wt% on an oxide basis. The Cu, Mg and Al contents of the LDH-9.5 through LDH-11.5 are much closer to their target values. From **Table 7-1**, it appears that cell parameter *a* remains relatively constant, while parameter *c* increases with increasing *pH*. The cell parameter *c* is a function of the interlayer distance. Studies of synthetic CO_3^{2-} containing Mg-Al,^{170,282} Ni-Al,¹⁷⁰ Mg-Ga²⁸² LDHs and natural Mg-Al LDHs^{283,284} have found that the *c* parameter decreases with increasing values of M^{3+} . This effect has been attributed to an increased electrostatic interaction between the negatively charged interlayers and increasingly positively charged brucite-like layers. From **Table 7-1**, the LDHs were found to contain decreasing amounts of M^{3+} (Al^{3+}) with an increase in synthesis *pH*, which correlate with the observed decrease in the *c* parameters.¹⁷⁶

Previous studies of Mg-Al LDHs prepared *via* co-precipitation have reported the formation of Al-rich (or Mg-deficient) LDHs at *pH* values below 9.^{187,285} Seron & Delorme studied the effect of co-precipitation *pH* on the Mg/Al content of LDHs using the increasing *pH* method, where an alkaline solution of NaOH and Na_2CO_3 was added at a constant rate to a reaction vessel containing a metal nitrate solution causing the *pH* of the solution to increase over time.¹⁸⁷ The precipitate was regularly withdrawn and analysed. Below a *pH* value of 8.5, they observed the formation of an Al species, likely $\text{Al}(\text{OH})_3$ ¹⁸³ or dawsonite, $\text{NaAlCO}_3(\text{OH})_2$.²¹⁶ At a *pH* value of 8.5, they observed the formation of an Mg-deficient LDH species, which incorporated more Mg upon further increase of the *pH* to 10. Tamura *et al.* calculated the solubilities of $\text{Al}(\text{OH})_3$, $\text{Mg}(\text{OH})_2$ and Mg-Al LDHs containing NO_3^- in the interlayer (Mg-Al- NO_3 LDH) as a function of *pH*.²⁸⁶ The domain diagram is shown in **Figure 7-7**. For LDHs prepared using the increasing *pH* method using NaOH as the co-precipitating agent, Al^{3+} is first expected to form $\text{Al}(\text{OH})_3$ and Mg^{2+} is slowly incorporated into the structure to produce Mg-Al LDHs. In contrast, for the decreasing *pH* method (addition of metal nitrate into alkali solution), the formation process of Mg-Al LDH is theorised to occur through the direct conversion of $\text{Al}(\text{OH})_4^-$ and $\text{Mg}(\text{OH})_2$.^{177,286,287} Impurity phases of $\text{Mg}(\text{OH})_2$ are generally not observed in the XRD patterns of Mg-Al LDHs prepared using the decreasing *pH* method, suggesting that the $\text{Al}(\text{OH})_4^-$ and Mg^{2+} are immediately converted to Mg-Al LDHs at high *pH*.^{177,287}

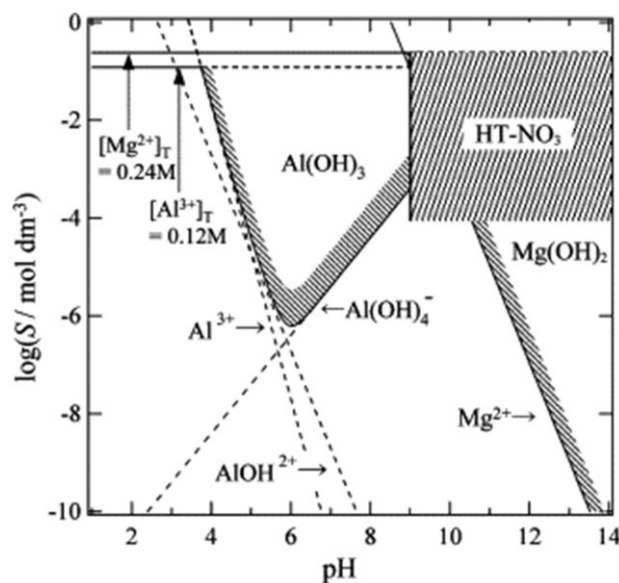
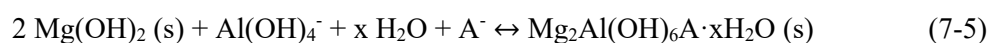


Figure 7-7: Domain diagram of $\text{Al}(\text{OH})_3$, $\text{Mg}(\text{OH})_2$, and Mg-Al-NO_3 LDHs. Solubility is denoted as S on the y axis. Reproduced with permission from Elsevier.²⁸⁶

To further investigate the formation of LDHs, the thermodynamic calculations carried out using SPANA in chapter 4 were re-examined. The calculations were performed for Mg-Al LDHs due to an absence of thermodynamic data for Cu-Mg-Al LDHs. A plot of the equilibrium concentrations of LDHs and constituent components as a function of pH is shown in **Figure 7-8**. The results show that Mg-Al LDHs are predicted to form in low equilibrium concentrations at pH 8.2. The formation of MgCO_3 and $\text{Al}(\text{OH})_3$ is favoured until a pH value of 9.5, where the equilibrium concentrations of Mg-Al LDHs become significant.

It is likely that the species involved in the formation of Mg-Al LDHs during co-precipitation at constant pH change with increasing pH .^{177,286,287} At lower pH values (~ 9), the reaction may proceed predominantly through reaction (7-4) (where A^- is the interlayer anion), where the predominant Al and Mg species are $\text{Al}(\text{OH})_3$ and Mg^{2+} , respectively, which may limit the amount Mg that can be incorporated into the Mg-Al LDH (lower Mg content in LDH-9, **Table 7-1**). With increasing pH , the predominant Al and Mg species increasingly become dissolved $\text{Al}(\text{OH})_4^-$ and $\text{Mg}(\text{OH})_2$, respectively, which may react more readily to form Mg-Al LDHs through reaction (7-5). The increasing stability of the dissolved $\text{Al}(\text{OH})_4^-$ with increasing pH may also explain the decreasing Al content in the LDHs, and the corresponding increase in the molar ratio of M^{2+}/M^{3+} in the materials (**Table 7-1**).



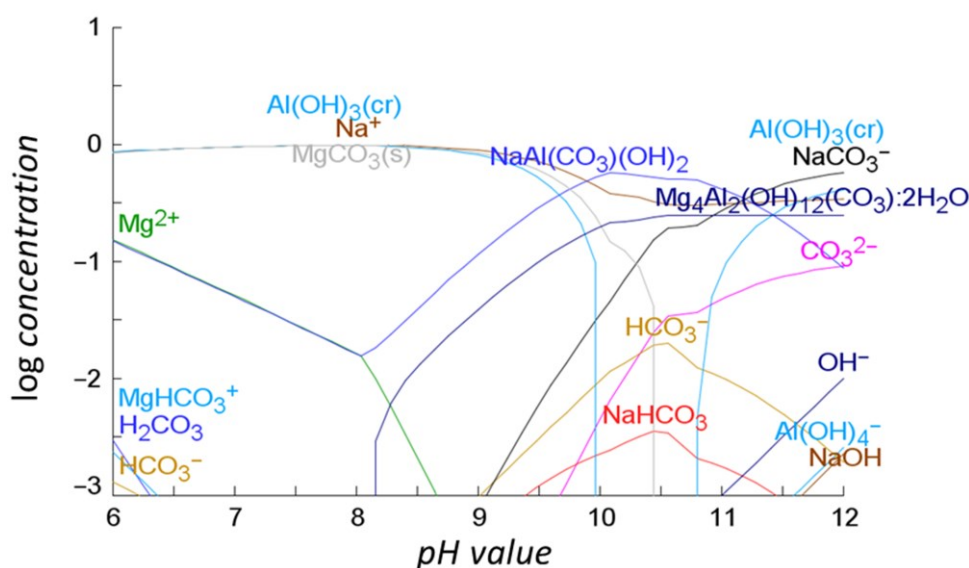


Figure 7-8: Plots of equilibrium compositions as a function of the pH value. The plot was generated with SPANA using data from DATABASE²¹² as well as literature values for the compounds listed in Table 4-3.

7.3.3 Structural characterisation

The morphology of the LDHs was examined using SEM (**Figure 7-9**). From the SEM images, the precipitated materials are composed of an agglomeration of platelet-like particles, characteristic of LDHs produced *via* co-precipitation.^{288,289} For each synthesis *pH*, the dimensions of 90 randomly assigned platelets over three SEM images (*i.e.* 30 platelets per image) at 150k magnification were analysed using ImageJ.²⁹⁰ The size distributions of the diameter (lateral width) and height (thickness) of the LDHs are shown in **Figure 7-10**, and the average dimensions are reported in **Table 7-3**. The broad size distributions observed in **Figure 7-10** and shown in **Table 7-3** are consistent for LDHs precipitated using co-precipitation due to the large difference in residence time between the first and last additions of the precipitating solutions.^{182,291} From **Table 7-3**, the diameter and height of the LDH platelets vary from 58 to 237 nm and 15 to 27 nm, respectively.

Table 7-3: LDH platelet dimensions. Determined using XRD and SEM for the LDHs co-precipitated at *pH* values between 9 and 11.5 for 300 min.

pH	<i>L</i> (003) (XRD)			Height (SEM)	<i>L</i> (110) (XRD)			Diameter (SEM)	Ratio of SEM platelet diameter to <i>L</i> (110) (-)
	(nm)				(nm)				
	Average	Upper	Lower	Average	Upper	Lower			
	(nm)	(nm)	(nm)	(nm)	(nm)	(nm)			
9	28	31	26	27 ± 6	12	13	11	201 ± 64	17
9.5	22	23	20	26 ± 5	10	11	10	170 ± 56	16
10	21	23	20	23 ± 4	17	19	16	253 ± 89	15
10.5	15	13	12	20 ± 3	8	9	8	118 ± 44	14
11	13	14	13	16 ± 3	7	7	6	71 ± 15	10
11.5	12	12.6	12	15 ± 2	7	7	6	63 ± 18	9

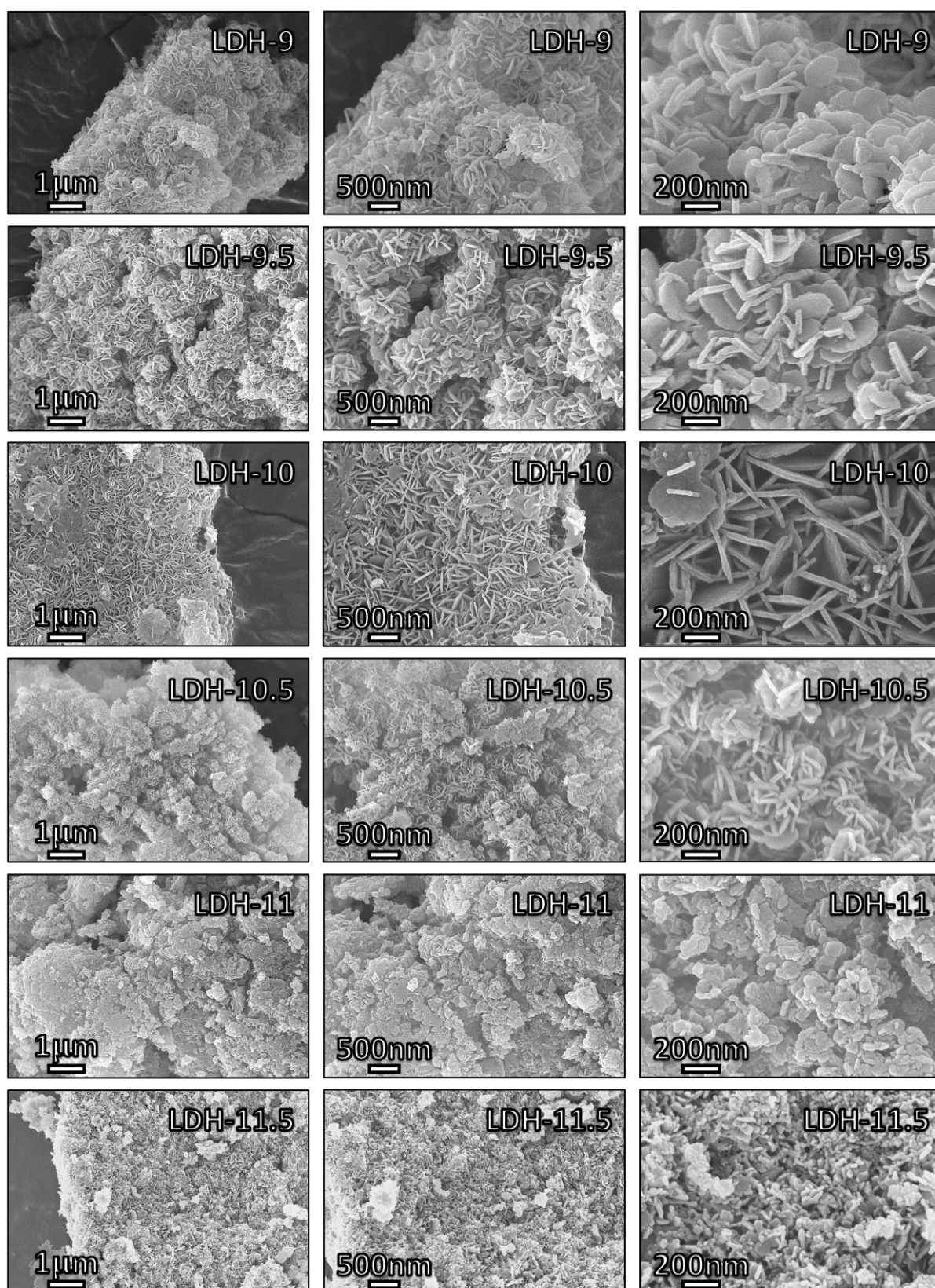


Figure 7-9: SEM images of LDHs co-precipitated at pH values between 9 and 11.5 for 300 min (as indicated). Left to right: magnification of 30k, 50k and 150k.

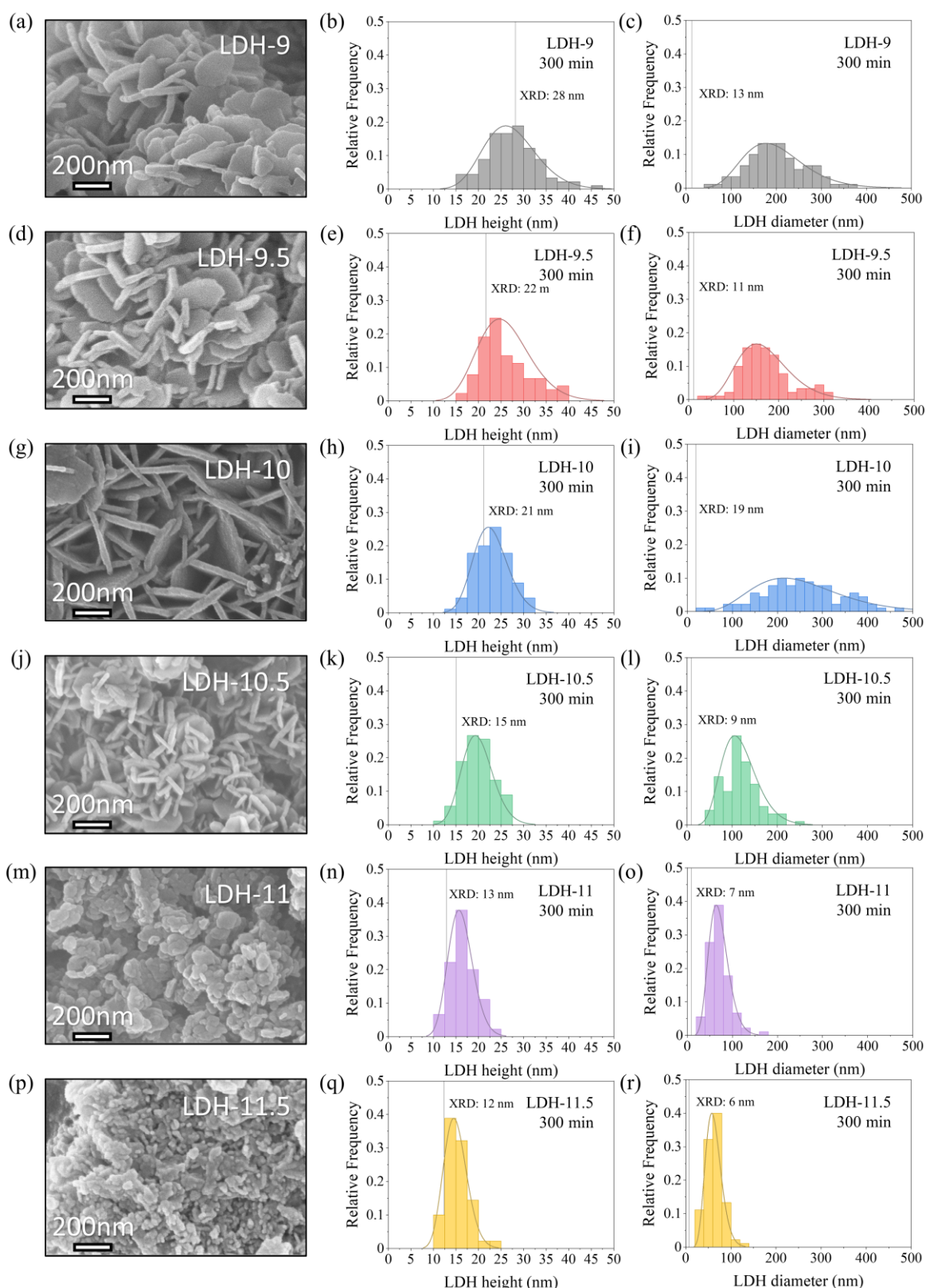


Figure 7-10: Determination of platelet dimensions using SEM. Left to right: SEM images at 200k magnification, distribution of LDH platelet heights and diameters based on 90 platelets over three SEM images at 150k magnification, respectively for (a-c) LDH-9; (d-f) LDH-9.5; (g-i) LDH-10; (j-l) ; LDH-10.5; (m-o) LDH-11; (p-q) LDH-11.5.

The XRD patterns of the LDHs were also used to study the dimensions of the LDH crystallites. The FWHM of the (003) and (110) reflections were used to calculate the size of the coherent crystallographic domains in the c direction ($L(003)$) and a-b plane ($L(110)$), respectively, using the Scherrer equation (**Table 7-3**). The height and diameter of the LDH crystallites correspond with the $L(003)$ and $L(110)$ reflections, respectively.²⁸⁰ **Figure 7-11** and **Figure 7-12** show the peak fitting of (003) and (110) reflections, respectively. As previously discussed, determining the characteristics of the broad (110) reflections required a peak fitting program due to the overlap with neighbouring reflections.

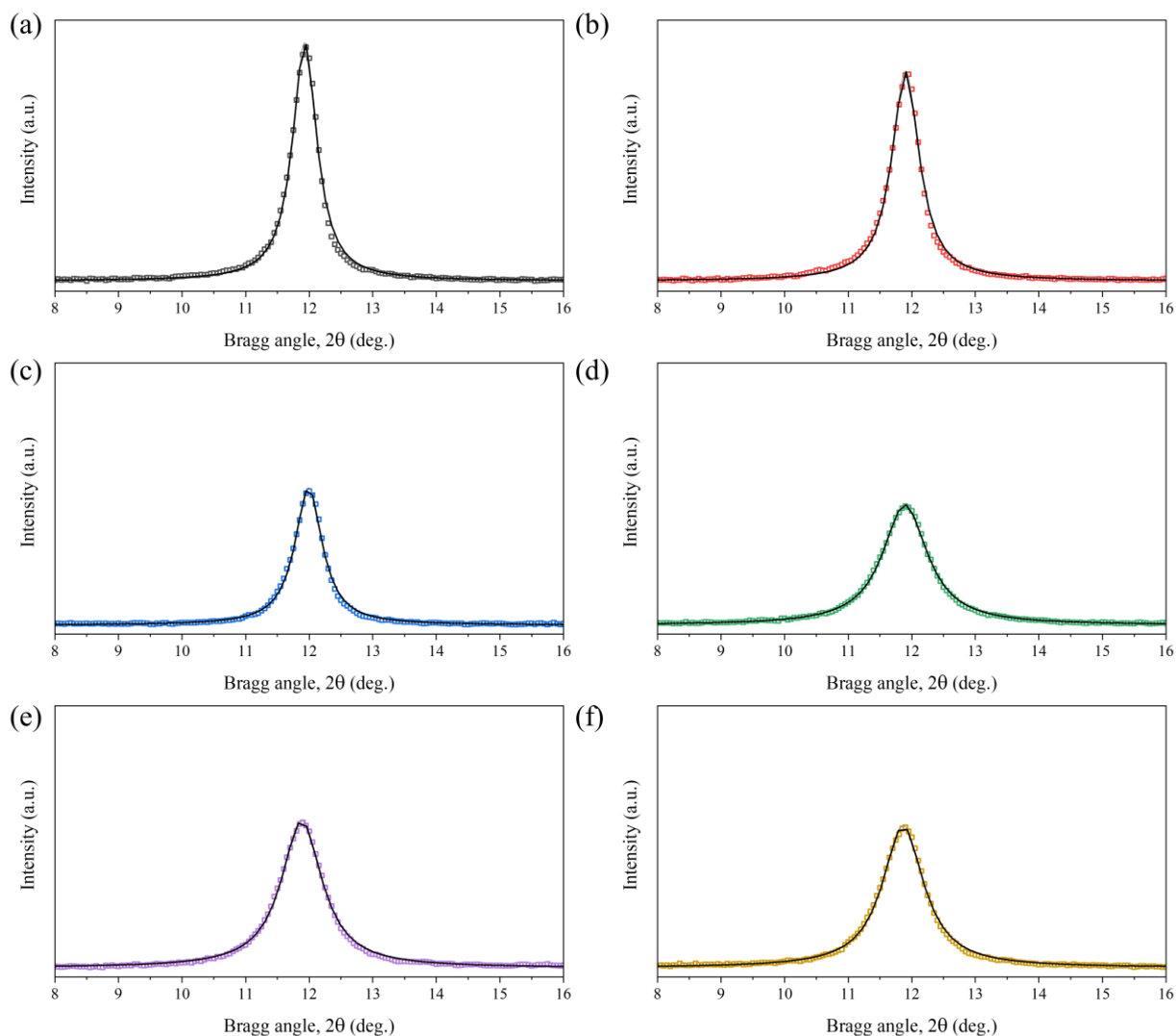


Figure 7-11: Results of peak fitting to determine cell parameter c and $FWHM_{003}$. For LDHs co-precipitated at (a) pH 9, (b) pH 9.5, (c) pH 10, (d) pH 10.5, (e) pH 11, and (f) pH 11.5 for 300 min.

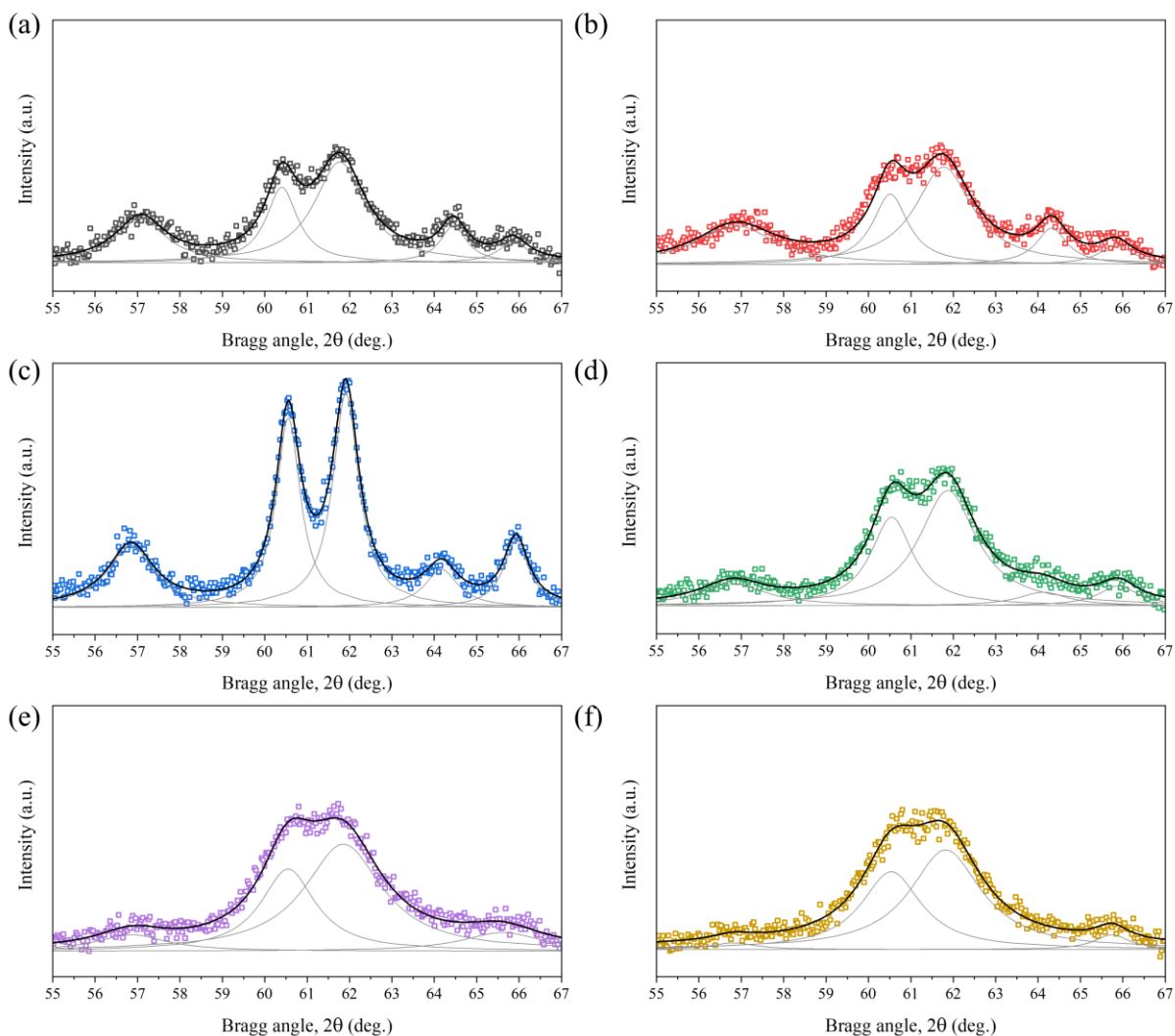


Figure 7-12: Results of peak fitting to determine cell parameter a and $FWHM_{110}$. For LDHs co-precipitated at (a) pH 9, (b) pH 9.5, (c) pH 10, (d) pH 10.5, (e) pH 11, and (f) pH 11.5 for 300 min.

From **Table 7-3**, the heights and diameters of the LDH platelets were found to decrease with increasing pH , except at pH 10, where a local maximum in the diameter was observed. Despite large uncertainties due to the low intensity of the (110) reflection and the assumptions of the Scherrer equation, the overall trends in diameter and height correspond well with SEM analysis (**Figure 7-13**). However, the platelet diameters observed using SEM significantly exceed those determined by evaluating the (110) reflections by an order of magnitude.

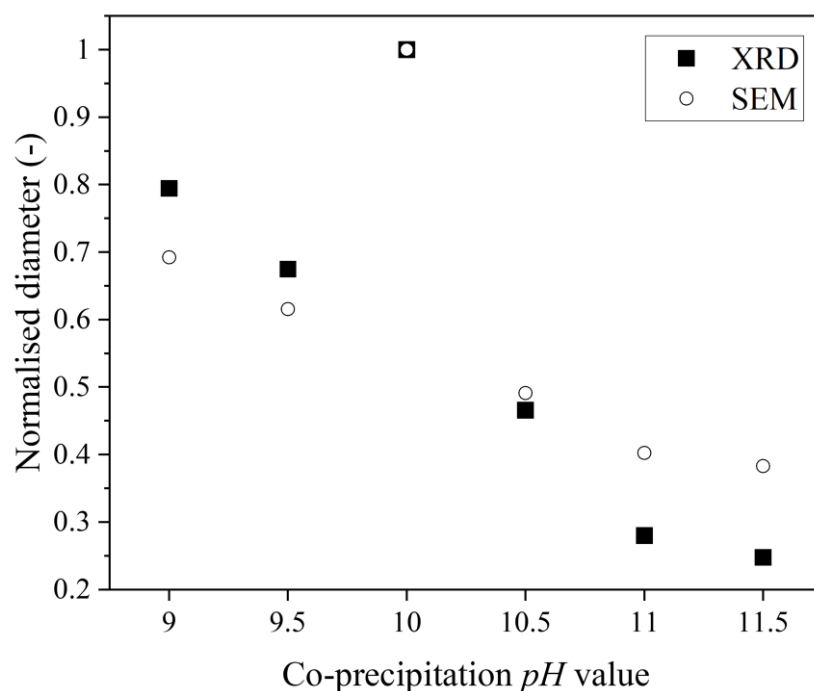


Figure 7-13: Normalised trend in platelet diameter determined by XRD and SEM analysis. LDHs were co-precipitated at a constant pH value between 9 and 11.5 for 300 min.

Materials containing Cu in octahedral sites are affected by the Jahn-Teller effect, where the electron configuration of Cu^{2+} causes distortion of the bond lengths and reduces the long-range order of the materials. Intissar *et al.* studied the impact of increasing Cu content on the “crystallinity” and particle size of $(\text{Mg}_{4-x}\text{Cu}_x)\text{Al}_2\text{OH}_{12}\text{CO}_3$ LDHs.²⁹² They observed that the FWHM of the (110) diffraction peak increased with Cu^{2+} content and concluded that the incorporation of Cu^{2+} decreases the crystallinity within the brucite-like layer of the LDH (**Figure 7-14a**). However, analysis of the SEM images provided by the authors reveals that the size of the LDH platelets synthesised at $x = 0$ and 2 were roughly equal (ca. 50 nm, **Figure 7-14b-c**). Data for the (110) and (113) reflections were extracted from the XRD patterns (**Figure 7-14a**) to calculate crystallite sizes of ~40 and ~15 nm for $x = 0$ and 2, respectively, demonstrating the incorporation of Cu into the LDH structure may not decrease the crystallinity, but decrease the long-range order of the crystallites in the ab plane and weaken the (110) reflection in the XRD pattern. Therefore, the mismatch of crystallite sizes determined from XRD and SEM in this chapter may partly be due to the Jahn-Teller effect rather than low crystallinity. However, this is unlikely to account for the extreme differences in sizes determined using the two techniques, *e.g.* the 17 nm and 250 nm platelet diameters of the LDH-10 determined using XRD and SEM analysis, respectively.

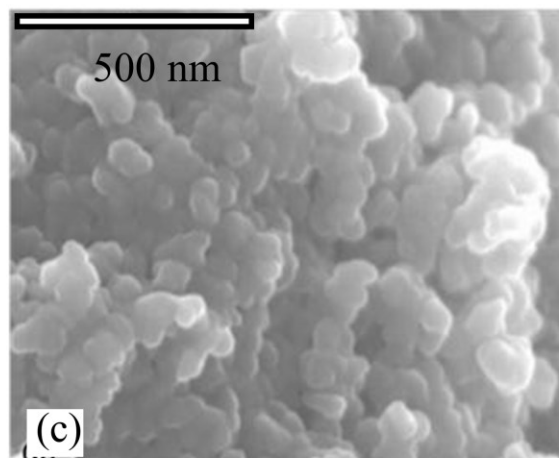
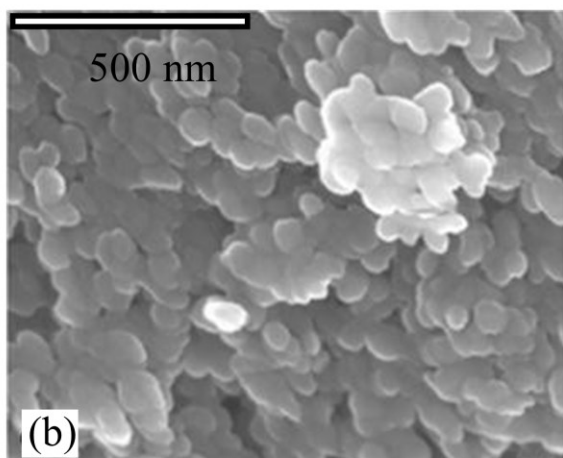
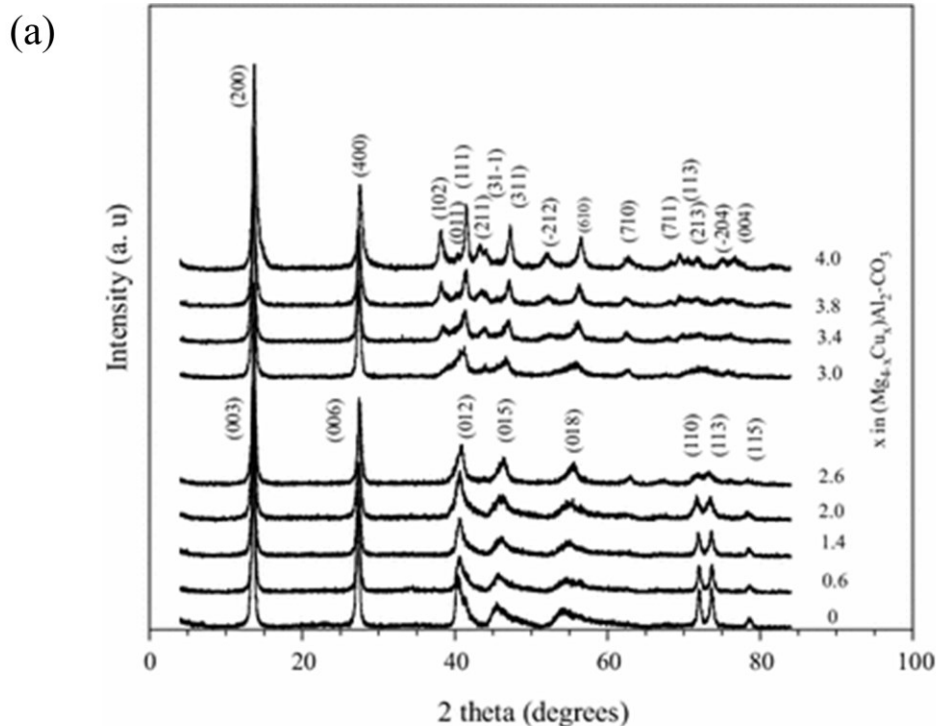


Figure 7-14: Effect of Cu content on properties of Cu-Mg-Al LDHs. (a) XRD patterns of $\text{Cu}_x\text{-Mg}_{(1-x)}\text{Al}_2$ LDHs, where $x = 0$ to 4. SEM images of $\text{Cu}_x\text{-Mg}_{(1-x)}\text{Al}_2$ LDHs where (b) $x = 0$, and (c) $x = 2$. Reproduced with permission from Springer Nature.²⁹²

A further consideration for the disparity between $L(110)$ and the diameter from SEM analysis is the polycrystalline nature of LDH platelets. Significant differences between the platelet diameters determined using XRD and SEM techniques has previously been reported for Ni-Al,²⁸⁰ Zn-Al,²²³ Mg-Al²⁹³ and Cu-Co-Fe²⁹⁴ LDHs, where the LDHs were found to form by non-coherent coalescence of crystallographic domains during synthesis.

The LDH platelets may be polycrystalline, formed of a relatively small number of crystallites in the c direction, which contributes to platelet height, and a large number in the a - b plane, which contributes to the platelet diameter (**Figure 7-15**). Galvão *et al.* investigated the surface energies of the Zn-Al LDHs using DFT calculations to understand the morphologies and formation mechanism of LDH platelets.²⁹⁵ When the surface and interaction energies were combined with morphological results (SEM and AFM), the authors determined that the edges of the LDHs sheets are more unstable than the surface of the platelet. As a result, it is more energetically favourable to form metal–oxygen bonds in the direction parallel to the layer than electrostatic interactions between the positively charged layers and the interlayer species. Therefore, crystallites were more likely to align in the a - b plane rather than the c direction resulting in LDH crystallites with greater diameters than heights. Galvão *et al.* found that the LDH platelet height was comprised of between one to three crystallites and well approximated by $L(003)$. However, the platelet diameter was found to be defined by around 8 to 11 crystallites, *i.e.* the $L(110)$ (~ 30 nm) significantly underestimated the average platelet diameter determined using AFM (~ 350 nm) due to the polycrystalline nature of the LDH platelet (**Figure 7-15**). Considering the Cu-Mg-Al LDHs in this chapter, the number of crystallites contributing to the overall structure was estimated by dividing the diameter and height observed using SEM by $L(110)$ and $L(003)$, respectively. From **Table 7-3**, the number of crystallites contributing to the platelet heights and diameters range from 1 to 2 and 9 to 15, respectively, which agree with the findings of Galvão *et al.*²⁹⁵ Although the number of crystallites in the a - b plane may be overestimated due to an underestimation of $L(110)$ due to the broadening introduced by the Jahn-Teller effect, which does not affect the stacking direction.

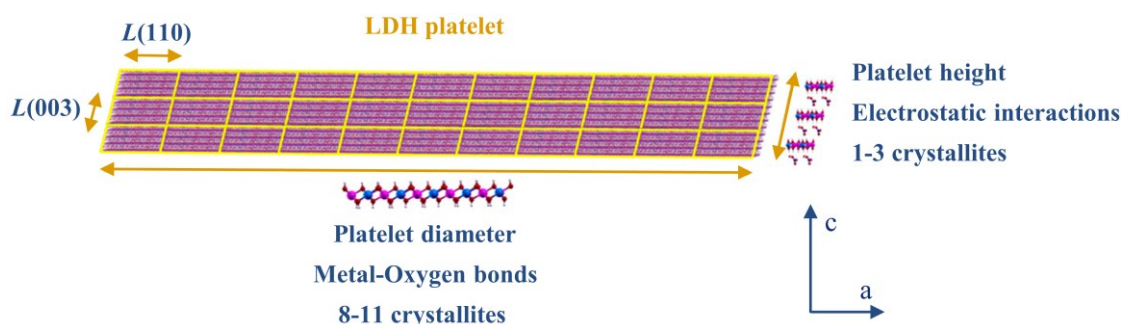


Figure 7-15: Number of crystallites and type of bonds responsible for the morphology of LDH particles. Reprinted (adapted) with permission from²⁹⁵. Copyright 2023 American Chemical Society.

7.3.4 Insights into the formation and growth of layered double hydroxides at different co-precipitation pH values

The growth of Cu-Mg-Al LDHs during co-precipitation at different pH values was studied by preparing the LDHs under constant addition of acid and alkaline solutions for 300 min. Samples were withdrawn at specified time intervals to track the platelet dimensions with time. All samples were analysed using

XRD. The changes in the FWHM of the basal (003) (FWHM_{003}) and non-basal (110) (FWHM_{110}) reflections and size of the coherent crystallographic domains, $L(003)$ and $L(110)$, with time are shown in **Figure 7-16**. For each pH , an increase in $L(003)$ was observed over 300 min. The $L(110)$ increased over 300 min for LDH-9 to 10.5 and remained relatively constant for LDH-11 and 11.5. From **Figure 7-16b**, the $L(110)$ of LDH-10 decreases at a greater rate and to a lower value than for the other pH values, indicating greater growth in the platelet diameter.

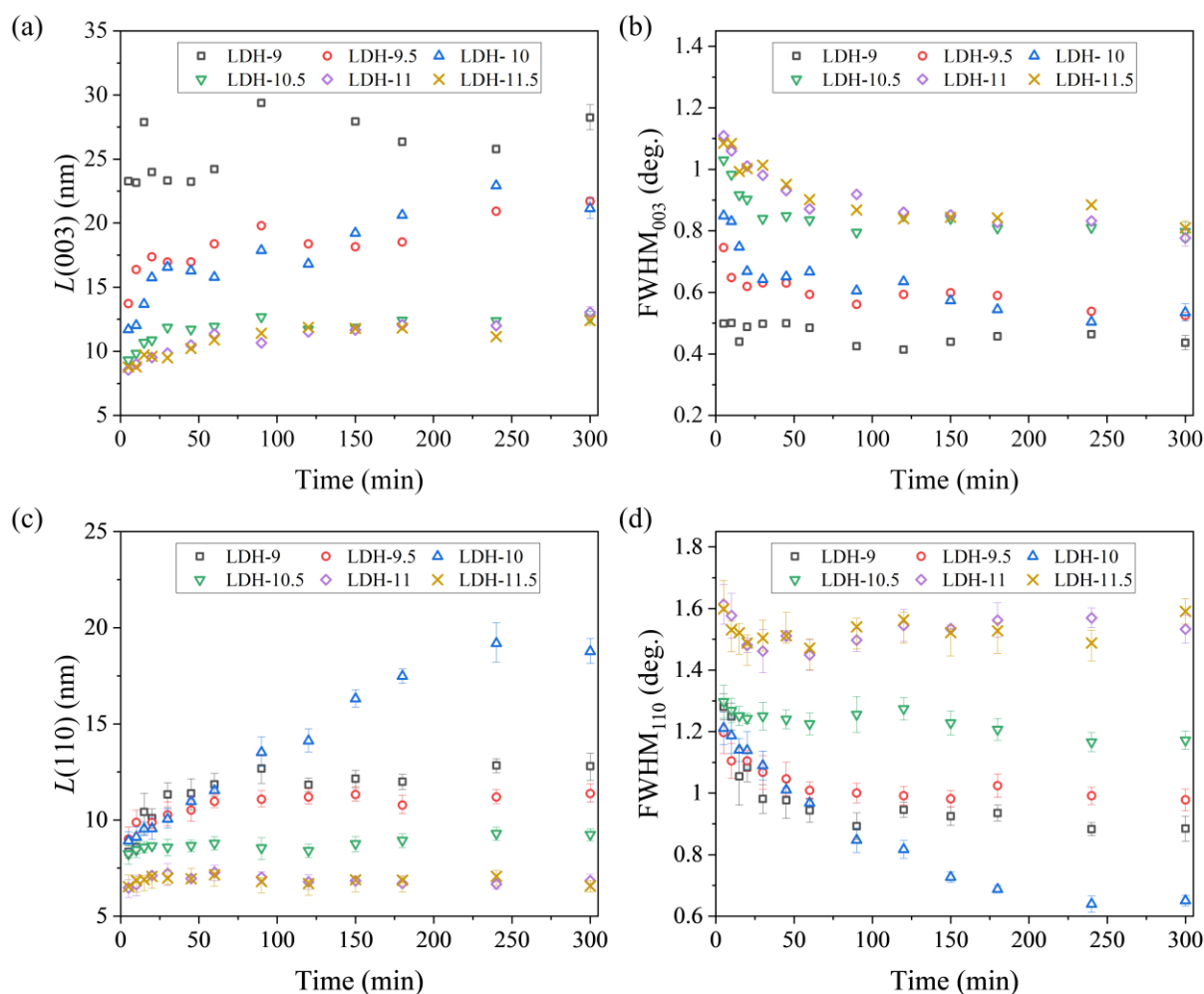


Figure 7-16: *FWHM and platelet dimensions determined by XRD analysis of LDHs co-precipitated at a constant pH value between 9 and 11.5 for 300 min. (a) $L(003)$, (b) FWHM_{003} , (c) $L(110)$ (d) FWHM_{110} of LDHs co-precipitated over 300 min. Platelet dimensions were calculated using the Scherrer equation.*

Samples withdrawn at 5, 30, 90 and 300 min were also characterised using SEM analysis (**Figure 7-17**). The distribution of the platelet diameters of each material is shown in **Figure 7-18**. The large spread in platelet diameters is common for co-precipitated materials. The trend in average particle size over time using SEM is shown in **Figure 7-19a**, and the normalised trends in diameter using XRD and SEM are compared in **Figure 7-19b**. As discussed previously, the platelet diameters determined using SEM

significantly exceed those determined using XRD. However, a comparison of the normalised trends shows that a similar trend in platelet diameter is observed using both techniques, and a maximum platelet diameter is observed for LDH-10.

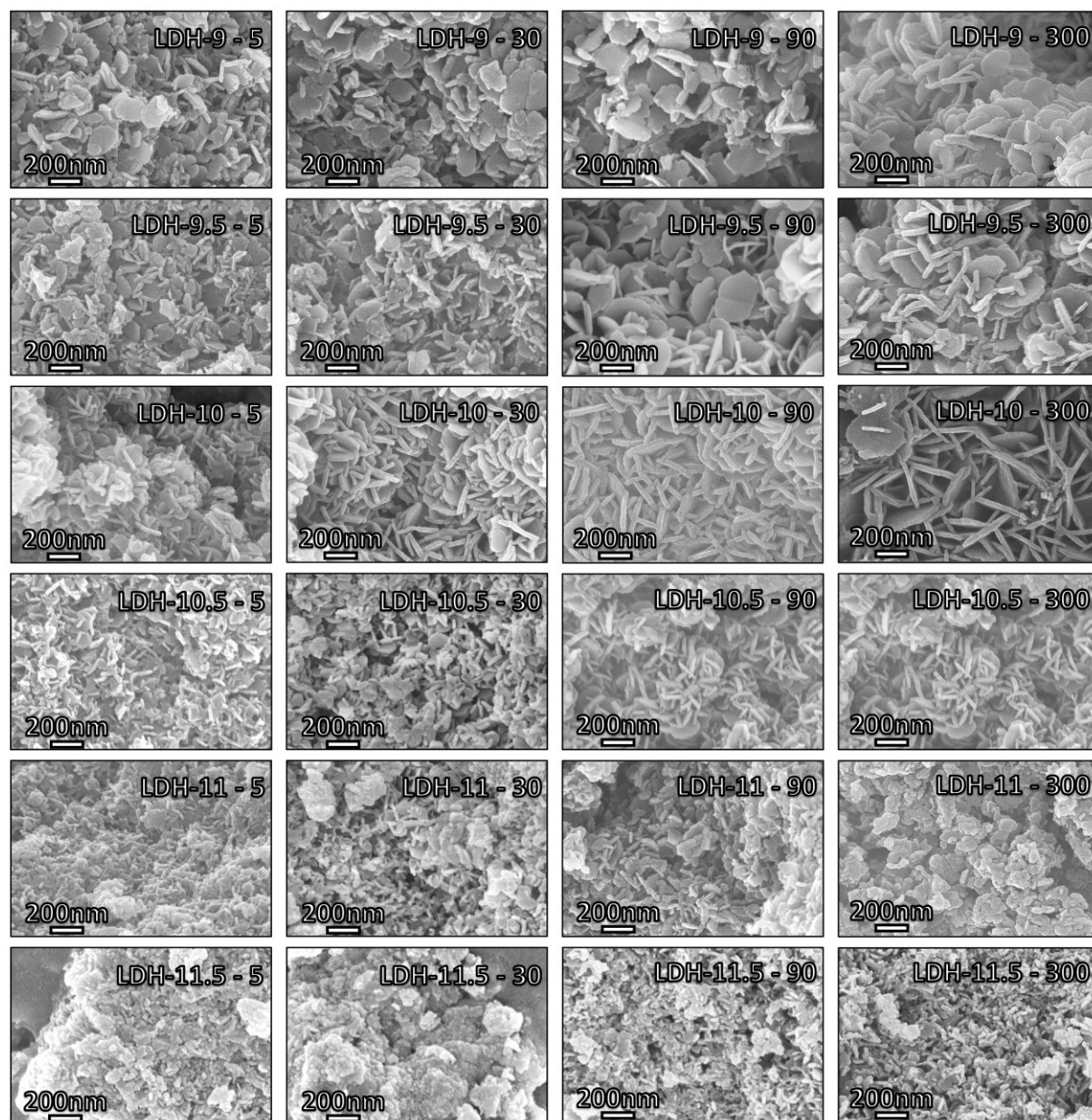


Figure 7-17: SEM images of LDHs co-precipitated at a constant pH value between 9 and 11.5 (as indicated) at 100k magnification. Left to right: samples withdrawn after 5, 30, 90 and 300 min.

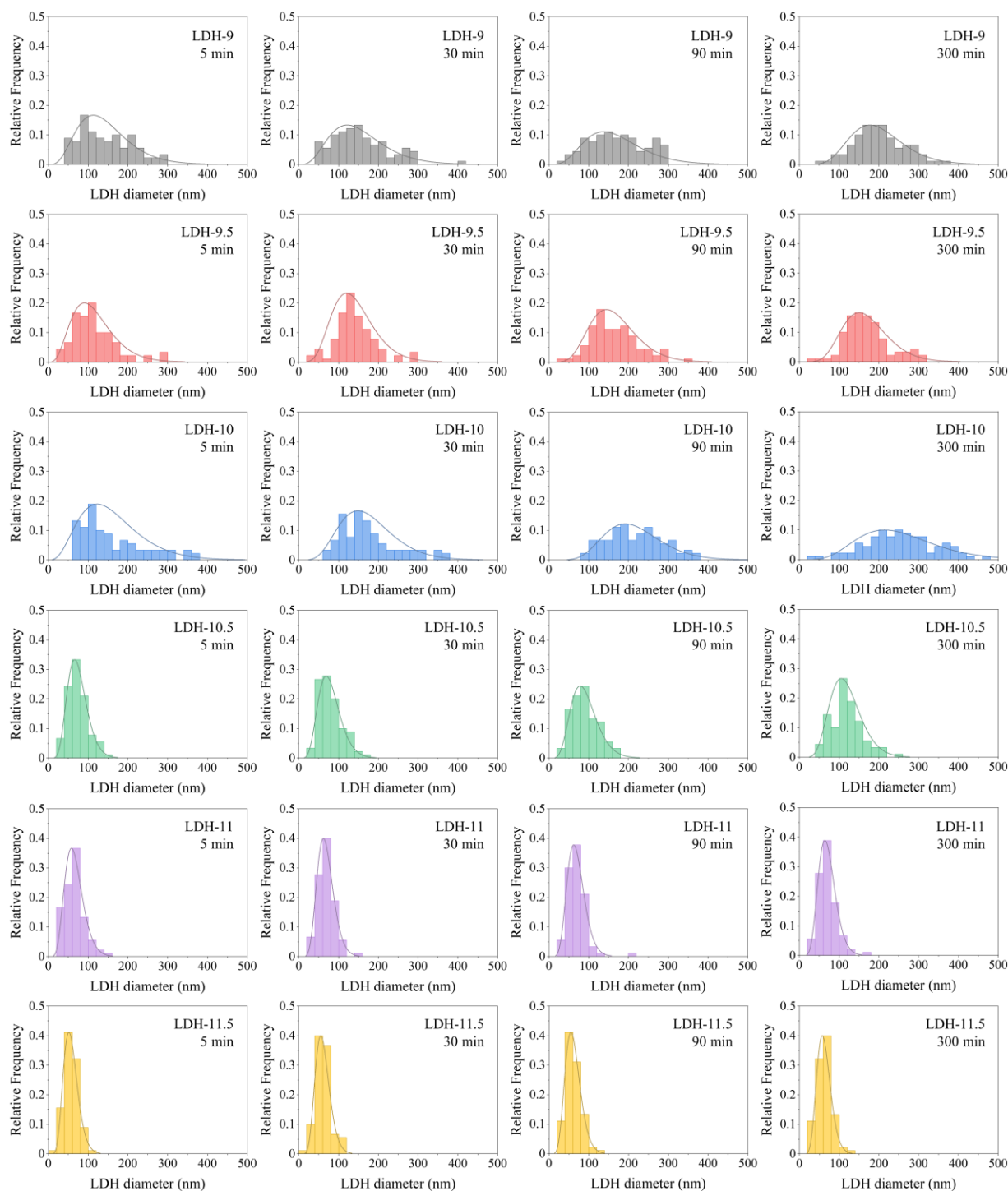


Figure 7-18: Distribution of LDH platelet diameters for LDHs co-precipitated at a constant pH value between 9 and 11.5. Left to right: samples withdrawn after 5, 30, 90 and 300 min. Platelet dimensions are based on 60 platelets over two SEM images (150k magnification) for LDHs synthesised for 5, 30, 90 min and 90 platelets over three SEM images (150k magnification) for LDHs synthesised for 300 min.

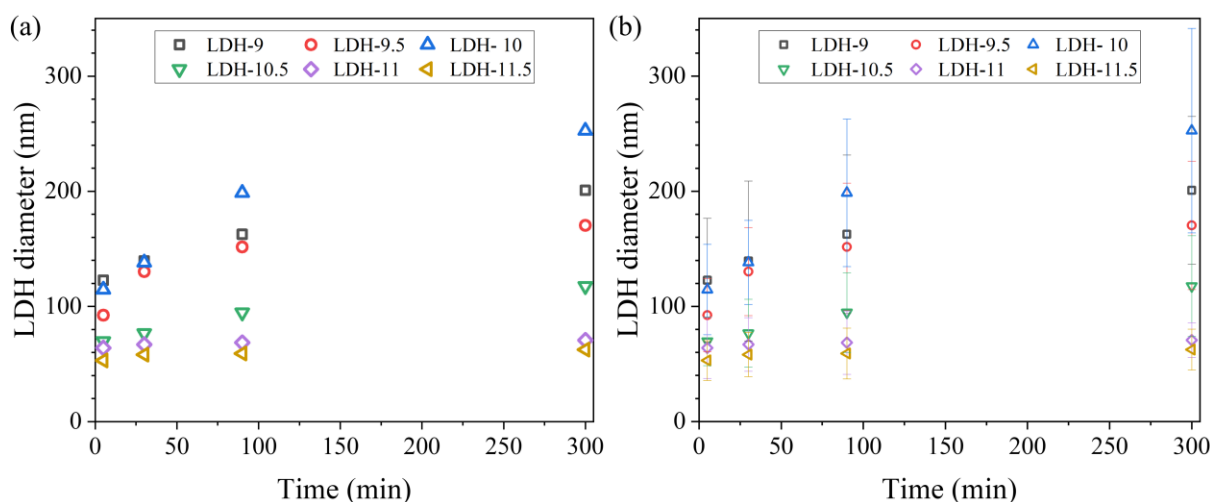


Figure 7-19: Platelet dimensions determined from SEM analysis of LDHs co-precipitated at a constant pH value between 9 and 11.5 for 300 min. (a) LDH diameter (b) LDH diameter including error bars equal to the standard deviation.

In general, co-precipitation comprises three main processes, nucleation, crystal growth and aggregation, each complex and challenging to study.²⁹⁶ Furthermore, the processes during aging are similarly complex and can involve crystal growth, aggregation and other phenomena, such as Ostwald ripening. Supersaturation conditions are needed for co-precipitation to occur and can be achieved by controlling the pH of the solution. At low supersaturation conditions, the nucleation rate is lower, resulting in larger primary crystallites. However, at high supersaturation conditions, the rate of nucleation dominates crystal growth resulting in smaller primary crystallites. Therefore, smaller LDH crystallites would be expected with an increase in synthesis pH and supersaturation conditions.¹⁸² However, while this trend is generally observed over the pH range (**Table 7-3**), the results from SEM and XRD show a large increase in the platelet diameter for LDH-10.

The LDHs co-precipitated at constant pH close to their isoelectric point (IEP; pH where zeta potential = 0) have been reported to show preferential growth in the a-b plane, where the surface charge density is lowest.^{173,186} LDHs are comprised of positively charged brucite-like layers with charge-compensating interlayer anions. The development of electrical charges in LDHs is relatively unstudied compared to metal hydroxides without structural charges, and cationic clays; however, pH has been shown to significantly affect their surface charge distribution in solution.²⁹⁷ LDHs consist of brucite-like layers composed of edge-sharing metal hydroxide octahedrons along the crystallographic a-b plane. The positive structural charge of the layers is derived from the substitution of M^{2+} by M^{3+} ions in the brucite-like layers. The permanent positive charge of the layers is fully compensated by negatively charged anions when LDHs are dried. However, when immersed in an aqueous solution, some anions are released from the structure, which results in excess surface charge and the development of an electric

double layer. In addition, the hydroxyl groups at the basal surface and edges of the LDH layers protonate (positively charged groups) at low pH values and deprotonate (negatively charged groups) at high pH values.

Zeta potential measurements determined an IEP of $\sim pH$ 9.8 for the Cu-Mg-Al LDHs (**Figure 7-20**). A recently developed empirical relationship developed by Yu and Hou was also used to predict the pH at the point of zero charge (pH_{PZC}) of the LDHs.^{298,299} Yu and Hou modified an electrostatic model used to determine the pH_{PZC} developed by Parks³⁰⁰ and improved by Yoon *et al.*³⁰¹ by considering the effective net structural charges of the LDHs that arise from the replacement of M^{2+} by M^{3+} ions in the brucite-like layers. For an LDH containing n distinct components, the general model is given in equation (7-4):

$$pH_{PZC} = A + B\sigma_{st} - C \sum_{i=1}^n f_i \left(\frac{v_p}{L} \right)_i - \log \left(\frac{1 - 2\alpha_{PZNC}}{1 + 2\alpha_{PZNC}} \right) \quad (7-4)$$

where f_i is the atomic fraction of component i ; v_p is the Pauling bond valence, defined as the formal charge of the central metal ion (Z) divided by its coordination number (CN), *i.e.* $v = Z/CN$; L is the sum of the mean M–O bond length at the interior of the solid crystal (\bar{L}) and the O–H, *i.e.* $L = \bar{L} + r_{O-H}$; $(v_p/L)_i$ is the v_p/L of component i ; α_{PZNC} is a parameter defined by $\alpha_{PZNC} = \sigma_{st}/eN_sN_s$, where e is the elementary charge and N_s is the total density of surface hydroxyls; and A , B , and C are empirical constants equal to 14.16, 6.34 m^2/C , and 3.27 nm, respectively. The empirical constants were determined by Yu and Hou using experimental pH_{PZC} data for Mg-Al, Mg-Fe, Mg-Fe-Al, Zn-Mg-Al, Zn-Al, and Zn-Fe-Al LDHs.²⁹⁸ The physical constants used to calculate the pH_{PZC} are shown in **Table 7-4**.

Table 7-4: Physical constants for calculation of pH_{PZC} . (O–H distance is taken as 0.101 nm³⁰¹)

M–O bond	\bar{L} (nm)	v	v/L (nm ⁻¹)
Mg–O	0.206 ³¹	1/2	1.086
Al–O	0.189 ³¹	1/3	1.723
Cu–O	0.210 ³²	1/2	1.073

Li *et al.* found that the difference between the IEP and pH_{PZC} for an LDH is due to its effective net structural charge.³⁰² Most of the structural charge of the positively charged layers is screened by the intercalated anions. The remaining non-screened charge is the effective net structural charge. The

effective net structural charge of an LDH depends on x (the substitution of M^{2+} by M^{3+} ions) and charge screening by the interlayer anion.^{298,303} The effective net structural charge can be approximated by $0.8x$ for NO_3^- , $0.35x$ for Cl^- , and $0.03x$ for CO_3^{2-} , and reflects the relative ease of interlayer anion exchange ($NO_3^- > Cl^- > CO_3^{2-}$).^{298,304} The low (close to zero) net structural charge for LDHs with CO_3^{2-} as interlayer anions has been observed by Rojas *et al.*³⁰⁴ They synthesised LDHs with increasing amounts of CO_3^{2-} (and decreasing amounts of Cl^-) in the interlayer and found that the behaviour of the LDHs became increasingly similar to that of a metal hydroxide as the CO_3^{2-} content was increased. Therefore, as for metal hydroxides, the IEP of LDHs containing solely CO_3^{2-} in their interlayers can be approximated by the pH_{PZC} .^{298,302} A pH_{PZC} of 9.95 was calculated for the Cu-Mg-Al LDHs, and a value of 10.02 was determined for Mg-Al LDHs with CO_3^{2-} as the interlayer anion, close to reported Mg-Al LDH IEP values of pH 10.^{183,186,305} The experimentally and empirically determined IEPs of the Cu-Mg-Al LDHs are consistent with observations in this chapter of increased growth in the platelet diameter for LDH-10.

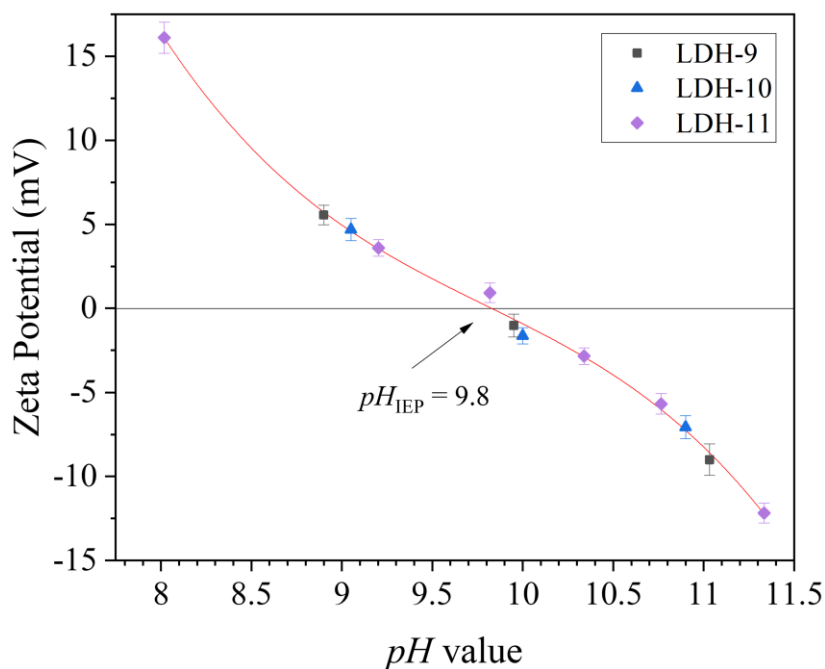


Figure 7-20: Results of the zeta potential measurements for the LDHs synthesised at pH 9, 10 and 11. Zeta potentials were measured using a ZetaPALS (Brookhaven Instruments) at 25°C. The LDHs were dispersed in 10 mM NaCl using an ultrasonic probe and two solutions of 10 mM NaOH and 10 mM HCl were used to adjust the pH of the dispersion.

Another important consideration for the growth mechanisms of LDHs synthesised at different pH values is the predominant metal species present in solution during co-precipitation. It has been shown that as the pH increases, the predominant Al species becomes increasingly dissolved $Al(OH)_4^-$ and decreasingly $Al(OH)_3$, and the predominant Mg species becomes increasingly $Mg(OH)_2$ and

decreasingly Mg^{2+} (**Figure 7-7**). Wang *et al.* studied the effect of synthesis *pH* on the morphology of Mg-Al LDHs produced *via* co-precipitation at constant *pH*.^{173,186} They found that LDHs synthesised below the IEP resembled boehmite ($\gamma\text{-AlO(OH)}$) due to the slow incorporation of Mg^{2+} into an Al(OH)_3 matrix (reaction (7-4)). At *pH* 10, there may be an interplay between nucleation and thermodynamics where the nucleation rate is greater, but the growth rate of the crystallite is also greater due to the faster reaction of Al(OH)_4^- and Mg(OH)_2 species (reaction (7-5)) compared to the reaction between Al(OH)_3 and Mg^{2+} (reaction (7-4)). In addition, the effects of electrostatics may also affect the platelet growth at *pH* 10, as discussed in the previous paragraph. Above the IEP, where the nucleation rate further increases, the crystallites likely grow slowly due to the negative surface charge of the LDH and repulsion between the charges on the ions in solution (Al(OH)_4^- and CO_3^{2-}), resulting in smaller crystallite sizes. The maximum growth observed during co-precipitation at a *pH* close to the IEP in this chapter (and elsewhere^{173,186}) is likely the result of a complex interaction between competing nucleation, electrostatic and thermodynamic factors. While the best understanding from existing studies has been presented, additional work is needed, including developing electrostatic models of LDHs, to increase the fundamental understanding of the co-precipitation of charged solids, which goes beyond the scope of this thesis.

The porosity of the LDHs is determined by the size of the LDH platelets and how they stack together. From **Figure 7-9** and **Figure 7-17**, LDH-9, LDH-9.5 and LDH-10 bulk materials are comprised of relatively large platelets randomly stacked together, whereas LDH-10.5, LDH-11 and LDH-11.5 are comprised of smaller platelets that pack together much more closely. The materials can therefore be separated into two groups, porous (LDH-9 through 10) and less porous (LDH-10.5 through 11.5), which was confirmed experimentally using MIP in the next section.

The results of this section show that the choice of *pH* during co-precipitation can have a significant effect on the LDH characteristics. LDHs synthesised at lower *pH* values (9, 9.5 and 10) recorded broader platelet size distributions and larger platelet heights and diameters than the materials synthesised at higher *pH* values (10.5, 11 and 11.5). These differences were attributed to the effects of *pH* on the supersaturation, thermodynamics and surface charge of the LDHs during growth. Considering scale-up, LDHs with different platelet sizes and porosities can be easily obtained by adjusting the *pH*. This was demonstrated in chapter 5, where porous and non-porous LDHs were used to produce MMOs with different characteristics suitable for use in different scaled-up reactor systems for chemical looping processes. Batch sizes at the kilogram scale have already been achieved using standard laboratory equipment. Further scale-up of the LDHs synthesised at lower *pH* may require additional steps to better control the platelet size distribution, such as a colloid mill, to separate nucleation and growth into separate steps.^{291,306}

7.4 Thermal and structural evolution of layered double hydroxide precursors during calcination to form mixed metal oxides

A TGA was used to study the thermal evolution of the LDHs to MMOs during calcination. **Figure 7-21a** shows the weight loss and derivative weight loss with respect to the temperature of the LDH-10 during calcination. Mass spectroscopy was used to identify the components released during calcination (**Figure 7-21b**). From **Figure 7-21**, the weight loss occurred in three distinct steps:

- (I) 12.8 wt% in the temperature range 50 to 165°C due to the loss of interlayer water and some loss of hydroxyls ($m/z = 17$ and 18), and a small signal associated with NO_3^- originating from the metal nitrate solution used for co-precipitation of the LDHs ($m/z = 14, 30$ and 46),
- (II) 17.6 wt% between 250 to 500°C due to complete dehydroxylation of the brucite-like layers and a small amount of decomposition of interlayer carbonate anions ($m/z = 28$ and 44), and
- (III) 4.9 wt% associated with the complete decarbonation of the LDHs.

The LDHs synthesised at *pH* values other than 10 showed similar overall weight losses (~35 wt%) and weight losses for each step (**Table 7-5**). The molecular formulas of the LDHs (**Table 7-5**) were determined by fitting the derivative weight loss profiles (**Figure 7-22**) and using the molar ratio of metals from the results of XRF (**Table 7-1**). The molecular formulas correspond well with naturally occurring hydrotalcite, $(\text{Mg}_{0.75}\text{Al}_{0.25}(\text{OH})_2(\text{CO}_3)_{0.125} \cdot 0.5\text{H}_2\text{O})$. The CO_3^{2-} content of the LDHs may be underestimated as a small amount of CO_3^{2-} is released in the temperature range 100 to 400°C (**Figure 7-21b**).

Analysis of the derivative weight loss profiles (**Figure 7-22**) shows that the peak above 500°C associated with the decomposition of CO_3^{2-} narrows, increases in magnitude and moves to a higher temperature with increasing *pH*. This could be related to the faulted structure of the LDH. Earlier analysis of the faulted structure of the LDHs carried out using FAULTS (**Table 7-1**) determined that the prevalence of stacking faults increased with co-precipitation *pH*. Although the effect of stacking faults on the thermal properties of LDHs is relatively unknown, the increase in stacking faults could result in the carbonate anion being more strongly intercalated in the LDH structure, requiring higher temperatures for the complete decarbonation of the material.

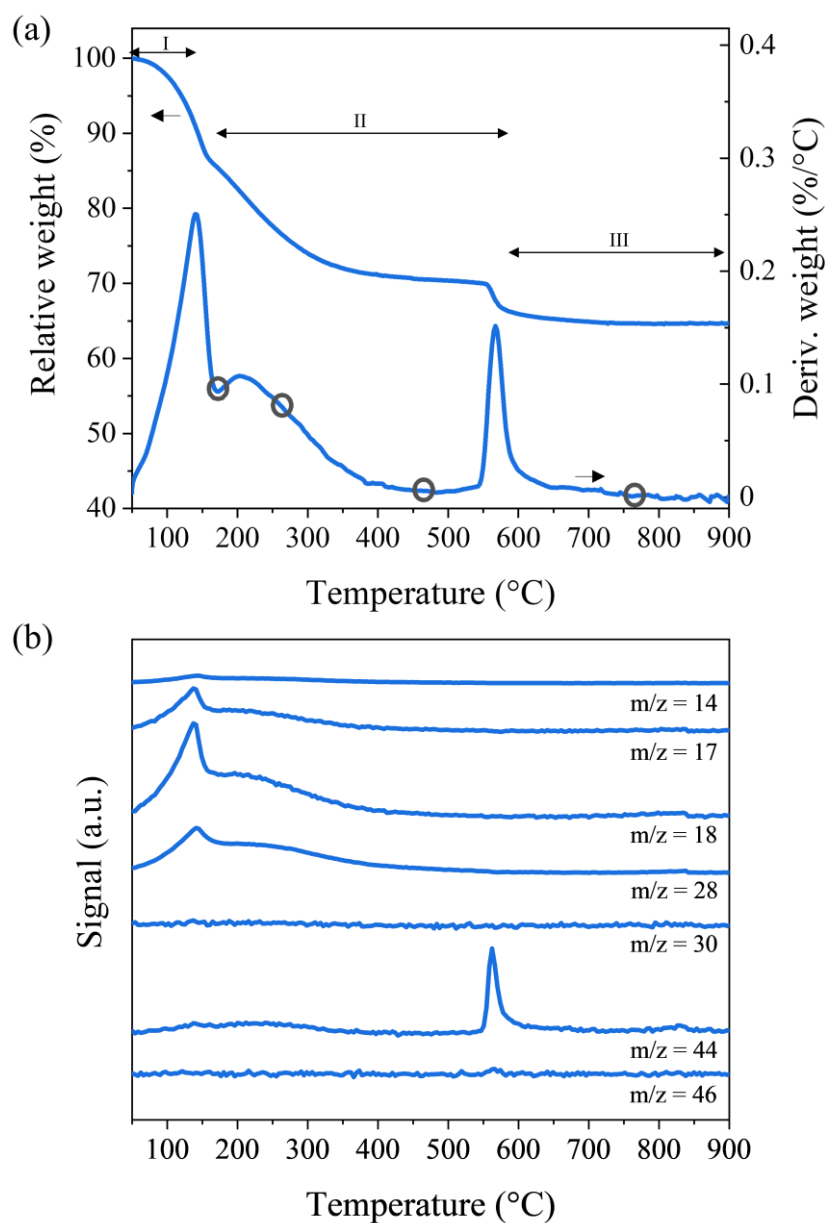


Figure 7-21: Thermogravimetric analysis profiles during calcination of LDH-10. (a) Relative weight and derivative weight profile and (b) selected MS signals during calcination of the LDH-10 from 50 to 900°C in a TGA using a heating rate of $10^{\circ}\text{C min}^{-1}$.

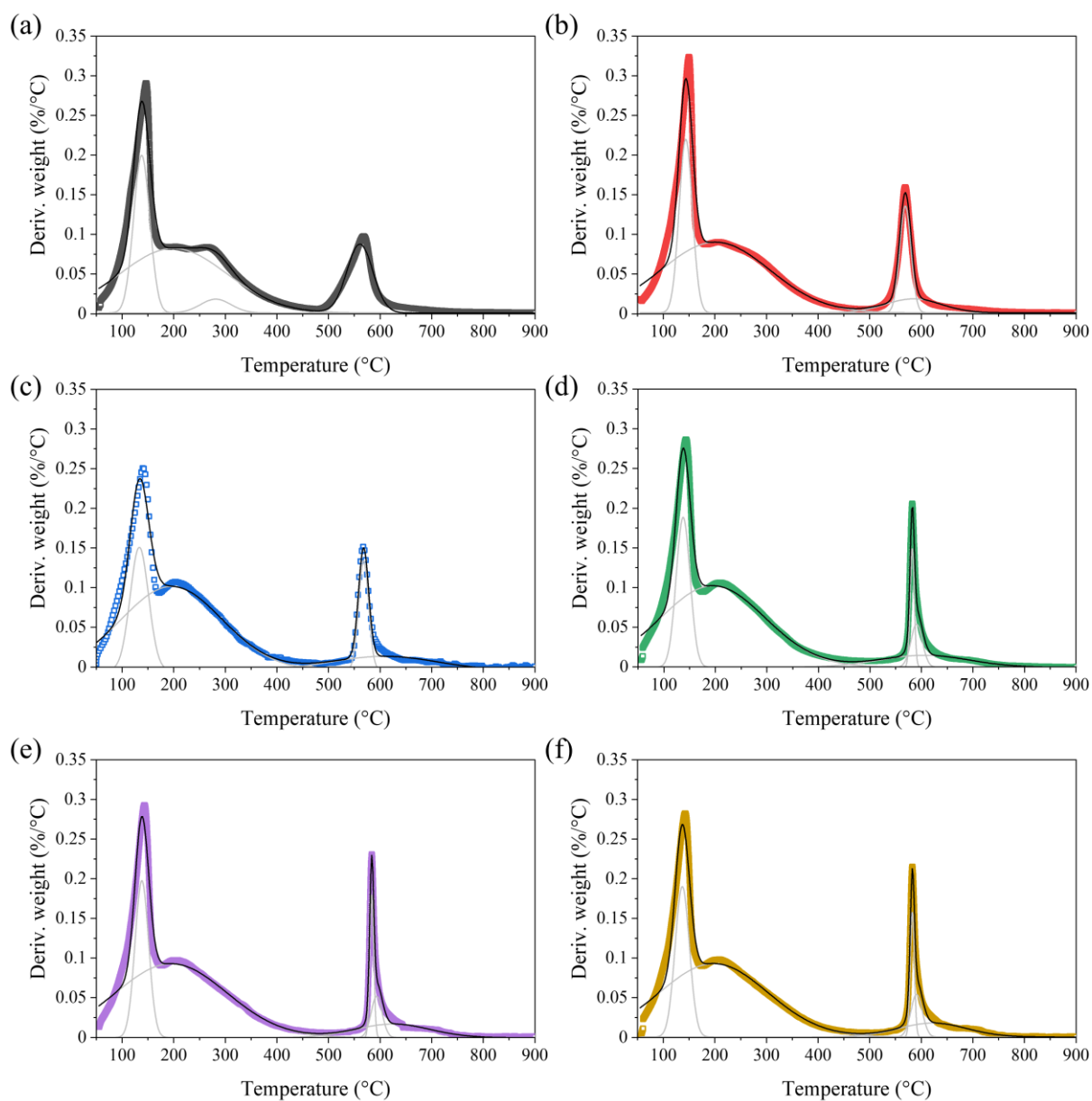


Figure 7-22: Derivative weight profiles for LDHs co-precipitated at a constant pH value between 9 and 11.5. Results of derivative weight profile fittings for LDHs co-precipitated at (a) pH 9, (b) pH 9.5, (c) pH 10, (d) pH 10.5, (e) pH 11, and (f) pH 11.5. The LDHs were calcined in a TGA over a temperature range of 50 to 900°C using a heating rate of 10°C min⁻¹.

Table 7-5: Results of derivative weight profile fittings and formulae of LDHs co-precipitated at a constant *pH* value between 9 and 11.5.

pH	H₂O (wt%)	OH (wt%)	CO₃ (wt%)	LDH formula
9	22.0	62.7	15.3	[Cu _{0.49} Mg _{0.11} Al _{0.39} (OH) ₂](CO ₃) _{0.14} •0.66H ₂ O
9.5	19.3	64.3	16.4	[Cu _{0.50} Mg _{0.16} Al _{0.34} (OH) ₂](CO ₃) _{0.14} •0.57H ₂ O
10	17.6	65.6	16.8	[Cu _{0.50} Mg _{0.16} Al _{0.34} (OH) ₂](CO ₃) _{0.14} •0.50H ₂ O
10.5	16.9	66.7	16.4	[Cu _{0.50} Mg _{0.17} Al _{0.33} (OH) ₂](CO ₃) _{0.14} •0.47H ₂ O
11	17.3	66.3	16.4	[Cu _{0.50} Mg _{0.17} Al _{0.33} (OH) ₂](CO ₃) _{0.14} •0.49H ₂ O
11.5	17.8	65.9	16.3	[Cu _{0.50} Mg _{0.17} Al _{0.33} (OH) ₂](CO ₃) _{0.14} •0.51H ₂ O

FTIR was used to investigate the structure of the LDHs dried at 50°C (**Figure 7-23a**). The broad band centred around 3400 cm⁻¹ was assigned to the stretching mode of OH groups in the brucite-like layers and from interlayer water molecules. A broad weak shoulder at 2950 cm⁻¹ was assigned to the hydrogen bonds between interlayer water molecules and interlayer carbonate anions. The weak band at 1630 cm⁻¹ is due to the angular deformation of the water molecules. The series of IR bands in the spectral region below 1000 cm⁻¹ are due to Cu-O, Al-O and Mg-O vibrations. The band at 1355 cm⁻¹ was assigned to the ν_3 mode of the interlayer carbonate anions. No bands associated with NO₃⁻ were observed in the spectra. The FTIR spectra of the materials co-precipitated at different *pH* values are similar, showing the same bands of similar intensity. The inherent variability of FTIR measurements for materials with different physical characteristics meant no conclusions were drawn between the slight variations in intensity for the LDHs.

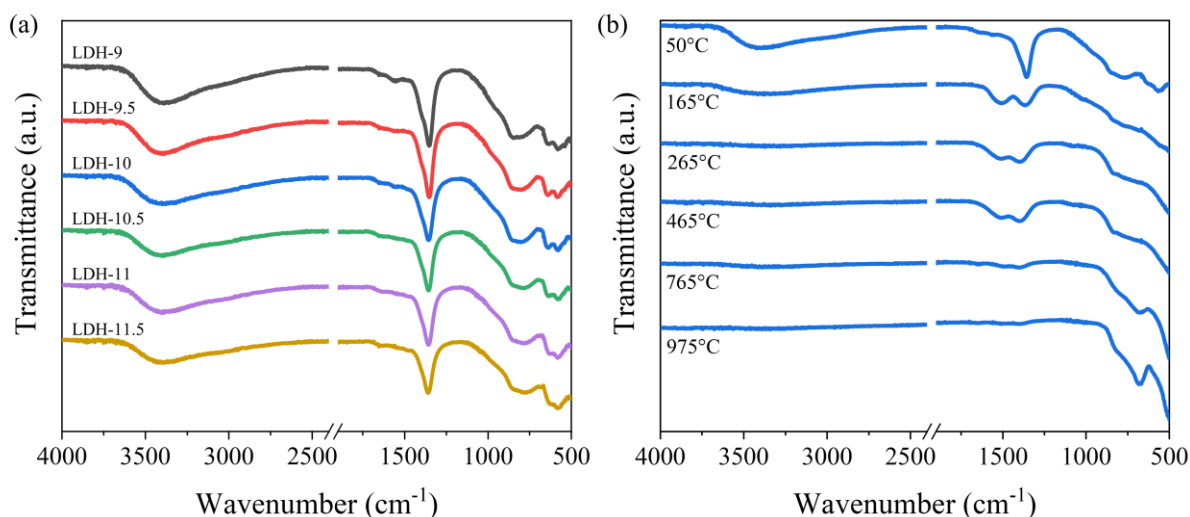


Figure 7-23: FTIR spectra of the LDHs. FTIR spectra of (a) the LDHs co-precipitated at constant pH between 9 and 11.5 (b) LDH-10 calcined at varying temperatures (as indicated). Samples were calcined at each temperature under air and for 3 h.

FTIR and XRD were also used to investigate the changes in the material during calcination. The LDHs were calcined at four additional temperatures between 50 and 975°C which correspond with the circles in **Figure 7-23** at four key stages during calcination:

- (i) loss of interlayer water (165°C),
- (ii) mid-loss of hydroxyl groups (265°C),
- (iii) complete loss of hydroxyl groups (465°C), and
- (iv) the loss of carbonate groups (765°C).

From **Figure 7-23**, the intensity of the bands associated with interlayer water and OH groups decrease with calcination temperature and largely disappear by 465°C. The carbonate ν_3 band splits into two bands at 1330 and 1540 cm^{-1} upon calcination and is still weakly present in the FTIR spectra even at 765°C. XRD was used to investigate the changes in the structure of the materials during calcination (**Figure 7-24**). The XRD patterns at 165 and 265°C show that the layered structure did not completely collapse with the loss of interlayer water molecules and dehydroxylation of the brucite-like layers. Instead, the formation of metaphases at 165 and 265°C was observed, characterised by a slight contraction of basal spacing (rightward shift of the (003) reflection) and the absence of the (006) reflection. Reflections associated with CuO appear at 765°C, while the spinel MgAl_2O_4 peaks appear in the 975°C pattern.

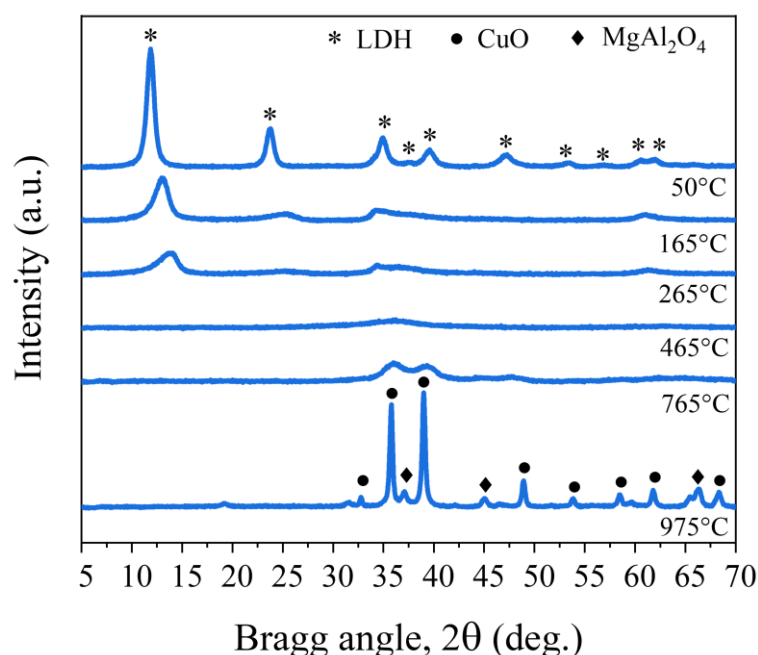


Figure 7-24: Phase composition of LDH-10 as a function of calcination temperature (as indicated). Samples were calcined at each temperature under air and for 3 h.

The morphologies of the dried LDH-10 and calcined MMO-10 were examined using SEM (**Figure 7-9** and **Figure 7-26**, respectively). From the SEM images, the morphology of the LDH is largely retained upon calcination. MIP and N₂ adsorption techniques were used to study the changes in the pore size distribution of the LDH-10 during calcination. From the results in Appendix A2, there was a decent agreement between the pore size distributions determined using MIP and N₂ adsorption for pores below 100 nm. However, pores above 100 nm are beyond the resolution of N₂ adsorption. The SEM images clearly show the presence of larger pores above 100 nm in the LDH-10. Therefore, MIP was used to determine the pore size distributions of the remaining materials. The data from pores above 10000 nm were neglected to avoid overstated results due to the filling of the external surface and inter-particle voids (discussed in Appendix A2). From **Figure 7-25**, two regions of pores exist in the LDH-10: (i) a mesoporous region from 10 to 100 nm, and (ii) a macroporous region between 100 and ~2000 nm. The shape of the pore size distribution for pores above 100 nm may not be fully representative of the actual distribution due to the softness of the samples. However, the results give an indication of the total pore volume of the materials. With increasing calcination temperature, the pore size distributions shift to a smaller average pore size but retain a similar distribution shape.

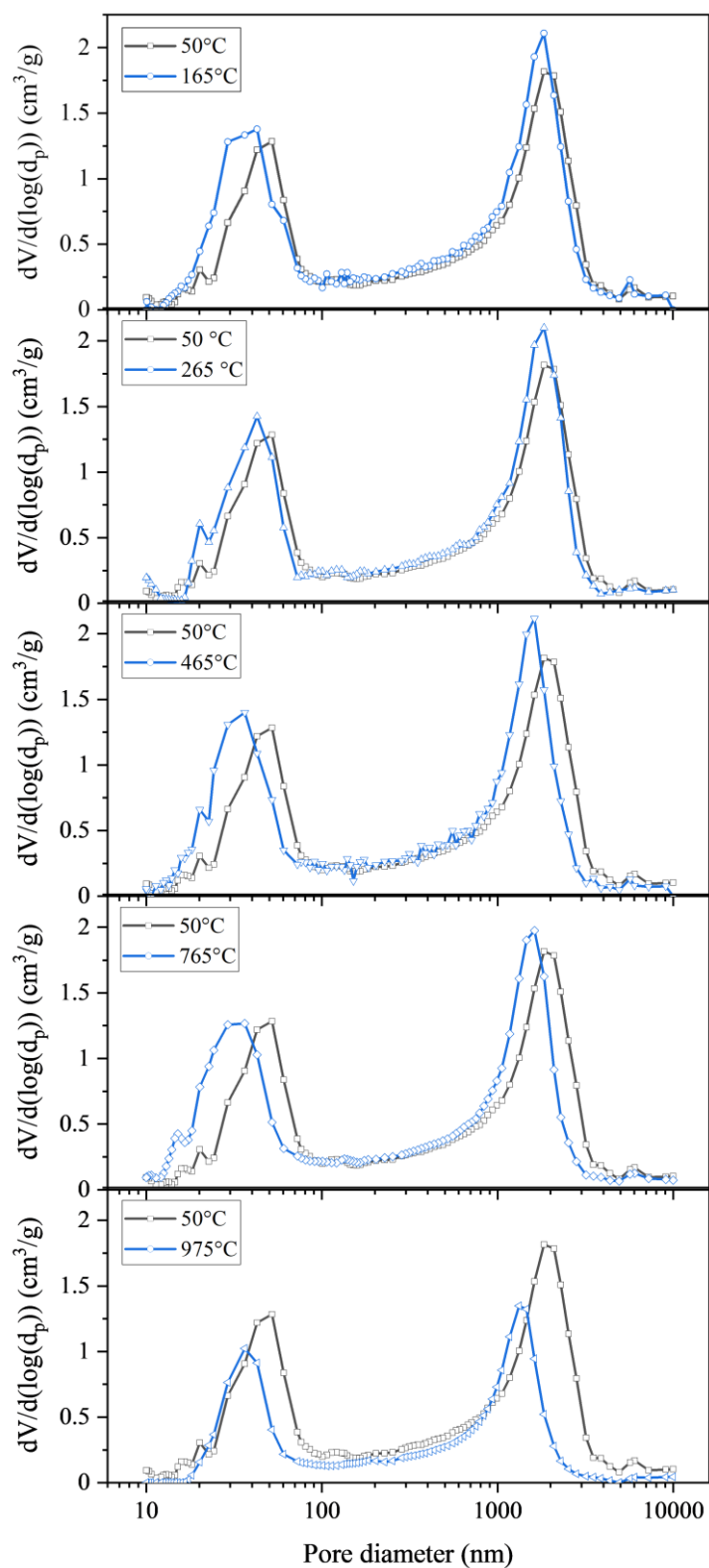


Figure 7-25: Pore size distribution of LDH-10 as a function of calcination temperature (as indicated). Pore size distributions were determined using MIP analysis and samples were calcined at the desired temperature under air and for 3 h.

7.5 Characterisation of mixed metal oxides

One aim of this chapter was to investigate how the pH value during co-precipitation impacts the structure and performance of MMOs in chemical looping systems. From the SEM images of the LDHs (Figure 7-9) and MMOs (Figure 7-26), the MMOs retain the characteristic morphology of their LDH precursors, with some formation of grains observed. MIP was used to study the pore size distribution of the MMOs. The pore volumes recorded using MIP were combined with the skeletal density obtained from He pycnometry to determine the porosity and envelope density of the materials iteratively.

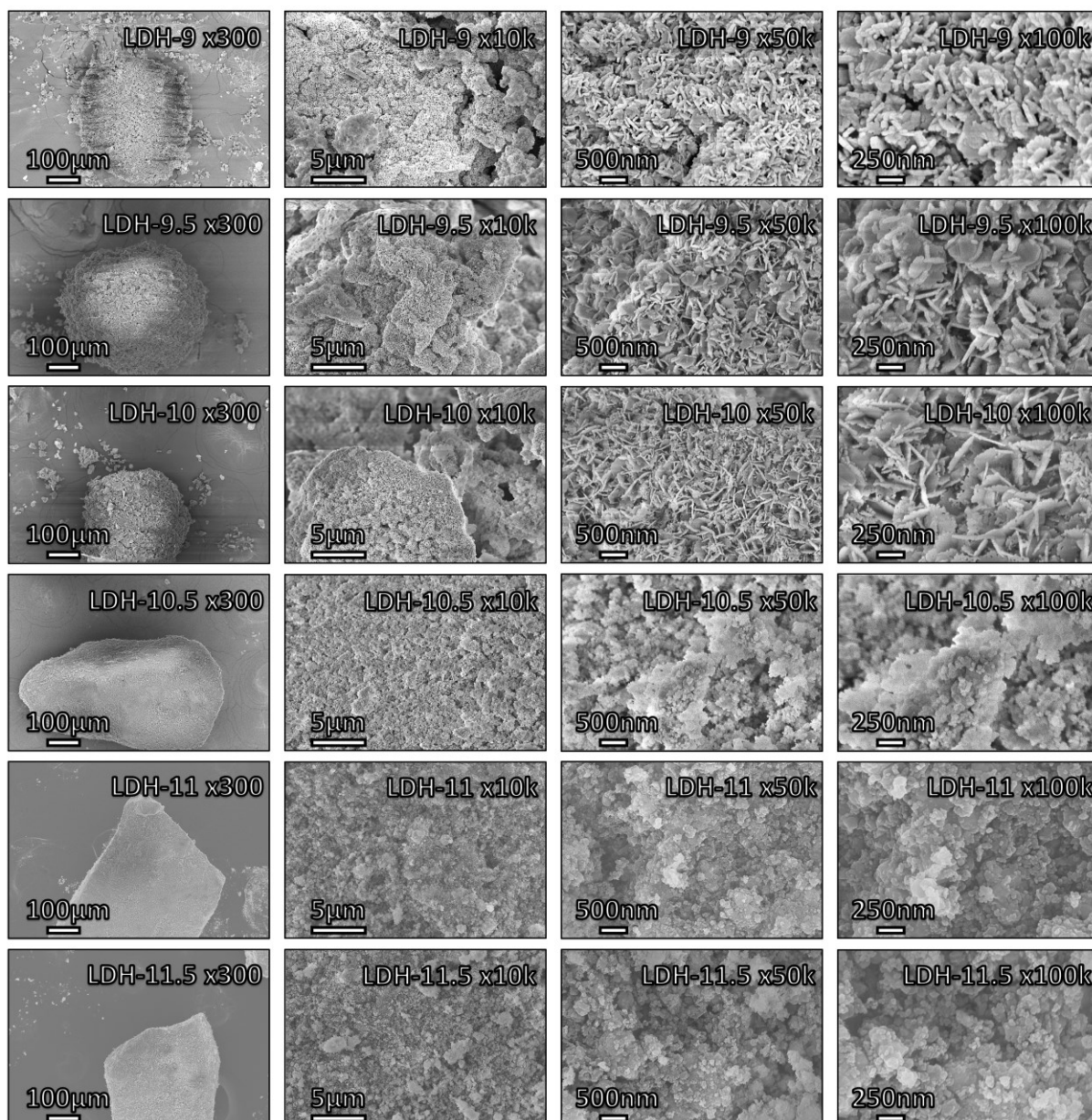


Figure 7-26: SEM images of MMOs derived from LDHs co-precipitated at a constant pH value between 9 and 11.5 for 300 min (as indicated). Left to right: at 300, 10k, 50k and 100k magnification.

The pore size distributions of the calcined MMOs presented in **Figure 7-27** show that the pore size distributions of the MMO-9, MMO-9.5 and MMO-10 are much broader than the materials synthesised at higher pH values. A large porous region exists in the MMO-9, MMO-9.5 and MMO-10, stretching from pore diameters of ~ 700 to 3000 nm. These materials show a somewhat bimodal pore size distribution, with a region of smaller pores from ~ 60 to 400 nm. The pore size distributions of the MMO-11 and MMO-11.5 are mesoporous and unimodal, consisting of small pores in the region of 30 to 100 nm. The MMO-10.5 is a combination of the two types of distribution, somewhat bimodal but with a higher proportion of pore volume in the lower pore diameter region than the higher pore diameter region, in contrast to the MMO-9, MMO-9.5 and MMO-10. The trends in pore size distribution agree with the shape of the platelets and the morphology of the corresponding aggregated LDH structures (**Figure 7-9**). The larger platelets aggregate less effectively, creating large voids, whereas the smaller platelets can pack together more tightly, resulting in a less porous structure.

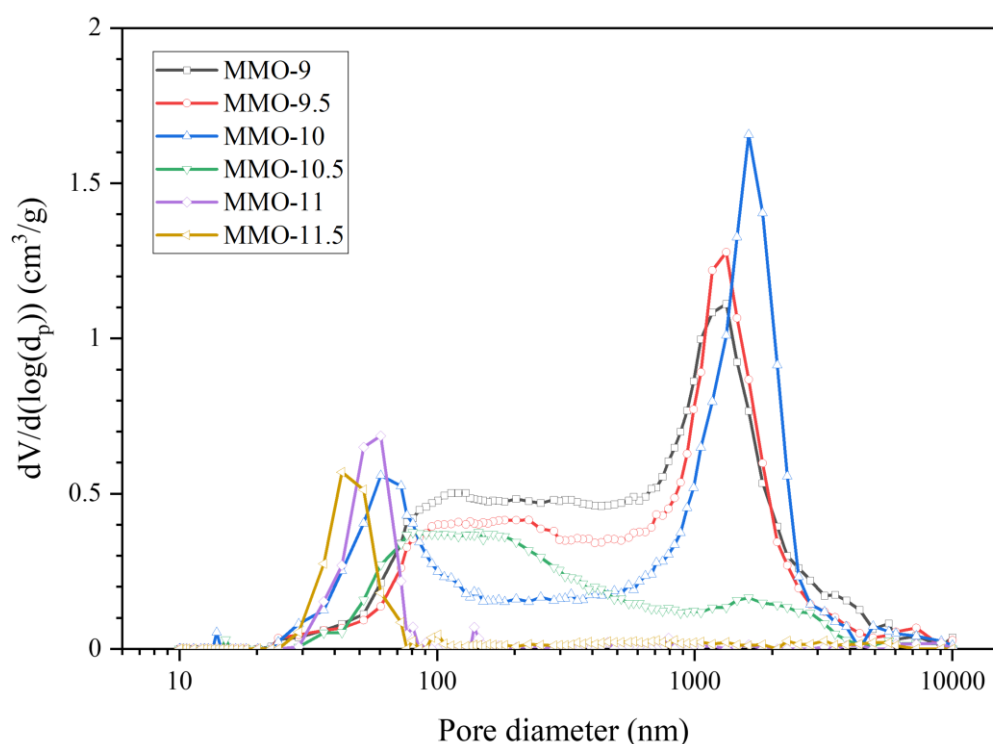


Figure 7-27: Pore size distributions of MMOs. Derived from LDHs co-precipitated at a constant pH value between 9 and 11.5 (as indicated) determined using MIP.

Pore volume data from MIP in the size range 10 to 10000 nm was used to calculate the envelope density and porosity. As expected from the pore size distributions, the porosities of MMO-9, MMO-9.5 and MMO-10 are much higher than MMO-10.5, MMO-11 and MMO-11.5. The porosities recorded for MMO-9, MMO-9.5 and MMO-10 are very high (ca. 85%), and the pore volumes used to calculate these values may have been overestimated by MIP, particularly at higher pore diameters. Therefore, the theoretical porosities of the materials were estimated by considering the platelets as disks and using a

correlation developed by Zou and Yu to determine the porosity of randomly packed disks.³⁰⁷ The sphericities of the platelets were determined using the dimensions calculated from SEM images of the LDHs (**Table 7-3**). The theoretical porosities of the MMOs are lower than those determined using MIP analysis, particularly for the MMO-9 and MMO-9.5. The inherent difficulties in measuring the platelet dimensions using SEM, the use of surface platelet dimensions rather than those forming the internal structure of the LDH bulk, and the applicability of using the correlation may have contributed to the disparity between values. However, the overall trend in porosities is similar. The porosities of the MMOs may have to be re-evaluated for future use, *e.g.* in kinetic models.

Table 7-6: Porosity and crushing strengths of the MMOs. Derived from LDHs co-precipitated at a constant *pH* value between 9 and 11.5.

Material	Porosity (%)	Theoretical porosity (%)*	Crushing strength (N)
MMO-9	86.7	63.7	< 1 N
MMO-9.5	84.8	60.3	< 1 N
MMO-10	88.2	76.7	< 1 N
MMO-10.5	67.4	57.3	1.2 ± 0.3 N
MMO-11	45.7	50.3	3.0 ± 0.7 N
MMO-11.5	34.8	49.3	6.9 ± 1.0 N

Footnote: *The theoretical porosity was estimated using correlations given by Zou and Yu for randomly packed disks.³⁰⁷ The sphericity of the platelets were determined using dimensions calculated from SEM images (**Table 7-3**).

The attrition of oxygen carriers during operation in fluidised bed systems generates undesired fines, requiring downstream filtration and increasing operating costs due to oxygen carrier replacement.^{308,309} Attrition generally occurs due to abrasion and fragmentation during operation due to a combination of thermal, mechanical and chemical stresses. The crushing strength of a particle is commonly used as an indicator of the resistance of a particle towards mechanical stresses during long-term cycling in fluidised bed systems. The average force required to crush 30 particles in the size range 300–425 µm was determined using a 50 N force gauge (**Table 7-6**). The average crushing strength values of the MMOs vary from < 1 N to 6.9 ± 1.0 N. The low crushing strengths of the MMO-9, MMO-9.5 and MMO-10 materials were below the minimum resolution of the equipment (1 N) and were attributed to the high porosities of these materials. A minimum crushing strength value of 2 N has been proposed in the literature for using oxygen carriers in fluidised bed systems.⁸⁹ As discussed in chapter 5, owing to the poor mechanical stability of the MMO-9 through MMO-10.5, these materials are ruled out as potential

oxygen carriers for FBRs. However, these lower-strength materials could be used in fixed bed reactors. The significantly higher crushing strengths of the MMO-11 and MMO-11.5 make these materials suitable candidates for further screening in FBRs. The MMOs were also characterised using XRD. The XRD patterns shown in **Figure 7-28** confirmed the MMOs were comprised of CuO and an aluminate spinel phase, primarily MgAl_2O_4 .

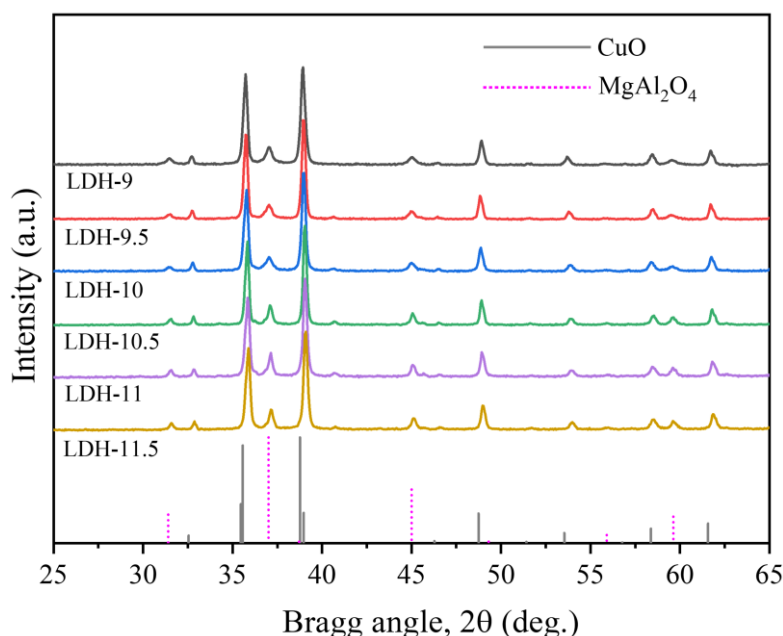


Figure 7-28: XRD patterns of MMOs derived from LDHs co-precipitated at a constant pH value between 9 and 11.5 for 300 min (as indicated). Reference patterns for CuO (JCPDS 80-1268; vertical lines) and MgAl_2O_4 (JCPDS 73-1959, vertical dashed lines).

7.6 Long-term performance of mixed metal oxides in chemical looping processes

The long-term performance of the Cu-Mg-Al MMOs as oxygen carriers for chemical looping processes was studied using a TGA. MMO particles in the 300–425 μm size range were used for redox cycling. To investigate the thermal and chemical stability of the MMOs, the materials were cycled for 100 CLOU (oxygen release of $\text{CuO} \rightarrow \text{Cu}_2\text{O}$) and 100 CLC (reduction of $\text{CuO} \rightarrow \text{Cu}$) cycles at 900 °C. The relative weight profiles for the first and last cycles and the overall cycling profiles are shown in **Figure 7-29** and **Figure 7-30** for the CLOU experiments and **Figure 7-31** and **Figure 7-32** for the CLC experiments. The average oxygen release (CLOU) and storage (CLC) capacities over 100 cycles are shown in **Table 7-7**.

There was good agreement between the experimental and theoretical oxygen release and storage capacities based on the elemental compositions determined by XRF (**Table 7-1**). Unlike pure CuO, which has been shown to deactivate rapidly during redox cycling,¹⁰¹ the comparison between the relative weight profiles for the first and last cycles shows the MMOs experienced limited chemical deactivation over 100 CLOU and CLC cycles in a TGA, except for MMO-9. The results for MMO-9.5 through 11.5 demonstrate the effectiveness of the MgAl_2O_4 stabilisation of CuO. In contrast, the MMO-9 experienced much slower rates of re-oxidation which required the oxidation period to be significantly extended from 2.5 min to 60 min to achieve full re-oxidation (**Figure 7-29** and **Figure 7-31**).

The amount of Mg in the MMO-9 is below the stoichiometric ratio for the formation of solely MgAl_2O_4 (**Table 7-1**). Therefore, it is likely that some CuO reacts with Al_2O_3 to form CuAl_2O_4 . The release of oxygen from CuAl_2O_4 produces CuAlO_2 , which has been reported to have significantly slower rates of re-oxidation than Cu_2O ,^{107,111} as shown in chapter 5 for the Cu-Al MMOs. However, the very slow rate of re-oxidation was unexpected, considering the considerable amount of Mg incorporated into the MMO and the high porosity of the material. One explanation that may have led to slower rates of re-oxidation observed for MMO-9 is that 10 vol% O_2/N_2 was used for re-oxidation in this chapter, compared to air (~21 vol%) in chapter 5, which reduces the thermodynamic driving force for re-oxidation. Similarly, the Cu-Al MMOs studied in chapter 5 showed rapid re-oxidation during CLC cycling, which was comparable to the re-oxidation rate of the Cu-Mg-Al MMOs. In this chapter, while the rate of re-oxidation (estimated by the gradient of the relative weight profiles) during CLC cycling (**Figure 7-31**) was faster than during CLOU cycling (**Figure 7-29**), the rate was much slower than the other MMOs and the re-oxidation period had to be extended to achieve full conversion.

An additional CLOU experiment was performed in the TGA at 900°C to investigate how increasing the amount of oxygen in the re-oxidation gas would affect the re-oxidation rate of the MMO-9. Air was used during the re-oxidation step and the MMO-9 was cycled five times. **Figure 7-33** shows the results of the additional experiment compared to the first cycle of MMO-9. The MMO-9 re-oxidised in air showed significantly faster rates of re-oxidation than the sample re-oxidised in 10 vol% O_2/N_2 . The sample completely re-oxidised in air within the 2.5 min re-oxidation period, and the rate increased over each of the five cycles but was slower than the re-oxidation rates of the other MMOs (**Figure 7-35**). These results suggest that the re-oxidation reactions in the oxygen carriers containing lower amounts of Mg are more sensitive to the thermodynamic driving force for re-oxidation at 900°C. These results are important because the outlet oxygen concentration of the air reactor flue gas in scaled-up systems should be kept as low as possible to avoid thermal losses that reduce the overall process efficiency,⁶⁵ with a target outlet oxygen concentration of 5% stated in the literature.⁶⁶ Therefore, oxygen concentrations close to those expected during operation should be used when evaluating the redox performance of potential oxygen carrier materials for chemical looping processes.

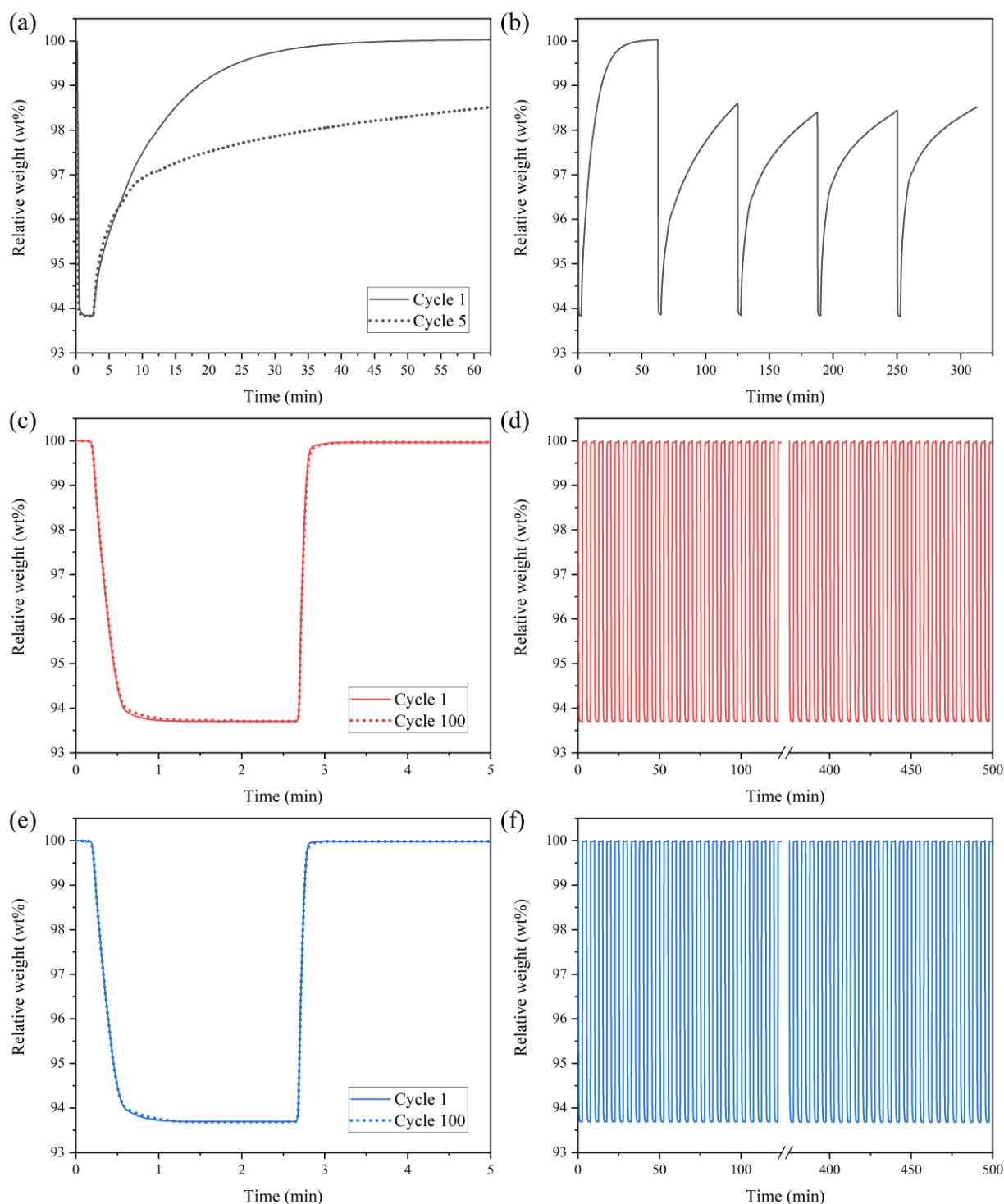


Figure 7-29: CLOU cycling profiles in a TGA at 900°C. First and last CLOU cycles and long-term profiles, respectively, for MMOs derived from LDHs co-precipitated for 300 min at (a-b) pH 9, (c-d) pH 9.5, and (e-f) pH 10. The re-oxidation period for MMO-9 was 60 min rather than the 2.5 min used for the remaining MMOs due to the extremely slow rates of re-oxidation observed in the TGA.

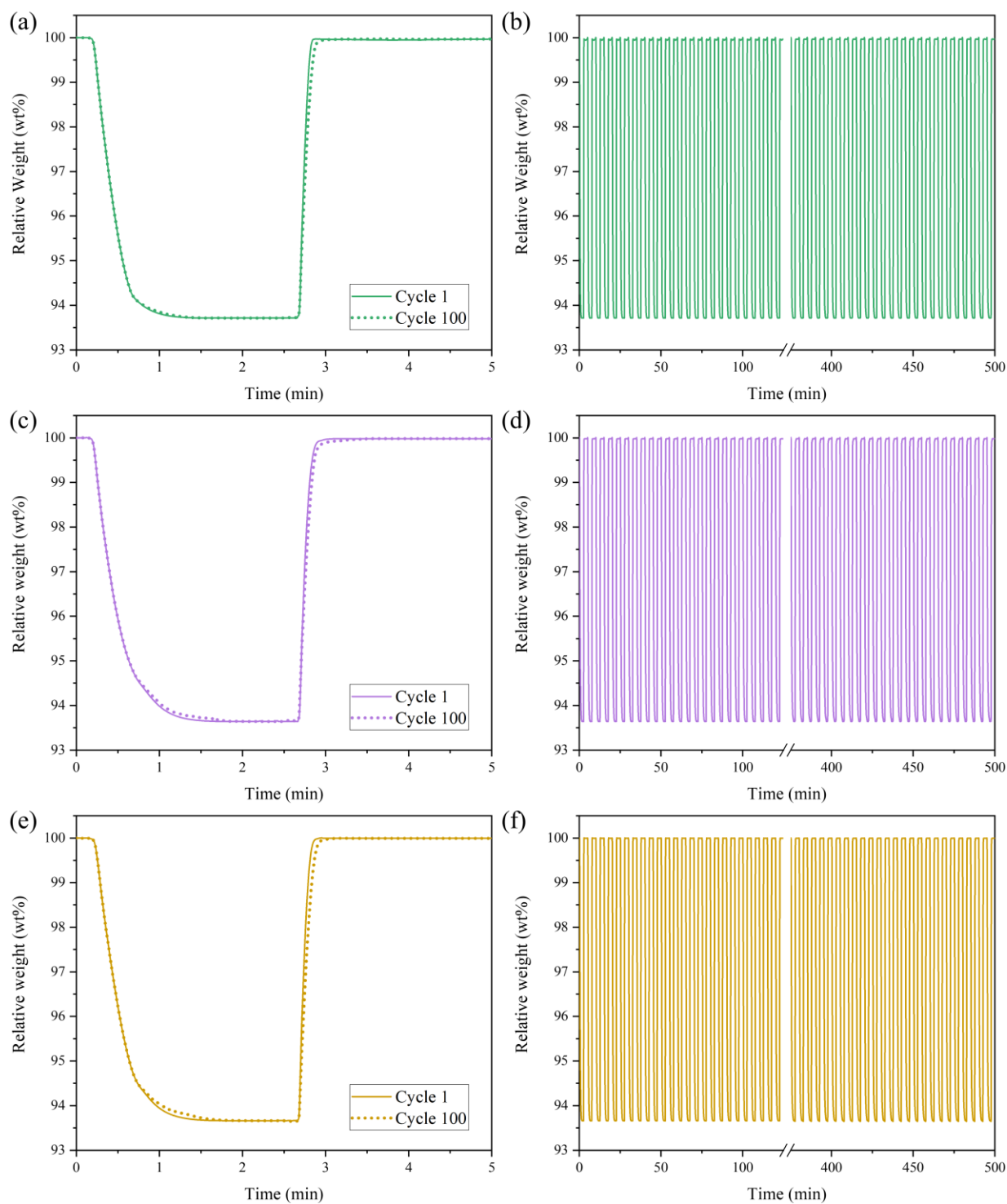


Figure 7-30: CLOU cycling profiles in a TGA at 900°C. First and last CLOU cycles and long-term profiles, respectively, for MMOs derived from LDHs co-precipitated for 300 min at (a-b) pH 10.5, (c-d) pH 11, and (e-f) pH 11.5.

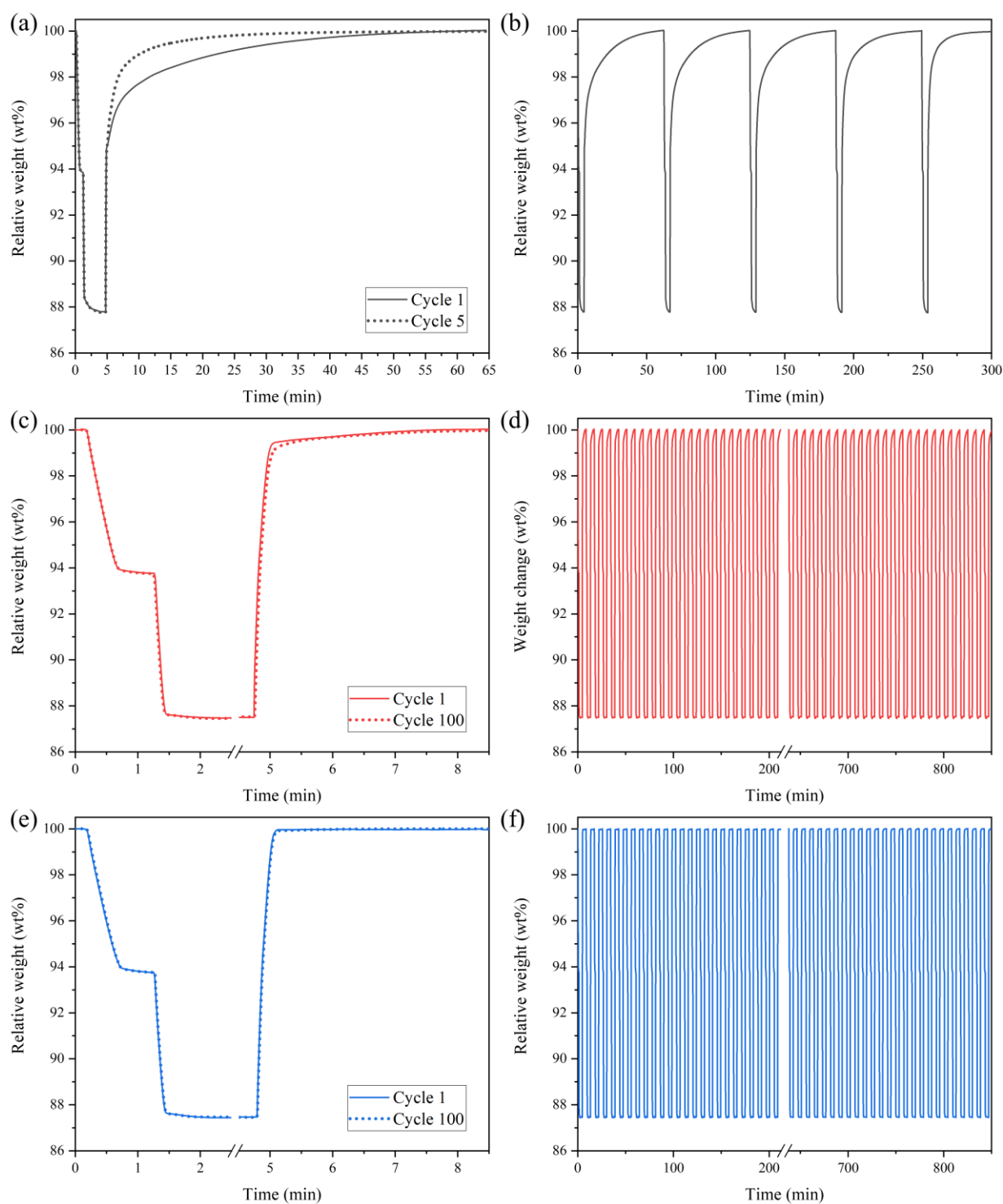


Figure 7-31: CLC cycling profiles in a TGA at 900°C. First and last CLC cycles and long-term profiles, respectively, for MMOs derived from LDHs co-precipitated for 300 min at (a-b) pH 9, (c-d) pH 9.5, and (e-f) pH 10. The re-oxidation period for MMO-9 was 60 min rather than the 2.5 min used for the remaining MMOs due to the extremely slow rates of re-oxidation observed in the TGA.

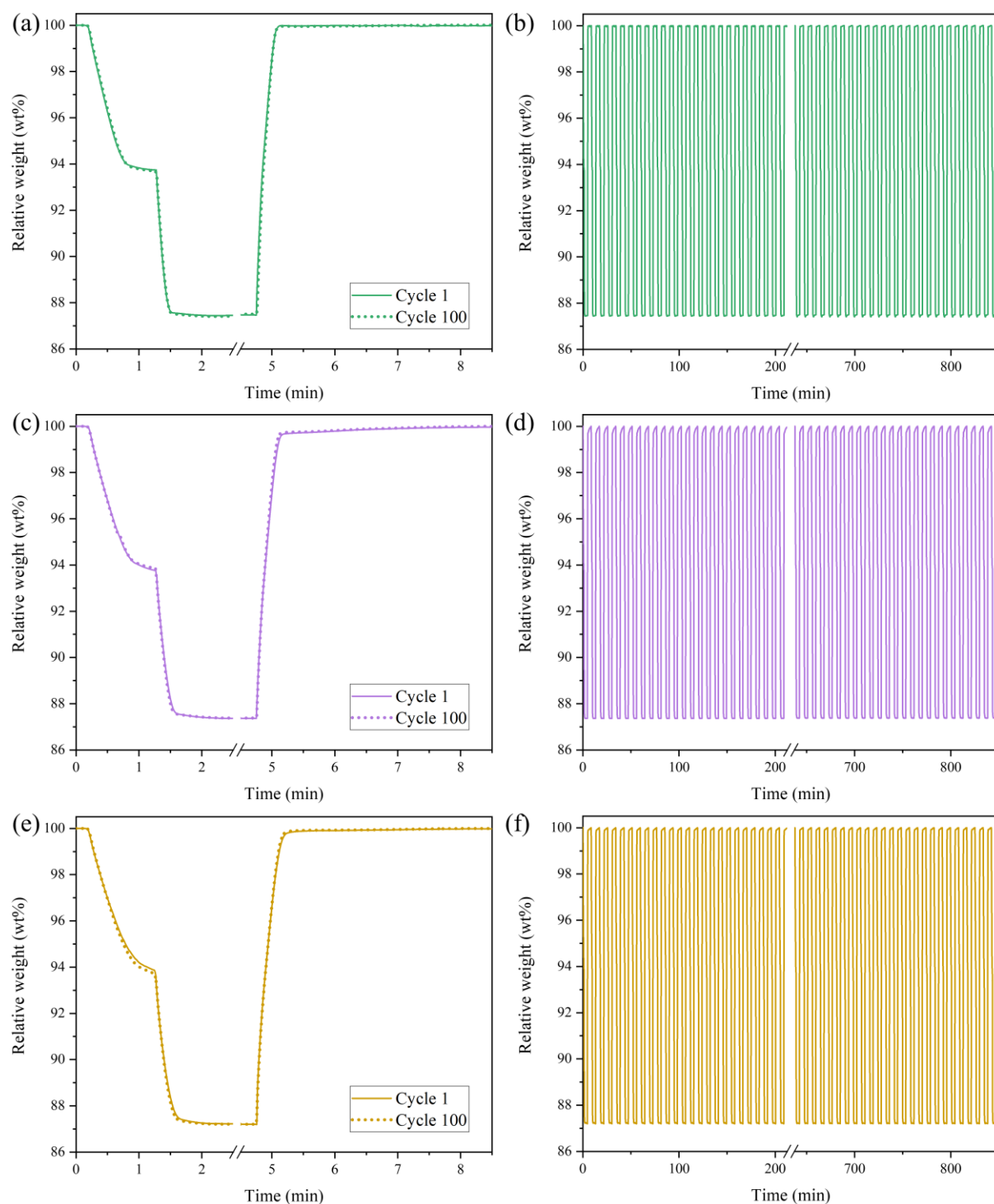


Figure 7-32: CLC cycling profiles in a TGA at 900°C. First and last CLOU cycles and long-term profiles, respectively, for MMOs derived from LDHs co-precipitated for 300 min at (a-b) pH 10.5, (c-d) pH 11, and (e-f) pH 11.5.

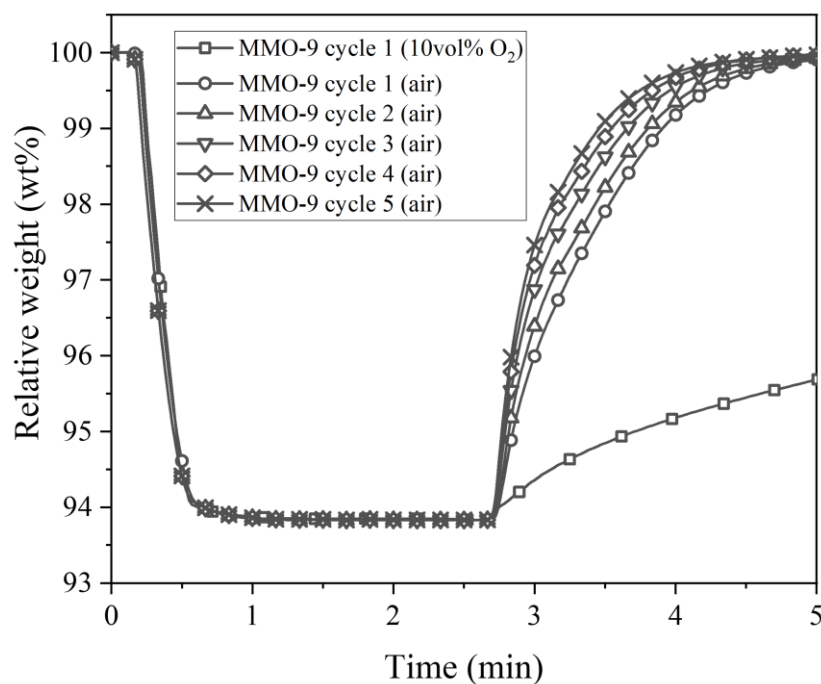


Figure 7-33: Comparison of relative weight profiles of MMO-9 tested in a TGA at 900°C under CLOU conditions using re-oxidation atmospheres of 10 vol% O₂/N₂ and air (as indicated).

Table 7-7: Theoretical and experimentally determined oxygen release and storage capacities, porosities and crushing strengths of the MMOs derived from LDHs co-precipitated at a constant *pH* value between 9 and 11.5 for 300 min.

Material	Theoretical R _{OR} ¹ (go ₂ /goc)	R _{OR} (go ₂ /goc)	Theoretical R _{OS} ¹ (go ₂ /goc)	R _{OS} (go ₂ /goc)	Maximum observed rate of oxygen release (mmolo ₂ s ⁻¹ goc ⁻¹)	Porosity (%)
MMO-9	0.062	0.062	0.124	0.122	0.137	86.7
MMO-9.5	0.063	0.063	0.126	0.125	0.130	84.8
MMO-10	0.063	0.063	0.126	0.126	0.138	88.2
MMO-10.5	0.063	0.064	0.126	0.128	0.099	67.4
MMO-11	0.063	0.065	0.127	0.128	0.091	45.7
MMO-11.5	0.064	0.067	0.127	0.129	0.084	34.8

Footnote: ¹based on CuO content from XRF

This chapter aims to understand how the co-precipitation pH impacts the structure and performance of MMOs in chemical looping systems. A comparison of the relative weight profiles for the first CLOU and CLC cycles is shown in **Figure 7-34**. The oxygen release rates of the MMOs during the first CLOU cycle are shown in **Figure 7-35**, and the maximum rates of oxygen release determined over the first three cycles are given in **Table 7-7**.

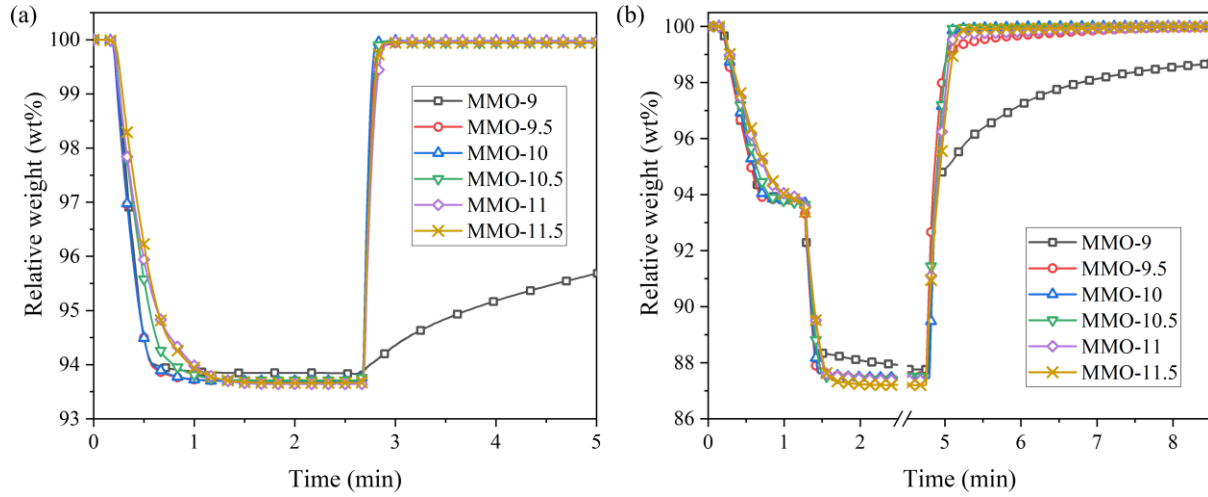


Figure 7-34: Comparison of relative weight profiles of MMOs tested in a TGA at 900°C. (a) CLOU cycling mode, and (b) CLC cycling mode.

From **Table 7-7**, the maximum observed rates of oxygen release are higher for the MMOs with higher porosities. The maximum rates of the MMO-9, MMO-9.5 and MMO-10 are similar as expected due to their similar porosities. However, the differences in rates between these MMOs, or the true maximum rate, may have been limited by the maximum rate of oxygen diffusion in the TGA. Therefore, the maximum rate of oxygen transfer from the particle surface to the bulk was calculated using equation (7-5),¹¹⁰

$$N_{O_2} = C \cdot D \cdot \frac{\pi d_{pan}^2}{4h} \cdot \ln \left(\frac{1 - y_{O_2,b}}{1 - y_{O_2,s}} \right) \quad (7-5)$$

where N_{O_2} is the molar flow rate of oxygen, C is the molar gas concentration, D is the molecular diffusivity of O_2 in N_2 (from the Chapman-Enskog theory²⁰⁰), d_{pan} and h are the diameter and height of the TGA pan, respectively, and y_s and y_b are the molar fractions of oxygen at the particle surface and in the bulk of the TGA, respectively.

At 900°C, the maximum rate of oxygen transfer was determined to be $1.66 \mu\text{mol s}^{-1}$ for $y_s = 0.014$ (equilibrium value at 900°C) and $y_b = 0$. The maximum observed rate of oxygen release for the MMO-10 was $\sim 0.42 \mu\text{mol s}^{-1}$, which represents 25% of the maximum possible rate calculated using equation

(7-5). Despite the low masses (~ 3 mg) and high gas flow rates (200 ml min^{-1}) used for the TGA cycling experiments to minimise the effects of external mass transfer, the oxygen released by the particles may not have been effectively swept from the TGA pan, increasing y_{bulk} and lowering the maximum rate of oxygen transfer. Therefore, external mass transfer limitations could have partially concealed any differences between the maximum rates of oxygen release for the MMO-9, MMO-9.5 and MMO-10 materials. However, **Figure 7-35** clearly shows the differences between the oxygen release rates from the more porous (MMO-9, MMO-9.5 and MMO-10) and less porous (MMO-10.5, MMO-11, MMO-11.5) MMOs were effectively captured in the TGA.

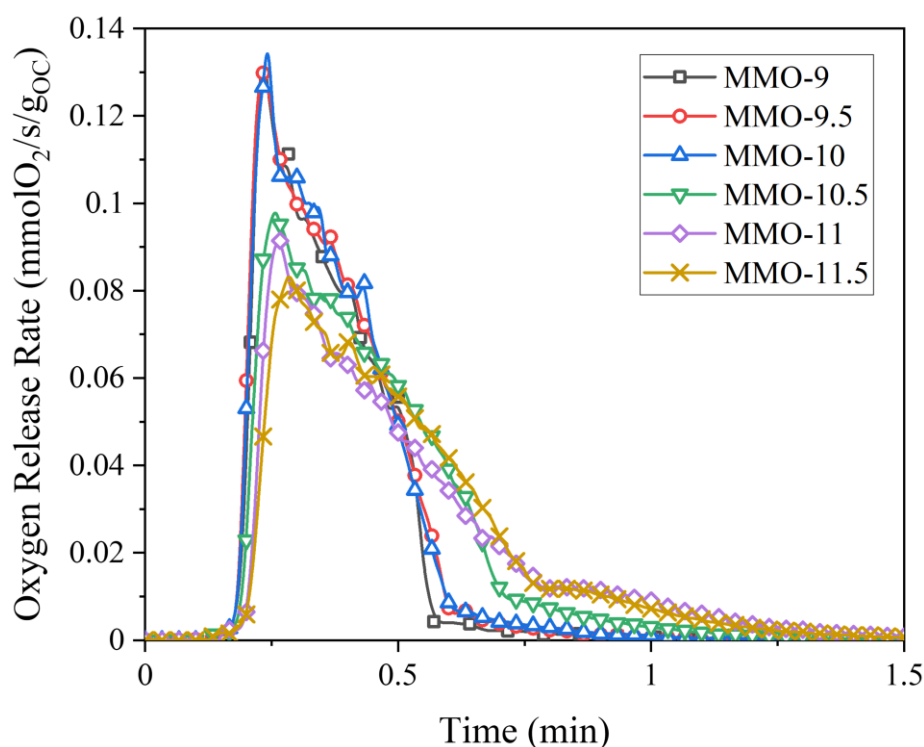


Figure 7-35: Oxygen release rates during oxygen release phase of the CLOU cycle.

Synthetic oxygen carriers must demonstrate significantly superior stabilities over long-term redox cycling to be used in chemical looping systems over cheaper oxygen carriers based on natural ores or wastes. Two MMOs were selected for further testing to assess the effectiveness of the LDH-MMO design strategy. Interconnected FBRs⁵⁷ and alternating fixed bed reactors³⁴ have been proposed for scaled-up CLC reactor systems. In FBRs, oxygen carriers experience greater mechanical stresses, and therefore particles with higher mechanical stabilities are desired to reduce particle attrition and oxygen carrier make-up rates.³¹⁰ In contrast, oxygen carriers in packed bed systems experience lower mechanical stresses, but larger particles are required to maintain a low pressure drop in the system which may increase internal mass transfer resistances.³¹¹ The use of more porous oxygen carriers can improve internal mass transfer and rates of reaction. From **Table 7-7**, the MMO-10 possess low

crushing strength and high porosity while the MMO-11 have higher crushing strength and lower porosity. Therefore, the MMO-10 and MMO-11 were selected for further testing.

The stabilities of the MMOs were assessed over 500 CLC cycles in a TGA at 900 °C. The first and last cycle for each MMO is shown in **Figure 7-36**. The MMO-10 showed almost no signs of sintering over 500 cycles, although this may have been masked by external mass transfer limitations in the TGA, as discussed previously. The MMO-11 also experienced very little deactivation during the reduction periods, but some deactivation can be seen during re-oxidation at high conversions. The oxygen carriers did not experience any mechanical stresses in the TGA. However, similar MMOs derived from LDHs synthesised at *pH* 11 in chapter 5 showed excellent stability over 100 CLOU cycles and 20 CLCP cycles in an FBR.²¹¹

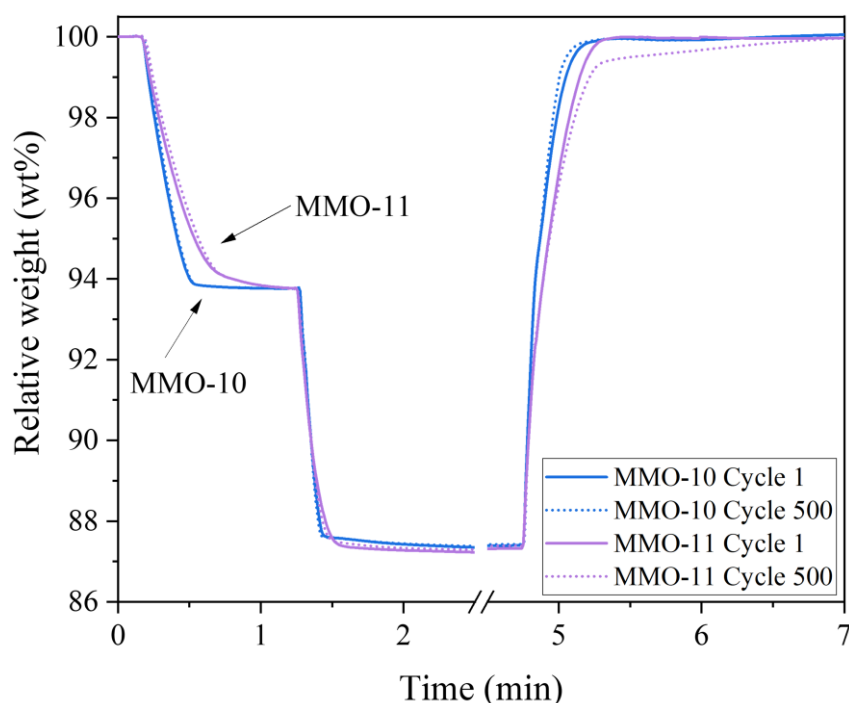


Figure 7-36: Results of the 500 CLC cycle experiments in a TGA at 900°C. Relative weight profiles for the first and last CLC cycles for extended cycling of the MMO-10 and MMO-11.

The near-constant conversion and limited sintering of the MMO-10 and MMO-11 over 500 CLC cycles (**Figure 7-36**) confirmed the effective stabilisation of CuO by MgAl_2O_4 in oxygen carriers produced *via* the LDH-MMO design strategy. Further testing of the MMO-11 in an FBR is needed to verify their mechanical stability over extended redox cycling.

7.7 Concluding remarks

This chapter investigated the effect of co-precipitation *pH* on the material characteristics of LDHs and MMOs and the performance of Cu-Mg-Al MMOs in chemical looping systems. LDHs were co-

precipitated at a constant *pH* between *pH* 9 and 11.5 for 300 min using an automated co-precipitation rig. The amount of Mg in the LDHs was found to increase with increasing *pH*. The diameter and height of the LDH platelets were observed to generally decrease with increasing *pH*, except for LDHs synthesised at *pH* 10 where the platelets grew fast in the radial direction. The larger diameter platelets synthesised at *pH* 10 were attributed to a combination of supersaturation, thermodynamic and electrostatic factors. Calcination of the LDHs resulted in the formation of highly dispersed CuO in an aluminate support. SEM and MIP analysis found the MMO generally retained the particle morphology of the LDH precursor.

The long-term performance of the MMOs was assessed for 100 CLOU and CLC cycles in a TGA at 900°C. The formation of MgAl_2O_4 rather than CuAl_2O_4 was critical for the effective stabilisation of CuO and to avoid the slow re-oxidation of the oxygen carrier and maintain stable oxygen release and storage capacities over extended redox cycling. The more porous MMOs synthesised at *pH* 9, 9.5 and 10 showed much higher rates of oxygen release than the less porous materials synthesised at *pH* 10.5, 11 and 11.5 – although mass transfer limitations may have concealed the true maximum rates of oxygen release of the more porous MMOs in the TGA. An additional CLOU experiment performed in the TGA at 900°C using MMO-9 demonstrated that it is crucial to evaluate potential oxygen carriers using gas compositions that reflect industrial conditions.

To further demonstrate the strength of the LDH-MMO design strategy, MMO-10 and MMO-11 were cycled for 500 CLC cycles in a TGA at 900°C. MMO-10 are characterised by lower crushing strength and higher porosity suitable for packed bed reactors, while the MMO-11 have higher crushing strength and lower porosity, more suitable for FBRs. The results from the 500 CLC cycle experiments at high temperatures indicate that the Cu-Mg-Al LDH-derived MMOs are promising oxygen carrier materials, and the particle morphology is tuneable for different reactor systems. The results of this chapter show Cu-Mg-Al MMOs are promising candidates for further development and scale-up for use in chemical looping processes utilising either fluidised or fixed bed reactors.

The insights gained into the growth of LDH platelets over long synthesis times may aid the scale-up of these materials for industrial applications. LDHs are known for their anion exchange capabilities, making them attractive for catalysis, drug delivery, and water treatment applications. The porosity of LDHs plays a crucial role in these applications as it allows for the efficient transport of molecules and ions in and out of the material. In this chapter, the structural properties of the LDHs could be tuned by altering the synthesis *pH*. The chemical versatility of LDHs in terms of the composition and $\text{M}^{2+}/\text{M}^{3+}$ molar ratio unlocks many possibilities for different chemical looping processes beyond power generation²⁰ and industrial processes that utilise LDHs and MMOs.

Chapter 8

Conclusions and future work

8.1 Conclusions

This thesis has focused on evaluating CuO-based oxygen carriers derived from LDH precursors for chemical looping processes. From the literature surveyed in chapter 2, the use of solid fuels for CLC is more complicated than for gaseous fuels owing to the additional gasification step required to overcome the slow reactions between the solid oxygen carrier and fuel char. CLOU is a variant of CLC that overcomes the slow char gasification step by using oxygen carriers that can release gaseous oxygen in the fuel reactor, improving the combustion and CO₂ capture efficiencies of the process. Of the potential CLOU candidate materials, CuO-based oxygen carriers have shown high reactivities and oxygen storage capacities but are prone to sintering and agglomeration at high temperatures. In previous studies, Al₂O₃ has been used as a support to improve the mechanical and thermal stability of the CuO-based oxygen carriers. However, CuO and Al₂O₃ can react to form the spinel CuAl₂O₄ during high-temperature calcination and redox cycling that is relatively stable to decomposition during CLOU. The addition of Mg to the Cu-Al system has been shown to stabilise the oxygen release capacity of CuO-based oxygen carriers by inhibiting the formation of CuAl₂O₄ through the preferential formation of an MgAl₂O₄ support phase.

The preparation of CuO-based oxygen carriers using conventional methods is generally limited to low loadings of active metal oxide due to the poor dispersion of CuO in the support. The preparation of oxygen carriers *via* the calcination of Cu-Al LDHs precursors has been shown to achieve a high degree of dispersion of active metal oxide within the support after calcination due to the mixing of metals in the LDH structure. The presence of Na was crucial to effectively inhibit the formation of CuAl₂O₄ by the formation of NaAl₂O₄. However, it remains challenging to precisely control the content of Na-containing species which originate from the precipitation agent used for co-precipitation of the LDHs.

Therefore, it is desirable to tune the synthetic chemistry of the Cu-Mg-Al LDH precursors to minimise the formation of Na-containing impurities and achieve a more stable long-term cycling performance.

The aim of this thesis was to evaluate the performance of CuO/Al₂O₃ and CuO/MgAl₂O₄ oxygen carriers derived from the calcination of Cu-Al and Cu-Mg-Al LDHs, respectively, prepared *via* co-precipitation at constant *pH*. This section summarises the main findings of this thesis. It lists the relevant project objectives and highlights the results achieved in each chapter.

8.1.1 *Development of Cu-Mg-Al layered double hydroxides and derived oxygen carriers for chemical looping processes*

The work in this chapter was carried out to meet the following project objective:

- Develop novel CuO-based oxygen carriers supported on Al₂O₃ and MgAl₂O₄ by tuning the synthetic chemistry of the layered double hydroxide precursors prepared *via* co-precipitation at constant *pH*.

The incorporation of Mg into the Cu-Al LDH system was investigated by varying the molar ratio of Cu:Mg:Al from 3:0:2 to 3:1:2. The LDHs were prepared *via* co-precipitation at a constant *pH* value of 9.5 using (i) 1 M NaOH and 1 M Na₂CO₃, or (ii) 2 M NaOH. Each material synthesised had an LDH structure and a Cu:Mg:Al molar ratio close to their target value. The Na content of the LDH precursors was found to decrease with increasing amounts of Mg in the Cu-Mg-Al system. In addition, the LDHs prepared using solely NaOH were found to contain much lower Na contents compared to those prepared using NaOH and Na₂CO₃. The thermodynamic calculations carried out determined that the formation of insoluble Na-containing species (i.e. dawsonite) occurred when CO₃²⁻ was present in the solution but was thermodynamically suppressed in the presence of Mg. Therefore, the LDHs synthesised using high amounts of Mg in the metal ion solution and those prepared using solely NaOH contained low amounts of Na.

HAADF-STEM imaging analysis and EDS elemental mapping were carried out to compare the degree of elemental dispersion and morphology of the MMOs synthesised from LDHs prepared using different co-precipitating agents and molar ratios of Cu:Mg:Al. The materials synthesised using solely NaOH showed a much denser structure with a poorer dispersion of CuO than those prepared using NaOH and Na₂CO₃. These observations were attributed to the interlayer anions (NO₃⁻ or CO₃²⁻) present in the solution during LDH formation. The 3:1:2 Cu-Mg-Al MMOs prepared using NaOH and Na₂CO₃ and the 3:2 Cu-Al MMOs prepared using solely NaOH were selected for further characterisation and testing in chapter 5.

8.1.2 Long-term redox cycling of Cu-Mg-Al layered double hydroxide-derived oxygen carriers in thermogravimetric and fluidised bed systems

The work in this chapter was carried out to meet the following project objective:

- Assess the chemical, thermal and mechanical stabilities of the oxygen carriers over long-term redox cycling in a thermogravimetric analyser and a laboratory-scale fluidised bed reactor.

The Cu-Mg-Al MMOs demonstrated fast reaction rates, high oxygen capacity, and excellent stability against sintering over multiple cycles of reduction and oxidation between CuO - Cu_2O - Cu in a TGA. The MgAl_2O_4 spinel phase remained inert during calcination and cycling and effectively inhibited the formation of CuAl_2O_4 . In contrast, the Cu-Al MMOs consisting of $\text{CuO}/\text{CuAl}_2\text{O}_4$ had slower oxidation and re-oxidation rates and were observed to deactivate over 100 CLOU cycles in a TGA.

In an FBR, the structural properties of the LDH precursors determined the performance of the derived MMOs over 100 CLOU cycles. The synthesis pH was determined to be an important parameter for tuning the mechanical properties of the MMOs. An increase in co-precipitation pH from 9.5 to 11 was found to decrease the porosity and increase the crushing strength of the MMOs while maintaining the desired molar ratio of Cu:Mg:Al. As a result, the higher-strength MMOs suffered much less attrition and retained high conversion over 100 full cycles of oxygen release and re-oxidation (over 65 h of operation in total). A similar trend was observed for Cu-Mg-Al MMOs synthesised from LDHs with higher contents of Cu in their structure co-precipitated at pH values of 9.5 and 11.

The near-constant conversion in the FBR confirmed the stability of the materials over extended redox cycling under CLOU conditions and showed the potential of Cu-Mg-Al MMOs as promising candidates for other chemical looping applications. Therefore, the performance of the Cu-Mg-Al MMO-11 under CLCP conditions was studied for 20 cycles in an FBR using CO and CH_4 ($\text{CuO} \rightarrow \text{Cu}$). The oxygen carriers demonstrated high thermal, chemical and mechanical stability under the harsher reduction conditions, suggesting their potential suitability for scale-up and testing in pilot facilities. Therefore, the kinetics of oxygen release from the oxygen carriers were investigated in the next chapter to aid reactor design.

8.1.3 Kinetics of oxygen release from CuO-based mixed metal oxides derived from layered double hydroxides

The work in this chapter was carried out to meet the following project objective:

- Model the intrinsic kinetics of the oxygen release reaction of the oxygen carriers to aid with the scale-up of chemical looping reactors.

Kinetic information is essential for designing and modelling chemical looping reactors. In this chapter, an adapted effectiveness factor-based kinetic model was used to determine the pseudo-intrinsic kinetics of oxygen release from 312-11-MMOs using an FBR and TGA. The sample masses and gas flow rates were chosen to minimise mass transfer resistances. The intrinsic rate constants for oxygen uncoupling were obtained for the temperature range 850 to 962°C by accounting for internal and external mass transfer effects in the effectiveness factor-based model. An activation energy of $51 \pm 3 \text{ kJ mol}^{-1}$ and a pre-exponential factor of 0.0567 s^{-1} were calculated for the oxygen release reaction using an Arrhenius expression. The ratio of external mass transfer rates to measured rates of oxygen release was found to be approximately 5 at high temperatures, suggesting that the rates of oxygen release at higher temperatures may have been slightly limited by external mass transfer. However, the removal of data points at the high end of the temperature range did not significantly change the activation energy obtained by fitting the Arrhenius expression.

8.1.4 *Effect of co-precipitation pH on the growth of Cu-Mg-Al layered double hydroxides and the structure and performance of derived mixed metal oxides*

The work in this chapter was carried out to meet the following project objectives:

- Investigate the formation mechanism of the Cu-Mg-Al layered double hydroxides by varying the co-precipitation *pH* value during co-precipitation.
- Assess the effect of the *pH* value during co-precipitation on the structure of the layered double hydroxides and oxygen carriers and the performance of the oxygen carriers in chemical looping processes.

To investigate the effect of co-precipitation *pH*, LDHs were co-precipitated at a constant *pH* between *pH* 9 and 11.5 for 300 min using an automated rig. The results of XRF indicated that the amount of Mg in the LDHs increased with increasing *pH*. The diameter and height of the LDH platelets and porosity of the material were observed to generally decrease with increasing *pH*, except for LDHs synthesised at *pH* 10, where the platelets grew fast in the radial direction. These larger diameter platelets synthesised at *pH* 10 were attributed to an interplay of supersaturation, thermodynamic and electrostatic factors.

The long-term performance of the MMOs was assessed for 100 CLOU and CLC cycles in a TGA at 900 °C. The formation of MgAl_2O_4 rather than CuAl_2O_4 was critical for the effective stabilisation of CuO and to avoid the slow re-oxidation of the oxygen carrier and maintain stable oxygen release and storage capacities over extended redox cycling. The more porous MMOs synthesised at *pH* 9, 9.5 and 10 showed much higher rates of oxygen release than the less porous materials synthesised at *pH* 10.5, 11 and 11.5 – although mass transfer limitations may have concealed the true maximum rates of oxygen release of the more porous MMOs in the TGA.

The MMOs prepared from LDHs synthesised at *pH* 10 and 11 were cycled for 500 CLC cycles in a TGA at 900 °C to test the LDH-MMO stabilisation strategy. MMO-10 has a lower crushing strength and higher porosity suitable for packed bed reactors, while the MMO-11 has a higher crushing strength and lower porosity, more suitable for FBRs. The results from the 500 CLC cycle experiments at high temperatures indicate that the Cu-Mg-Al LDH-derived MMOs are promising oxygen carriers, and the particle morphology is tuneable for different reactor systems. The results of this chapter demonstrate that Cu-Mg-Al MMOs are promising candidates for further development and scale-up for use in chemical looping processes utilising either fluidised or fixed bed reactors.

8.2 Future work

The work carried out in this thesis could be extended to realise the full potential of the LDH-MMO design strategy for the development of oxygen carriers for chemical looping processes. Potential areas of future work are detailed in this section.

8.2.1 *Further insights into the layered double hydroxide and mixed metal oxide materials*

The formation mechanism of LDHs is a complex process that is not yet fully understood. While the work carried out in this thesis has contributed to the understanding of LDH formation, many questions remain. To address the remaining knowledge gaps, research could focus on several key areas: (i) developing an electrostatic model of LDHs, and (ii) conducting a systematic study to investigate the impact of co-precipitation parameters (such as molar concentrations of the metal ion and co-precipitating solutions and the rate of addition of these solutions) on the nucleation and growth of LDHs. Additional material characterisation methods not explored in this work, including Raman spectroscopy, small-angle X-ray scattering (SAXS) and HR-TEM, could be used to study the textural and crystallographic features of the LDHs.

Another aspect that deserves further research is a better understanding of the metal-support interactions in the MMOs. It remains challenging to fully understand the interfaces between the Cu phases and the support due to the difficulties characterising the sintering behaviour at high temperatures. In this work, the CuO nanoparticles were well dispersed in the support. According to thermogravimetric analysis as well as ex-situ and in-situ XRD analysis, the gaseous oxygen is predominantly released from crystalline CuO, confirming that the content of CuAl_2O_4 or $\text{Mg}(\text{Cu})\text{Al}_2\text{O}_4$ is negligible. Nevertheless, residual Cu species may be incorporated into the spinel support at the grain boundaries of the CuO nanoparticles and Mg-Al spinel support, which likely form reducible CuAl_2O_4 or $\text{Mg}(\text{Cu})\text{Al}_2\text{O}_4$ overlayers, which in turn function as physical barrier layers to separate CuO nanoparticles from sintering or further immobilise Cu phases in the support. These strong active phase-support interactions and the local electronic transfer merit further study in the future.

8.2.2 *Further considerations for the material preparation method*

This thesis focused on understanding the relationship between the LDH precursor and the properties of the MMOs during redox cycling. The MMOs were prepared by calcining the precursors and subsequently crushing and sieving to obtain suitable particle size ranges for use in FBRs. Although the CuO-based particles maintained their physical structures during testing, the mechanical properties and shapes of particles used in different types of reactors should be considered. For chemical looping processes using FBRs, attrition of particles is a critical obstacle for commercialisation. The redox reactions at high temperatures generate significant chemical stresses, while thermal sintering generates additional mechanical and thermal stresses, which tend to induce structural changes and lead to a decline of the mechanical strength of the oxygen carriers in reactors. Advanced particle manufacturing technologies (that enable the production of near-spherical particles), such as spray drying and granulation, might further improve the mechanical strength and reduce attrition. For use in packed bed reactors, large-scale pelletising techniques could be used to prepare suitable particle shapes with enhanced mechanical strength.

Scaling up the preparation methods of oxygen carriers is an important step in transitioning these materials from laboratory to pilot-scale operation. While batch sizes at the kilogram scale have already been achieved using standard laboratory equipment, the co-precipitation method could introduce significant challenges for scale-up – including uniformity issues. In this thesis, studying the LDH formation over long synthesis times should aid the scale-up of the preparation method. It was observed that the LDHs formed extremely quickly during co-precipitation and that the residence time has different effects on the particle growth depending on the pH of the solution. The LDHs synthesised above the IEP showed limited particle growth with increasing synthesis time, and therefore, the residence time should not significantly impact the LDH characteristics. Therefore, a continuous process could be investigated to scale up materials co-precipitated above the IEP. The dimensions of the LDH platelets co-precipitated at or below the IEP was dependent on the co-precipitation duration. A batch process at or below the IEP could be investigated to determine whether the morphology and porosity of the materials could be controlled by changing the rate of solution addition or co-precipitation duration.

The preparation method used in this thesis to produce the MMOs involves calcining the LDHs and crushing and sieving the calcined material to the desired particle size fractions. However, crushing and sieving inevitably generates a significant amount of fines that cannot be used as oxygen carriers directly. However, the fines should retain the high chemical stability of the MMOs. Therefore, a future project could investigate recycling these waste materials using particle-formation methods, *e.g.* spray drying.

The economic feasibility of an oxygen carrier is often a significant factor for their application in large-scale units. Therefore, it would be beneficial to perform a cost analysis of the scaled-up synthesis

procedure. A life cycle assessment could also be carried out to understand and optimise the energy consumption and environmental impact of the process. Alternative feed materials could also be considered, *e.g.* metal chlorides instead of metal nitrates and alternative sources of alkali.

8.2.3 *Further considerations for operation at scale*

Future investigations to test oxygen carriers in larger-scale chemical looping systems are needed to validate their performance under more realistic operating conditions. This can be achieved through collaborations with research groups who have developed pilot-scale chemical looping reactors. Additionally, it would be beneficial to develop more efficient screening tools to evaluate the attrition resistance of the oxygen carriers. One such method is an attrition jet cup in accordance with ASTM D5757. While most studies measure the attrition resistance or crushing strength of oxidised oxygen carrier particles, it is important to consider that reduced oxygen carriers are more porous and likely the weakest state during redox cycling. Therefore, the attrition resistance of reduced oxygen carriers could be explored to investigate whether any strong correlations with survivability in fluidised bed systems can be made.

In future work, the oxygen release kinetics of the higher CuO loading oxygen carriers developed in chapter 5 could be determined using the effectiveness factor-based model. An alternative oxygen sensor with a higher sampling frequency, such as a UEGO, could be used to extract the oxygen release kinetics and compared with the results using the gas analyser used in this thesis.

This thesis determined that the MMOs derived from LDHs synthesised for long co-precipitation durations at or below the IEP had characteristics that were suitable for fixed bed reactors. Therefore, a fixed bed reactor configuration could be investigated using the existing FBR set-up by manufacturing a quartz liner containing a disc for a bed of particles to be loaded. The effectiveness of CuO stabilisation using the LDH-MMO would be tested in this system, where sintering and agglomeration is more likely due to the higher amount of contact between the particles.

The CLOU process was developed to improve the performance of CLC using solid fuels. However, the impurities present in solid fuels, such as coal, biomass or wastes, could significantly impact the performance of the oxygen carriers. A better understanding of the interactions of the oxygen carriers developed in this thesis with typical fuel impurities, such as alkali metals, sulphur and chlorine, is needed to validate the use of synthetic oxygen carriers rather than natural or waste materials. Cycling experiments in a TGA with intensified amounts of fuel impurities could be conducted to explore if there are any detrimental effects to the chemical or mechanical stability of the oxygen carrier.

8.2.4 *Exploration of new layered double hydroxide systems to produce mixed metal oxides for chemical looping processes*

The structural diversity of LDHs enables versatile combinations of metal ions to be highly dispersed in their structure, producing MMOs with high dispersions of active metal species in a support phase upon calcination. This LDH-MMO design strategy has the potential to inspire the development of highly stable oxygen carriers for many emerging chemical looping processes. Chemical looping water splitting (CLWS) for hydrogen production is one such process which typically uses oxygen carriers based on Fe_2O_3 as the active metal oxide. As discussed in chapter 2, Fe_2O_3 -based oxygen carriers experience severe sintering that leads to severe deactivation during redox cycling, especially during the transition from FeO to metallic Fe , the reverse of which is crucial for hydrogen production from steam oxidation.

The research presented in this thesis has shown the extremely high stability of CuO -based oxygen carriers developed using the LDH-MMO design strategy over 500 CLOU cycles, supporting the development of $\text{Fe}_2\text{O}_3/\text{MgAl}_2\text{O}_4$ oxygen carriers for CLWS as a natural extension of this work. Early results for the preparation of Fe-Mg-Al LDHs and MMOs have been promising, with initial CLC cycling experiments showing effective stabilisation of Fe_2O_3 against sintering and deactivation over 100 CLC cycles. However, further investigation is required to explore the effectiveness of the LDH-MMO design strategy to produce oxygen carriers for chemical looping processes.

Appendix

Appendix A1: Initial parametric study for the synthesis of layered double hydroxides

From the literature review of LDH syntheses carried out in chapter 2, the co-precipitation pH, solution concentrations, and aging time are critical synthesis parameters for the preparation of LDHs. This thesis builds upon previous work by Song *et al.* to develop Cu-Al LDHs and MMOs for chemical looping processes.¹⁵⁶ In their work, the concentration of metal ion and alkaline solutions were 2 M, an aging time of 3 h was used and a pH of 9.5 was maintained during co-precipitation. In this section, a small study of synthesis parameters was carried out for LDHs with a target Cu:Mg:Al molar ratio of 3:1:2. XRD and N₂ adsorption analysis were used to study the materials. The XRD spectra contain peaks corresponding to CeO₂ that arise from mixing 10 wt% CeO₂ in the sample for qualitative comparison of the sample crystallinity.

Metal ion and alkaline solution concentrations equal to 0.5, 1 and 2 M were investigated. A pH value of 9.5 was maintained during co-precipitation and the precipitates were aged for 3 h before washing. From **Figure A1-1**, the results of XRD show that increasing the solution concentration slightly increased the intensity of the (003) peak centred at ~ 12°. The pore size distribution determined using N₂ adsorption results did not significantly change upon increasing the solution concentrations from 0.5 to 2 M (**Figure A1-2**). Therefore, a 2 M concentration was used for each solution to increase the amount of material synthesised per unit volume.

The effect of aging duration after co-precipitation was investigated using 30 min, 3 h and 6 h durations. The results in **Figure A1-3** and **Figure A1-4** show the aging time did not significantly affect properties of the precipitates determined using XRD and N₂ adsorption. Therefore, aging times of 30 min or 3 h were used for the syntheses in this thesis.

LDHs were prepared using a co-precipitation pH value of 9.5, 10.5 and 11.5. From **Figure A1-5**, the co-precipitation pH was found to have a significant effect on the XRD patterns of the LDHs. The results of N₂ adsorption also showed a distinctly different pore size distribution of the materials (**Figure A1-6**). Therefore, the effect of co-precipitation pH was investigated throughout this thesis, and a pH value of 9.5 was used for the initial syntheses.

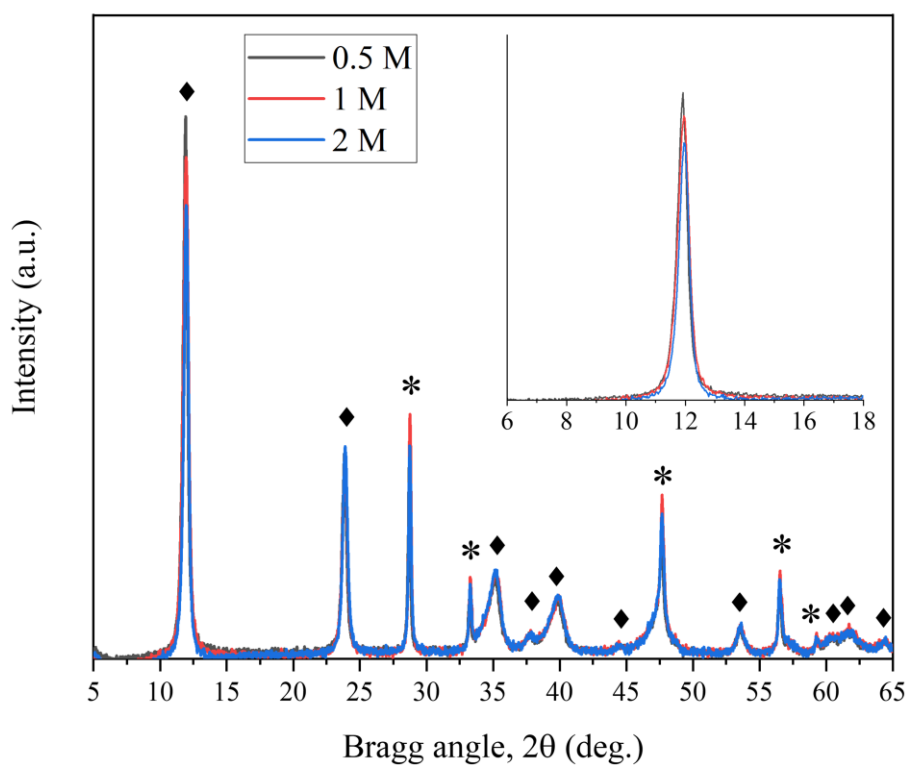


Figure A1-1: XRD patterns of LDHs as a function metal ion and co-precipitating solution concentration ◆ = LDH * = CeO_2 .

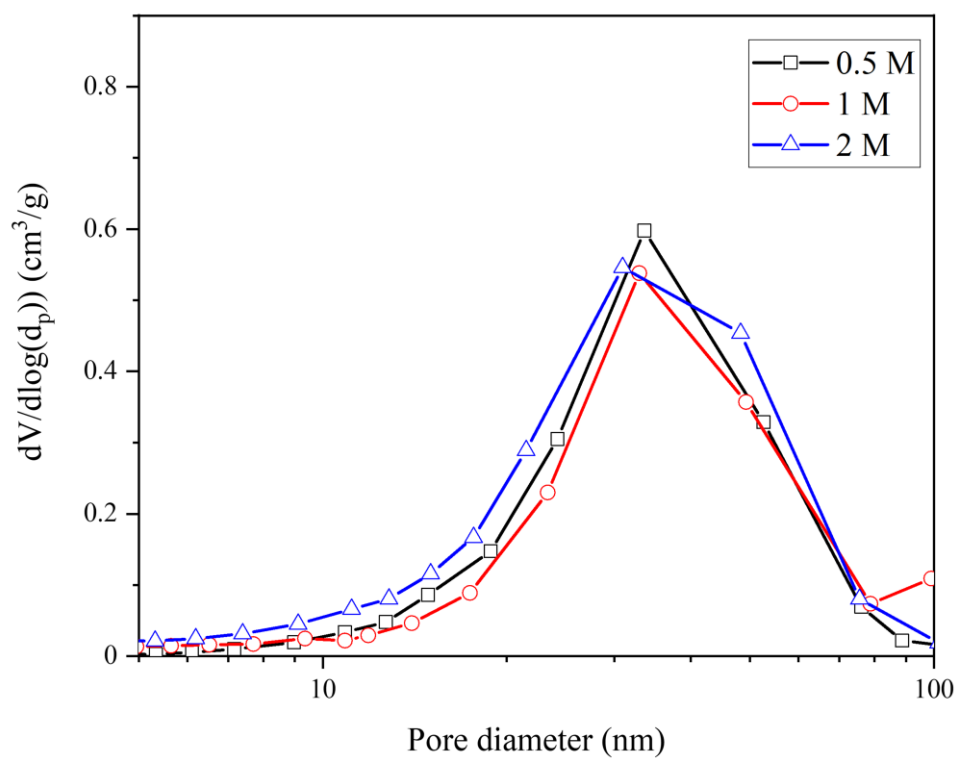


Figure A1-2: Pore size distribution of LDHs determined using N_2 adsorption as a function metal ion and co-precipitating solution concentration.

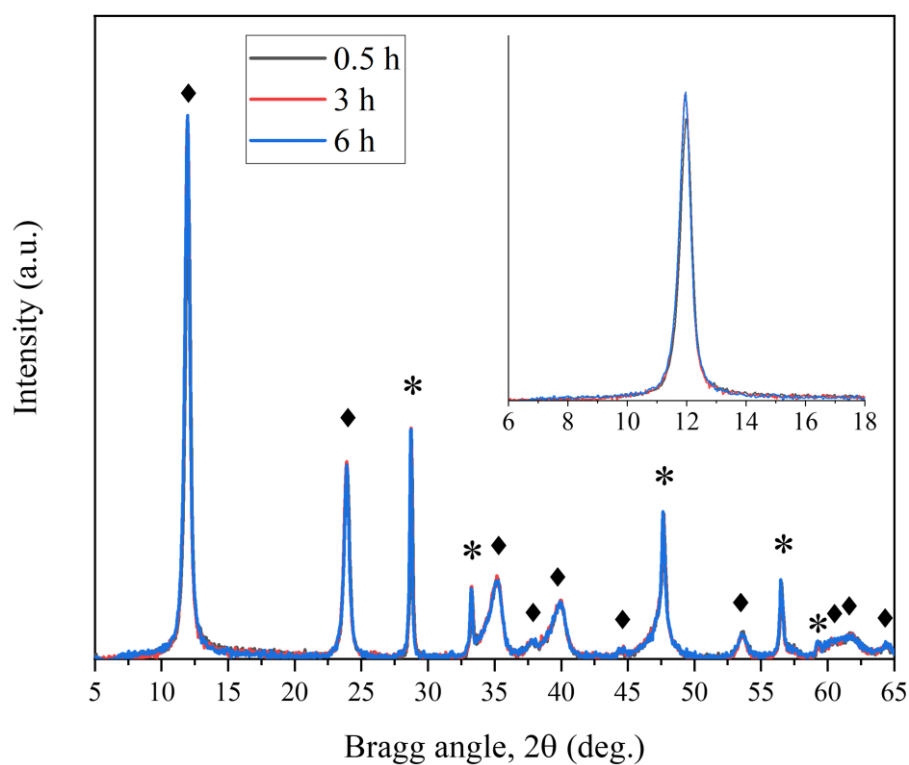


Figure A1-3: XRD patterns of LDHs as a function of aging time after co-precipitation. ◆ = LDH * = CeO_2 .

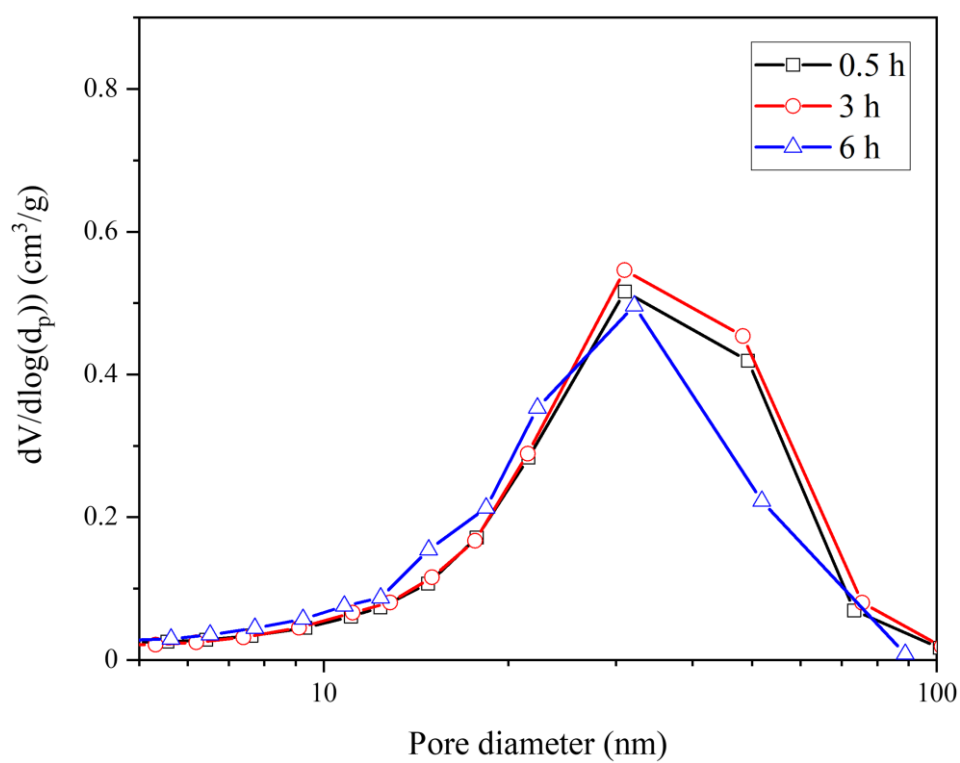


Figure A1-4: Pore size distribution of LDHs determined using N_2 adsorption as a function of aging time after co-precipitation.

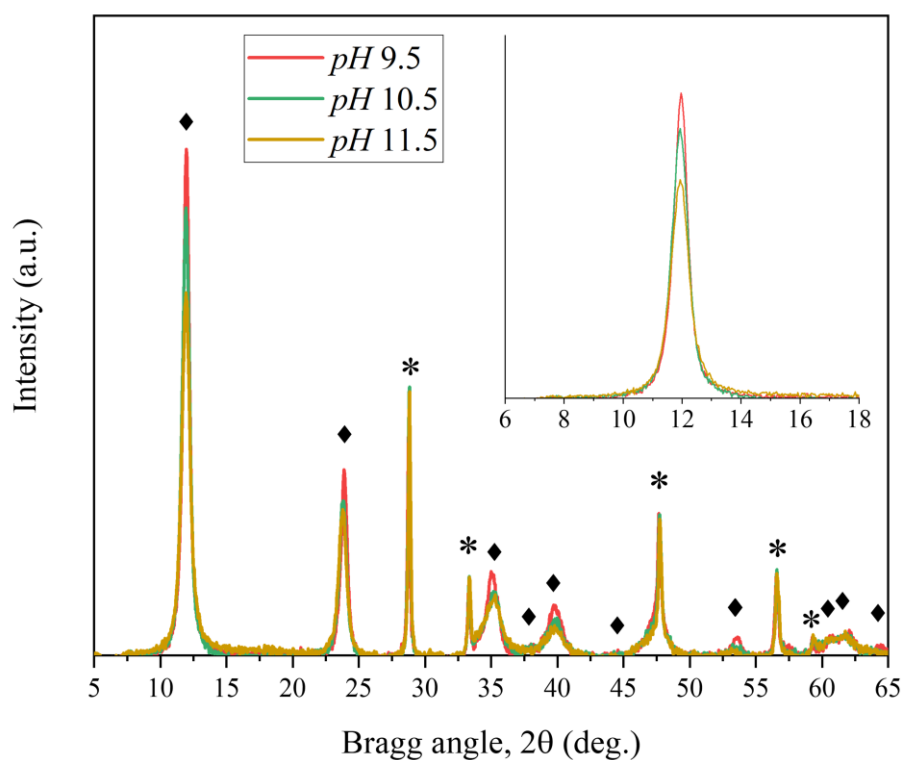


Figure A1-5: XRD patterns of LDHs as a function of co-precipitation pH. ◆ = LDH * = CeO_2 .

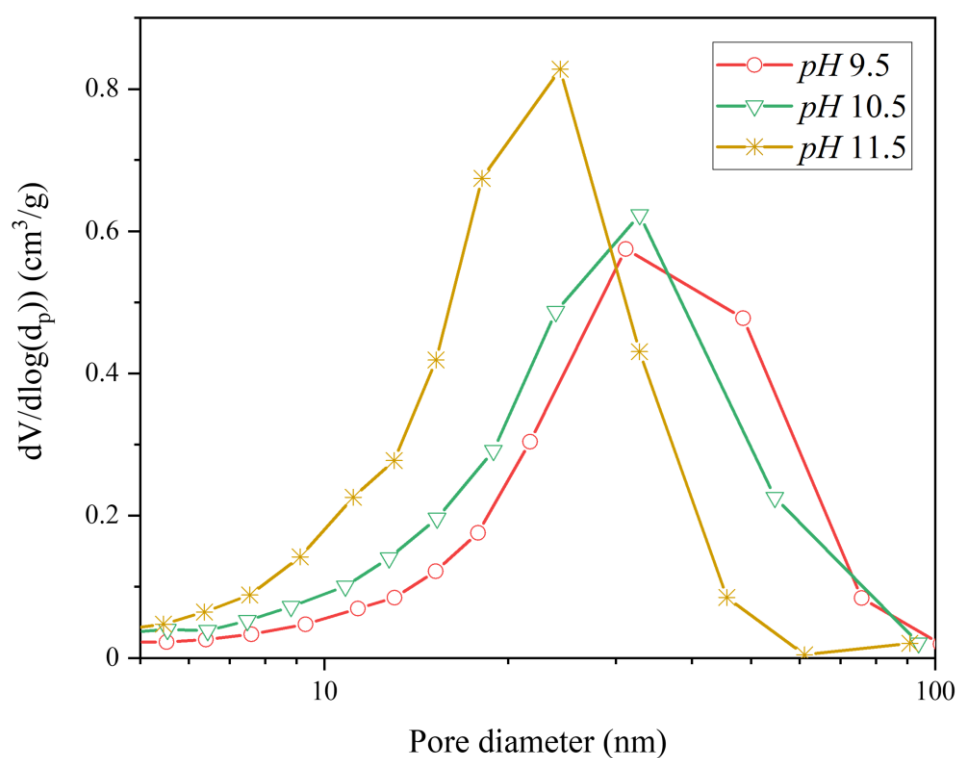


Figure A1-6: Pore size distribution of LDHs determined using N_2 adsorption as a function of co-precipitation pH.

Appendix A2: Comparison of pore size distribution of materials using N₂ adsorption and MIP

The pore size distribution of LDH materials is commonly investigated using N₂ adsorption analysis in the literature. The technique works on the principle of the physical adsorption of N₂ gas onto the surface of a material at cryogenic temperatures (~77 K). The BJH theory is used to determine the pore size distribution by analysing the volume of gas adsorbed during the decrease of p/p_0 from 0.995 to 0.05 using a modified Kelvin equation. The pore size distributions were estimated from the desorption branch of the adsorption-desorption isotherm. The BJH theory assumes all pores are straight and cylindrical. The log differential pore volume (dV) as a function of pore diameter, $dV/d(\log D_p)$ for calcined MMO-10 determined using N₂ adsorption is presented in **Figure A2-1**. The log distribution scale provides a better indication of the pore regions of the materials as a linear scale would obscure the micro- and meso-porosity of the materials.

MIP was also carried out to measure the pore size distribution and pore volume of the LDH materials. Mercury has exceptionally high interfacial tension and therefore behaves as a non-wetting fluid and will not spontaneously penetrate pores by capillary action – it must be forced into the pores by the application of external pressure. The required pressure is inversely proportional to the pore diameter. By measuring the volume of mercury that intrudes into the sample with each pressure change, the volume of pores at different stages of intrusion (and pore diameters) is known. A total pressure range of 0.7 – 2275 bar was used for mercury intrusion, corresponding to a pore diameter range of 18 μm – 5 nm, respectively. However, only the pore volumes for the pore diameter range 5 to 10000 nm were used for further calculations. MIP was used to analyse the pore size distribution of the materials beyond the resolution of N₂ adsorption. The log differential pore volume as a function of pore diameter, $dV_p/d(\log D_p)$ for calcined MMO-10 determined using MIP is presented in **Figure A2-1**.

Figure A2-1 shows a comparison of the MIP and N₂ adsorption techniques that were used to study the changes in the pore size distribution of the LDH-10 during calcination. There was decent agreement between the pore size distributions determined using MIP and N₂ adsorption for pores below 100nm. However, pores above 100 nm are beyond the resolution of N₂ adsorption. SEM images clearly showed the presence of larger pores above 100 nm in the LDH-10. Therefore, MIP was used to determine the pore size distributions of the remaining materials. The data from pores above 10000 nm were neglected to avoid overstated results due to the filling of the external surface and inter-particle voids shown in **Figure A2-2**.

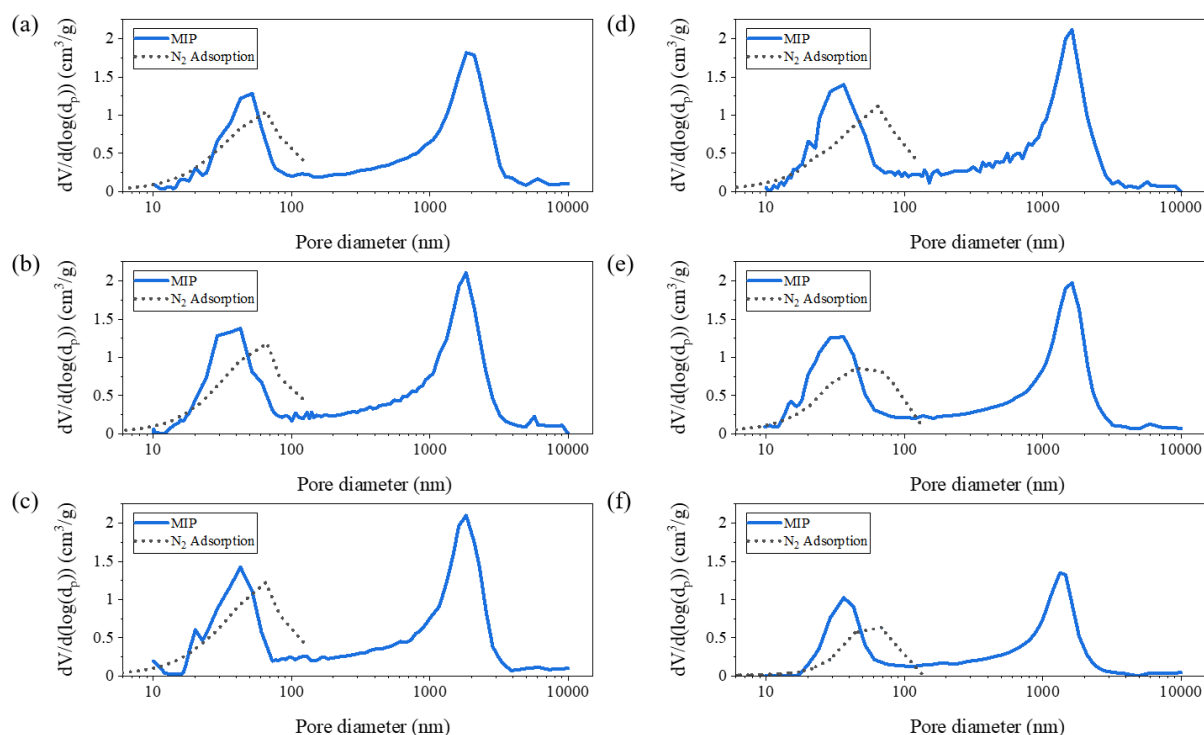


Figure A2-1: Pore size distribution of LDH-10 as a function of calcination temperature determined using N_2 adsorption and MIP. Samples were calcined at (a) 50°C (b) 165°C (c) 265°C (d) 465°C (e) 765°C (f) 975°C. LDH-10 was prepared via co-precipitation for 300 min at pH 10. Samples were calcined at the desired temperature under air and for 3 h.

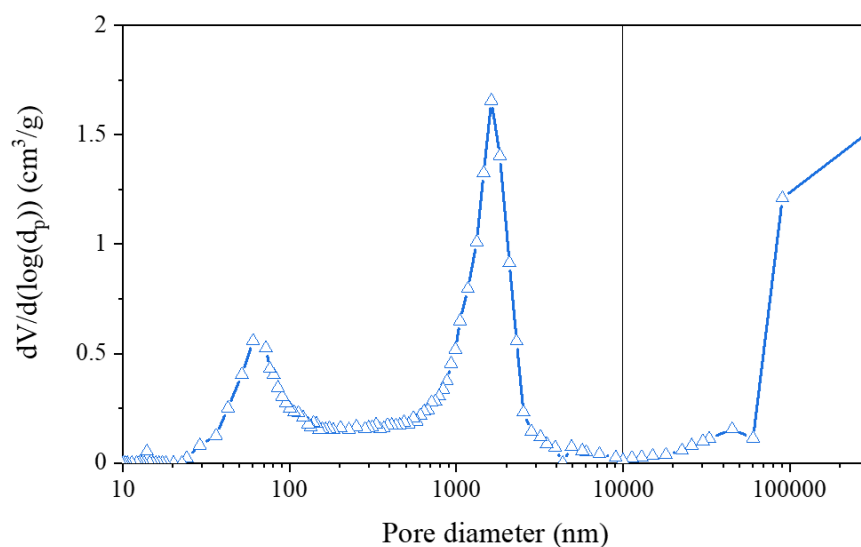


Figure A2-1: Pore size distribution of MMO-10 as a function of calcination temperature determined using MIP. Line shows the cut off at 10000 nm between interparticle and intraparticle filling.

Copyright permissions

Type of work:	Name of work	Reference	Copyright holder	Permission approved	License No.
Figure	Figure 2-3: iG-CLC fuel reactor scheme. Coal is used as a representative solid fuel, <i>adapted from Adanez et al.</i> ⁵⁰	⁵⁰	Elsevier	Yes	5521880504730
Figure	Figure 2-4: CLOU fuel reactor scheme. Coal is used as a representative solid fuel, adapted from <i>Adanez et al.</i> ⁵⁰	⁵⁰	Elsevier	Yes	5521880504730
Figure	Figure 7-14: Effect of Cu content on properties of Cu-Mg-Al LDHs. (a) XRD patterns of CuX-Mg _(1-x) Al ₂ LDHs, where x = 0 to 4. SEM images of CuX-Mg _(1-x) Al ₂ LDHs where (b) x = 0, and (c) x = 2. Reproduced with permission from Springer Nature. ²⁹²	²⁹²	Springer Nature	Yes	5490260312668
Figure	Figure 7-15: Number of crystallites and type of bonds responsible for the morphology of LDH particles. Reprinted (adapted) with permission from ²⁹⁵ . Copyright 2023 American Chemical Society.	²⁹⁵	2023 American Chemical Society	Yes	-
Figure	Figure 7-3: Structure of LDH materials. (a) hexagonally packed atom positions in the brucite-like layer; and stacking of layers with (b) trigonal P-type (e.g. AC=CA), and (c,d) octahedral O-type interlayer sites (e.g. AC-BA and AC-AC) . Only the lower hydroxyl groups of the upper layer is shown. Large circles are hydroxyl groups, small circles are cations. Adapted from Bookin and Drits. ²⁶³	²⁶³	Springer Nature	Yes	5521880983051
Figure	Figure 7-4: Scheme for derivation of two-layer polytypes. Adapted from Bookin and Drits. ²⁶³	²⁶³	Springer Nature	Yes	5521880983051

Figure	Figure 7-7: Domain diagram of $\text{Al}(\text{OH})_3$, $\text{Mg}(\text{OH})_2$, and Mg-Al-NO_3 LDHs. Solubility is denoted as S on the y axis. Reproduced with permission from Elsevier. ²⁸⁶	286	Elsevier	Yes	5490141488306
Table	Table 2-3: Cu ores used as oxygen carriers in CLC systems, adapted from Matzen et al. ¹³⁷	137	Elsevier	Yes	5521880724815
Table	Table 6-1: Results of kinetic studies of CuO-based oxygen carriers for CLOU processes, adapted from Tian et al. ²⁴⁴	244	Elsevier	Yes	5521870650487

Nomenclature

Roman letters

Ar	Archimedes number
A_C	Cross-sectional area of the reactor tube
A_o	Cross-sectional area of the spout orifice
B_i	Peak broadening of the instrument calibration standard
B_{obs}	Observed peak broadening
C	Molar gas concentration
$CCCOC$	Cost per tonne of CO ₂ captured caused by the oxygen carrier, CCCOC,
CN	Coordination number
$C_{O_2,b}$	Bulk O ₂ concentration
$C_{O_2,eq}$	Equilibrium O ₂ concentration
d	Interplanar spacing
D	Molecular diffusivity of O ₂ in N ₂
D_{AB}	Bulk diffusion
D_b	Bubble diameter
D_r	Diameter of the reactor tube
D_e	Effective diffusivity

D_K	Knudsen diffusion
d_p	Mean bed particle diameter
d_{pan}	Diameter of TGA pan
$f(X)$	Conversion function
g	Acceleration due to gravity
$g_{\text{O}_2}/g_{\text{OC}}$	Mass of oxygen released per mass of oxygen carriers
$\text{GtCO}_{2,\text{eq}} \text{ yr}^{-1}$	Gigatonne CO ₂ equivalent per year
H	Height of the fluidising bed
H_{mf}	Height of the fluidising bed at minimum fluidisation
h	Height of the TGA pan
K	Crystallite shape factor
k	Kinetic constant
k_B	Boltzmann constant
k_g	External mass transfer coefficient
k_G	Mass transfer coefficient from a bubble to its surface
k_i	Intrinsic kinetic constant
k_o	Observed kinetic constant
kW_{th}	Kilowatt thermal
L	Crystallite size

L	Sum of the mean M-O bond length and the O-H bond length
M^{2+}	Divalent metal cation
M^{3+}	Trivalent metal cation
Me_xO_y	Oxidised oxygen carrier
Me_xO_{y-1}	Reduced oxygen carrier
M_i	Molecular weight of component i
$m_{O_2, released}$	Mass of fully oxygen released sample (CLOU)
m_{OC}	Mass of oxygen carrier charge
m_{ox}	Mass of fully oxidised oxygen carrier
m_{red}	Mass of fully reduced oxygen carrier (CLC)
MW_{th}	Megawatt thermal
MW_{O_2}	Molecular weight of oxygen
N	Number of bubbles per unit volume
n	Diffraction order
n_{out}	Molar flow rate of the effluent gas
N_{O_2}	Molar flow rate of oxygen
P	Pressure
p_{O_2}	Oxygen partial pressure
p_{O_2eq}	Equilibrium oxygen partial pressures

Q	Equivalent flow rate to and from the bubble
q	Rate of exchange between a bubble and the particulate phase
Re	Reynolds number
Re_{mf}	Reynolds number at minimum fluidisation
Re_p	Reynolds number of the particles in the particulate phase
R_{OR}	Oxygen release capacity
R_{OS}	Oxygen storage capacity
r_p	Particle radius
S	Surface area of a rising bubble
S_A	Surface area
Sc	Schmidt number
SE	Specific emissions of the fuel
Sh	Sherwood number
SI	Solids inventory
T	Temperature
t	Time
t_d	Dead time
$t_{lifetime}$	Average lifetime of the oxygen carrier particle
u	Superficial velocity

u_A	Absolute rising velocity of bubble
u_b	Rising velocity of bubble in a stagnant fluid
u_{mf}	Minimum fluidisation velocity
V_b	Bubble volume
V_{bed}	Volume of the bed
V_p	Pore volume
W_s	Flow rate into all bubbles from particulate phases
X	Conversion
X_f	Cross flow factor
y_b	Mole fraction of oxygen in the bulk
$y_{CO_2,out}$	Mole fraction of CO_2 in the product gas
y_{O_2}	Mole fraction of oxygen
$y_{O_2,inert}$	Mole fraction of oxygen during the oxidation or reduction phases of cycling in the absence of oxygen carriers
$y_{O_2,sample}$	Mole fraction of oxygen during the oxidation or reduction phases of cycling in the presence of oxygen carriers
y_s	Mole fraction of oxygen at the particle surface
Z	Charge of the central metal ion

Greek letters

α_R	Archimedes constant
β	Peak position
β_R	Archimedes constant
δ	Oxygen non-stoichiometric coefficient
ε	Porosity
ε_{mf}	Voidage at minimum fluidisation
ε_{12}	Energy parameter
η	Effectiveness factor
η_{CO_2}	CO ₂ capture efficiency
θ	Angle between the incident X-ray and diffracting plane
θ_{cone}	Angle of the Cone of the quartz liner
λ	Wavelength
μ_g	Viscosity of the fluidising gas
ν	Kinematic viscosity
ν_g	Volumetric flow rate
ν_m	Molar volume of a gas
ν_p	Pauling bond valence
$(\sum \nu)_i$	Diffusion volumes of species i

ρ_g	Density of the fluidising gas
ρ_p	Envelope density
ρ_{sk}	Skeletal density
σ_{12}^2	Collision diameter
τ	Tortuosity factor
τ_{GM}	Contribution to the convolution of the signal by the gas mixing in the piping
τ_{GM}	Contribution to the convolution of the signal by the sample analyser
τ_{MIX}	Contribution to convolution of signal by the overall measurement system
ϕ	Thiele modulus
Ω	Collision integral

Abbreviations

ATR	Attenuated total reflectance
BET	Brunauer–Emmett–Teller
BJH	Barrett-Joyner-Halenda
BECCS	Bioenergy with carbon capture and sequestration/storage
CCS	Carbon capture and sequestration/storage
CCUS	Carbon capture and utilisation or sequestration/storage
CLC	Chemical looping combustion
CLCP	Chemical looping combustive purification
CLOU	Chemical looping with oxygen uncoupling
CLWS	Chemical looping water splitting
CP	Co-precipitation
EDS	Energy-dispersive X-ray spectroscopy
FBR	Fluidised bed reactor
FG	Freeze-granulation
FTIR	Fourier-transform infrared spectroscopy
FWHM	Full width at half maximum
GHG	Greenhouse gas
HAADF	High-angle annular dark-field

ICP	Inductively coupled plasma
iG-CLC	In-situ gasification chemical looping combustion
IM	Impregnation
IPCC	Intergovernmental Panel on Climate Change
LDH	Layered double hydroxide
MEA	Monoethanolamine
MFC	Mass flow controller
MIP	Mercury intrusion porosimetry
MM	Mechanical mixing
MMO	Mixed metal oxide
MM-P	Mechanical mixing followed by pelletising by pressure
SATP	Standard atmospheric temperature and pressure
SEM	Scanning electron microscopy
SP	Spray drying
STEM	Scanning transmission electron microscopy
SUCCESS	Scale-up of Oxygen Carrier for Chemical Looping Combustion using Environmentally Sustainable Materials
TEM	Transmission electron microscopy
TGA	Thermogravimetric analyser
XRD	X-ray diffraction

Bibliography

- 1 IPCC. Climate Change 2014 Mitigation of Climate Change. 2014; **100**: 2017.
- 2 IPCC. Special report: Global warming of 1.5°C. 2018.
- 3 Jewell J, McCollum D, Emmerling J, Bertram C, Gernaat DEHJ, Krey V *et al.* Limited emission reductions from fuel subsidy removal except in energy-exporting regions. *Nature* 2018; **554**: 229–233.
- 4 Erickson P, van Asselt H, Koplow D, Lazarus M, Newell P, Oreskes N *et al.* Why fossil fuel producer subsidies matter. *Nature* 2020; **578**: E1–E4.
- 5 IPCC. Global Warming of 1.5°C: Strengthening and Implementing the Global Response. 2018.
- 6 IPCC. *Climate Change 2022: Impacts, Adaptation, and Vulnerability. Contribution of Working Group II to the Sixth Assessment Report of the Intergovernmental Panel on Climate Change*. 2022.
- 7 National Statistics. DUKES chapter 5: statistics on electricity from generation through to sales. Fuel used in generation. 2022.
- 8 Ember. Global Electricity Review 2022. <https://ember-climate.org/insights/research/global-electricity-review-2022/>.
- 9 Pfenninger S, Keirstead J. Renewables, nuclear, or fossil fuels? Scenarios for Great Britain's power system considering costs, emissions and energy security. *Appl Energy* 2015; **152**: 83–93.
- 10 Bui M, Adjiman CS, Bardow A, Anthony EJ, Boston A, Brown S *et al.* Carbon capture and storage (CCS): The way forward. *Energy Environ Sci* 2018; **11**: 1062–1176.
- 11 Reiner D. *Carbon Capture and Storage*. The Royal Society of Chemistry, 2020 doi:10.1039/9781788012744.
- 12 Kearns D, Liu H, Consoli C. Technology Readiness and Costs of CCS. 2021.
- 13 HM Treasury. Build Back Better: our plan for growth. 2021.
- 14 HM Treasury. Spring Budget 2023. 2023.
- 15 Kanniche M, Gros-Bonnivard R, Jaud P, Valle-Marcos J, Amann J-M, Bouallou C. Pre-combustion, post-combustion and oxy-combustion in thermal power plant for CO₂ capture. *Appl Therm Eng* 2010; **30**: 53–62.
- 16 Kheirini M, Ahmed S, Rahmanian N. Comparative Techno-Economic Analysis of Carbon Capture Processes: Pre-Combustion, Post-Combustion, and Oxy-Fuel Combustion Operations. *Sustainability* 2021; **13**.<https://www.mdpi.com/2071-1050/13/24/13567>.
- 17 Alalwan HA, Alminshid AH. CO₂ capturing methods: Chemical looping combustion (CLC) as a promising technique. *Sci Total Environ* 2021; **788**: 147850.
- 18 Lyngfelt A, Brink A, Langørgen Ø, Mattisson T, Rydén M, Linderholm C. 11,000 h of chemical-looping combustion operation—Where are we and where do we want to go? *Int J Greenh Gas*

- Control* 2019; **88**: 38–56.
- 19 Adánez J, Abad A, Mendiara T, Gayán P, de Diego LF, García-Labiano F. Chemical looping combustion of solid fuels. *Prog Energy Combust Sci* 2018; **65**: 6–66.
 - 20 Zhu X, Imtiaz Q, Donat F, Müller CR, Li F. Chemical looping beyond combustion – a perspective. *Energy Environ Sci* 2020; **13**: 772–804.
 - 21 Mattisson T, Lyngfelt A, Leion H. Chemical-looping with oxygen uncoupling for combustion of solid fuels. *Int J Greenh Gas Control* 2009; **3**: 11–19.
 - 22 Pérez-Vega R, Abad A, Gayán P, de Diego LF, García-Labiano F, Adánez J. Development of $(\text{Mn}_{0.77}\text{Fe}_{0.23})_2\text{O}_3$ particles as an oxygen carrier for coal combustion with CO_2 capture via in-situ gasification chemical looping combustion (iG-CLC) aided by oxygen uncoupling (CLOU). *Fuel Process Technol* 2017; **164**: 69–79.
 - 23 Liu G, Lisak G. Cu-based oxygen carriers for chemical looping processes: Opportunities and challenges. *Fuel* 2023; **342**: 127828.
 - 24 Abdalla A, Mohamedali M, Mahinpey N. Recent progress in the development of synthetic oxygen carriers for chemical looping combustion applications. *Catal Today* 2023; **407**: 21–51.
 - 25 Niass T, Kislear J, Powell M, Buchanan J, Svalestuen J, Park A *et al.* Accelerating Breakthrough Innovation in Carbon Capture, Utilization, and Storage. 2017.
 - 26 Daneshmand-Jahromi S, Sedghkerdar MH, Mahinpey N. A review of chemical looping combustion technology: Fundamentals, and development of natural, industrial waste, and synthetic oxygen carriers. *Fuel* 2023; **341**: 127626.
 - 27 Lewis WK, Gilliland ER, Sweeney MP. Metal oxides in fluidized powder beds. *Chem Eng Prog* 1951; **47**: 251–256.
 - 28 Lewis WK, Gilliland ER. Production of Pure Carbon Dioxide. 1954; US Patent: No.2,665,971.
 - 29 Richter HJ, Knoche KF. Reversibility of combustion processes. *ACS Symp Ser* 1983; **No. 235**: 71–85.
 - 30 Ishida M, Zheng D, Akehata T. Evaluation of a chemical-looping-combustion power-generation system by graphic exergy analysis. *Energy* 1987; **12**: 147–154.
 - 31 Ishida M, Jin H. A Novel Combustor Based on Chemical-Looping Reactions and Its Reaction Kinetics. *J. Chem. Eng. Japan*. 1994; **27**: 296–301.
 - 32 Gonzalez-Garay A, Bui M, Freire Ordóñez D, High M, Oxley A, Moustafa N *et al.* Hydrogen Production and Its Applications to Mobility. *Annu Rev Chem Biomol Eng* 2022; **13**: 501–528.
 - 33 Hossain MM, de Lasa HI. Chemical-looping combustion (CLC) for inherent separations—a review. *Chem Eng Sci* 2008; **63**: 4433–4451.
 - 34 Han L, Bollas GM. Dynamic optimization of fixed bed chemical-looping combustion processes. *Energy* 2016; **112**: 1107–1119.
 - 35 Chen C, Lee H-H, Chen W, Chang Y-C, Wang E, Shen C-H *et al.* Study of an Iron-Based Oxygen Carrier on the Moving Bed Chemical Looping System. *Energy & Fuels* 2018; **32**: 3660–

- 3667.
- 36 Nandy A, Loha C, Gu S, Sarkar P, Karmakar MK, Chatterjee PK. Present status and overview of Chemical Looping Combustion technology. *Renew Sustain Energy Rev* 2016; **59**: 597–619.
 - 37 Aronsson J, Pallarès D, Lyngfelt A. Modeling and scale analysis of gaseous fuel reactors in chemical looping combustion systems. *Particuology* 2017; **35**: 31–41.
 - 38 Kolbitsch P, Pröll T, Hofbauer H. Modeling of a 120 kW chemical looping combustion reactor system using a Ni-based oxygen carrier. *Chem Eng Sci* 2009; **64**: 99–108.
 - 39 Bougamra A, Huilin L. Modeling of chemical looping combustion of methane using a Ni-based oxygen carrier. *Energy and Fuels* 2014; **28**: 3420–3429.
 - 40 Zerobin F, Penthor S, Bertsch O, Pröll T. Fluidized bed reactor design study for pressurized chemical looping combustion of natural gas. *Powder Technol* 2017; **316**: 569–577.
 - 41 Li J, Zhang H, Gao Z, Fu J, Ao W, Dai J. CO₂ Capture with Chemical Looping Combustion of Gaseous Fuels: An Overview. *Energy & Fuels* 2017; **31**: 3475–3524.
 - 42 Lee D, Nam H, Kim H, Hwang B, Baek J-I, Ryu H-J. Experimental screening of oxygen carrier for a pressurized chemical looping combustion. *Fuel Process Technol* 2021; **218**: 106860.
 - 43 Cabello A, Abad A, de las Obras Loscertales M, Bartocci P, García-Labiano F, de Diego LF. Exploring design options for pressurized chemical looping combustion of natural gas. *Fuel* 2023; **342**: 126983.
 - 44 de Diego LF, Serrano A, García-Labiano F, García-Díez E, Abad A, Gayán P *et al.* Bioethanol combustion with CO₂ capture in a 1kWth Chemical Looping Combustion prototype: Suitability of the oxygen carrier. *Chem Eng J* 2016; **283**: 1405–1413.
 - 45 Moldenhauer P, Rydén M, Mattisson T, Hoteit A, Jamal A, Lyngfelt A. Chemical-looping combustion with fuel oil in a 10 kW pilot plant. *Energy and Fuels* 2014; **28**: 5978–5987.
 - 46 Cao Y, Li B, Zhao HY, Lin CW, Sit SP, Pan WP. Investigation of asphalt (Bitumen)-fuelled chemical looping combustion using durable copper-based oxygen carrier. *Energy Procedia* 2011; **4**: 457–464.
 - 47 Jakob M, Steckel JC. *The Political Economy of Coal: Obstacles to Clean Energy Transitions*. Taylor & Francis, 2022.
 - 48 Bhui B, Vairakannu P. Prospects and issues of integration of co-combustion of solid fuels (coal and biomass) in chemical looping technology. *J Environ Manage* 2019; **231**: 1241–1256.
 - 49 Staničić I, Brorsson J, Hellman A, Mattisson T, Backman R. Thermodynamic Analysis on the Fate of Ash Elements in Chemical Looping Combustion of Solid Fuels—Iron-Based Oxygen Carriers. *Energy & Fuels* 2022; **36**: 9648–9659.
 - 50 Adanez J, Abad A, Garcia-Labiano F, Gayan P, De Diego LF. Progress in chemical-looping combustion and reforming technologies. *Prog Energy Combust Sci* 2012; **38**: 215–282.
 - 51 Abad A, Mattisson T, Lyngfelt A, Rydén M. Chemical-looping combustion in a 300 W continuously operating reactor system using a manganese-based oxygen carrier. *Fuel* 2006; **85**:

- 1174–1185.
- 52 Pérez-astray A, Adánez-rubio I, Mendiara T, Izquierdo MT, Abad A, Gayán P. Comparative study of fuel-N and tar evolution in chemical looping combustion of biomass under both iG-CLC and CLOU modes. *Fuel* 2018; **236**: 598–607.
 - 53 Adánez J, Abad A, Mendiara T, Gayán P, de Diego LF, García-Labiano F. Chemical looping combustion of solid fuels. *Prog Energy Combust Sci* 2018; **65**: 6–66.
 - 54 Chen H, Cheng M, Liu L, Li Y, Li Z, Cai N. Coal-fired chemical looping combustion coupled with a high-efficiency annular carbon stripper. *Int J Greenh Gas Control* 2020; **93**: 102889.
 - 55 Mendiara T, Adánez-Rubio I, Gayán P, Abad A, de Diego LF, García-Labiano F *et al.* Process Comparison for Biomass Combustion: In Situ Gasification-Chemical Looping Combustion (iG-CLC) versus Chemical Looping with Oxygen Uncoupling (CLOU). *Energy Technol* 2016; **4**: 1130–1136.
 - 56 Mendiara T, Pérez-Astray A, Izquierdo MT, Abad A, de Diego LF, García-Labiano F *et al.* Chemical Looping Combustion of different types of biomass in a 0.5 kWth unit. *Fuel* 2018; **211**: 868–875.
 - 57 Lyngfelt A, Leckner B. A 1000 MWth boiler for chemical-looping combustion of solid fuels – Discussion of design and costs. *Appl Energy* 2015; **157**: 475–487.
 - 58 Mei D, Linderholm C, Lyngfelt A. Performance of an oxy-polishing step in the 100 kWth chemical looping combustion prototype. *Chem Eng J* 2021; **409**: 128202.
 - 59 Ridha FN, Duchesne MA, Lu X, Lu DY, Filippou D, Hughes RW. Characterization of an ilmenite ore for pressurized chemical looping combustion. *Appl Energy* 2016; **163**: 323–333.
 - 60 Mendiara T, de Diego LF, García-Labiano F, Gayán P, Abad A, Adánez J. Behaviour of a bauxite waste material as oxygen carrier in a 500Wth CLC unit with coal. *Int J Greenh Gas Control* 2013; **17**: 170–182.
 - 61 Neil B, Meier GH, Pettit FS. *Introduction to the High Temperature Oxidation of Metals*. Cambridge University Press, 2006.
 - 62 Jerndal E, Mattisson T, Lyngfelt A, Combustion C, After O. Thermal analysis of chemical-looping combustion. 2006. doi:10.1205/cherd05020.
 - 63 Bale CW, Bélisle E, Chartrand P, Decterov SA, Eriksson G, Hack K *et al.* FactSage Thermochemical Software and Databases (FactSage 7.0). *CALPHAD* 2016; **54**: 35–55.
 - 64 Hallberg P, Jing D, Rydén M, Mattisson T, Lyngfelt A. Chemical looping combustion and chemical looping with oxygen uncoupling experiments in a batch reactor using spray-dried $\text{CaMn}_{1-x}\text{M}_x\text{O}_{3-\delta}$ ($\text{M} = \text{Ti}, \text{Fe}, \text{Mg}$) particles as oxygen carriers. *Energy and Fuels* 2013; **27**: 1473–1481.
 - 65 Rydén M, Leion H, Mattisson T, Lyngfelt A. Combined oxides as oxygen-carrier material for chemical-looping with oxygen uncoupling. *Appl Energy* 2014; **113**: 1924–1932.
 - 66 Azimi G, Magnus R, Lyngfelt H, Leion T, Anders M. $(\text{Mn}_z\text{Fe}_{1-z})_y\text{O}_x$ Combined Oxides as

- Oxygen Carrier for Chemical-Looping with Oxygen Uncoupling. *VTT Publ* 2003; **59**: 3–194.
- 67 Topal H, Atimtay AT, Durmaz A. Olive cake combustion in a circulating fluidized bed. *Fuel* 2003; **82**: 1049–1056.
 - 68 Fennell P, Anthony B. *Calcium and Chemical Looping Technology for Power Generation and Carbon Dioxide (CO₂) Capture*. 2015.
 - 69 Arjmand M, Hedayati A, Azad A-M, Leion H, Rydén M, Mattisson T. Ca_xLa_{1-x}Mn_{1-y}M_yO_{3-δ} (M = Mg, Ti, Fe, or Cu) as Oxygen Carriers for Chemical-Looping with Oxygen Uncoupling (CLOU). *Energy & Fuels* 2013; **27**: 4097–4107.
 - 70 Galinsky N, Sendi M, Bowers L, Li F. CaMn_{1-x}B_xO_{3-δ} (B = Al, V, Fe, Co, and Ni) perovskite based oxygen carriers for chemical looping with oxygen uncoupling (CLOU). *Appl Energy* 2016; **174**: 80–87.
 - 71 Galinsky N, Mishra A, Zhang J, Li F. Ca_{1-x}A_xMnO₃ (A = Sr and Ba) perovskite based oxygen carriers for chemical looping with oxygen uncoupling (CLOU). *Appl Energy* 2015; **157**: 358–367.
 - 72 Dueso C, Thompson C, Metcalfe I. High-stability, high-capacity oxygen carriers: Iron oxide-perovskite composite materials for hydrogen production by chemical looping. *Appl Energy* 2015; **157**: 382–390.
 - 73 Mu L, Huo Z, Chu F, Wang Z, Shang Y, Yin H *et al.* Assessment of the Redox Characteristics of Iron Ore by Introducing Biomass Ash in the Chemical Looping Combustion Process: Biomass Ash Type, Constituent, and Operating Parameters. *ACS Omega* 2021; **6**: 21676–21689.
 - 74 Kennedy JR, Khadilkar AB, Bhattacharya S, Pisupati S V. Modeling the Impact of Operating Variables on Ash Agglomeration in Chemical Looping Combustion of Solid Fuels. *Ind Eng Chem Res* 2021; **60**: 17970–17979.
 - 75 Morris JD, Sheraz S, Chilton S, Nimmo W. Mechanisms and mitigation of agglomeration during fluidized bed combustion of biomass : A review. *Fuel* 2018; **230**: 452–473.
 - 76 García-Labiano F, De Diego LF, Adánez J, Abad A, Gayán P. Temperature variations in the oxygen carrier particles during their reduction and oxidation in a chemical-looping combustion system. *Chem Eng Sci* 2005; **60**: 851–862.
 - 77 Imtiaz Q, Armutlulu A, Donat F, Naeem MA, Müller CR. Preventing Agglomeration of CuO-Based Oxygen Carriers for Chemical Looping Applications. *ACS Sustain Chem Eng* 2021; **9**: 5972–5980.
 - 78 Fan L. Chemical Looping Systems for Fossil Energy Conversions. 2010; : 420.
 - 79 Werther J, Reppenhagen J, Yang WC. Handbook of Fluidization and Fluid Particles System. In: Dekker M (ed). 2003.
 - 80 Liu F, Kang W, Song C, Jia Z, Chen W, Yang L. Crack propagation and attrition mechanism of oxygen carriers in chemical looping process. *Fuel* 2022; **310**: 122326.
 - 81 Cabello A, Gayán P, García-Labiano F, De Diego LF, Abad A, Adánez J. On the attrition

- evaluation of oxygen carriers in Chemical Looping Combustion. *Fuel Process Technol* 2016; **148**: 188–197.
- 82 De Vos Y, Jacobs M, Van Der Voort P, Van Driessche I, Snijkers F, Verberckmoes A. Development of Stable Oxygen Carrier Materials for Chemical Looping Processes—A Review. *Catalysts* 2020; **10**. doi:10.3390/catal10080926.
 - 83 Patzschke CF. *Copper manganese oxides as oxygen carriers for chemical looping air separation for near- zero emission power generation*. PhD Thesis. Imperial College London. 2018.
 - 84 Krell A, Bales A. Grain Size-Dependent Hardness of Transparent Magnesium Aluminate Spinel. *Int J Appl Ceram Technol* 2011; **8**: 1108–1114.
 - 85 Adánez-Rubio I, Nilsson A, Izquierdo MT, Mendiara T, Abad A, Adánez J. Cu-Mn oxygen carrier with improved mechanical resistance: Analyzing performance under CLC and CLOU environments. *Fuel Process Technol* 2021; **217**: 106819.
 - 86 Bayham S, Straub D, Weber J. Operation of a 50-kWth chemical looping combustion test facility under autothermal conditions. *Int J Greenh Gas Control* 2019; **87**: 211–220.
 - 87 Mattisson T, Järnäs A, Lyngfelt A. Reactivity of some metal oxides supported on alumina with alternating methane and oxygen - Application for chemical-looping combustion. *Energy and Fuels* 2003; **17**: 643–651.
 - 88 Johansson M, Mattisson T, Lyngfelt A. Investigation of Mn_3O_4 with stabilized ZrO_2 for chemical-looping combustion. *Chem Eng Res Des* 2006; **84**: 807–818.
 - 89 Rydén M, Moldenhauer P, Lindqvist S, Mattisson T, Lyngfelt A. Measuring attrition resistance of oxygen carrier particles for chemical looping combustion with a customized jet cup. *Powder Technol* 2014; **256**: 75–86.
 - 90 Kramp M, Thon A, Hartge E-U, Heinrich S, Werther J. The Role of Attrition and Solids Recovery in a Chemical Looping Combustion Process. *Oil Gas Sci Technol – Rev d'IFP Energies Nouv* 2011; **66**: 277–290.
 - 91 Peltola P, Tynjälä T, Ritvanen J, Hyppänen T. Mass, energy, and exergy balance analysis of chemical looping with oxygen uncoupling (CLOU) process. *Energy Convers Manag* 2014; **87**: 483–494.
 - 92 Rasi NM, Karcz A, Ponnurangam S, Mahinpey N. Insight into MgO-supported NiO reactivity from atomic-scale electronegativity for oxygen carrier design and catalyst production applications. *Catal Today* 2022; **404**: 244–252.
 - 93 Zhao H, Zhang Y, Wei Y, Gui J. Understanding CuO-support interaction in Cu-based oxygen carriers at a microcosmic level. *Proc Combust Inst* 2017; **36**: 4069–4077.
 - 94 Leion H, Larring Y, Bakken E, Bredesen R, Mattisson T, Lyngfelt A. Use of $CaMn_{0.875}Ti_{0.125}O_3$ as oxygen carrier in chemical-looping with oxygen uncoupling. *Energy and Fuels* 2009; **23**: 5276–5283.
 - 95 Mattisson T, Jing D, Lyngfelt A, Rydén M. Experimental investigation of binary and ternary

- combined manganese oxides for chemical-looping with oxygen uncoupling (CLOU). *Fuel* 2016; **164**: 228–236.
- 96 Zhang Z, Hills TP, Scott SA, Fennell PS. Spouted bed reactor for kinetic measurements of reduction of Fe_2O_3 in a CO_2/CO atmosphere Part I: Atmospheric pressure measurements and equipment commissioning. *Chem Eng Res Des* 2016; **114**: 307–320.
 - 97 Chuang SY, Dennis JS, Hayhurst AN, Scott SA. Development and performance of Cu-based oxygen carriers for chemical-looping combustion. *Combust Flame* 2008; **154**: 109–121.
 - 98 Li F, Sun Z, Luo S, Fan LS. Ionic diffusion in the oxidation of iron - Effect of support and its implications to chemical looping applications. *Energy Environ Sci* 2011; **4**: 876–880.
 - 99 Idziak K, Czakiert T, Krzywanski J, Zylka A, Kozłowska M, Nowak W. Safety and environmental reasons for the use of Ni-, Co-, Cu-, Mn- and Fe-based oxygen carriers in CLC/CLOU applications: An overview. *Fuel* 2020; **268**: 117245.
 - 100 Adánez J, De Diego LF, García-Labiano F, Gayán P, Abad A, Palacios JM. Selection of oxygen carriers for chemical-looping combustion. *Energy and Fuels* 2004; **18**: 371–377.
 - 101 De Diego LF, García-Labiano F, Adánez J, Gayán P, Abad A, Corbella BM *et al.* Development of Cu-based oxygen carriers for chemical-looping combustion. *Fuel* 2004.
 - 102 Imtiaz Q, Kierzkowska AM, Müller CR. Coprecipitated, copper-based, alumina-stabilized materials for carbon dioxide capture by chemical looping combustion. *ChemSusChem* 2012; **5**: 1610–1618.
 - 103 Adánez-Rubio I, Gayán P, Garcia-Labiano F, De Diego LF, Adánez J, Abad A. Development of CuO-based oxygen-carrier materials suitable for Chemical-Looping with Oxygen Uncoupling (CLOU) process. *Energy Procedia* 2011; **4**: 417–424.
 - 104 Penthor S, Mattisson T, Adánez J, Bertolin S, Masi E, Larring Y *et al.* The EU-FP7 Project SUCCESS – Scale-up of Oxygen Carrier for Chemical Looping Combustion using Environmentally Sustainable Materials. *Energy Procedia* 2017; **114**: 395–406.
 - 105 Penthor S, Zerobin F, Mayer K, Pröll T, Hofbauer H. Investigation of the performance of a copper based oxygen carrier for chemical looping combustion in a 120kW pilot plant for gaseous fuels. *Appl Energy* 2015; **145**: 52–59.
 - 106 Cabello A, Abad A, Mendiara T, Izquierdo MT, de Diego LF. Outstanding performance of a Cu-based oxygen carrier impregnated on alumina in chemical looping combustion. *Chem Eng J* 2023; **455**: 140484.
 - 107 Arjmand M, Azad A-M, Leion H, Lyngfelt A, Mattisson T. Prospects of Al_2O_3 and MgAl_2O_4 -Supported CuO Oxygen Carriers in Chemical-Looping Combustion (CLC) and Chemical-Looping with Oxygen Uncoupling (CLOU). *Energy & Fuels* 2011; **25**: 5493–5502.
 - 108 Chuang SY, Dennis JS, Hayhurst AN, Scott SA. Kinetics of the oxidation of a co-precipitated mixture of Cu and Al_2O_3 by O_2 for chemical-looping combustion. *Energy and Fuels* 2010; **24**: 3917–3927.

- 109 Jacob KT, Alcock CB. Thermodynamics of CuAlO_2 and CuAl_2O_4 and Phase Equilibria in the System Cu_2O - CuO - Al_2O_3 . *J Am Ceram Soc* 1975; **58**: 192–195.
- 110 Donat F, Hu W, Scott SA, Dennis JS. Characteristics of Copper-based Oxygen Carriers Supported on Calcium Aluminates for Chemical-Looping Combustion with Oxygen Uncoupling (CLOU). *Ind Eng Chem Res* 2015; **54**: 6713–6723.
- 111 Imtiaz Q, Broda M, Müller CR. Structure-property relationship of co-precipitated Cu-rich, Al_2O_3 - or MgAl_2O_4 -stabilized oxygen carriers for chemical looping with oxygen uncoupling (CLOU). *Appl Energy* 2014; **119**: 557–565.
- 112 Adánez-Rubio I, Gayán P, Abad A, de Diego LF, García-Labiano F, Adánez J. Evaluation of a Spray-Dried $\text{CuO}/\text{MgAl}_2\text{O}_4$ Oxygen Carrier for the Chemical Looping with Oxygen Uncoupling Process. *Energy & Fuels* 2012; **26**: 3069–3081.
- 113 Arjmand M, Keller M, Leion H, Mattisson T, Lyngfelt A. Oxygen release and oxidation rates of MgAl_2O_4 - supported CuO oxygen carrier for chemical-looping combustion with oxygen uncoupling (CLOU). *Energy and Fuels* 2012; **26**: 6528–6539.
- 114 Bhavsar S, Tackett B, Veser G. Evaluation of iron- and manganese-based mono- and mixed-metallic oxygen carriers for chemical looping combustion. *Fuel* 2014; **136**: 268–279.
- 115 Patzschke CF. *Copper manganese oxides as oxygen carriers for chemical looping air separation for near- zero emission power generation*. PhD Thesis. Imperial College London. 2018.
- 116 Lyngfelt A. Chemical-looping combustion of solid fuels - Status of development. *Appl Energy* 2014; **113**: 1869–1873.
- 117 Galvita V, Hempel T, Lorenz H, Rihko-Struckmann LK, Sundmacher K. Deactivation of Modified Iron Oxide Materials in the Cyclic Water Gas Shift Process for CO-Free Hydrogen Production. *Ind Eng Chem Res* 2008; **47**: 303–310.
- 118 Liu L, Zachariah MR. Enhanced performance of alkali metal doped Fe_2O_3 and $\text{Fe}_2\text{O}_3/\text{Al}_2\text{O}_3$ composites as oxygen carrier material in chemical looping combustion. *Energy and Fuels* 2013; **27**: 4977–4983.
- 119 Zhu M, Song Y, Chen S, Li M, Zhang L, Xiang W. Chemical looping dry reforming of methane with hydrogen generation on $\text{Fe}_2\text{O}_3/\text{Al}_2\text{O}_3$ oxygen carrier. *Chem Eng J* 2019; **368**: 812–823.
- 120 Zhu M, Chen S, Soomro A, Hu J, Sun Z, Ma S *et al*. Effects of supports on reduction activity and carbon deposition of iron oxide for methane chemical looping hydrogen generation. *Appl Energy* 2018; **225**: 912–921.
- 121 Bhavsar S, Najera M, Veser G. Chemical Looping Dry Reforming as Novel, Intensified Process for CO_2 Activation. *Chem Eng Technol* 2012; **35**: 1281–1290.
- 122 Rydén M, Cleverstam E, Johansson M, Lyngfelt A, Mattisson T. Fe_2O_3 on Ce-, Ca-, or Mg-stabilized ZrO_2 as oxygen carrier for chemical-looping combustion using NiO as additive. *AIChE J* 2010; **56**: 2211–2220.
- 123 Mattisson T, Keller M, Linderholm C, Moldenhauer P, Rydén M, Leion H *et al*. Chemical-

- looping technologies using circulating fluidized bed systems: Status of development. *Fuel Process Technol* 2018; **172**: 1–12.
- 124 Adánez-Rubio I, Abad A, Gayán P, Adánez I, De Diego LF, García-Labiano F *et al.* Use of Hopcalite-Derived Cu-Mn Mixed Oxide as Oxygen Carrier for Chemical Looping with Oxygen Uncoupling Process. *Energy and Fuels* 2016; **30**: 5953–5963.
 - 125 Adánez-Rubio I, Pérez-Astray A, Mendiara T, Izquierdo MT, Abad A, Gayán P *et al.* Chemical looping combustion of biomass: CLOU experiments with a Cu-Mn mixed oxide. *Fuel Process Technol* 2018; **172**: 179–186.
 - 126 García-Labiano F, Adánez J, de Diego LF, Gayán P, Abad A. Effect of pressure on the behavior of copper-, iron-, and nickel-based oxygen carriers for chemical-looping combustion. *Energy and Fuels* 2006; **20**: 26–33.
 - 127 Rydén M, Lyngfelt A, Mattisson T. Combined manganese/iron oxides as oxygen carrier for chemical looping combustion with oxygen uncoupling (CLOU) in a circulating fluidized bed reactor system. *Energy Procedia* 2011; **4**: 341–348.
 - 128 Lambert A, Delquie C, Clémeneçon I, Comte E, Lefebvre V, Rousseau J *et al.* Synthesis and characterization of bimetallic Fe/Mn oxides for chemical looping combustion. *Energy Procedia* 2009; **1**: 375–381.
 - 129 Hallberg P, Rydén M, Mattisson T, Lyngfelt A. $\text{CaMnO}_{3.8}$ Made from Low Cost Material Examined as Oxygen Carrier in Chemical-looping Combustion. *Energy Procedia* 2014; **63**: 80–86.
 - 130 Dai X, Yu C, Wu Q. Comparison of LaFeO_3 , $\text{La}_{0.8}\text{Sr}_{0.2}\text{FeO}_3$, and $\text{La}_{0.8}\text{Sr}_{0.2}\text{Fe}_{0.9}\text{Co}_{0.1}\text{O}_3$ perovskite oxides as oxygen carrier for partial oxidation of methane. *J Nat Gas Chem* 2008; **17**: 415–418.
 - 131 Marek E, Hu W, Gaultois M, Grey CP, Scott SA. The use of strontium ferrite in chemical looping systems. *Appl Energy* 2018; **223**: 369–382.
 - 132 Lau CY, Dunstan MT, Hu W, Grey CP, Scott SA. Large scale in silico screening of materials for carbon capture through chemical looping. *Energy Environ Sci* 2017; **10**: 818–831.
 - 133 Larring Y, Pishahang M, Tolchard J, Lind AM, Sunding MF, Stensrød RE *et al.* Fabrication process parameters significantly affect the perovskite oxygen carriers materials (OCM) performance in chemical looping with oxygen uncoupling (CLOU). *J Therm Anal Calorim* 2020; **140**: 577–589.
 - 134 Technische Universitaet Wien. Industrial steam generation with 100% carbon capture and insignificant efficiency penalty - Scale-Up of oxygen Carrier for Chemical-looping combustion using Environmentally Sustainable materials. 2017.
 - 135 Kwong KY, Harrison ARP, Gebers JC, Dennis JS, Marek EJ. Chemical Looping Combustion of a Biomass Char in Fe_2O_3 -, CuO -, and $\text{SrFeO}_{3-\delta}$ -Based Oxygen Carriers. *Energy & Fuels* 2022; **36**: 9437–9449.
 - 136 Porrazzo R, White G, Ocone R. Techno-economic investigation of a chemical looping

- combustion based power plant. *Faraday Discuss* 2016; **192**: 437–457.
- 137 Matzen M, Pinkerton J, Wang X, Demirel Y. Use of natural ores as oxygen carriers in chemical looping combustion: A review. *Int J Greenh Gas Control* 2017; **65**: 1–14.
 - 138 Fossdal A, Bakken E, Øye BA, Schøning C, Kaus I, Mokkelbost T *et al.* Study of inexpensive oxygen carriers for chemical looping combustion. *Int J Greenh Gas Control* 2011; **5**: 483–488.
 - 139 Zhao H, Wang K, Fang Y, Ma J, Mei D, Zheng C. Characterization of natural copper ore as oxygen carrier in chemical-looping with oxygen uncoupling of anthracite. *Int J Greenh Gas Control* 2014; **22**: 154–164.
 - 140 Wang P, Howard B, Means N, Shekhawat D, Berry D. Coal Chemical-Looping with Oxygen Uncoupling (CLOU) Using a Cu-Based Oxygen Carrier Derived from Natural Minerals. *Energies* 2019; **12**. doi:10.3390/en12081453.
 - 141 Wen Y, Li Z, Xu L, Cai N. Experimental Study of Natural Cu Ore Particles as Oxygen Carriers in Chemical Looping with Oxygen Uncoupling (CLOU). *Energy & Fuels* 2012; **26**: 3919–3927.
 - 142 Tian H, Siriwardane R, Simonyi T, Poston J. Natural Ores as Oxygen Carriers in Chemical Looping Combustion. *Energy & Fuels* 2013; **27**: 4108–4118.
 - 143 Yang W, Zhao H, Wang K, Zheng C. Synergistic effects of mixtures of iron ores and copper ores as oxygen carriers in chemical-looping combustion. *Proc Combust Inst* 2015; **35**: 2811–2818.
 - 144 Guo L, Zhao H, Zheng C. Synthesis Gas Generation by Chemical-Looping Reforming of Biomass with Natural Copper Ore as Oxygen Carrier. *Waste and Biomass Valorization* 2015; **6**: 81–89.
 - 145 Wang K, Zhao H, Tian X, Fang Y, Ma J, Zheng C. Chemical-Looping with Oxygen Uncoupling of Different Coals Using Copper Ore as an Oxygen Carrier. *Energy & Fuels* 2015; **29**: 6625–6635.
 - 146 Wang K, Tian X, Zhao H. Sulfur behavior in chemical-looping combustion using a copper ore oxygen carrier. *Appl Energy* 2016; **166**: 84–95.
 - 147 Tian X, Zhao H, Wang K, Ma J, Zheng C. Performance of cement decorated copper ore as oxygen carrier in chemical-looping with oxygen uncoupling. *Int J Greenh Gas Control* 2015; **41**: 210–218.
 - 148 Gu Z, Zhang L, Lu C, Qing S, Li K. Enhanced performance of copper ore oxygen carrier by red mud modification for chemical looping combustion. *Appl Energy* 2020; **277**: 115590.
 - 149 Lyngfelt A, Thunman H. *Carbon Dioxide Capture for Storage in Deep Geologic Formations*. Elsevier: Amsterdam, 2005.
 - 150 Adánez-Rubio I, Abad A, Gayán P, De Diego LF, García-Labiano F, Adánez J. Biomass combustion with CO₂ capture by chemical looping with oxygen uncoupling (CLOU). *Fuel Process Technol* 2014; **124**: 104–114.
 - 151 Guo L, Zhao H, Ma J, Mei D, Zheng C. Comparison of Large-Scale Production Methods of

- Fe₂O₃/Al₂O₃ Oxygen Carriers for Chemical-Looping Combustion. *Chem Eng Technol* 2014; **37**: 1211–1219.
- 152 Izquierdo MT, García-Labiano F, Abad A, Cabello A, Gayán P, de Diego LF *et al.* On the optimization of physical and chemical stability of a Cu/Al₂O₃ impregnated oxygen carrier for chemical looping combustion. *Fuel Process Technol* 2021; **215**: 106740.
 - 153 Song H, Shah K, Doroodchi E, Wall T, Moghtaderi B. Reactivity of Al₂O₃- or SiO₂-Supported Cu-, Mn-, and Co-Based Oxygen Carriers for Chemical Looping Air Separation. *Energy & Fuels* 2014; **28**: 1284–1294.
 - 154 Jing D, Mattisson T, Ryden M, Hallberg P, Hedayati A, Van Noyen J *et al.* Innovative Oxygen Carrier Materials for Chemical-Looping Combustion. *Energy Procedia* 2013; **37**: 645–653.
 - 155 Adánez-Rubio I, Abad A, Gayán P, De Diego LF, García-Labiano F, Adánez J. Identification of operational regions in the Chemical-Looping with Oxygen Uncoupling (CLOU) process with a Cu-based oxygen carrier. *Fuel* 2012; **102**: 634–645.
 - 156 Song Q, Liu W, Bohn CD, Harper RN, Sivaniah E, Scott SA *et al.* A high performance oxygen storage material for chemical looping processes with CO₂ capture. *Energy Environ Sci* 2013; **6**: 288–298.
 - 157 High M, Patzschke CF, Zheng L, Zeng D, Xiao R, Fennell PS *et al.* Hydrotalcite-Derived Copper-Based Oxygen Carrier Materials for Efficient Chemical-Looping Combustion of Solid Fuels with CO₂ Capture. *Energy & Fuels* 2022; **36**: 11062–11076.
 - 158 Wei G, He F, Zhao W, Huang Z, Zhao K, Zhao Z *et al.* Experimental Investigation of Fe–Ni–Al Oxygen Carrier Derived from Hydrotalcite-like Precursors for the Chemical Looping Gasification of Biomass Char. *Energy & Fuels* 2017; **31**: 5174–5182.
 - 159 Zhao Y, Li Y, Jin B, Liang Z. Layered double hydroxide derived bifunctional Ca-Fe-Mg material for integrated CO₂ capture and utilization via chemical looping strategy. *Chem Eng J* 2022; **431**: 133826.
 - 160 Mendes PCD, Song Y, Ma W, Gani TZh, Lim KH, Kawi S *et al.* Opportunities in the design of metal@oxide core-shell nanoparticles. *Adv Phys X* 2023; **8**: 2175623.
 - 161 Luo Z, Zhao G, Pan H, Sun W. Strong Metal–Support Interaction in Heterogeneous Catalysts. *Adv Energy Mater* 2022; **12**: 2201395.
 - 162 Neyman KM, Kozlov SM. Quantifying interactions on interfaces between metal particles and oxide supports in catalytic nanomaterials. *NPG Asia Mater* 2022; **14**: 59.
 - 163 Goebel J, Joo JB, Dahl M, Yin Y. Synthesis of tailored Au@TiO₂ core-shell nanoparticles for photocatalytic reforming of ethanol. *Catal Today* 2014; **225**: 90–95.
 - 164 Park J-N, Zhang P, Hu Y-S, McFarland EW. Synthesis and characterization of sintering-resistant silica-encapsulated Fe₃O₄ magnetic nanoparticles active for oxidation and chemical looping combustion. *Nanotechnology* 2010; **21**: 225708.
 - 165 Ma S, Chen S, Zhu M, Zhao Z, Hu J, Wu M *et al.* Enhanced sintering resistance of Fe₂O₃/CeO₂

- oxygen carrier for chemical looping hydrogen generation using core-shell structure. *Int J Hydrogen Energy* 2019; **44**: 6491–6504.
- 166 Xu Z, Zhao H, Wei Y, Zheng C. Self-assembly template combustion synthesis of a core-shell CuO@TiO₂-Al₂O₃ hierarchical structure as an oxygen carrier for the chemical-looping processes. *Combust Flame* 2015; **162**: 3030–3045.
 - 167 Abad A, Adánez J, García-Labiano F, de Diego LF, Gayán P, Celaya J. Mapping of the range of operational conditions for Cu-, Fe-, and Ni-based oxygen carriers in chemical-looping combustion. *Chem Eng Sci* 2007; **62**: 533–549.
 - 168 García-Labiano F, Gayán P, Adánez J, De Diego LF, Forero CR. Solid waste management of a chemical-looping combustion plant using Cu-based oxygen carriers. *Environ Sci Technol* 2007; **41**: 5882–5887.
 - 169 Abelló S, Mitchell S, Santiago M, Stoica G, Pérez-Ramírez J. Perturbing the properties of layered double hydroxides by continuous coprecipitation with short residence time. *J Mater Chem* 2010; **20**: 5878–5887.
 - 170 Brindley G, Kikkawa S. A crystal-chemical study of Mg, Al and Ni, N hydroxy-perchlorates and hydroxycarbonates. *Am Miner* 1979; **64**: 836--843.
 - 171 Richardson IG. Zn- and Co-based layered double hydroxides: prediction of the *a* parameter from the fraction of trivalent cations and *vice versa*. *Acta Crystallogr Sect B* 2013; **69**: 414–417.
 - 172 Wang Q, O'Hare D. Recent Advances in the Synthesis and Application of Layered Double Hydroxide (LDH) Nanosheets. *Chem Rev* 2012; **112**: 4124–4155.
 - 173 Wang Q, Gao Y, Luo J, Zhong Z, Borgna A, Guo Z *et al.* Synthesis of nano-sized spherical Mg₃Al–CO₃ layered double hydroxide as a high-temperature CO₂ adsorbent. *RSC Adv* 2013; **3**: 3414–3420.
 - 174 Toby BH, Von Dreele RB. GSAS-II: the genesis of a modern open-source all purpose crystallography software package. *J Appl Crystallogr* 2013; **46**: 544–549.
 - 175 Cavani F, Trifirò F, Vaccari A. Hydrotalcite-type anionic clays: Preparation, properties and applications. *Catal Today* 1991; **11**: 173–301.
 - 176 de la Calle C, Pons C-H, Roux J, Rives V. A crystal-chemical study of natural and synthetic anionic clays. *Clays Clay Miner* 2003; **51**: 121–132.
 - 177 Bocclair JW, Braterman PS, Jiang J, Lou S, Yarberry F. Layered Double Hydroxide Stability. 2. Formation of Cr(III)-Containing Layered Double Hydroxides Directly from Solution. *Chem Mater* 1999; **11**: 303–307.
 - 178 Miyata S. Physico-Chemical Properties of Synthetic Hydrotalcites in Relation to Composition. *Clays Clay Miner* 1980; **28**: 50–56.
 - 179 Costantino U, Marmottini F, Nocchetti M, Vivani R. New Synthetic Routes to Hydrotalcite-Like Compounds – Characterisation and Properties of the Obtained Materials. *Eur J Inorg Chem* 1998; **1998**: 1439–1446.

- 180 Evans DG, Slade RCT. Structural Aspects of Layered Double Hydroxides. In: Duan X, Evans DG (eds). *Layered Double Hydroxides*. Springer Berlin Heidelberg: Berlin, Heidelberg, 2006, pp 1–87.
- 181 Chaillot D, Bennici S, Brendlé J. Layered double hydroxides and LDH-derived materials in chosen environmental applications: a review. *Environ Sci Pollut Res* 2021; **28**: 24375–24405.
- 182 He J, Wei M, Li B, Kang Y, Evans DG, Duan X. Preparation of Layered Double Hydroxides. In: Duan X, Evans DG (eds). *Layered Double Hydroxides*. Springer Berlin Heidelberg: Berlin, Heidelberg, 2006, pp 89–119.
- 183 Adachi-Pagano M, Forano C, Besse J-P. Synthesis of Al-rich hydrotalcite-like compounds by using the urea hydrolysis reaction—control of size and morphology. *J Mater Chem* 2003; **13**: 1988–1993.
- 184 Paikaray S, Hendry MJ. Formation and crystallization of $\text{Mg}^{2+}\text{-Fe}^{3+}\text{-SO}_4^{2-}\text{-CO}_3^{2-}$ -type anionic clays. *Appl Clay Sci* 2014; **88–89**: 111–122.
- 185 Yun SK, Pinnavaia TJ. Water Content and Particle Texture of Synthetic Hydrotalcite-like Layered Double Hydroxides. *Chem Mater* 1995; **7**: 348–354.
- 186 Wang Q, Tay HH, Guo Z, Chen L, Liu Y, Chang J *et al.* Morphology and composition controllable synthesis of Mg-Al- CO_3 hydrotalcites by tuning the synthesis pH and the CO_2 capture capacity. *Appl Clay Sci* 2012; **55**: 18–26.
- 187 Seron A, Delorme F. Synthesis of layered double hydroxides (LDHs) with varying pH: A valuable contribution to the study of Mg/Al LDH formation mechanism. *J Phys Chem Solids* 2008; **69**: 1088–1090.
- 188 Cheah LA, Manohara G V, Maroto-Valer MM, Garcia S. Impact of Synthesis Method and Metal Salt Precursors on the CO_2 Adsorption Performance of Layered Double Hydroxides Derived Mixed Metal Oxides. *Front Energy Res* 2022; **10**. doi:10.3389/fenrg.2022.882182.
- 189 Oh J-M, Hwang S-H, Choy J-H. The effect of synthetic conditions on tailoring the size of hydrotalcite particles. *Solid State Ionics* 2002; **151**: 285–291.
- 190 Zeng H-Y, Deng X, Wang Y-J, Liao K-B. Preparation of Mg-Al hydrotalcite by urea method and its catalytic activity for transesterification. *AIChE J* 2009; **55**: 1229–1235.
- 191 Berber MR, Hafez IH, Minagawa K, Katoh M, Mori T, Tanaka M. Uniform nanoparticles of hydrotalcite-like materials and their textural properties at optimized conditions of urea hydrothermal treatment. *J Mol Struct* 2013; **1033**: 104–112.
- 192 Hickey L, Klopogge JT, Frost RL. The effects of various hydrothermal treatments on magnesium-aluminium hydrotalcites. *J Mater Sci* 2000; **35**: 4347–4355.
- 193 Tao Q, Zhang Y, Zhang X, Yuan P, He H. Synthesis and characterization of layered double hydroxides with a high aspect ratio. *J Solid State Chem* 2006; **179**: 708–715.
- 194 Labajos FM, Rives V, Ulibarri MA. Effect of hydrothermal and thermal treatments on the physicochemical properties of Mg-Al hydrotalcite-like materials. *J Mater Sci* 1992; **27**: 1546–

- 1552.
- 195 Ermrich M, Oppen D. XRD for the Analyst: Getting Acquainted with the Principles. 2013.
- 196 Patterson AL. The Scherrer Formula for X-Ray Particle Size Determination. *Phys Rev* 1939; **56**: 978–982.
- 197 Smilgies D-M. Scherrer grain-size analysis adapted to grazing-incidence scattering with area detectors. Erratum. *J Appl Crystallogr* 2013; **46**: 286–286.
- 198 Thommes M, Kaneko K, Neimark A V., Olivier JP, Rodriguez-Reinoso F, Rouquerol J *et al.* Physisorption of gases, with special reference to the evaluation of surface area and pore size distribution (IUPAC Technical Report). *Pure Appl Chem* 2015; **87**: 1051–1069.
- 199 Boot-Handford ME. *The Utilisation of Biomass as a fuel for Chemical Looping Combustion*. PhD Thesis. Imperial College London. 2015.
- 200 Cussler EL. *Diffusion: Mass Transfer in Fluid Systems*. 3rd ed. Cambridge University Press, 2009 doi:10.1017/CBO9780511805134.
- 201 Fuller EN, Schettler PD, Giddings JC. New Method for Prediction of Binary Gas-Phase Diffusion Coefficients. *Ind Eng Chem Res* 1966; **58**: 18–27.
- 202 Hirschfelder J, Curtiss CF, Bird RB. *Molecular Theory of Gases and Liquids*. Wiley: New York, 1954.
- 203 Poling BE, Prausnitz JM, O’Connell JP. *The properties of gases and liquids*. 5th ed. McGraw-Hill, 2007.
- 204 Cui H, Grace JR. Spouting of biomass particles: A review. *Bioresour Technol* 2008; **99**: 4008 – 4020.
- 205 Zhang Z. *The Effect of Sulfur on Chemical Looping Combustion with Iron Oxides*. PhD Thesis. Imperial College London. 2014.
- 206 Fennell PS, Pacciani R, Dennis JS, Davidson JF, Hayhurst AN. The Effects of Repeated Cycles of Calcination and Carbonation on a Variety of Different Limestones, as Measured in a Hot Fluidized Bed of Sand. *Energy & Fuels* 2007; **21**: 2072–2081.
- 207 Tighe C. *Reactions of the Oxides of Nitrogen with Carbonaceous Particles*. PhD Thesis. University of Cambridge. 2009.
- 208 Fan G, Li F, Evans DG, Duan X. Catalytic applications of layered double hydroxides: recent advances and perspectives. *Chem Soc Rev* 2014; **43**: 7040–7066.
- 209 Xu M, Wei M. Layered Double Hydroxide-Based Catalysts: Recent Advances in Preparation, Structure, and Applications. *Adv Funct Mater* 2018; **28**: 1802943.
- 210 Jiang X, Nie X, Guo X, Song C, Chen JG. Recent Advances in Carbon Dioxide Hydrogenation to Methanol via Heterogeneous Catalysis. *Chem Rev* 2020; **120**: 7984–8034.
- 211 High M, Patzschke CF, Zheng L, Zeng D, Gavalda-Diaz O, Ding N *et al.* Precursor engineering of hydrotalcite-derived redox sorbents for reversible and stable thermochemical oxygen storage. *Nat Commun* 2022; **13**: 5109.

- 212 Puigdomènech I, Colàs E, Grivé M, Campos I, García D. A tool to draw chemical equilibrium diagrams using SIT: Applications to geochemical systems and radionuclide solubility. *MRS Online Proc Libr* 2014; **1665**: 111–116.
- 213 Ingri N, Kokołowicz W, Sillén LG, Warnqvist B. High-speed computers as a supplement to graphical methods V. HALTAFALL, a general program for calculating the composition of equilibrium mixtures. *Talanta* 1967; **14**: 1261–1286.
- 214 Eriksson G. An algorithm for the computation of aqueous multi-component, multiphase equilibria. *Anal Chim Acta* 1979; **112**: 375–383.
- 215 Johnson JW, Oelkers EH, Helgeson HC. SUPCRT92: A software package for calculating the standard molal thermodynamic properties of minerals, gases, aqueous species, and reactions from 1 to 5000 bar and 0 to 1000°C. *Comput Geosci* 1992; **18**: 899–947.
- 216 Krupka KM, Cantrell KJ, McGrail BP. Thermodynamic Data for Geochemical Modeling of Carbonate Reactions Associated with CO₂ Sequestration – Literature Review. United States, 2010 <https://www.osti.gov/biblio/992369>.
- 217 Bernard E, Zucha WJ, Lothenbach B, Mäder U. Stability of hydrotalcite (Mg-Al layered double hydroxide) in presence of different anions. *Cem Concr Res* 2022; **152**: 106674.
- 218 Lothenbach B, Winnefeld F. Thermodynamic modelling of the hydration of Portland cement. *Cem Concr Res* 2006; **36**: 209–226.
- 219 Johnson CA, Glasser FP. Hydrotalcite-like minerals (M₂Al(OH)₆(CO₃)_{0.5}.XH₂O, where M = Mg, Zn, Co, Ni) in the environment: synthesis, characterization and thermodynamic stability. *Clays Clay Miner* 2003; **51**: 357.
- 220 Takaya Y, Wu M, Kato Y. Unique Environmental Conditions Required for Dawsonite Formation: Implications from Dawsonite Synthesis Experiments under Alkaline Conditions. *ACS Earth Sp Chem* 2019; **3**: 285–294.
- 221 Hunter BM, Hieringer W, Winkler JR, Gray HB, Müller AM. Effect of interlayer anions on [NiFe]-LDH nanosheet water oxidation activity. *Energy Environ Sci* 2016; **9**: 1734–1743.
- 222 Kim A, Varga I, Adhikari A, Patel R. Recent Advances in Layered Double Hydroxide-Based Electrochemical and Optical Sensors. *Nanomaterials* 2021; **11**.
- 223 Tichit D, Layrac G, Gérardin C. Synthesis of layered double hydroxides through continuous flow processes: A review. *Chem Eng J* 2019; **369**: 302–332.
- 224 Sun X, Dey SK. Insights into the synthesis of layered double hydroxide (LDH) nanoparticles: Part 2. Formation mechanisms of LDH. *J Colloid Interface Sci* 2015; **458**: 160–168.
- 225 Tian X, Wei Y, Zhao H. Experimental Investigation of a CuO/Al₂O₃ Oxygen Carrier for Chemical-Looping Combustion. *Fuel* 2017; **209**: 402–410.
- 226 San Pio MA, Martini M, Gallucci F, Roghair I, van Sint Annaland M. Kinetics of CuO/SiO₂ and CuO/Al₂O₃ oxygen carriers for chemical looping combustion. *Chem Eng Sci* 2018; **175**: 56–71.
- 227 Chung C, Qin L, Shah V, Fan L-S. Chemically and physically robust commercially-viable iron-

- based composite oxygen carriers sustainable over 3000 redox cycles at high temperatures for chemical looping applications. *Energy Environ Sci* 2017; **10**: 2318–2323.
- 228 Zheng X, Che L, Hao Y, Su Q. Cycle performance of Cu-based oxygen carrier based on a chemical-looping combustion process. *J Energy Chem* 2016; **25**: 101–109.
- 229 Arjmand M, Azad A-M, Leion H, Mattisson T, Lyngfelt A. Evaluation of CuAl₂O₄ as an Oxygen Carrier in Chemical-Looping Combustion. *Ind Eng Chem Res* 2012; **51**: 13924–13934.
- 230 Grant R. Argon recycling offers per wafer cost reduction opportunity. Power Energy Solut. http://cdn.pes.eu.com/assets/misc_dec/argon-recycle-pdf-153930238664.pdf (accessed 17 Jun2022).
- 231 Hu W, Donat F, Scott SA, Dennis JS. The interaction between CuO and Al₂O₃ and the reactivity of copper aluminates below 1000°C and their implication on the use of the Cu-Al-O system for oxygen storage and production. *RSC Adv* 2016; **6**: 113016–113024.
- 232 Mills SJ, Christy AG, Génin J-MR, Kameda T, Colombo F. Nomenclature of the hydrotalcite supergroup: natural layered double hydroxides. *Mineral Mag* 2012; **76**: 1289–1336.
- 233 Chiu J, Andrus H. Alstom’s chemical looping technology program update. In: *Proceedings of the 2014 National Energy Technology CO₂ Capture Technology Meeting, Pittsburg, PA, USA*. 2013.
- 234 Staničić I, Cañete Vela I, Backman R, Maric J, Cao Y, Mattisson T. Fate of lead, copper, zinc and antimony during chemical looping gasification of automotive shredder residue. *Fuel* 2021; **302**: 121147.
- 235 Ströhle J, Orth M, Epple B. Design and operation of a 1MWth chemical looping plant. *Appl Energy* 2014; **113**: 1490–1495.
- 236 Behrens M, Kasatkin I, Kühl S, Weinberg G. Phase-Pure Cu,Zn,Al Hydrotalcite-like Materials as Precursors for Copper rich Cu/ZnO/Al₂O₃ Catalysts. *Chem Mater* 2010; **22**: 386–397.
- 237 Dionigi F, Zeng Z, Sinev I, Merzdorf T, Deshpande S, Lopez MB *et al.* In-situ structure and catalytic mechanism of NiFe and CoFe layered double hydroxides during oxygen evolution. *Nat Commun* 2020; **11**: 2522.
- 238 Song F, Hu X. Exfoliation of layered double hydroxides for enhanced oxygen evolution catalysis. *Nat Commun* 2014; **5**: 4477.
- 239 Shi R, Wang Z, Zhao Y, Waterhouse GIN, Li Z, Zhang B *et al.* Room-temperature electrochemical acetylene reduction to ethylene with high conversion and selectivity. *Nat Catal* 2021; **4**: 565–574.
- 240 Bénézech P, Palmer DA, Anovitz LM, Horita J. Dawsonite synthesis and reevaluation of its thermodynamic properties from solubility measurements: Implications for mineral trapping of CO₂. *Geochim Cosmochim Acta* 2007; **71**: 4438–4455.
- 241 Abad A, Adánez-Rubio I, Gayán P, García-Labiano F, de Diego LF, Adánez J. Demonstration of chemical-looping with oxygen uncoupling (CLOU) process in a 1.5kWth continuously

- operating unit using a Cu-based oxygen-carrier. *Int J Greenh Gas Control* 2012; **6**: 189–200.
- 242 Hu W, Donat F, Scott SA, Dennis JS. Kinetics of oxygen uncoupling of a copper based oxygen carrier. *Appl Energy* 2016; **161**: 92–100.
- 243 Song H, Shah K, Doroodchi E, Wall T, Moghtaderi B. Analysis on Chemical Reaction Kinetics of CuO/SiO₂ Oxygen Carriers for Chemical Looping Air Separation. *Energy & Fuels* 2014; **28**: 173–182.
- 244 Tian X, Su M, Zhao H. Kinetics of redox reactions of CuO@TiO₂–Al₂O₃ for chemical looping combustion and chemical looping with oxygen uncoupling. *Combust Flame* 2020; **213**: 255–267.
- 245 Means NC, Burgess WA, Howard BH, Smith MW, Wang P, Shekhawat D. Examining and Modeling Oxygen Uncoupling Kinetics of Cu-Based Oxygen Carriers for Chemical Looping with Oxygen Uncoupling (CLOU) in a Drop Tube Fluidized Bed Reactor. *Energy & Fuels* 2019; **33**: 5610–5619.
- 246 Sahir AH, Sohn HY, Leion H, Lighty JS. Rate Analysis of Chemical-Looping with Oxygen Uncoupling (CLOU) for Solid Fuels. *Energy & Fuels* 2012; **26**: 4395–4404.
- 247 Clayton CK, Whitty KJ. Measurement and modeling of decomposition kinetics for copper oxide-based chemical looping with oxygen uncoupling. *Appl Energy* 2014; **116**: 416–423.
- 248 Adánez-Rubio I, Gayán P, Abad A, García-Labiano F, de Diego LF, Adánez J. Kinetic analysis of a Cu-based oxygen carrier: Relevance of temperature and oxygen partial pressure on reduction and oxidation reactions rates in Chemical Looping with Oxygen Uncoupling (CLOU). *Chem Eng J* 2014; **256**: 69–84.
- 249 Zhang Y, Geng P, Zheng Y. Exploration and practice to improve the kinetic analysis of char-CO₂ gasification via thermogravimetric analysis. *Chem Eng J* 2019; **359**: 298–304.
- 250 Fan Y, Yao JG, Zhang Z, Sceats M, Zhuo Y, Li L *et al.* Pressurized calcium looping in the presence of steam in a spout-fluidized-bed reactor with DFT analysis. *Fuel Process Technol* 2018; **169**: 24–41.
- 251 Satterfield CN. *Heterogeneous Catalysis in Practice*. McGraw-Hill: New York; London, 1980.
- 252 Wakao N, Funazkri T. Effect of fluid dispersion coefficients on particle-to-fluid mass transfer coefficients in packed beds: Correlation of sherwood numbers. *Chem Eng Sci* 1978; **33**: 1375–1384.
- 253 La Nauze RD, Jung K, Kastl J. Mass transfer to large particles in fluidised beds of smaller particles. *Chem Eng Sci* 1984; **39**: 1623–1633.
- 254 Wen CY, Yu YH. A generalized method for predicting the minimum fluidization velocity. *AIChE J* 1966; **12**: 610–612.
- 255 Kunii D, Levenspiel O. CHAPTER 3 - Fluidization and Mapping of Regimes. In: Kunii D, Levenspiel O (eds). *Fluidization Engineering (Second Edition)*. Butterworth-Heinemann: Boston, 1991, pp 61–94.

- 256 Davidson JF, Harrison D. *Fluidised Particles*. Cambridge University Press, 1963.
- 257 Davidson JF, Harrison D, Darton RC, LaNauze RD. The two-phase theory of fluidization and its application to chemical reactors. In: *Chemical Reactor Theory, A Review*. Prentice-Hall, 1977, pp 583–685.
- 258 Hayhurst AN, Parmar MS. Measurement of the mass transfer coefficient and Sherwood number for carbon spheres burning in a bubbling fluidized bed. *Combust Flame* 2002; **130**: 361–375.
- 259 Liu W, Lim JY, Saucedo MA, Hayhurst AN, Scott SA, Dennis JS. Kinetics of the reduction of wüstite by hydrogen and carbon monoxide for the chemical looping production of hydrogen. *Chem Eng Sci* 2014; **120**: 149–166.
- 260 Saucedo MA, Butel M, Scott SA, Collings N, Dennis JS. Significance of gasification during oxy-fuel combustion of a lignite char in a fluidised bed using a fast UEGO sensor. *Fuel* 2015; **144**: 423–438.
- 261 Wu L, Peng B, Li Q, Wang Q, Yan X, Lin Q *et al*. Formation of high crystalline LDH sludge for removing Cu and Zn from wastewater by controlled double-jet precipitation. *Environ Sci Pollut Res* 2019; **26**: 19665–19675.
- 262 Clark I, Dunne PW, Gomes RL, Lester E. Continuous hydrothermal synthesis of $\text{Ca}_2\text{Al}(\text{OH})_2(\text{NO}_3)_2$ layered double hydroxides: The impact of reactor temperature, pressure and NaOH concentration on crystal characteristics. *J Colloid Interface Sci* 2017; **504**: 492–499.
- 263 Bookin AS, Drits VA. Polytype diversity of the hydrotalcite-like minerals I. possible polytypes and their diffraction features. *Clays Clay Miner* 1993; **41**: 551–557.
- 264 Drits VA, Bookin AS. *Crystal Structure and X-ray Identification of Layered Double Hydroxides*. Nova Science Publishers, 2006.
- 265 Valente JS, Hernandez-Cortez J, Cantu MS, Ferrat G, López-Salinas E. Calcined layered double hydroxides Mg-Me-Al (Me: Cu, Fe, Ni, Zn) as bifunctional catalysts. *Catal Today* 2010; **150**: 340–345.
- 266 Costantino U, Costantino F, Elisei F, Latterini L, Nocchetti M. Coupling physical chemical techniques with hydrotalcite-like compounds to exploit their structural features and new multifunctional hybrids with luminescent properties. *Phys Chem Chem Phys* 2013; **15**: 13254–13269.
- 267 Mohammadi S, Esmailpour A, Doustkhah E, Assadi MHN. Stability Trends in Mono-Metallic 3d Layered Double Hydroxides. *Nanomaterials* 2022; **12**. doi:10.3390/nano12081339.
- 268 Sławiński WA, Sjøstad AO, Fjellvåg H. Stacking Faults and Polytypes for Layered Double Hydroxides: What Can We Learn from Simulated and Experimental X-ray Powder Diffraction Data? *Inorg Chem* 2016; **55**: 12881–12889.
- 269 Radha A V., Shivakumara C, Kamath PV. DIFFaX simulations of stacking faults in layered double hydroxides (LDHs). *Clays Clay Miner* 2005; **53**: 520–527.
- 270 Radha A V., Thomas GS, Kamath PV, Antonyraj CA, Kannan S. Thermal decomposition of Co-

- Al layered double hydroxide: Identification of precursor to oxide with spinel structure. *Bull Mater Sci* 2010; **33**: 319–324.
- 271 Thomas GS, Radha A V., Kamath PV, Kannan S. Thermally induced polytype transformations among the Layered Double Hydroxides (LDHs) of Mg, Zn with Al. *J Phys Chem B* 2006; **110**: 12365–12371.
- 272 Leont'eva NN, Drozdov V, Bel'skaya B, Cherepanova S V. Structural Analysis of Defects in Layered Double Hydroxides and Related Mixed Oxides. *Russ J Gen Chem* 2020; **90**: 509–522.
- 273 Bookin AS, Cherkashin VI, Drits VA. Polytype diversity of the hydrotalcite-like minerals II. determination of the polytypes of experimentally studied varieties. *Clays Clay Miner* 1993; **41**: 558 – 564.
- 274 Krivovichev S V, Yakovenchuk VN, Zolotarev AAJ, Ivanyuk GN, Pakhomovsky YA. Cation ordering and superstructures in natural layered double hydroxides. *Chimia (Aarau)* 2010; **64**: 730–735.
- 275 Radha A V., Kamath PV, Shivakumara C. Order and disorder among the layered double hydroxides: combined Rietveld and DIFFaX approach. *Acta Crystallogr Sect B Struct Sci* 2007; **63**: 243–250.
- 276 Shivaramaiah R, Navrotsky A. Energetics of Order–Disorder in Layered Magnesium Aluminum Double Hydroxides with Interlayer Carbonate. *Inorg Chem* 2015; **54**: 3253–3259.
- 277 Treacy MMJ, Deem MW, Newsam JM. DIFFaX version 1.812; <http://www.public.asu.edu/~mtreacy/DIFFaX.html>. 2005; 1–71.
- 278 Casas-Cabanas M, Reynaud M, Rikarte J, Horbach P, Rodríguez-Carvajal J. FAULTS: A program for refinement of structures with extended defects. *J Appl Crystallogr* 2016; **49**: 2259–2269.
- 279 Faour A, Prévot V, Taviot-Gueho C. Microstructural study of different LDH morphologies obtained via different synthesis routes. *J Phys Chem Solids* 2010; **71**: 487–490.
- 280 Faour A, Mousty C, Prevot V, Devouard B, De Roy A, Bordet P *et al.* Correlation among Structure, Microstructure, and Electrochemical Properties of NiAl–CO₃ Layered Double Hydroxide Thin Films. *J Phys Chem C* 2012; **116**: 15646–15659.
- 281 Fu Q, Wang C, Wu C, Wu Y, Dai X, Jin W *et al.* Investigating the combined effects of wide stacking faults and grain size on the mechanical properties and corrosion resistance of high-purity Mg. *J Alloys Compd* 2022; **927**: 167018.
- 282 Bellotto M, Rebours B, Clause O, Lynch J, Bazin D, Elkaïm E. A Reexamination of Hydrotalcite Crystal Chemistry. *J Phys Chem* 1996; **100**: 8527–8534.
- 283 Allmann R. The crystal structure of pyroaurite. *Acta Crystallogr Sect B* 1968; **24**: 972–977.
- 284 Arakcheeva A V, Pushcharovskii DY, Rastsvetaeva RK, Atencio D, Lubman GU. Crystal structure and comparative crystal chemistry of Al₂Mg₄(OH)₁₂(CO₃)·3H₂O, a new mineral from the hydrotalcite-manasseite group. *Crystallogr Reports* 1996; **41**: 972–981.

- 285 Xu ZP, Lu GQ (Max). Hydrothermal Synthesis of Layered Double Hydroxides (LDHs) from Mixed MgO and Al₂O₃: LDH Formation Mechanism. *Chem Mater* 2005; **17**: 1055–1062.
- 286 Tamura H, Chiba J, Ito M, Takeda T, Kikkawa S, Mawatari Y *et al.* Formation of hydrotalcite in aqueous solutions and intercalation of ATP by anion exchange. *J Colloid Interface Sci* 2006; **300**: 648–654.
- 287 Bocclair JW, Braterman PS. Layered Double Hydroxide Stability. 1. Relative Stabilities of Layered Double Hydroxides and Their Simple Counterparts. *Chem Mater* 1999; **11**: 298–302.
- 288 Wu M, Guo E, Li Q, Mi J, Fan H. Mesoporous Zn-Fe-based binary metal oxide sorbent with sheet-shaped morphology: Synthesis and application for highly efficient desulfurization of hot coal gas. *Chem Eng J* 2020; **389**: 123750.
- 289 Han B, Gomez MA, Yao S, Chen Y, Li S, Zhang D *et al.* A new and improved synthesis method for the formation of ZnFe-CO₃ and ZnFe-SO₄ Hydrotalcites free from impurities. *Appl Clay Sci* 2019; **181**: 105215.
- 290 Schneider CA, Rasband WS, Eliceiri KW. NIH Image to ImageJ: 25 years of image analysis. *Nat Methods* 2012; **9**: 671–675.
- 291 Zhao Y, Li F, Zhang R, Evans DG, Duan X. Preparation of Layered Double-Hydroxide Nanomaterials with a Uniform Crystallite Size Using a New Method Involving Separate Nucleation and Aging Steps. *Chem Mater* 2002; **14**: 4286–4291.
- 292 Intissar M, Seron A, Giovannelli F, Autret C, Motelica-Heino M, Delorme F. Effect of copper content on the synthesis and properties of (Mg_{4-x}Cu_x)Al₂OH₁₂CO₃·nH₂O layered double hydroxides. *J Mater Sci* 2015; **50**: 1427–1434.
- 293 Delidovich I, Palkovits R. Structure–performance correlations of Mg–Al hydrotalcite catalysts for the isomerization of glucose into fructose. *J Catal* 2015; **327**: 1–9.
- 294 Said S, Elhossieny M, Riad M, Mikhail S. Pristine Cu (Co)/Fe layered double hydroxides (Co(Cu)/Fe-LDH) as active catalysts for the transalkylation of toluene to trimethylbenzenes. *Mol Catal* 2018; **445**: 213–222.
- 295 Galvão TLP, Neves CS, Zheludkevich ML, Gomes JRB, Tedim J, Ferreira MGS. How Density Functional Theory Surface Energies May Explain the Morphology of Particles, Nanosheets, and Conversion Films Based on Layered Double Hydroxides. *J Phys Chem C* 2017; **121**: 2211–2220.
- 296 Lok M. Coprecipitation. In: *Synthesis of Solid Catalysts*. John Wiley & Sons, Ltd, 2009, pp 135–151.
- 297 Rojas Delgado R, Arandigoyen Vidaurre M, De Pauli CP, Ulibarri MA, Avena MJ. Surface-charging behavior of Zn–Cr layered double hydroxide. *J Colloid Interface Sci* 2004; **280**: 431–441.
- 298 Yu M, Hou W. Predicting Points of Zero Net Charge of Layered Double Hydroxides. *Langmuir* 2018; **34**: 12619–12624.

- 299 Yu M, Du N, Hou W. Model prediction of the point of zero net charge of layered double hydroxides and clay minerals. *Colloids Surfaces A Physicochem Eng Asp* 2021; **611**: 125860.
- 300 Parks GA. The Isoelectric Points of Solid Oxides, Solid Hydroxides, and Aqueous Hydroxo Complex Systems. *Chem Rev* 1965; **65**: 177–198.
- 301 Yoon RH, Salman T, Donnay G. Predicting points of zero charge of oxides and hydroxides. *J Colloid Interface Sci* 1979; **70**: 483–493.
- 302 Li DX, Hou WG, Li SP, Hao MT, Zhang GY. The Isoelectric Point and the Points of Zero Charge of Fe-Al-Mg Hydrotalcite-like Compounds. *Chinese Chem Lett* 2004; **15**: 224–227.
- 303 Leggat RB, Taylor SA, Taylor SR. Adhesion of epoxy to hydrotalcite conversion coatings: I. Correlation with wettability and electrokinetic measurements. *Colloids Surfaces A Physicochem Eng Asp* 2002; **210**: 69–81.
- 304 Rojas R, Barriga C, De Pauli CP, Avena MJ. Influence of carbonate intercalation in the surface-charging behavior of Zn–Cr layered double hydroxides. *Mater Chem Phys* 2010; **119**: 303–308.
- 305 Huang X, Yang X, Li G, Ezech CI, Sun C, Snape C. Hybrid Two-step Preparation of Nanosized MgAl Layered Double Hydroxides for CO₂ Adsorption. In: Kyzas G, Lazaridis N (eds). *Sorption in 2020s*. IntechOpen: Rijeka, 2019 doi:10.5772/intechopen.86608.
- 306 Bai S, Li T, Wang H, Tan L, Zhao Y, Song Y-F. Scale-up synthesis of monolayer layered double hydroxide nanosheets via separate nucleation and aging steps method for efficient CO₂ photoreduction. *Chem Eng J* 2021; **419**: 129390.
- 307 Zou RP, Yu AB. Evaluation of the packing characteristics of mono-sized non-spherical particles. *Powder Technol* 1996; **88**: 71–79.
- 308 Bayham SC, Breault R, Monazam E. Particulate solid attrition in CFB systems – An assessment for emerging technologies. *Powder Technol* 2016; **302**: 42–62.
- 309 Schruben JS, Vaux WG. Attrition in the bubbling zone of a steady-state fluidised bed. *Chem Eng Commun* 1985; **33**: 337–347.
- 310 Siriwardane R, Riley J, Benincosa W, Bayham S, Bobek M, Straub D *et al.* Development of CuFeMnAlO_{4+δ} oxygen carrier with high attrition resistance and 50-kWth methane/air chemical looping combustion tests. *Appl Energy* 2021; **286**: 116507.
- 311 Noorman S, Gallucci F, van Sint Annaland M, Kuipers JAM. A theoretical investigation of CLC in packed beds. Part 1: Particle model. *Chem Eng J* 2011; **167**: 297–307.